

DEVELOPMENT OF NANO CARBON AND CONDUCTING
POLYMERS BASED TERNARY COMPOSITES FOR
SUPERCAPATTERY

JAVED IQBAL

FACULTY OF SCIENCE

UNIVERSITI MALAYA

KUALA LUMPUR

2020

**DEVELOPMENT OF NANO CARBON AND
CONDUCTING POLYMERS BASED TERNARY
COMPOSITES FOR SUPERCAPATTERY**

JAVED IQBAL

**THESIS SUBMITTED IN FULFILMENT OF THE
REQUIREMENTS FOR THE DEGREE OF DOCTOR OF
PHILOSOPHY**

**DEPARTMENT OF CHEMISTRY
FACULTY OF SCIENCE
UNIVERSITI MALAYA
KUALA LUMPUR**

2020

UNIVERSITI MALAYA

ORIGINAL LITERARY WORK DECLARATION

Name of Candidate: **JAVED IQBAL**

Matric No: **SHC 160062**

Name of Degree: **DOCTOR OF PHILOSOPHY**

Title of Thesis:

**DEVELOPMENT OF NANO CARBON AND CONDUCTING POLYMERS
BASED TERNARY COMPOSITES FOR SUPERCAPATTERY**

Field of Study:

MATERIAL CHEMISTRY

I do solemnly and sincerely declare that:

- (1) I am the sole author/writer of this Work;
- (2) This Work is original;
- (3) Any use of any work in which copyright exists was done by way of fair dealing and for permitted purposes and any excerpt or extract from, or reference to or reproduction of any copyright work has been disclosed expressly and sufficiently and the title of the Work and its authorship have been acknowledged in this Work;
- (4) I do not have any actual knowledge nor do I ought reasonably to know that the making of this work constitutes an infringement of any copyright work;
- (5) I hereby assign all and every rights in the copyright to this Work to the University of Malaya ("UM"), who henceforth shall be owner of the copyright in this Work and that any reproduction or use in any form or by any means whatsoever is prohibited without the written consent of UM having been first had and obtained;
- (6) I am fully aware that if in the course of making this Work I have infringed any copyright whether intentionally or otherwise, I may be subject to legal action or any other action as may be determined by UM.

Candidate's Signature

Date:

Subscribed and solemnly declared before,

Witness's Signature

Date:

Name:

Designation:

DEVELOPMENT OF NANO CARBON AND CONDUCTING POLYMERS BASED TERNARY COMPOSITES FOR SUPERCAPATERY

ABSTRACT

Although significant efforts have been devoted on the development of energy storage systems such as batteries and fuel cells in the past decades, the low power density, short cyclic life and high maintenance cost have kept them away from many applications. Alternatively, supercapattery which has the characteristic features of batteries as well as supercapacitors has gained much attention because of its rapid charge/discharge mechanism, long life cycle, and high power density. However, supercapattery generally suffers from poor energy density. This research aims to develop carbon and conducting polymers based ternary nanocomposites for high performance supercapattery. Pristine metal oxide nanostructures suffer from high particle aggregations which lead to decrease the electrochemically active sites, therefore, conducting matrices are used to develop the nanocomposites. In this work, hydrothermal route was used to develop ternary nanocomposites of metal oxide (cobalt oxide, Co_3O_4), noble metals (silver (Ag) and gold (Au)) and carbonaceous matrices such as multiwalled carbon nanotubes (MWCNTs), reduced graphene oxide (rGO) as well as conducting polymers such as polypyrrole (PPy) and polyaniline (PANI). The synthesized ternary nanocomposites were characterized by various analytical techniques. The electrochemical performances were studied through cyclic voltammetry, galvanostatic charge-discharge and electrochemical impedance spectroscopy techniques. In the first system, ternary nanocomposites of multiwalled carbon nanotubes intercalated with cobalt oxide nanograins and decorated with silver nanoparticles (NPs) were synthesized and used for supercapattery application. The fabricated device Ag/ Co_3O_4 @MWCNTs//activated carbon (AC) delivered maximum energy and power density values of 16.50 Wh kg^{-1} and 297.50 W kg^{-1} , respectively. In the second system, gold nanoparticles were used instead of silver to synthesize the ternary

nanocomposite (Au/Co₃O₄@MWCNTs) to check the effect on the device performance by changing the noble metal. The supercapattery device demonstrated splendid cycling stability with a retention value of 91.90 % in 1 M KOH (potassium hydroxide) electrolyte for over 3500 cycles with an energy density of 18.80 Wh kg⁻¹ at a power density of 302.00 W kg⁻¹. In the third system, ternary nanocomposite was synthesized with rGO instead of MWCNTs and evaluated its (Ag/Co₃O₄@rGO) performance as positive electrode material in supercapattery. The assembled devices found to deliver the highest energy density 23.63 Wh kg⁻¹ at a power density of 440.00 W kg⁻¹. In the fourth system, polypyrrole was used as a conducting platform to synthesize the ternary nanocomposite and subsequently used to develop two electrodes assembly (Ag/Co₃O₄@PPy//AC). The resultant device achieved the maximum energy density of 24.79 Wh kg⁻¹ with the corresponding power density, 554.40 W kg⁻¹. In the fifth system, polypyrrole was replaced with polyaniline to develop ternary nanocomposite, *i.e.*, Ag/Co₃O₄@PANI. The fabricated device (Ag/Co₃O₄@PANI//AC) based on ternary nanocomposite deliver energy density and power density, 14.01 Wh kg⁻¹ and 165.00 W kg⁻¹, respectively. From the obtained results, it can be understood that all the five systems incorporated with carbonaceous matrices and conducting polymers as a conducting platform produced excellent results. This work ventures the frontiers of carbonaceous materials and conducting polymers based ternary nanocomposites for energy storage devices.

Keywords: Ternary nanocomposites, supercapattery, metal oxides, carbonaceous materials, conducting polymers, noble metals, electrode material.

PEMBANGUNAN KARBON NANO DAN POLIMER KONDUKTIF BERASASKAN KOMPOSIT PERTIGAAN UNTUK SUPERKAPATERI

ABSTRAK

Walaupun usaha gigih telah ditumpukan pada pembangunan sistem penyimpanan tenaga seperti bateri dan sel bahan bakar dalam dekad yang lalu, kepadatan daya yang rendah, kitaran hayat yang pendek dan kos penyelenggaraan yang tinggi telah menghalang mereka daripada digunakan untuk banyak aplikasi. Secara alternatif, superkapateri yang mempunyai ciri-ciri bateri serta superkapasitor telah banyak mendapat perhatian kerana mekanisma caj/discaj yang pantas, kitaran hayat yang panjang, dan ketumpatan kuasa yang tinggi. Walau bagaimanapun, superkapateri secara umumnya mengalami ketumpatan tenaga yang lemah. Tujuan penyelidikan ini adalah untuk membina karbon dan polimer berasaskan komposit nano ternari untuk prestasi superkapateri yang tinggi. Struktur nano logam oksida murni mengalami agregasi zarah yang tinggi yang mengakibatkan pengurangan tapak aktif elektrokimia. Oleh itu, matriks konduktif digunakan untuk membangunkan komposit nano. Dalam kerja ini, laluan hidroterma digunakan untuk membangunkan komposit ternari logam oksida (kobalt oksida, Co_3O_4), logam mulia (perak (Ag) dan emas (Au)) dan matriks karbon seperti karbon tiub nano pelbagai dinding (MWCNTs), grafina oksida terturun (rGO) serta polimer konduktif seperti polypyrrole (PPy) dan polyaniline (PANI). Nanocomposites ternary yang disintesis dicirikan oleh pelbagai teknik analisis. Persembahan elektrokimia dikaji melalui teknik kitaran voltametri, cas-discaj galvanostatik dan spektroskopi elektrokimia impedans. Dalam sistem pertama, komposit nano karbon tiub nano pelbagai dinding diselang-selikan dengan butiran nano kobalt oksida dan dihiasi dengan partikel nano perak telah disintesis dan digunakan untuk aplikasi superkapateri. Peranti yang telah dibuat, $\text{Ag}/\text{Co}_3\text{O}_4@\text{MWCNTs}/\text{activated carbon (AC)}$ memberikan nilai maksimum tenaga dan kepadatan daya masing-masing sebanyak 16.50 Wh kg^{-1} dan 297.50 W kg^{-1} . Dalam sistem kedua, partikel nano emas telah digunakan untuk menggantikan perak

untuk mensintesis komposit nano ternari ($\text{Au}/\text{Co}_3\text{O}_4@\text{MWCNTs}$) untuk memeriksa kesan prestasi peranti dengan mengubah logam mulia. Peranti supercapateri menunjukkan kestabilan kitaran yang bagus dengan nilai pengekaln 91.90 % dalam 1 M KOH elektrolit untuk kitaran lebih daripada 3500 kitaran dengan ketumpatan tenaga sebanyak 18.80 Wh kg^{-1} pada ketumpatan kuasa sebanyak 302.00 W kg^{-1} . Dalam sistem ketiga, komposit nano ternari disintesis dengan rGO menggantikan MWCNTs dan prestasinya ($\text{Ag}/\text{Co}_3\text{O}_4@ \text{rGO}$) dinilai sebagai bahan elektrod positif dalam supercapateri. Peranti yang dipasang memberikan ketumpatan tenaga tertinggi, 23.63 Wh kg^{-1} pada ketumpatan kuasa sebanyak 440.00 W kg^{-1} . Secara keseluruhannya, tiga sistem di mana matriks karbon digunakan sebagai platform konduktif menghasilkan keputusan yang sangat baik. Dalam sistem keempat, polypyrrole digunakan sebagai platform untuk mensintesis komposit nano ternari dan seterusnya digunakan untuk membina pemasangan dua elektrod ($\text{Ag}/\text{Co}_3\text{O}_4@\text{PPy}/\text{AC}$). Peranti yang dihasilkan mencapai kepadatan tenaga maksimum sebanyak 24.79 Wh kg^{-1} dengan ketumpatan kuasa yang sama sebanyak 554.40 W kg^{-1} . Dalam sistem kelima, polypyrrole digantikan dengan polyaniline untuk membina komposite nano ternari, iaitu, $\text{Ag}/\text{Co}_3\text{O}_4@\text{PANI}$. Peranti yang telah dibina ($\text{Ag}/\text{Co}_3\text{O}_4@\text{PANI}/\text{AC}$) berdasarkan komposit nano ternari memberikan kepadatan tenaga dan kepadatan upaya, masing-masing sebanyak 14.01 Wh kg^{-1} dan 165.00 W kg^{-1} . Keseluruhannya, kesemua lima sistem di mana matriks karbon dan polimer konduktif digunakan sebagai platform konduktif menghasilkan keputusan yang sangat baik. Kerja ini meneroka sempadan bahan-bahan karbon dan polimer konduktif berasaskan komposit nano ternari untuk peranti penyimpanan tenaga.

Katakunci: komposit nano ternari, superkapateri, logam oksida, bahan-bahan karbon, polimer konduktif, logam-logam mulia, bahan elektrod.

ACKNOWLEDGEMENTS

First and foremost, praises and thanks to **ALLAH Almighty** for His showers of countless blessings and strength given unto me to complete my doctoral studies.

Special thanks are due to my supervisors, **Professor Dr. Ramesh T Subramaniam, Associate Professor Dr. Ramesh Kasi and Associate Professor Dr. Sharifah Mohammad** who have gone beyond a mere supervision by providing me with intellectual discussions, constant encouragement, excellent learning environment and more over their friendly behavior allowed me to discuss every single issue without any hesitation regarding academic, administrative and social issues. I improved my scientific writing skills from their critical evaluations of my research articles which enabled me to publish my research work in high quality and well reputed international scientific journals.

I am highly indebted to thank Dr. Numan Arshid, who has introduced me to the supercapattery technology and helped me throughout my research work. His thoughtful suggestions always helped me to produce quality work, are highly regarded. I would like to thank all my group mates Dr. Shahid Bashir, Dr. Fatin Saiha, Dr. Chong Mee Yoke, Miss Shahira Saidi, Miss Khuzaimah Aziz and Ms. Maryam Hina for their help, providing friendly lab environment and for rescuing me whenever I need help. I would also like to pay humble gratitude to my Universiti Malaya fellows Dr. Saqib Rafique, Dr Shahid Mehmood, Mr. Tawab Shah, Mr. Mohammad Usman and Mr. Ali Akbar for their wonderful discussions on scientific and social issues as well as enjoying quality fun time with them during my stay at Universiti Malaya.

I am also immensely indebted and very grateful for the support of my wife and family members, to whom I dedicate this thesis.

TABLE OF CONTENTS

ABSTRACT	iii
ABSTRAK	v
ACKNOWLEDGEMENT	vii
TABLE OF CONTENTS	viii
LIST OF FIGURE	xv
LIST OF TABLES	xxiii
LIST OF SYMBOLS AND ABBREVIATIONS	xxiv
CHAPTER 1: INTRODUCTION	1
1.1 Research Background	1
1.2 Hypothesis	6
1.3 Aims and Objectives of Research	8
1.4 Outline of Thesis	9
CHAPTER 2: LITERATURE REVIEW	11
2.1 Supercapacitors	11
2.1.1 Overview	11
2.1.2 Working Principle	13
2.1.3 Charge Storage in Electrical Double Layer Capacitors	13

2.1.4	Charge Storage in Pseudocapacitors	16
2.1.5	Supercapattery	18
2.1.6	Applications of Supercapattery	19
2.1.6.1	Stationary Electrical Energy Storage	20
2.1.6.2	Portable Power Systems	20
2.2	Electrode Materials for Electrochemical Energy Storage Systems	21
2.2.1	Carbonaceous Materials	21
2.2.1.1	Activated Carbon.....	23
2.2.1.2	Carbon Black.....	24
2.2.1.3	Fullerene.....	25
2.2.1.4	Graphite.....	26
2.2.1.5	Carbon Nanotubes (CNTs).....	27
2.2.1.6	Graphene	32
2.2.1.7	Graphene Oxide (GO)	33
2.2.1.8	Reduced Graphene Oxide (rGO).....	36
2.2.2	Conducting Polymers	39
2.2.2.1	Polypyrrole	41
2.2.2.2	Polyaniline.....	43

2.2.3	Transition Metal Oxides (TMO)	46
2.2.3.2	Properties of Metal Oxides.....	53
2.2.3.3	Cobalt Oxide (Co ₃ O ₄).....	55
2.3	Noble Metals.....	56
2.4	Ternary Nanocomposites as Electrode Material.....	59
CHAPTER 3: MATERIALS AND METHODS		61
3.1	Materials	61
3.2	Synthesis of Ternary Nanocomposites	62
3.2.1	Functionalization of Multiwalled Carbon Nanotubes	63
3.2.2	Synthesis of Graphene Oxide	63
3.2.3	Synthesis of Cobalt Oxide Nanograins.....	64
3.2.4	Synthesis of Polypyrrole	64
3.2.5	Synthesis of Polyaniline	65
3.2.6	Synthesis of Multiwalled Carbon Nanotubes Based Ternary Nanocomposites, (Ag/Co ₃ O ₄ @MWCNTs) and (Au/Co ₃ O ₄ @MWCNTs).....	65
3.2.7	Synthesis of Reduced Graphene Oxide Based Ternary Nanocomposite, (Ag/Co ₃ O ₄ @rGO)	66

3.2.8	Synthesis of Conducting Polymers Based Ternary Nanocomposites, (Ag/Co ₃ O ₄ @PPy) and (Ag/Co ₃ O ₄ @PANI).....	66
3.3	Characterization Techniques	67
3.3.1	Electron Microscopy Studies.....	67
3.3.2	X-ray Diffraction Analysis	68
3.3.3	X-ray Photoelectron Spectroscopy Analysis	68
3.4	Electrochemical Analysis	69
3.4.1	Preparation of Electrodes	69
3.4.2	Electrochemical Studies	70
CHAPTER 4: RESULTS AND DISCUSSION		71
4.1	Multiwalled Carbon Nanotubes Based Ternary Nanocomposites.....	71
4.2	System 1: Multiwalled Carbon Nanotubes Incorporated with Silver Nanoparticles and Cobalt Oxide Nanograins (Ag/Co ₃ O ₄ @MWCNTs), Ternary Nanocomposite.....	74
4.2.1	Surface Morphology Study	74
4.2.2	X-ray diffraction Analysis.....	77
4.2.3	X-ray Photoelectron Spectroscopy (XPS) Analysis	78
4.2.4	Electrochemical Analysis of Co ₃ O ₄ , Co ₃ O ₄ @MWCNTs and Ag/Co ₃ O ₄ @MWCNTs, Ternary Nanocomposite.....	79

4.2.5	Electrochemical Performance of Assembled, Ag/Co ₃ O ₄ @MWCNTs//AC Supercapattery	86
4.3	System 2: Gold Nanoparticles, Cobalt oxide Nanograins and Multiwalled Carbon Nanotubes Based Ternary Nanocomposite, (Au/Co ₃ O ₄ @MWCNTs) ...	91
4.3.1	Surface Morphology Study	91
4.3.2	X-ray diffraction Analysis.....	93
4.3.3	X-ray Photoelectron Spectroscopy (XPS) Analysis.....	94
4.3.4	Electrochemical Analysis of Gold, Cobalt Oxide, and Multiwalled Carbon Nanotubes, (Au/Co ₃ O ₄ @MWCNTs) Based Ternary Nanocomposite	95
4.3.5	Electrochemical Performance of Assembled Au/Co ₃ O ₄ @MWCNTs//AC Supercapattery	101
4.4	Reduced Graphene Oxide Based Ternary Nanocomposite	105
4.5	System 3: Silver Nanoparticles and Cobalt Oxide Nanograins Grown on Reduced Graphene Oxide, (Ag/Co ₃ O ₄ @rGO)	106
4.5.1	Surface Morphology Study	106
4.5.2	X-ray diffraction Analysis.....	109
4.5.3	X-ray Photoelectron Spectroscopy (XPS) Analysis.....	110
4.5.4	Electrochemical Analysis of Silver Nanoparticles and Cobalt Oxide Nanograins Grown on Reduced Graphene Oxide, (Ag/Co ₃ O ₄ @rGO).....	112

4.5.5	Electrochemical Performance of Assembled Ag/Co ₃ O ₄ @rGO//AC Supercapattery	120
4.6	Conducting Polymers Based Ternary Nanocomposites	124
4.7	System 4: Polypyrrole (PPy) Incorporated with Silver Nanoparticles and Cobalt Oxide Nanograins (Ag/Co ₃ O ₄ @PPy) Based Ternary Nanocomposite.....	126
4.7.1	Surface Morphology Study	126
4.7.2	X-ray diffraction Analysis.....	128
4.7.3	X-ray Photoelectron Spectroscopy (XPS) Analysis.....	129
4.7.4	Electrochemical Analysis of Polypyrrole (PPy), Co ₃ O ₄ @PPy, and Ag/Co ₃ O ₄ @PPy Ternary Nanocomposite.....	131
4.7.5	Electrochemical Performance of Assembled Ag/Co ₃ O ₄ @PPy//AC Supercapattery	136
4.8	System 5: Polyaniline (PANI) Incorporated with Silver Nanoparticles and Cobalt Oxide (Ag/Co ₃ O ₄ @PANI) Based Ternary Nanocomposite.....	141
4.8.1	Surface Morphology Study	141
4.8.2	X-ray diffraction Analysis.....	142
4.8.3	X-ray Photoelectron Spectroscopy (XPS) Analysis.....	144
4.8.4	Electrochemical Analysis of Polyaniline Incorporated with Silver Nanoparticles and Cobalt Oxide Nanograins Based Ternary Nanocomposite	145

4.8.5	Electrochemical Performance of Assembled Ag/Co ₃ O ₄ @PANI//AC Supercapattery	151
4.9	Comparison of the Developed Systems	156
CHAPTER 5: CONCLUSION		160
5.1	Conclusion	160
5.2	Future Work	164
REFERENCES		165
LIST OF PUBLICATIONS AND PAPERS PRESENTED		185

LIST OF FIGURES

Figure 1.1	: Ragone plot presentation of various energy storage systems (Kötz & Carlen, 2000)..	2
Figure 2.1	: Models for a surface with positive charge on electrical double layer system: (a)Helmholtz model, (b) the Chapman and Gouy model, and (c) the model given by Stern with the IHP and OHP, d gives the separation of the double layer defined by Helmholtz model. Ψ and ψ_0 depict the electrode surface potential and that of the electrode/electrolyte interface, individually (Zhang & Zhao, 2009).	15
Figure 2.2	: Hierarchical classification of supercapacitors and construction of supercapattery.	19
Figure 2.3	: Different types of carbon materials used for electrochemical applications.	23
Figure 2.4	: (a) Solid filling of fullerene lattice structure and (b) Lattice structure of fullerene.	25
Figure 2.5	: Stacked graphene sheets in graphite.	26
Figure 2.6	: Graphically illustration of (a) SWCNTs and (b) MWCNTs.....	27
Figure 2.7	: Figure 2.7: Schematic illustration of pristine and functionalized CNTs.	31
Figure 2.8	: (a) Honeycomb lattice structure of graphene, (b) graphical presentation of sp^2 hybridized orbitals of carbon atoms which forms σ -bonds and π -bonds.....	33
Figure 2.9	: Graphene oxide containing functional groups on its honeycomb matrix.	34
Figure 2.10	: rGO containing less functional groups compared to GO on its honeycomb lattice.	37
Figure 2.11	: Structural formula of pyrrole monomer	42
Figure 2.12	: Schematic illustration of polyaniline in different oxidation states (Le et al., 2017).	44
Figure 3.1	: Schematic illustration of the synthesis of the ternary nanocomposites by hydrothermal method.	63

Figure 4.1	: Schematic representation of the formation of ternary nanocomposite of cobalt oxide nanoparticles intercalated in MWCNTs matrix and decorated with noble metal M(Ag/Au)..	73
Figure 4.2	: FESEM images of (a) Co_3O_4 nanograins, (b) $\text{Co}_3\text{O}_4@\text{MWCNTs}$ binary nanocomposite (c) low magnification image of $\text{Ag}/\text{Co}_3\text{O}_4@\text{MWCNTs}$ ternary nanocomposites, and (d) high magnification image of $\text{Ag}/\text{Co}_3\text{O}_4@\text{MWCNTs}$ ternary nanocomposites.....	75
Figure 4.3	: HRTEM images of $\text{Ag}/\text{Co}_3\text{O}_4@\text{MWCNTs}$ ternary nanocomposite (a) at low and (b) at high magnifications.....	75
Figure 4.4	: (a) FESEM image of the $\text{Ag}/\text{Co}_3\text{O}_4@\text{MWCNTs}$ nanocomposite at low magnification used for EDS, (b) EDS spectrum of $\text{Ag}/\text{Co}_3\text{O}_4@\text{MWCNTs}$ nanocomposite, (c) elemental mapping of Ag, (d) elemental mapping of Co, (e) elemental mapping of C, (f) elemental mapping showing the uniform distribution of C, Ag and Co in the $\text{Ag}/\text{Co}_3\text{O}_4@\text{MWCNTs}$ ternary nanocomposites.....	76
Figure 4.5	: XRD patterns of pure Co_3O_4 nanograins, $\text{Co}_3\text{O}_4@\text{MWCNTs}$ and $\text{Ag}/\text{Co}_3\text{O}_4@\text{MWCNTs}$ nanocomposites.	78
Figure 4.6	: (a) XPS survey scanning of the $\text{Ag}/\text{Co}_3\text{O}_4@\text{MWCNTs}$, ternary nanocomposites. The high resolution spectra (b) C <i>1s</i> region, (c) Co <i>2p</i> region, (d) O <i>1s</i> region and (e) Ag <i>3d</i> region.....	79
Figure 4.7	: (a) Comparison of CV curves of pure Co_3O_4 and bare Ni foam. Cyclic voltammograms at diverse scan rates (b) Co_3O_4 nanograins, (c) $\text{Co}_3\text{O}_4@\text{MWCNTs}$, (d) $\text{Ag}/\text{Co}_3\text{O}_4@\text{MWCNTs}$, ternary nanocomposite and (e) comparison of CV curves of pure Co_3O_4 nanograins, $\text{Co}_3\text{O}_4@\text{MWCNTs}$ and $\text{Ag}/\text{Co}_3\text{O}_4@\text{MWCNTs}$ at a scan rate of 3 mV s^{-1}	82
Figure 4.8	: Discharge curves of (a) Co_3O_4 nanograins, (b) $\text{Co}_3\text{O}_4@\text{MWCNTs}$ (c) $\text{Ag}/\text{Co}_3\text{O}_4@\text{MWCNTs}$ nanocomposites at diverse current densities (d) Comparative discharge curves of pure Co_3O_4 nanograins, $\text{Co}_3\text{O}_4@\text{MWCNTs}$ and $\text{Ag}/\text{Co}_3\text{O}_4@\text{MWCNTs}$ nanocomposites at a current density of 0.6 A g^{-1}	83
Figure 4.9	: (a) Specific capacity of Co_3O_4 nanograins, $\text{Co}_3\text{O}_4@\text{MWCNTs}$, and $\text{Ag}/\text{Co}_3\text{O}_4@\text{MWCNTs}$ nanocomposites at different current densities, (b) Nyquist plots of pure Co_3O_4 nanograins,	86

Co₃O₄@MWCNT, and Ag/Co₃O₄@MWCNTs nanocomposites.....

Figure 4.10	: (a) Schematic of the assembled Ag/Co ₃ O ₄ @MWCNTs//AC supercapattery, (b) comparative CV curves of Ag/Co ₃ O ₄ @MWCNTs as +ve and AC as -ve electrode carried out at the scan rate of 10 mV s ⁻¹ in a system of three electrodes cell in 1 M KOH electrolyte, (c) CV curve of Ag/Co ₃ O ₄ @MWCNTs//AC supercapattery measured at a diverse potential window at a scan rate of 10 mV s ⁻¹ and (d) CV curves of Ag/Co ₃ O ₄ @MWCNTs//AC supercapattery assessed at various scan rates.....	88
Figure 4.11	: GCD curves of Ag/Co ₃ O ₄ @MWCNTs//AC supercapattery at (a) different potential windows and (b) different current densities.....	90
Figure 4.12	: Cycling stability of Ag/Co ₃ O ₄ @MWCNTs//AC supercapattery and inset figure showing the energy density versus power density results.....	90
Figure 4.13	: FESEM images of (a) Co ₃ O ₄ @MWCNTs binary nanocomposite; (b) low and (c) high magnification images of Au/Co ₃ O ₄ @MWCNTs sample showing Co ₃ O ₄ and Au NPs decorated on MWCNTs network.	92
Figure 4.14	: TEM images of Au/Co ₃ O ₄ @MWCNTs ternary nanocomposite, (a) at low and (b) at high magnifications. The inset Figure 4.14(b) showing the Co ₃ O ₄ and Au nanoparticles.	92
Figure 4.15	: (a) EDS spectrum shows the elemental composition and, EDS-elemental mapping of (b) C, (c) Co, (d) O, (e) Au content of the Au/Co ₃ O ₄ @MWCNTs ternary nanocomposite. (f) Mix-verifies the even distribution of both the Co ₃ O ₄ and Au NPs on the MWCNTs network.....	93
Figure 4.16	: XRD pattern of the Co ₃ O ₄ , Co ₃ O ₄ @MWCNTs binary and Au/Co ₃ O ₄ @MWCNTs ternary nanocomposites scanned in the 2θ range of 10°-70°.....	93
Figure 4.17	: (a) A survey spectrum of Au/Co ₃ O ₄ @MWCNTs, ternary nanocomposites, core-level XPS spectra of (b) Au 4f, (c) O 1s, (d) C 1s and (e) Co 2p.....	95
Figure 4.18	: CV curves of (a) pristine Co ₃ O ₄ NPs (b) Co ₃ O ₄ @MWCNTs binary and (c) Au/Co ₃ O ₄ @MWCNTs ternary nanocomposite measured at varied scan rates. (d) CV curves to compare the	

	electrochemical performance of Co_3O_4 NPs, Co_3O_4 @MWCNTs binary and $\text{Au}/\text{Co}_3\text{O}_4$ @MWCNTs ternary nanocomposites recorded at 3 mV s^{-1}	98
Figure 4.19	: (a) Specific capacities of Co_3O_4 NPs, Co_3O_4 @MWCNTs binary and $\text{Au}/\text{Co}_3\text{O}_4$ @MWCNTs ternary nanocomposites at various scanning rates, (b) Nyquist plots of the Co_3O_4 NPs, Co_3O_4 @MWCNTs binary and $\text{Au}/\text{Co}_3\text{O}_4$ @MWCNTs ternary nanocomposites. Inset Figure 4.19(b) shows the EIS spectrum in high frequency region.	100
Figure 4.20	: GCD curves at various current densities, (a) Co_3O_4 , (b) Co_3O_4 @MWCNTs, (c) $\text{Au}/\text{Co}_3\text{O}_4$ @MWCNTs and (d) comparison curves for all three variants at a current density of 0.9 A g^{-1}	101
Figure 4.21	: (a) The graphical presentation of assembled supercapattery and comparative CV curves of $\text{Au}/\text{Co}_3\text{O}_4$ @MWCNTs, ternary nanocomposites and AC electrodes performed in a two electrodes cell in KOH aqueous solution at a scan rate of 10 mV s^{-1} . (b) CV curves of optimized $\text{Au}/\text{Co}_3\text{O}_4$ @MWCNTs, ternary nanocomposites based supercapattery measured at different potential windows. Galvanostatic charge-discharge curves of $\text{Au}/\text{Co}_3\text{O}_4$ @MWCNTs, ternary nanocomposite based supercapattery device at (c) high and (d) low current densities.	104
Figure 4.22	: (a) Nyquist plot of $\text{Au}/\text{Co}_3\text{O}_4$ @MWCNTs//AC assembled device, (b) cyclic performance of the $\text{Au}/\text{Co}_3\text{O}_4$ @MWCNTs, ternary nanocomposites electrode as a function of the number of cycles at a current density of 4.0 A g^{-1} in 1 M KOH . The inset shows the power density decay vs energy density of the assembled devices.	104
Figure 4.23	: FESEM micrographs of (a) Co_3O_4 @rGO binary nanocomposites (b) low and (c) high magnification images of the $\text{Ag}/\text{Co}_3\text{O}_4$ @rGO, ternary nanocomposite.	107
Figure 4.24	: TEM images of the $\text{Ag}/\text{Co}_3\text{O}_4$ @rGO ternary nanocomposite (a) at low and (b and inset) at high magnifications.	107
Figure 4.25	: (a) EDS spectrum of the $\text{Ag}/\text{Co}_3\text{O}_4$ @rGO, ternary nanocomposites, (b) compounded image demonstrating the even distribution of cobalt, silver, and carbon in the $\text{Ag}/\text{Co}_3\text{O}_4$ @rGO, ternary nanocomposites, (c) the representation of elemental scan of carbon, (d) Oxygen, (e) Cobalt, and (f) Silver.	108

Figure 4.26	: XRD patterns of pure Co_3O_4 nanograins (black), $\text{Co}_3\text{O}_4@\text{rGO}$ (red) and $\text{Ag}/\text{Co}_3\text{O}_4@\text{rGO}$ nanocomposite (blue).	110
Figure 4.27	: (a) Survey scanning of the $\text{Ag}/\text{Co}_3\text{O}_4@\text{rGO}$, ternary nanocomposites. High resolution spectra (b) $\text{C } 1s$ region, (c) $\text{O } 1s$ region, (d) $\text{Ag } 3d$ region and (e) $\text{Co } 2p_{2/3}$ region.....	112
Figure 4.28	: Cyclic voltammograms of (a) Co_3O_4 nanograins, (b) $\text{Co}_3\text{O}_4@\text{rGO}$, (c) $\text{Ag}/\text{Co}_3\text{O}_4@\text{rGO}$ ternary nanocomposite at diverse scanning rates and (d) comparison CV curves of pure Co_3O_4 nanograins, $\text{Co}_3\text{O}_4@\text{rGO}$ binary nanocomposite and $\text{Ag}/\text{Co}_3\text{O}_4@\text{rGO}$ ternary nanocomposite at 5 mV s^{-1} scan rate.	114
Figure 4.29	: Charge-discharge plots at various current densities of (a) Co_3O_4 nanograins, (b) $\text{Co}_3\text{O}_4@\text{rGO}$, (c) $\text{Ag}/\text{Co}_3\text{O}_4@\text{rGO}$ and (d) comparative charge-discharge plots of unaided Co_3O_4 , $\text{Co}_3\text{O}_4@\text{rGO}$ and $\text{Ag}/\text{Co}_3\text{O}_4@\text{rGO}$ ternary nanocomposite at a constant current density (1.0 A g^{-1}).	116
Figure 4.30	: Specific capacity of Co_3O_4 nanograins (black), $\text{Co}_3\text{O}_4@\text{rGO}$ (red), and $\text{Ag}/\text{Co}_3\text{O}_4@\text{rGO}$ (blue) nanocomposites at different current densities.	117
Figure 4.31	: Nyquist plots of pure Co_3O_4 nanograins, $\text{Co}_3\text{O}_4@\text{rGO}$, and $\text{Ag}/\text{Co}_3\text{O}_4@\text{rGO}$ nanocomposites and the inset Figure is showing high frequency region.....	120
Figure 4.32	: (a) Graphical presentation of the assembled $\text{Ag}/\text{Co}_3\text{O}_4@\text{rGO}//\text{AC}$ supercapattery, (b) voltammograms of $\text{Ag}/\text{Co}_3\text{O}_4@\text{rGO}$ and AC electrode performed at a scanning rate of 10 mV s^{-1} in a three electrodes cell in 1 M KOH solution, (c) CVs of $\text{Ag}/\text{Co}_3\text{O}_4@\text{rGO}//\text{AC}$ device assessed at diverse scanning rates and (d) GCD curves of $\text{Ag}/\text{Co}_3\text{O}_4@\text{rGO}//\text{AC}$ supercapattery at different current densities.	123
Figure 4.33	: (a) Nyquist plots for $\text{Ag}/\text{Co}_3\text{O}_4@\text{rGO}//\text{AC}$ supercapattery. Figure 4.33(b) showing the cycling stability of $\text{Ag}/\text{Co}_3\text{O}_4@\text{rGO}//\text{AC}$ supercapattery and the inset plot is for energy density decay versus power density.	123
Figure 4.34	: FESEM images of (a) pure PPy, (b) $\text{Co}_3\text{O}_4@\text{PPy}$, binary nanocomposite, (c) $\text{Ag}/\text{Co}_3\text{O}_4@\text{PPy}$, ternary nanocomposite and inset Figure 4.30(c) showing Co_3O_4 and Ag NPs well linked on the PPy.	127
Figure 4.35	: TEM images of ternary nanocomposite, $\text{Ag}/\text{Co}_3\text{O}_4@\text{PPy}$ (a) low magnification and (b) high magnification.....	127

Figure 4.36	: TEM images of ternary nanocomposite, Ag/Co ₃ O ₄ @PPy (a) low magnification and (b) high magnification.....	128
Figure 4.37	: XRD pattern of PPy, Co ₃ O ₄ , Co ₃ O ₄ @PPy binary and Ag/Co ₃ O ₄ @PPy, ternary nanocomposites scanned in the 2θ range of 5°- 80°.....	128
Figure 4.38	: (a) Survey scan spectra of ternary nanocomposite Ag/Co ₃ O ₄ @PPy and the presentation of high resolution spectra of C 1s (b), O 1s (c), N 1s (d), Co 2p _{3/2} (e) and (f) Ag 3d.	130
Figure 4.39	: CV curves of (a) PPy, (b) Co ₃ O ₄ @PPy binary and (c) Ag/Co ₃ O ₄ @PPy ternary nanocomposites measured at varied scan rates. (d) CV curves to compare electrochemical performance of PPy, Co ₃ O ₄ @PPy binary and Ag/Co ₃ O ₄ @PPy, ternary nanocomposites recorded at 3 mV s ⁻¹	132
Figure 4.40	: GCD cures at various current densities, (a) PPy, (b) Co ₃ O ₄ @PPy, (c) Ag/Co ₃ O ₄ @PPy and (d) comparison curves for all three variants at current density of 1.4 A g ⁻¹	133
Figure 4.41	: Showing specific capacity versus current density decay of PPy, Co ₃ O ₄ @PPy binary and Ag/Co ₃ O ₄ @PPy ternary nanocomposites.....	135
Figure 4.42	: Nyquist plots of pure PPy, Co ₃ O ₄ @PPy, and Ag/Co ₃ O ₄ @PPy nanocomposites. Inset Figure shows the high frequency region of the plot.	136
Figure 4.43	: (a) Graphical presentation of the assembled supercapattery incorporating ternary nanocomposites, Ag/Co ₃ O ₄ @PPy as a positive material, (b) voltammograms of Ag/Co ₃ O ₄ @PPy and AC electrodes performed at a scanning rate of 10 mV s ⁻¹ in a standard three electrodes cell system in 1 M KOH solution, (c) CV of assembled Ag/Co ₃ O ₄ @PPy//AC device assessed at diverse potential in 1 M KOH electrolyte and (d) CV curves of Ag/Co ₃ O ₄ @PPy//AC supercapattery at different scanning rates from 3 to 100 mV s ⁻¹	138
Figure 4.44	: (a) Galvanostatic charge-discharge curves of supercapattery devices using Ag/Co ₃ O ₄ @PPy, ternary nanocomposites as a positive electrode material at various current densities ranging from 0.7 to 3.0 A g ⁻¹ (b) Cyclic performance of the Ag/Co ₃ O ₄ @PPy ternary nanocomposites electrode in an assembled device as a function of the number of cycles at a current density of 3.0 A g ⁻¹ in 1 M KOH. The inset Figure	139

	4.44(b) shows the power density decay vs energy density of the assembled devices.	
Figure 4.45	: FESEM images of (a) PANI, (b) $\text{Co}_3\text{O}_4@\text{PANI}$ binary nanocomposite, (c) $\text{Ag}/\text{Co}_3\text{O}_4@\text{PANI}$ ternary nanocomposite and inset Figure 4.45(c) showing the high magnification image of Co_3O_4 and Ag NPs decorated on PANI matrix.	141
Figure 4.46	: TEM images of ternary nanocomposite, $\text{Ag}/\text{Co}_3\text{O}_4@\text{PANI}$ and inset image focused on the Co_3O_4 and Ag nanoparticles embedded in the PANI matrix.	142
Figure 4.47	: (a) EDS spectrum shows the elemental composition and verify the even distribution of both the Co_3O_4 and Ag NPs on the PANI matrix. EDS-elemental mapping is presented by (b) C, (c) N, (d) O, (e) C and (f) Ag contents of the $\text{Ag}/\text{Co}_3\text{O}_4@\text{PANI}$ ternary nanocomposite.	142
Figure 4.48	: XRD pattern of PANI, Co_3O_4 , $\text{Co}_3\text{O}_4@\text{PANI}$ binary and $\text{Ag}/\text{Co}_3\text{O}_4@\text{PANI}$ ternary nanocomposite scanned in the 2θ range of 5° - 80°	143
Figure 4.49	: a) XPS survey scan spectra of ternary nanocomposite, $\text{Ag}/\text{Co}_3\text{O}_4@\text{PANI}$. The representation of high-resolution spectra of C $1s$ (b), O $1s$ (c), N $1s$ (d), Co $2p_{3/2}$ (e) and (f) Ag $3d$	145
Figure 4.50	: CV curves of (a) PANI, (b) $\text{Co}_3\text{O}_4@\text{PANI}$ binary and (c) $\text{Ag}/\text{Co}_3\text{O}_4@\text{PANI}$ ternary nanocomposite measured at varied scan rates and (d) CV curves to compare electrochemical performance of PANI, $\text{Co}_3\text{O}_4@\text{PANI}$ binary and $\text{Ag}/\text{Co}_3\text{O}_4@\text{PANI}$ ternary nanocomposite recorded at a scan rate of 3 mV s^{-1}	147
Figure 4.51	: GCD curves at various current densities, (a) PANI, (b) $\text{Co}_3\text{O}_4@\text{PANI}$, (c) $\text{Ag}/\text{Co}_3\text{O}_4@\text{PANI}$ and (d) comparison of GCD curves for all three variants at current density of 1.5 A g^{-1}	149
Figure 4.52	: Specific capacity versus current density plot of PANI, $\text{Co}_3\text{O}_4@\text{PANI}$ and $\text{Ag}/\text{Co}_3\text{O}_4@\text{PANI}$ nanocomposites.	150
Figure 4.53	: Nyquist plot of pure PANI, $\text{Co}_3\text{O}_4@\text{PANI}$, and $\text{Ag}/\text{Co}_3\text{O}_4@\text{PANI}$ nanocomposites. Inset Figure shows the enlarged high frequency region.	151

Figure 4.54	: (a) Graphical presentation of the assembled supercapattery incorporating ternary nanocomposites, Ag/Co ₃ O ₄ @PANI as a positive electrode material and AC as a negative electrode material, (b) CVs of Ag/Co ₃ O ₄ @PANI and AC at a scanning rate of 3 mV s ⁻¹ in a standard three electrodes cell system in 1 M KOH, (c) CV scans of two electrodes assembled device at different potential windows and (d) CV curves of Ag/Co ₃ O ₄ @PANI//AC supercapattery at different scanning rates from 3 to 200 mV s ⁻¹ in 1 M KOH electrolyte in two electrodes cell system.....	153
Figure 4.55	: (a) Charge-discharge plots of the assembled device, Ag/Co ₃ O ₄ @PANI//AC supercapattery at different potentials at current density 0.2 A g ⁻¹ and (b) charge-discharge plots at various current densities ranging from 0.2 to 2.0 A g ⁻¹ at potential 1.5 V.....	154
Figure 4.56	: (a) Cycling stability studies of Ag/Co ₃ O ₄ @PANI//AC supercapattery. Inset Figure 4.56(a) shows the energy density versus power density studies relations and (b) Nyquist plot of the assembled device.....	154

LIST OF TABLES

Table 3.1	: Materials and Chemicals	61
Table 4.1	: Comparison of specific capacity, power density, energy density and capacity retention of all five ternary nanocomposites based systems	159

Universiti Malaya

LIST OF SYMBOLS AND ABBREVIATIONS

AC	:	Activated carbon
CB	:	Carbon black
CPs	:	Conducting polymers
CV	:	Cyclic voltammetry
CVD	:	Chemical Vapor Deposition
EDS	:	Energy dispersive X-ray spectroscopy
EDL	:	Electrical double layer
EDLCs	:	Electrical double layer capacitors
EIS	:	Electrochemical impedance spectroscopy
ESCA	:	Electron Spectroscopy for Chemical Analysis
ESR	:	Equivalence series resistance
FESEM	:	Field emission scanning electron microscopy
GCD	:	Galvanostatic charge-discharge
GO	:	Graphene Oxide
HRTEM	:	High resolution transmission electron microscopy
IHP	:	Internal Helmholtz plane
MTMO	:	Mixed transition metal oxides

MWCNTs	:	Multiwalled carbon nanotubes
OHP	:	Outer Helmholtz plane
PANI	:	Polyaniline
PP	:	Potassium persulfate
PPy	:	Polypyrrole
Q_s	:	Specific capacity
rGO	:	Reduced graphene oxide
TEM	:	Transmission electron microscope
TMO	:	Transition Metal Oxides
XPS	:	X-ray Photoelectron Spectroscopy
XRD	:	X-ray diffraction

CHAPTER 1: INTRODUCTION

1.1 Research Background

The demand of renewable energy resources has become a prime interest of the modern age because of the reduction of fossil, environmental pollution and their unaffordable growing cost (Azar et al., 2003; Jacobsson & Johnson, 2000). Solar and wind power energy are the fascinating alternative renewable energy resources (Khare et al., 2016). The limitations of these renewable resources are weather and day-night dependent efficiency of the systems. In order to overcome these issues, backup storage is needed to be integrated with the systems for disruption free power supply (Evans et al., 2009; Khare et al., 2016). Among several known energy storage devices, electrochemical method of energy storage like supercapacitors is paid much attention of the scientists worldwide (González et al., 2016; Wang et al., 2012; Zhi et al., 2013). They became on the horizon as shining stars due to the distinctive features of long cyclic life, eminent energy density, gratified power density, rapid charge-discharge mechanism, wide operating temperature range and on top of that environmental friendliness which makes them acceptable in the present era. Supercapacitors store charge electrostatically and electrochemically (Miller & Simon, 2008; Trasatti & Kurzweil, 1994). It has the characteristic features of electrical double-layer capacitors (EDLCs) and batteries (Shukla et al., 2000; Simon et al., 2014). EDLCs store charge electrostatically and normally carbonaceous materials are used in their fabrication (Sharma & Bhatti, 2010). Whereas, redox reactions are implied in batteries in the mechanism of charge storage and the redox-active materials are used in them (also called pseudocapacitive materials) (Weber et al., 2011). Thus, supercapacitor comprises of two charge storage systems, *i.e.*, capacitors and batteries play their role to obtain the maximum benefits of both mechanisms. Therefore, supercapacitor possesses the enhanced power density and good energy density features of capacitors and batteries,

respectively. Further development and engineering strategies have been exploited by scientists to make supercapacitors an advanced energy storage system.

The Ragone plot shown below in Figure 1.1 is a standard method to envisage the energy storage routine of numerous devices (Kötz & Carlen, 2000). Supercapacitors possess small energy density due to their physical ability of charge storage and feature of capacitors, while massive power densities when compared with that of the batteries and the fuel cells. Whereas, batteries and fuel cells are associated with increased energy densities but lower power densities because of the sluggish reaction kinetics. So, the electrochemical supercapacitors have the ability to build up the bridge between capacitors and batteries or that of the fuel cells. They propose the advances in the maintenance of the high energy density of batteries with minimum compromise on the enhanced power density offered by the supercapacitors. This aspect could introduce noteworthy advantages in the application of peak power delivery, such as braking of regenerative, acceleration of the electric vehicle and uninterrupted power supply.

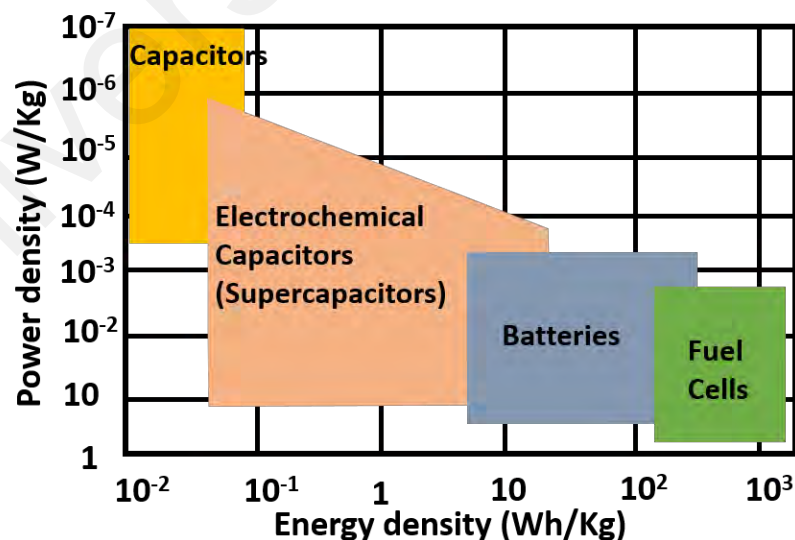


Figure 1.1: Ragone plot presentation of various energy storage systems (Kötz & Carlen, 2000).

Among the other research area, the prime focus of the researchers was on nanotechnology in the 20th century due to the diversity in properties of nanomaterials. They have been successfully exploited in various areas such as optoelectronics, energy storage, energy conversion, fuel cells, biomedical, sensing, and electrochemical applications. The commonly known nanomaterials are the transition metal oxides which came in the limelight of nanotechnology due to their extraordinary physiochemical, optical, and magnetic properties. In the recent past, nanostructures of metal oxides and noble metals have been exploited for energy storage and conversion applications. As a standalone material, metal oxide NPs undergo particle aggregation resulting in the reduction of active sites of the nanograins which in turn causing the rapid capacity fading and geometrical changes throughout in the repeated cyclic charge-discharge process. The current problem foregrounds to explore the suitable strategies to overcome the degree of particles aggregation, increase of active sites which in turn could improve the capacity fading and their potential for energy storage applications.

Carbonaceous and conducting polymer materials with charismatic properties are suitable for electrochemical energy storage devices which make them ideal building block for such applications. These materials are capable of survive over a wide range of temperature, and it is worthy of using in compact applications due to light weight compared to metal and alloys.

The carbonaceous materials such as multiwalled carbon nanotubes (MWCNTs), graphene, and conducting polymers (CPs) when incorporated with other nanomaterials, for example, metal oxide and noble metal (Ag, Au) nanoparticles (NPs), the resultant nanocomposites show remarkable electrochemical performance. Therefore, such nanocomposites based on ternary materials (noble metal, metal oxides and carbonaceous material/CPs) have become primarily important in energy storage applications. The

scientists continue to focus on their development by facile methods, characterizations by modern techniques and finally exploitation in various electrochemical applications such as in supercapacitors and batteries. The underlying electrochemical mechanism during the course of charge-discharge process of the devices is equally important to understand in order to improve the efficiency and to apply the new engineering strategies. The incorporation of carbon matrix (MWCNTs and graphene) and conducting polymers together with other nanomaterials (noble metals and metal oxides) can provide additional effect leading to the enhanced electrochemical activity of ternary nanocomposites. Therefore, the synthesis of novel ternary nanocomposites and their applications for electrochemical energy storage systems to be a focus of research in electrochemistry. The scientific concern and intellectual eagerness of scientists are to dig out new boundaries of applications for the carbonaceous and conducting polymers-based metal and metal oxide ternary nanocomposites by excavating their deportment in the course of oxidation reduction reactions. The recent advances on ternary nanocomposites revealed their prime role in various applications such as electrochemical sensing, electrocatalysis, photocatalysis, solar cells, adsorption, and energy storage applications (Chabot et al., 2014; Choi et al., 2010; Roy-Mayhew & Aksay, 2014). In ternary nanocomposites, fast charge transfer kinetics mechanism is facilitated by the highly conductive carbon matrices and conducting polymers. Furthermore, the nucleation sites for the even growth of metal and metal oxide nanoparticles in the synthesis process are provided by the electronegative functional groups on the surface of the conducting matrix. Besides that, nanoparticles of metal oxides with a significant surface area to volume ratio have fantabulous electro-catalytic activities and fast electron transfer kinetics.

Conventionally, the metal oxides, graphite or glassy carbon are the known materials which were used as electrode materials in energy storage devices before the discovery of graphene. Graphene was added in the library of carbonaceous material in 1999. It is

single layered and has a 2D hexagonal honeycomb structure. The discovery of graphene brought a revolution in the area of nanotechnology due to its conducting properties, large specific area, tensile strength and wide electrochemical potential window. The most studied material is graphene, especially, in the area of electrochemistry. The number of articles on graphene increased exponentially since its discovery. Due to its remarkable properties, graphene has attracted the attention of researchers working in the areas of energy storage applications such as batteries and supercapacitors. The theoretical specific surface area of the graphene is $2630 \text{ m}^2 \text{ g}^{-1}$ which is larger than other carbonaceous material, for example, carbon black possesses less than $900 \text{ m}^2 \text{ g}^{-1}$ whereas carbon nanotubes carry from 100 to $1000 \text{ m}^2 \text{ g}^{-1}$. However, carbon nanotubes which are cylindrically rolled hollow sheet of graphene, also offer exceptionally good mechanical strength, thermal and electronic properties.

Conducting polymers (CPs) are another class of pseudocapacitive material which possess rapid and reversible oxidation-reduction processes, show good conductivity and relatively low cost as well. The well-known conducting polymers such as polypyrrole (PPy), polyaniline (PANI), polythiophene (PTh), poly (p-phenylene vinylene) (PPV) and poly (3,4-ethylenedioxy thiophene) (PEDOT) have been used in various energy storage and energy conversion devices. Their synthesis is carried out either by chemical or electrochemical oxidation of monomer and they offer conductivity through a conjugated bond system along the polymer backbone. Among the CPs, PPy and PANI are the most exploited polymers as electrodes materials in electrochemical energy storage systems due to their remarkable electroactivity, high doping level and high specific capacity. Moreover, they show good environmental stability, tunable conductivity and can be easily synthesized. The cyclic stability of CPs remains as an issue which hindered their use as electrode material in electrochemical devices. The degradation of CPs during charge-discharge mechanism resulting to break the polymeric conjugated system and

consequently, the loss of conductivity is observed. The composites of CPs with metal and metal oxides show better performance compared to the pure one. They possess better cyclic stability as well as electroactivity, particularly, when used as electrode material in electrochemical storage devices.

1.2 Hypothesis

1) The allotrope of graphite, MWCNTs are one of the carbonaceous materials which present splendid electrical conductivity (10^5 S cm^{-1}) and mechanical strength (60 GPa). These prominent attributes make them worthy material for applications in energy storage devices. Another large edge plane to the basal plane ratio of MWCNTs makes them ideal conductive matrix. The suitable aspect for electrochemical application is edge-like graphite sites which are highly active for redox reactions.

2) The graphene is a two-dimensional honeycomb structured thin sheet of atoms where every carbon atom is sp^2 hybridized. The three hybridized orbitals ($2s$, $2p_x$ and $2p_y$) form sigma bonds with the adjacent carbon atoms and un-hybridized ($2p_z$) orbitals form a conjugated π -bond perpendicular to the graphene lattice in which delocalized electrons are responsible for the distinctive electronic charge carrier mobility. As an ideal matrix, it possesses many distinctive characteristics, for example, it has theoretically high surface area ($2630 \text{ m}^2 \text{ g}^{-1}$), high electrical conductivity (10^6 S cm^{-1}), remarkable mechanical flexibility, thermal, and chemical stability. Graphene-based materials provide conducting networks along with the advantage of diminishing the danger of large volume changes during charge-discharge cycles.

3) Conducting polymers such as polypyrrole and polyaniline can be easily incorporated with nanoparticles of noble metals and metal oxides by facile synthesis method to form nanocomposites. The development of such ternary nanocomposites can

lead to the synergetic effect between electrical conductivity and redox properties of polypyrrole and polyaniline based ternary nanocomposites.

4) Metal oxides such as cobalt oxide (Co_3O_4) with a high degree of synthetic control produce tailored nanostructures and their composites which have a great potential for electrochemical applications. The simplicity of the synthesis protocol, fantabulous chemical durability, prognosticating ratio of the total surface atoms and versatile-surface morphologies are the featured properties which make them suitable candidates (Jafarian et al., 2003). It demonstrates p-type conductivity at low temperature with a direct band gap (2.10 eV) and indirect band gap (1.6 eV). In Co_3O_4 , cobalt ions exist in two oxidation states such as Co^{2+} and Co^{3+} , which are situated at the interstitial tetrahedral and octahedral sites of the closed packed face-centered cubic structure formed by the oxygen ions, respectively. The distribution of Co^{2+} and Co^{3+} over the tetrahedral and octahedral sites, respectively, offers diverse polar sites in Co_3O_4 crystals along with high surface to volume ratio and prominent catalytic activity which can promote not only in determining the charges but also enhances fast charge transfer kinetics on the electrode surface (Numan et al., 2017). Therefore, Co_3O_4 being a capacitive material (battery grade) supposed to possess excellent energy storage features.

5) Co_3O_4 nanograins undergo high particle aggregation, which considerably reduces their active sites, causing rapid capacity fading and structural distortion during charge-discharge reaction (Fang et al., 2013). Therefore, the possible strategy to overcome this barrier is to incorporate Co_3O_4 nanograins with highly conductive platforms. Carbon materials such as multiwalled carbon nanotubes, graphene, and conducting polymers are the ideal platform which not only facilitates the charge transfer mechanism but also prevent the agglomeration of nanoparticles, leading to increase the cycling stability and electrochemical surface area (Shahid et al., 2017). Moreover, the conducting matrices

such as graphene, MWCNTs and CPs provide nucleation sites for the even growth of nanoparticles (metal and metal oxides).

6) Noble metals such as silver and gold are highly conductive due to their narrow band-gap feature. The transition metal oxides are semiconductor in nature having wide band-gap, therefore, noble metals can enhance the electroactivity of the transition metal oxides by facilitating the electrons shuttling through transfer channels when they are mixed in optimized manner in the development of composite materials.

1.3 Aims and Objectives of Research

The aim of the thesis is to develop novel ternary nanocomposite materials based on carbon matrices/CPs with metal oxide and noble metal nanoparticles with enhanced electrochemical performance as well as excellent cyclic stability. The supported metal oxide can execute redox response required for energy storage while on the other hand carbonaceous matrices (MWCNTs and rGO) and CPs (PPy and PANI) can provide highly conductive platform and noble metals offer synergistic effect which helps to promote charge transport mechanism.

The challenging attempt in this project was to plan a simple, cost-effective, time-saving, and low temperature development protocol for the synthesis of first metal oxide (Co_3O_4) nanograins and then ternary nanocomposites of metal oxide and noble metal on carbonaceous matrices and CPs. Moreover, the developed ternary nanocomposites should have good energy storage ability, so that they can be used as electrode materials for energy storage applications (supercapattery).

In order to achieve the above goals, following major objectives were established and achieved;

- 1) To develop ternary nanocomposites of Co_3O_4 and noble metals with MWCNTs, reduced graphene oxide (rGO), and conducting polymers (PPy and PANI).
- 2) To characterize the as synthesized ternary nanocomposites by various morphological and structural analytical techniques such as field emission scanning electron microscopy (FESEM), energy dispersive X-ray spectroscopy (EDS), high resolution transmission electron microscopy (HRTEM), X-ray diffraction (XRD), and X-ray photoelectron spectroscopy (XPS).
- 3) To analyze the electrochemical performance of the synthesized ternary nanocomposites and assembled supercapattery in terms of cyclic voltammetry (CV), galvanostatic charge-discharge (GCD) and electrochemical impedance spectroscopy (EIS).
- 4) To compare the performance of the fabricated ternary nanocomposites for supercapattery.

1.4 Outline of the Thesis

This thesis comprises of five chapters. First chapter provides the introduction of the background, motivation, and hypothesis of this work and research objectives. Second chapter enlightens the working principles of supercapacitors and electrode materials such as carbonaceous materials, conducting polymers, metal oxides, noble metals and the nanocomposites of cobalt oxide and noble metals with carbon nanotubes, graphene, and conducting polymers. Moreover, the importance of ternary nanocomposites for energy storage devices is also briefly explained. In the third chapter, the parameters and methods for the development of electrode materials, their analytical characterization and electrochemical application have been written in detail. Fourth chapter is about the results and discussion of all developed systems $\text{Ag}/\text{Co}_3\text{O}_4@\text{MWCNTs}$, $\text{Au}/\text{Co}_3\text{O}_4@\text{MWCNTs}$, $\text{Ag}/\text{Co}_3\text{O}_4@\text{rGO}$, $\text{Ag}/\text{Co}_3\text{O}_4@\text{PPy}$ and $\text{Ag}/\text{Co}_3\text{O}_4@\text{PANI}$ ternary nanocomposites. Their

morphological, structural and electrochemical studies are presented. The assembled devices based on these ternary nanocomposites are evaluated finally in terms of energy density, power density and retention capacity. Fifth chapter is dedicated to the conclusions of the thesis and the suggested future work.

Universiti Malaya

CHAPTER 2: LITERATURE REVIEW

A detail on energy storage devices, particularly electrochemical energy storage system such as supercapacitors, its fundamental principle, construction, and their great advantages have been highlighted. This chapter also enlightens the basics of carbonaceous materials, conducting polymers, metal oxides, and noble metals and a thorough understanding of their chemistry.

The chapter comprises four parts. The first part, working principle of supercapacitors and their applications and benefits.

The second part is dedicated to electrode materials *i.e.*, capacitive (carbonaceous materials) and pseudocapacitive (metal oxides and conducting polymers), their types and applications. Graphene and multiwalled carbon nanotubes (MWCNTs) have special features among the family of carbonaceous materials. Similarly, conducting polymers and metal oxides have been discussed in detail with emphasis on their application in electrochemical storage devices.

The third part of the chapter explains the noble metals and their uses.

The fourth and last part is about ternary nanocomposite materials with reference to their application as efficient electrode materials for supercapacitors.

2.1 Supercapacitors

2.1.1 Overview

The first charge storage device named Leyden jar was invented in the middle of the 18th century by two scientists, Pieter van Musschenbroek of Kamin and Dean Kliest at Leyden (Conway, 1999).

The Leyden jar typically comprises of a glass jar which holds conducting medium such as an acidic electrolyte. A foil of metal is surfaced on the internal and external surfaces, and a metallic terminal is projected in the vertical direction through the lid of the jar to establish the contact with the inner foil. A dielectric glass medium is inserted in between the conducting metallic coatings at internal and external surfaces. This was the basic construction of the early capacitor. The internal and external surfaces accumulated equal but at the same time opposite charges. The acidic electrolyte was responsible for charging the two layers of Leyden jar which was generally accomplished with the help of electrostatic generators such as the Hawkesbee machine. Initially, its given name was the condenser.

Another scientists, Alessandro Volta back in the early of the 20th century altered the Leyden jar into electrophoresis which was capable of generating charge by the electrostatic induction and was operated manually (Brusso & Chaparala, 2014). Then, the newly designed device was constructed with robust plastic instead of glass which acted as dielectric material sandwiched in between the two metallic plates. Nevertheless, the Becker who was General Electric employee in the mid-20th century introduced and patented first commercial electrochemical capacitor constructed with carbon electrodes and aqueous electrolyte utilizing the phenomena of the interfacial double layer for electrical storage. The SOHO Corporation marketed supercapacitor in 1966 which was composed of carbon electrodes and alkyl ammonium salt as a solid electrolyte. Its prime feature was that it could hold high energy density with wide operating potential window (3.4 – 4.0 V). Later, in 1975, Conway *et al* introduced a supercapacitor based on similar charge storage process like batteries. They used transition metal oxide which was pseudocapacitive such as RuO₂ as an electrode material in the construction of pseudocapacitor. The material with pseudocapacitive properties stores energy through oxidation reduction mechanism contrary to the supercapacitors based on carbon

electrodes which operate through electric double layer effect. In pseudocapacitors, the charge storage mechanism is similar to that of batteries but with much enhanced reversibility (Conway, 1999).

Therefore, supercapacitors can be categorized into two types based on their charge storage mechanism as mentioned above. Further details have been given below.

2.1.2 Working Principle

There are two types of supercapacitors which have been differentiated based on their charge storage mechanism, either by chemical reaction or by electric double layer effect. So, the main categories are electric double-layer capacitor (EDLC) and pseudocapacitor. EDLCs are generally developed with electrodes composed of carbonaceous materials. Therefore, EDLCs store charge through the double layer system of charges that develop at the electrode/electrolyte interface (Chong et al., 2017). On the other hand, pseudocapacitors involve fast and reversible electrochemical reaction, also called faradaic reactions in order to store the charge on their electrodes composed of pseudocapacitive material (Omar et al., 2017). Generally, transition metal oxides, metal sulfides, conducting polymers and their composites are utilized for the fabrication of electrodes in pseudocapacitors. The characteristic feature of supercapacitor is that it can store energy by exploiting both mechanisms simultaneously depending upon the type of electrode material (Omar et al., 2017). The in-depth knowledge to understand the mechanism by which the charge is stored in both types of supercapacitors (EDLC and pseudocapacitor) is described here.

2.1.3 Charge Storage in Electrical Double Layer Capacitors

EDLCs are based on the mechanism of an electrostatic way of charge storage in which positive and negative charges gather at the carbonaceous electrode surfaces, separated by some dielectric medium or vacuum. Such mechanism of charge storage is likewise called

non-faradaic electrical storage. Many scientists proposed different models to explain the phenomena of electric double layers developed at the interface between electrode and electrolyte.

First of all, the electrical double layer concept was introduced and described by Helmholtz in 1879. He explained the distribution of charges at the interface of colloidal particles. According to Helmholtz, double layer comprised of oppositely charged double layers, separated by a fixed distance which is equal to molecular size so that it can be termed as an electrical condenser (shown in Figure 2.1(a)). The oppositely charged layers featured similar to the plates which were oppositely charged in conventional capacitor. Afterwards, the Helmholtz model was extended for the solid electrode interface as well.

In this approach, the negative and positive charge densities were well adjusted through the counter ions next to the electrode/electrolyte interface at a distance of atomic dimensions from the solid electrode surface. Afterwards, it was established that electrolyte ions are not stationary in the double layer then how they could be presented as compact array in the model as described by Helmholtz. The thermally affected fluctuations tended to keep them non-static.

In order to address this ambiguity, Chapman and Gouy modified Helmholtz model and propagated a model termed as a diffused double layer. In this model, the effect of thermal fluctuations was included and described the constant movement of electrolyte ions. Here in this model, counter ions coupled with the electrode were taken as 3D colonialization of cations and anions of the electrolyte with a diffused distribution (Figure 2.1(b)). The electrolyte ions on the electrode surface were considered as point charges with the net charge density equal to the opposite charge density. Although, the Chapman and Gouy model appeared to establish an over-estimation of the capacitance of double layers due to

the capacitance introduced by two separated layers of charges may rise inversely proportion manner to the distances in between them (Zhang & Zhao, 2009).

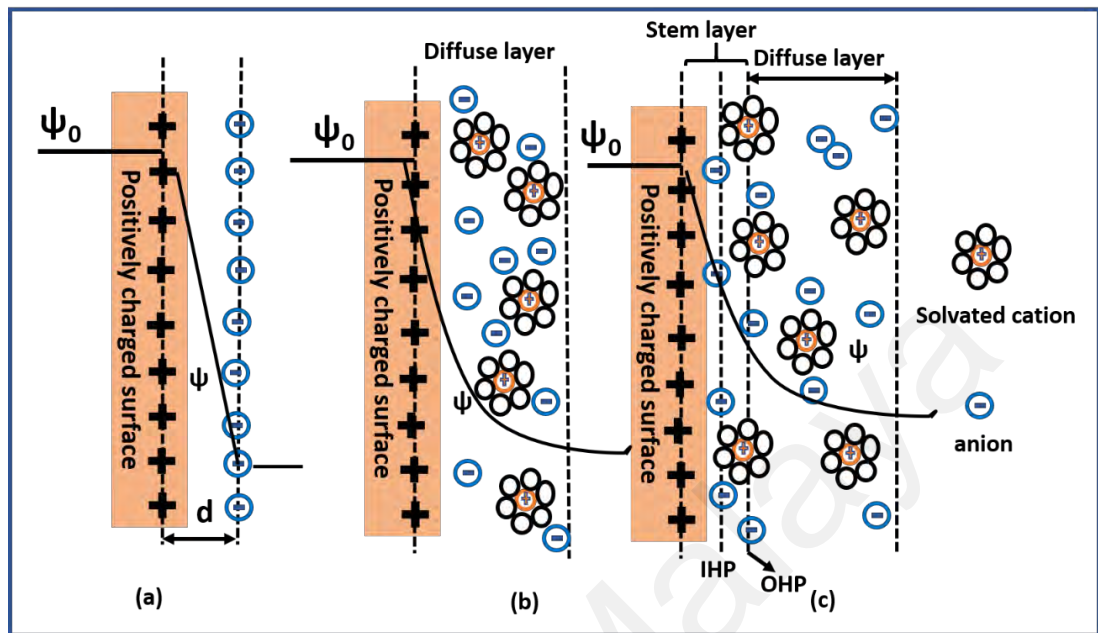


Figure 2.1: Models for a surface with positive charge on electrical double layer system: (a)Helmholtz model, (b) the Chapman and Gouy model, and (c) the model given by Stern with the IHP and OHP, d gives the separation of the double layer defined by Helmholtz model. Ψ and ψ_0 depict the electrode surface potential and that of the electrode /electrolyte interface, individually (Zhang & Zhao, 2009).

Stern in the early 20th century (1924) addressed the divergence of over estimation of double layer capacitance. Both Helmholtz and Gouy-Champan models were combined by Stern which was implemented on two different regions of ions distribution. He named the inner layer as Stern or compact and the outer layer as diffused layer (Conway, 1999). The Stern layer corresponds to the ion adsorption (in accordance to the Langmuir’s adsorption isotherm), where the ions usually are firmly adsorbed on electrode surface due to which it is also termed as compact layer. The internal Helmholtz plane (IHP) positioned in the stern layer mentions how far is the neighboring line of specifically adsorbed ions (ions directly contact the electrode). The outer Helmholtz plane (OHP) indicates the termination of the internal region and from where the diffuse layer starts as indicated in

Figure 2.1(c). The OHP mentions that the non-specifically adsorbed ions are likewise what the Chapman and Gouy model predicted.

The model helps to recognize the ions with their fixed sizes and hydration shells with their annular thickness. Thus, the determination of the geometric boundary on the compacted area of the adsorption layer of the electrode becomes easy. The total capacitance of the double electrical layers (C_{dl}) can be denoted by combining the capacitance of the two regions, the inner region looks like a diffused region capacitance (C_{diff}) and Helmholtz kind of compacted capacitance (C_H) between the double layers. Hence, C_{dl} can be stated as is given below.

$$\frac{1}{C_{dl}} = \frac{1}{C_H} + \frac{1}{C_{diff}} \quad (2.1)$$

The capacitance of the two discrete charge bearing layers is in inverse proportion with the distance through which they are separated as reported by Gouy-Chapman model. This directs to huge values of the capacitance because the limit of extremely small ions nearly advances to the surface of the electrodes. This type of overvaluation of the capacitance of double layer could be avoided inevitably through setting up a suitable gap of nearest approach bearing ions of finite size and so an inner region of compacted Helmholtz. The basic understandings of the phenomena of the electrode/electrolyte interface was based upon the Stern model until a detailed model by Grahame was presented on double layer capacitance in 1947 (Grahame, 1947).

2.1.4 Charge Storage in Pseudocapacitors

In EDL capacitance the storage of charges is conducted non-Faradaically or electrostatically, “pseudocapacitance” is complemented to this kind of capacitance. The “pseudocapacitance” is utilized to explain how an electrode material performs with the

electrochemical properties of a capacitive electrode but the storage of electrical charges is based on the entirely different mechanism (Brousse et al., 2015).

Pseudocapacitance encompasses the charge passage over the double layer which in origin is Faradaic, at the same time, the EDL capacitance instigates from the charge parting in the double layer molded between the liquid electrolyte and solid electrode interface. Pseudocapacitance comes for the thermodynamical motives in the change of potential (ΔV) and the range of charge acceptance (Δq) (Conway, 1999).

The equivalence derivative of the capacitance is shown below in equation 2.2.

$$C = \frac{d(\Delta q)}{d(\Delta V)} \quad (2.2)$$

Normally, two kinds of electrochemical reactions can constitute pseudocapacitance that is comprised of redox reaction on the surface of metal oxide along with the electrolyte ions and the doping and de-doping of an active polymer electrode material. The earlier process is created mainly on the mechanism of the surface and henceforth, it is extremely reliant on the surface area contributed by the electrode. The later development concerning the conducting/acting polymer is the main method and is less reliant on the surface area while a higher surface area is more advantageous in the spreading of electrolyte ions to and from the cell comprising electrodes (Burke, 2000). These cells comprising electrodes must hold a higher conductivity of the electrons for a better current collection and distribution.

The pseudocapacitance is acknowledged to create 1-5 % of the carbon-based capacitors having double layers because of oxygen-functionalities on the surface (with the reliance of conditions under which the material is prepared) based upon Faradaic reactions. At the same time, pseudocapacitors would always indicate a component of electrostatic double layer capacitance which is rounded by 5-10 %, in few cases may be

even higher, depending upon the pseudocapacitor electrode surface area. This contribution of the non-Faradaic process is in direct proportion to the interfacial surface area which is accessible electrochemically (Conway, 1999).

2.1.5 Supercapattery

Faradaic reactions can help to store high amount of energy in the batteries, but attached with an inadequate power density for the supply of energy shots (Ramadoss & Kim, 2013; Shan et al., 2016). At the same time, the EDLCs are being paid a great attention because of their better efficiency of a fast delivery of energy. Recently, carbonaceous materials are very famous to make EDLCs commercially. EDLC materials have the capability to store energy through a fast adsorption of ions (that is through non-Faradaic reaction), through which a fast charge storage recovery is also enabled. However, the energy density of the EDLC is a main challenge, which is not yet improved in aqueous electrolyte (Salunkhe et al., 2011) than batteries. The scientists are motivated to develop a novel device in which EDLC-type material can be used as a cathode and battery type material as an anode in order to be benefitted from non-faradaic and faradaic reactions in a single device. This can be called *supercapattery* (**supercapacitor + battery = supercapattery**) which is shown in the following Figure 2.2. Recently, the correct name was given by the scientists which was formerly known as hybrid supercapacitor. The battery material is promising for higher energy outputs and the EDLC material is for higher power. The development of novel materials that could carry electroactive sites abundantly as well as a vigorous crystal structure is seen with great endeavors. The scientific approaches could help to improve not only the specific capacity and the power density but also the cyclic stability of the resultant device. Present research was focused to fabricate a supercapattery to yield greatly the benefits of EDLCs and battery in a single device.

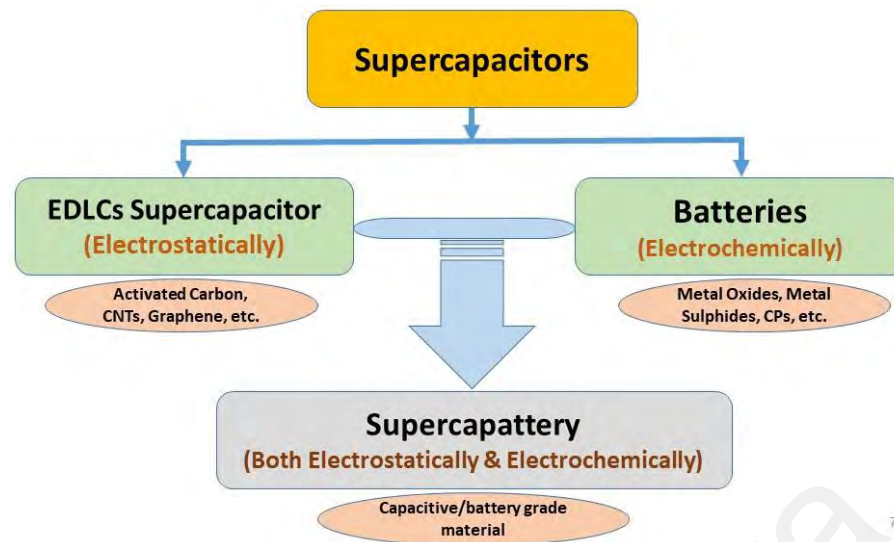


Figure 2.2: Hierarchical classification of supercapacitors and construction of supercapattery.

2.1.6 Applications of Supercapattery

The regenerative brake system is one of the vital applications of the supercapattery which are mostly employed in the hybrid electric automobiles. The automobiles not only need storage of energy for propulsion but also cruising power requirements (Douglas & Pillay, 2005). Conventionally, brake rotor along with the brake pad produce friction to slow down or completely stop the vehicle. This process converts the kinetic energy into heat. Whereas, the regenerative brake system enables the electric motor of the automobile to enter a reverse mode after applying the brake, which cause it to run in the reverse mode and hence slows down the vehicle's wheel. Motor acts as a generator while running in reverse mode and produces electricity and the produced electricity is supplied to the capacitor to build its energy storage. The stored energy is then utilized for propulsion or motor assistance that makes the vehicle fuel efficient. In practice, recurring acceleration and braking under certain driving conditions, i-ELOOP, enhance the fuel efficiency by nearly 10 % (Kurzweil & Garche, 2017).

2.1.6.1 Stationary Electrical Energy Storage

To store energy in micro-grids and power grids, the supercapattery are considered very useful. A power grid comprises of generating stations to produce electrical power, high voltage transmission and distribution lines for consumers. A micro-grid works at small scale that can be operative alone and works efficiently with the main power grid. Supercapattery ensures the stability of the grids by captivating energy and liberating it when needed as a prevention of fallouts, specifically when the power is being produced by some intermittent renewable energy sources. The alternating energy methods suchlike solar or wind methods when produce an increased amount of energy that penetrates the grids resulted in a drastically unstable output. To enhance the dependability and efficacy of the inexhaustible energy creating sources through supercapattery which could control the quality of the produced and distributed power very effectively. Maxwell Technologies® offer supercapacitors to resolve the problems (Kim et al., 2015). These supercapacitors can be useful for short term adequate power alternatives and offer slope rate control for longer substitutions.

2.1.6.2 Portable Power Systems

Supercapattery is also considered very useful for energy backing up appliances, and so can fill the power supply in case of short term power interruption. Supercapattery is seen to operate better than the batteries in terms of high voltage delivery in short interval of time. In addition, life of supercapattery much longer than batteries and no frequent replacements are needed which makes them highly cost effective. Supercapattery are remarkably being marketed for consumers energy backup appliances.

Normally, batteries are found poor in power deliveries while supercapattery suffers from a lower energy density to an enhanced load bearing for long intervals. Thus, a

combination of batteries and supercapacitors can overcome their drawbacks. The parallel usage of battery and supercapattery can compensate the serious load requirement of battery through the peak power need, at the same time, the battery can provide the average load (Kuperman & Aharon, 2011). The lessening of pulsed current flow of battery infers an enhanced battery life. The grouping of these two is specifically very advantageous in transportable power devices with high peak current demand. Supercapacitors are found to be applied mostly on satellite TV (to set channels and clock), coffee machines (for programming of its functions), and radio station memories in car audio system.

2.2 Electrode Materials for Electrochemical Energy Storage Systems

The materials used for electrochemical storage systems are the carbonaceous, transition metal oxides, metals, and conducting polymers. The carbonaceous substances like activated carbon, carbon nanotubes (single walled carbon nanotubes (SWCNTs) and multiwalled carbon nanotubes (MWCNTs)) and graphene are generally utilized as electrode materials for EDLCs obliging to their capacitive character. While the transition metal oxides and polymers hold the redox characters, so they are utilized as electrode materials for pseudocapacitors. The combination of capacitive materials (carbonaceous) as cathode and pseudocapacitive (transitions metal oxides, conducting polymers) as anode materials are employed in electrochemical supercapacitors to gain the benefits of both.

2.2.1 Carbonaceous Materials

Carbon is seen to be abundant in nature with its significant place in the periodic table. Its special intrinsic characteristics makes it a unique building block in several working atmospheres.

Carbon possesses an inert formation, exceptional firmness over the varied temperature window (sublimation at 3900 K and melting point at 4800 K at standard atmospheres), anti-corrosive nature against various reagents and low mass to volume ratio put it in appropriateness for light weight and compact applications (Savvatimskiy, 2005).

Due to easy handling, economic and abundance in nature make the carbon to be used commercially for the preparation of many materials for immense applications. At molecular level, the carbonaceous materials are typically graphitic crystallite structures. The one crystallite structure is basal plane form of 2-D sp^2 -hybridization, whereas the other is an edge plane of carbon atoms having the defective graphitic lines. The basal plane has wide surface area whereas the edge plane offers defect sites that are considered greatly appropriate for catalytic applications (Smith, 1983). Furthermore, carbonaceous materials possess supplementary electrochemical surface area because of their greatly porous structure or uneven morphology, better conductivity and outstanding thermal in addition to mechanical firmness which brings them in the list of ideal candidates for the applications of electrochemical devices (Kouhnavard et al., 2015; Wang et al., 2012).

Current development of the carbonaceous materials revealed their great role in electrochemical devices including energy storage and conversion devices (Meregalli & Parrinello, 2001; Zhang & Zhao, 2009). Few of the carbonaceous materials which are important to be used for electrochemical applications are discussed in the following section (Figure 2.3).

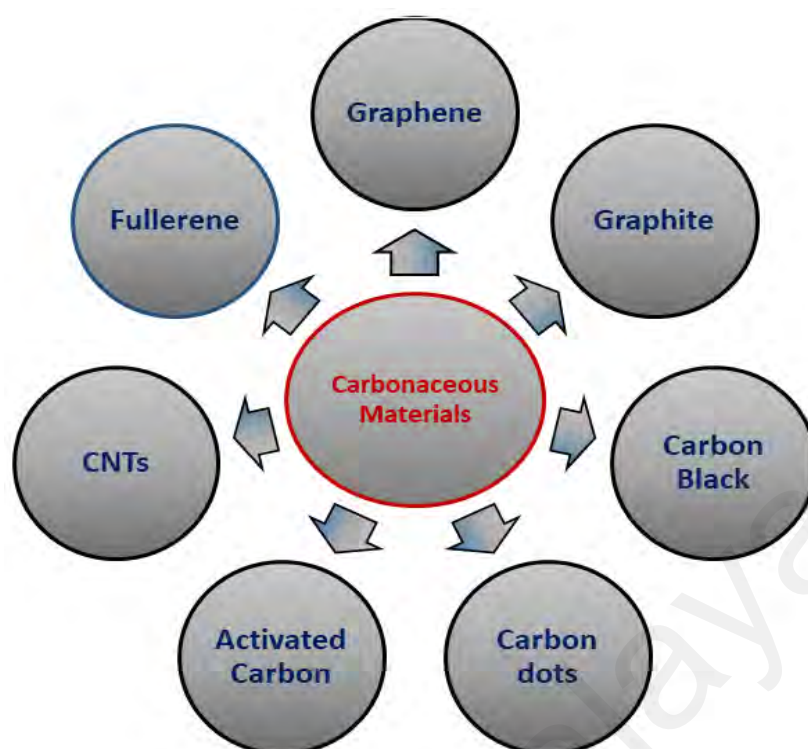


Figure 2.3: Different types of carbon materials used for electrochemical applications.

2.2.1.1 Activated Carbon

Activated carbon (AC) which is also termed as activated charcoal, is a carbon material that possesses very small pores (in the size of nm) and hence uplifts the surface area. About one gram of AC takes a surface area of 32,000 ft² (Dillon et al., 1989). The extremely enhanced surface area and a great mass to volume ratio are the main scientific attributes of significant investigations of adsorption and electrochemical applications (Paul, 2009). The naturally existed biomaterials like nut shells, peat, wood, coconut and coal possess significant carbon power which is physically and chemically activated to extract their power. The physical activation is carried out through high heating of carbon precursors between 700 to 1200 °C in the activating environment such as standard atmosphere, steam, and CO₂. Whereas, a chemical method of carbon activation needs to be processed chemically with couple of compounds like zinc chloride (ZnCl₂), phosphoric acid (H₃PO₄), potassium hydroxide (KOH), and sodium hydroxide (NaOH) (Zhang &

Zhao, 2009). These activation processes give an expressive improvement of nearly 300 m²g⁻¹ in their surface area and a significant enhancement in the micropores (nearly 2-50 nm) and the macropores (nearly 450 nm) in reliance with the used carbon precursor and activation process (Raymundo-Pinero et al., 2006). Because of their enhanced characteristics, the AC is broadly applied in several scientific areas including energy storage devices (Simon & Gogotsi, 2010). The potential applications of AC are highly investigated by scientific community for decades.

2.2.1.2 Carbon Black

The carbon black (CB) is normally created by partial combustion method of fuel products such as oil or gases and so have various subtypes depending upon the material of preparation. The sub-types of CB have been used in several applications in reliance on the respective properties each subtype possess. This is a material with para-crystalline carbon with a large surface area to volume ratio but still lower than what is offered by AC. The CBs are famous carbonaceous materials (Béguin et al., 2014; Krause et al., 2011; Schütter et al., 2015) with a typical diameter of their particles around 10 nm and are generally fused in agglomeration of a size of 100 nm. The conductivity of dry CBs in the powder form is around 10⁻¹ to 10² S cm⁻¹ (Schütter et al., 2015).

In recent years, the CBs are exploited as additional conductive material in the preparation of composite electrodes to use in lithium-ion batteries and EDLCs. The weight percentage of the CBs in these electrodes is around 5-10. Nonetheless, it is interestingly noticeable that the CBs are considered more accessible in their surfaces than those carbon materials having higher surface area. Because of its special character of absorbing electrolyte ions and outstanding conductivity, it is being used commercially in the form of acetylene black as electrode in the energy storage devices (Wissler, 2006). Additionally, CBs are easy to produce at greater scale and may also be economical.

2.2.1.3 Fullerene

Fullerene is also a form of carbonaceous material which is found as a large spheroidal, ellipsoidal, tubal or many other shapes of carbon molecule that comprises a hollow cage of sixty or more atoms of carbon. The buckminsterfullerene (C₆₀) is the famous most among the family of fullerene molecules after the name of Buckminster Fuller. Fullerenes are generally created through an arc discharge amongst the electrodes of the carbon in the inert atmosphere. The buckminsterfullerene shows an exclusive π -electron conjugated system that has a significant potential in electrochemical applications (Sathish et al., 2007; Shrestha et al., 2013; Shrestha et al., 2012). Figure 2.4 shows the structural makeup of the fullerene.

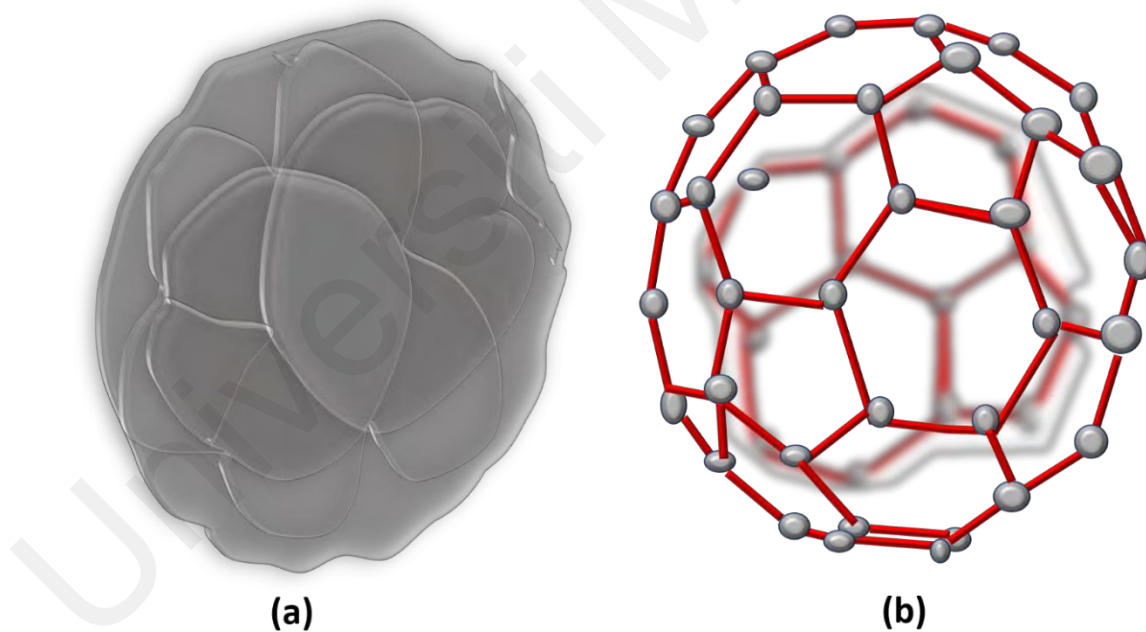


Figure 2.4: (a) Solid filling of fullerene lattice structure and (b) Lattice structure of fullerene.

2.2.1.4 Graphite

The naturally occurring crystalline form of carbon is called graphite which exists in igneous and metamorphic rocks and is composed in planer structure of graphene in parallel stacked layers distant by $\sim 0.334.8$ nm bounded by Van der Waals forces. Figure 2.5 depicts the parallel stacked layers (A, B and C) of graphene in graphite.

The hexagonal atomic structure of graphite reinforces its characteristics such as corrosion, mechanical stability, oxidation resistant, and temperature. Furthermore, π bonding delocalization in the hexagonal structure of graphite offers outstanding conductivity.

Though, its low absorption for neutron and X-ray makes it widely useable in nuclear and radioactive applications.

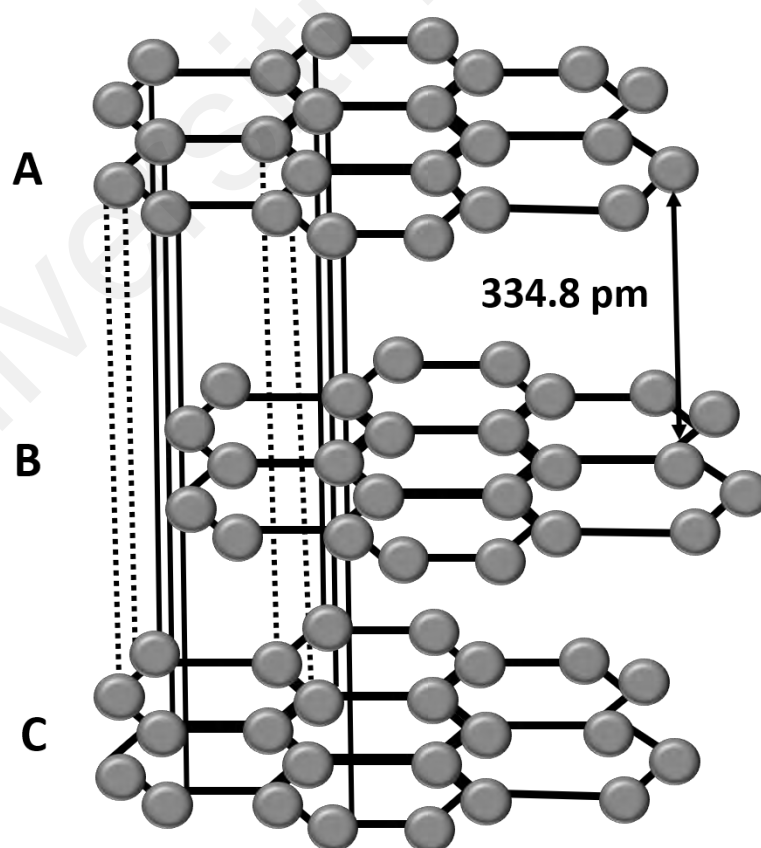


Figure 2.5: Stacked graphene sheets in graphite.

2.2.1.5 Carbon Nanotubes (CNTs)

The CNTs are usually found in tubular form composed of carbons which have diameters ranging in nm and μm in length. These CNTs are generally made by a reeling of a single sheet of graphene which is scientifically termed as single-walled CNTs or by a reeling of multiple sheets of graphene and so are called multiwalled CNTs. CNTs fall in the family of fullerene and show an outstanding chemical, mechanical, physical as well as thermal properties.

SWCNTs and MWCNTs are shown in Figure 2.6 clearly. The physicochemical characteristics of the CNTs vastly reliant on the diameter also the number of graphene layers in CNTs.

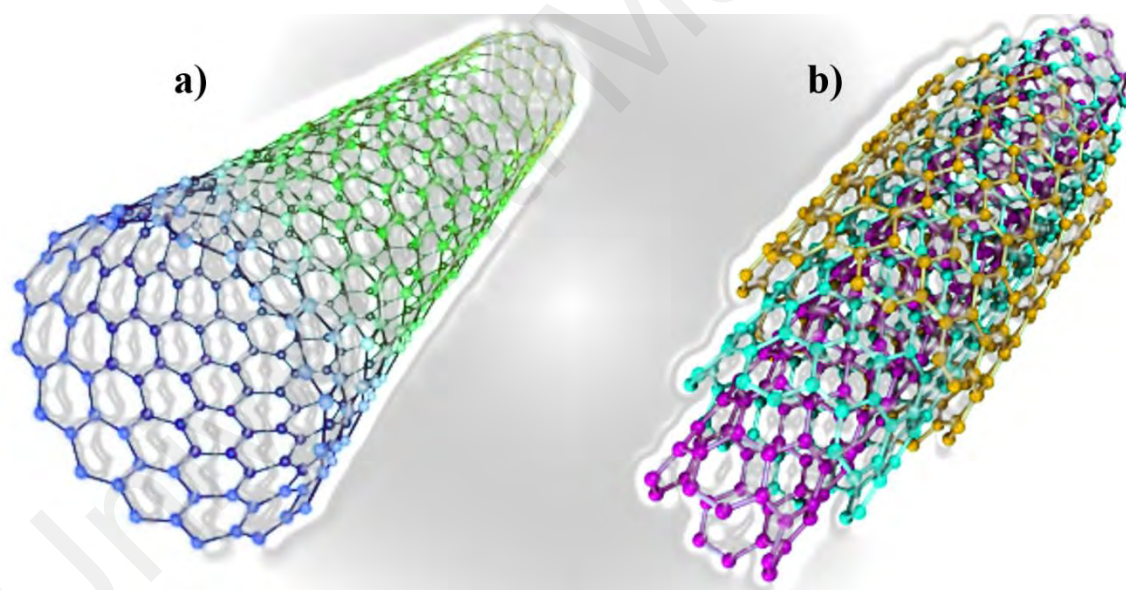


Figure 2.6: Graphically illustration of (a) SWCNTs and (b) MWCNTs.

(a) Synthesis of Carbon Nanotubes (CNTs)

There are several synthesis techniques for the preparation of CNTs reported back by many researchers from 1952 to 1987 (Baird et al., 1971; Baker & Waite, 1975; Koyama et al., 1972). A thorough study of the helical type of arrangement was reported in 1991 which was proved to be a breakthrough (Iijima, 1991). Since this breakthrough, several

methods were implemented for the preparation of such an exciting material which shows unique properties like much stronger than steel, harder even than a diamond and so possess much higher thermal conductivity, highly developed electric conductivity than other good electrical conductors like copper. All these characteristics set up a boom in academia and industries for several preparation techniques and few of the major methods of preparation are expressed as follows:

i) Chemical Vapor Deposition (CVD) Method

The CVD is the popular most preparation technique for CNTs. The process is generally associated with a thermal decomposition of the vapors of hydrocarbons when a metal catalyst is coated over the substrates. So, the name is given as a thermal CVD or a catalytic CVD to differentiate it from other existing CVD techniques for the preparation of different materials. The CNTs were first produced using CVD method in 1993 (Walker et al., 1959). In general method of CVD, the substrates are usually first given a coating of catalytic particles of metals like Fe or a combination of few catalytic metals (Inami et al., 2007). The coated substrates are then subjected to a higher temperature of around 700 °C. At the same time, the gases like nitrogen or hydrogen and few other gases from carbon family are introduced in the chamber. The gases from carbon family generally take up the active sites from the catalytic coated particles. The diameter of the CNTs strongly depends on the size of the catalytic particles.

ii) Laser Ablation Method

A graphite material is ablated with a pulsed laser in atmosphere of inert gas in the higher temperature reactors. The CNTs accumulate on the relatively cool side of the chamber from the condensation of the vaporized graphite material. This was first settled by Dr. Richard Smalley and his group at the Rice University. They were more basically

working on the ablation of different metals. After they know about CNTs, they started to ablate graphite to prepare mostly SWCNTs. The yield of this process is found to be 70 % which could create a controllable diameter depending upon the temperature of the reactor.

iii) Plasma Torch Method

The SWCNTs were also found to be produced by thermal plasma technique first reported in 2000 by a group of scientists in Canada. The aim of this technique was basically to produce the same conditions which were produced in the arc discharge and laser ablation techniques but the irradiating material (carbon source) was replaced with the carbon family gas rather than the graphite vapors. This technique was found to be more efficient for the SWCNTs than those require 10 times more energy to vaporize the graphite material. The yield was found to be even higher around 2 g min^{-1} than other techniques like laser ablation. The main steps are the introduction of the mixture of the carbon family gases into the torch of microwave plasma which is atomized via the atmospheric plasma which is found as a powerful flame. This flame gives subsequently some fumes which contain the SWCNTs along with the other by products like amorphous carbons and metallic nanoparticles.

iv) Arc Discharge Method

This is a procedure in which a direct current voltage is subjected diagonally to the two electrodes of graphite which are engulfed an inert gas nature like helium or hydrogen. To prepare MWCNTs on a cathode deposit, pure graphite rods are used. The gas environment plays a significant role and the pure hydrogen was found to be the best atmosphere to obtain MWCNTs with high crystallinity. A very fine tube with a diameter of less than 0.4 nm can be achieved in a DC arc discharge in the hydrogen atmosphere. In order to prepare SWCNTs through the arc discharge technique, catalytic metals are necessarily

introduced on the graphite anode, finally the SWCNTs can be collected as soot in the evaporation reactor. The production yield through this technique reaches 30 % for both SWCNTs and MWCNTs. Yet, there is a key hindrance of this procedure is the practice of very high temperature which may be above 1700 °C.

v) Functionalization of Carbon Nanotubes (CNTs)

All the raw synthetic CNTs are found to be extremely hydrophobic. Above all, the CNTs are not pure in raw form. Metallic residue and other by products are found on their tubular structure. So to get full potential of a CNT, this is very important to first modify its surface to get rid of all impurities such as amorphous carbons and metallic remnants and to make it highly functionalized with functional groups to convert their nature to hydrophilic (Sadegh & Shahryari-ghoshekandi, 2015). Usually, CNTs are functionalized through two main methods termed as covalent and non-covalent. The former was further subcategorized to functionalize the side wall and the defects. The robust oxidizing agents such as H₂SO₄, HNO₃ etc. are subjected to significantly introduce the defect around the CNTs, and so the functional groups of oxygen family are created throughout this treatment (Banerjee et al., 2005). Through this treatment, the metallic residues and the amorphous carbons could also be removed from the surfaces of the CNTs. The nanostructures of metal oxides could also be successfully incorporated by using oxygen containing functional groups. These groups assist as the nucleation sites for the nanostructures of the metal oxides. The non-covalent functionalization technique could be implemented with no destruction of the *sp*²-hybridized structure of the side wall of CNTs, which preserves the unique structure and the characteristics of CNTs. The pristine CNTs and functionalized CNTs are clearly shown in Figure 2.7.

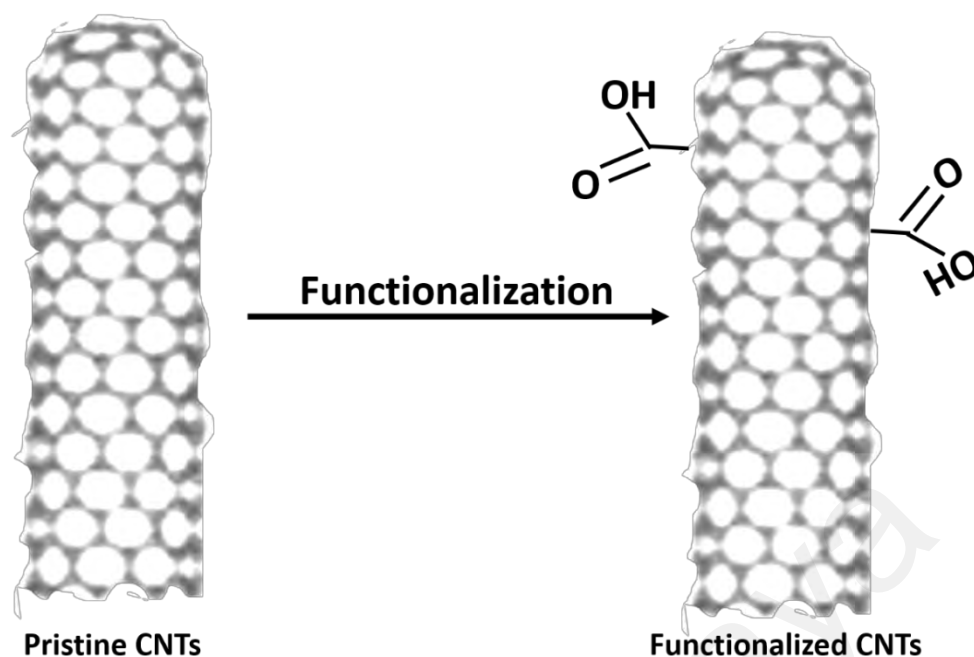


Figure 2.7: Schematic illustration of pristine and functionalized CNTs.

vi) Properties of Carbon Nanotubes (CNTs)

The sp^2 hybridized hollow structure of carbon atom is attributed to the strong physiochemical characteristics of the CNTs. The symmetric twist in the graphene sheets supplies a very high conductivity. The CNTs show metallic and semiconductor behavior because of the specific chirality. The electronic conductivity is more complex in MWCNTs because of the inter-wall interactions which cause a non-uniform distribution of current to the individual tubes. Whereas, this problem does not occur in SWCNTs.

Because of a strong bonding of each carbon atom with its neighboring three atoms, which attributes to a higher basal plane elastic modulus which makes CNTs outstandingly strong with much higher strength of SWCNTs than even steel. Whereas, the strength of the MWCNTs does not depend upon their diameters rather upon the disorder of the CNTs (O'connell, 2006). The CNTs can also recoup their lost positions after releasing an applied pressure from their tips which make the CNTs highly implemented in the research of high resolution probe microscopy. The CNTs are also found thermally conductive. The

CNTs provide high flexibility to non-axial strains whereas an outstanding strength to an axial strain (O'connell, 2006). When CNTs are composited with other materials like polymers and metal oxides, the composite materials improve their thermal and mechanical properties.

2.2.1.6 Graphene

The graphene is described naively as a single and very thin layer of graphite. Graphite already described above is an allotrope of carbon which means composed of the same atoms but are arranged differently and so make it uniquely different in properties altogether. This is remarkable to mention that graphene after isolation from graphite shows astounding characters which are merely one atom thick material makes it top ever discovered 2-D material. Yet, it possesses the highest strength, of 130 GPa, among all the known strong materials in the universe which is 100 times stronger than even steel. So, this incredibly strong material instead of being so thin is enough to be amazed of. The other unique properties are enlisted as its flexibility, transparency, high conductivity because of the high electron mobility at ambient temperature and moreover apparently impermeable for many fluids which make it an applicable material in all circles of life. Generally, graphene has a bond length of 0.142 nm and is sp^2 hybridized.

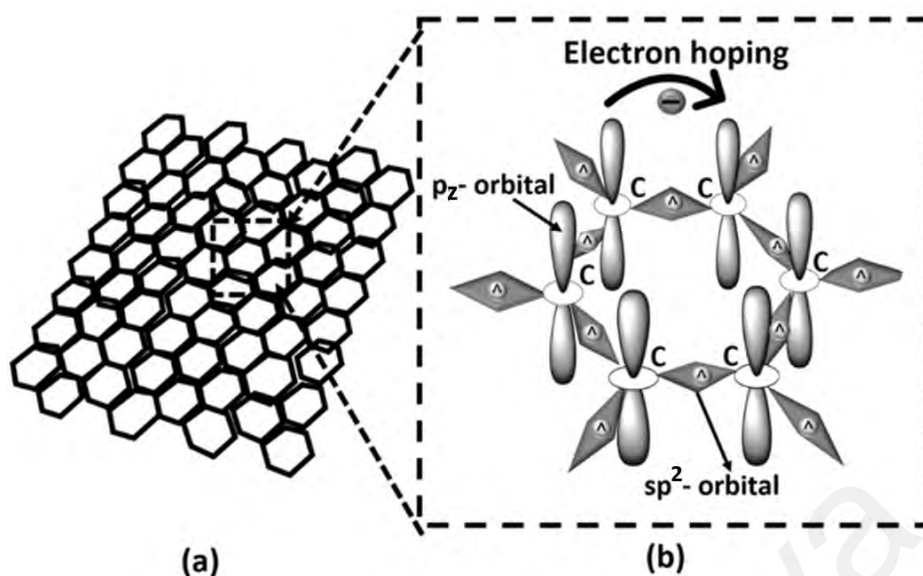


Figure 2.8: (a) Honeycomb lattice structure of graphene, (b) graphical presentation of sp^2 hybridized orbitals of carbon atoms which forms σ -bonds and π -bonds.

The π - π interaction supports the stacking of graphene sheets, that is why the top layer could only be put-upon for the electrochemical application (Figure 2.8). The de-stacking is possible when it is functionalized with the functional groups of the oxygen family. The electronegativity of the functional groups supports the de-stacking and enhance the surface area.

2.2.1.7 Graphene Oxide (GO)

The graphene when is functionalized with the functional groups of the oxygen family, this is converted to graphene oxide (GO) which could also be termed as graphitic acids or graphitic oxides, and the structure is shown in Figure 2.9. Strong oxidizing agents are utilized for the oxidation of the GO which produces yellowish gel or solid layers of graphene parted in an irregular way having larger spaces among them. The oxidizing graphite was first prepared by Benjamin in 1859 by using the mixture made of potassium chlorate and nitric acid (Banerjee et al., 2005) which was improved by Hummers and Offeman in 1957 by following an even easier and naive route by consuming a mixture of H_2SO_4 , $NaNO_3$, and $KMnO_4$ (Hummers & Offeman, 1958).

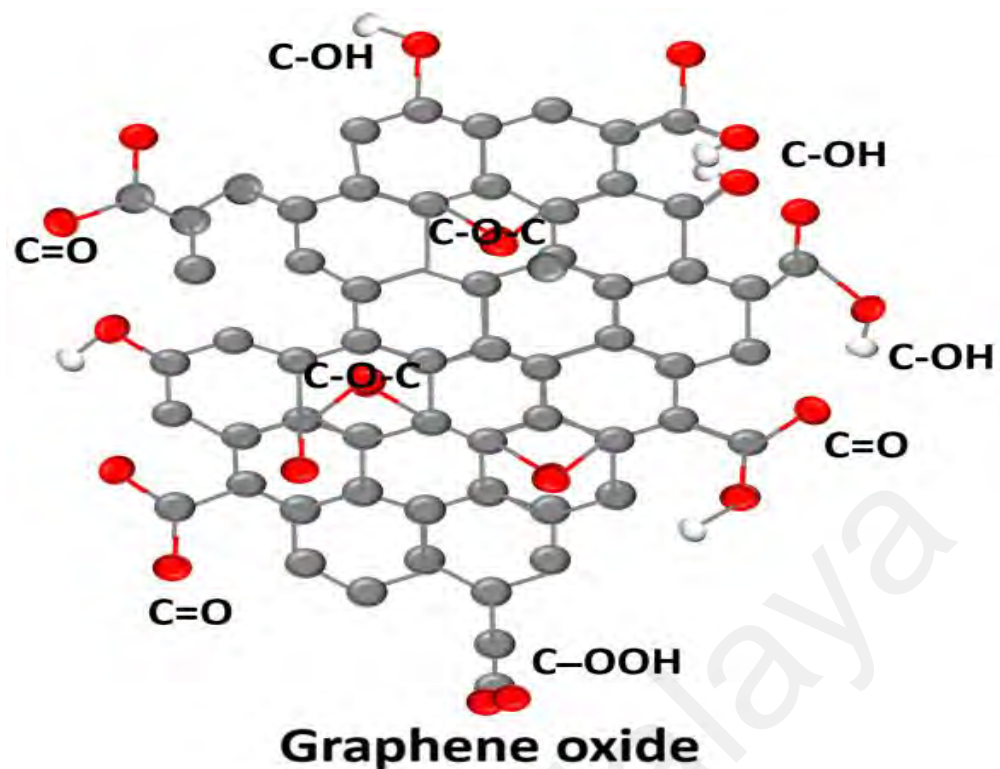


Figure 2.9: Graphene oxide containing functional groups on its honeycomb matrix.

The basal plane and the edges of the GO are decorated using functional groups of the oxygen family (hydroxyl and epoxy) which helps GO to be more hydrophilic in nature in order to facilitate the exfoliation and dispersion of GO when it is provided with water sonication. This supports a single layered and more stable yield of GO dispersion. The GO is different from graphene in its structural character though, they possess the similar character chemically. The graphene is sp^2 hybridized which makes it electrically more conductive whereas GO is less conductive due to the induction of the defects in sp^2 bonding from the functional groups. If the functional groups are removed, the electrical conductivity could be restored but a perfect removal is not yet reported.

(a) Synthesis of Graphene Oxide (GO)

The GO was synthesized firstly by Benjamin as described in the section above. Nevertheless, the process was so tedious and unsafe. Then, there came Hummers with his co-workers and introduced a new technique to synthesize GO at low temperatures which does not involve any explosions by using flakes of graphite as a source of graphene and then finally get it oxidized in an easy way (Hummers & Offeman, 1958). The whole process of preparation can be expressed in two easy steps. At first, the flakes from graphite source are oxidized using strong acids to create GO. The produced GO stands at its edges and basal plane with some functional groups (epoxide and hydroxyl), which enable GO to be hydrophilic. Then in the later stage, bulk GO is diluted through water sonication to achieve the single, double or more sheets of GO.

As a general recipe, 100 g of graphite flakes are mixed with the 50 g of NaNO_3 along with concentrated H_2SO_4 at a temperature of $66\text{ }^\circ\text{C}$ which is later cooled down to $0\text{ }^\circ\text{C}$, then, added approximately 300 g KMnO_4 under continuous stirring. Also, water is mixed to dilute the mixture of the prepared solution. The resultant is a colloidal mixture comprises 0.5 % of solid which is later purified to remove the residues and at the last stage, water is extracted by using P_2O_5 (Li et al., 2014).

(b) Properties of Graphene Oxide (GO)

The GO just as graphite oxide is generally designated as an electrical insulator, because of a possible distraction in the network of sp^2 bonding which is not entirely true. The competence of the GO for electronic conduction hinges on how much oxidization occurs in the compound and the synthesis technique followed. The parameter that disturbs the electric conductivity is the oxidization, so even a GO which has been oxidized highly may still be a very meager conductor of electricity. That means if GO would be extremely

reduced, it might be capable of conducting electricity, but it would still not be capable to perform with equally high quality as a graphene monolayer in relations of the electron mobility. Yet, several techniques are being utilized to encounter this problem, mainly through the referred techniques of functionalization, which is chemical modification of a substance in order to set its properties in reliance with any specific application of the material. The major properties that might require modifications are: 1) Dispersibility, 2) Hygroscopicity and 3) Toxicity (Loryuenyong et al., 2013; Zhang et al., 2009).

Functionalization is such a great technique that can entirely change the electrical properties of the GO and the resulting modified material could be exploited for limitless areas of applications. So, there are several methods of functionalization depending upon the area of utilization of materials.

2.2.1.8 Reduced Graphene Oxide (rGO)

The rGO as depicted in Figure 2.11 is the reduced form of GO which can be prepared by many methods to finally reduce the contents of oxygen in GO (Figure 2.10). Whereas, GO is a material which is obtained through the oxidation of the graphite which results in the extended interlayer parting as well as the functionalization of the basal planes of the graphite. The process of reduction of GO supports to eliminate the functional groups from its edges and the basal planes which actually restores the disturbed network of sp^2 hybridization of the chain of carbons and hence enhances the conductivity to an ample extent. In parallel, the repulsion created by the electronegativity of the functional group is also reduced which put the graphene sheets back in stacking. Though, the reduction is not achieved 100 %, this makes the rGO, also a holder of GO and pristine graphene character. As far as the conductivity of rGO is concerned, this is more than GO but smaller than the pristine graphene. Whereas, the interlayers parting of the graphene sheets in rGO become lesser than GO and more than that of graphite. The method by which the GO is

reduced is significantly important which affects greatly the quality of the produced rGO (Liu & Xue, 2015). There are several physical and chemical processes involved to reduce the GO. The physical and chemical techniques by which GO is converted to rGO are discussed below:

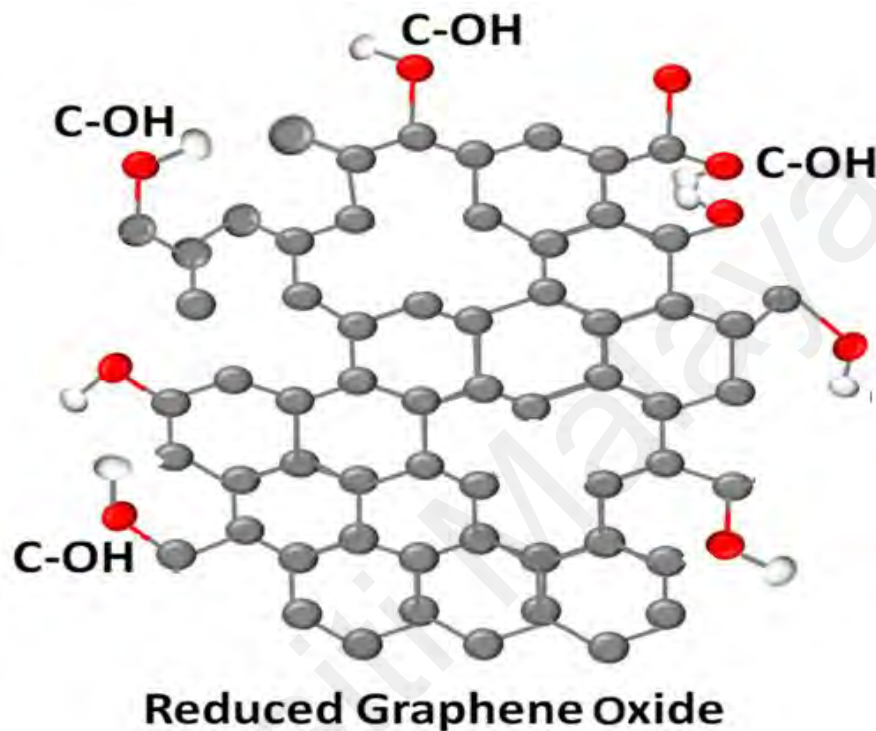


Figure 2.10: rGO containing less functional groups compared to GO on its honeycomb lattice.

1) Chemical Synthesis of Reduced Graphene Oxide (rGO)

One of the famous most and stronger chemical agent, named as hydrazine hydrate ($\text{H}_6\text{N}_2\text{O}$) is used to convert GO into a high quality of rGO. Yet, the technique is not green. Few other milder compounds (urea and ammonia) could be utilized for the reduction of GO but the resulted rGO does not hold a high degree of reduction. Some natural bio extracts are being utilized to reduce the GO but GO is not perfectly reduced.

2) Physical Methods

The GO can also be converted into rGO by simply heating the GO for quite a long duration at very high temperatures or by exposing GO to radiations like ultra-intense pulsed lasers and xenon flashtubes. The heating up to 1000 °C or more can even eliminate all functional groups from the basal planes of the GO and the resulted rGO through this technique possesses a very large surface area very near to the pristine graphene. Nevertheless, the high temperatures have the drawbacks of structural defects in the lattice of rGO.

3) Electrochemical Methods

The electrochemical treatment of the GO reduction shows great results in the form of a very high quality rGO which is structurally very close to the pristine graphene. The technique comprises of coatings of very thin layers of GO on the substrates of different materials like indium tin oxide, and glass etc. Each end of the coated substrates is supplied with the electrodes to create a circuit through GO. At the end, the linear sweep voltammetry is generally conducted on GO in a sodium phosphate buffer solution at a range of applied voltages. The reduction initiates at around 0.6 V and is maximized at around 0.87 V. Many experiments performed in the recent past on the electrochemical reduction of GO showed a large ratio of carbon and oxygen and the higher electronic conductivity than even silver. Moreover, this technique is not involved with hazardous chemicals which supports zero toxic wastes. Since, the GO is not easy to deposit GO in bulk upon the electrodes and so the scaling of this technique is still an issue to be investigated. Whereas, chemical reduction of GO is very scalable technique but unfortunately, the yielded rGO is not of high quality with less surface area and poor conductivity.

2.2.2 Conducting Polymers

The finding of electrically “metal-like” conducting polymers (CPs) has given rise to the field of electrochemically active polymer research field and appeared as a powerful choice for utilizing them as electrode materials in pseudocapacitive devices. Conducting polymers are the second group of the entrant materials for redox pseudocapacitors because they bear fast and reversible oxidation/reduction processes, good electrical conductivity, and low cost. Commonly used conducting polymers are polypyrrole (PPy), polyaniline (PANI), poly(3,4-ethylenedioxythiophene) (PEDOT), polythiophene (PTh), and poly(p-phenylenevinylene) (PPV) and can be exploited for various applications. CPs offer more compensations in the comparison of transition metal oxides; that is also a family of pseudocapacitors. The energy density and capacitance of CPs is much higher than what is offered by EDLC because the conducting polymers do not just have the capability of storing the charge in the electrical double layer but can go rapid Faradaic redox reactions. Furthermore, the decreased cost of manufacturing and low ESR fascinated huge curiosity in the associated research. They are classically synthesized likewise through a chemical or electrochemical oxidation of the monomer and rendered conductive via a conjugated bond system along with polymer backbone (Shirakawa et al., 1977). The general edifice of all CPs consists of a recurrently alternating single and double (C-C, C=C) bonds, creating an overlapping area of p-orbitals, and linking the successive single bonds. That permits a delocalization of π -electrons transversely at all the successively aligned *p*-orbitals, introducing a π -conjugated backbone thoroughly in the chains of polymer. The introduced π -conjugated backbone controls the formation and circulation of the charge carriers, consequently, make the intrinsic conducting polymers. This type of polymer building could affect the electrochemical performance critically through the mobility of ion and pores accessibility. Consequently, structural design of polymer becomes very important for higher efficiency and stability for charge storage.

There are two types of charging process such as p-doped with anions during oxidation and n-doped with cations while reduction. Early studies of n-doped materials were achieved on polyacetylene and ulterior on poly-p-phenylene. The polymers constructed in this way show high impedances when go through n-doping and hence do not fit to be used as negative electrodes (Friend et al., 1999). Fewer conducting polymers, such as PPy and PANI, would be p-doped only because of a requirement of a very negative potentials for n-doped, in the comparison of the potential limit of reduction of molecular solvent-based electrolytes (Wan et al., 2015). It was reported that p-doped polymers show more stability against degradation when compared with n-doped polymers; for this reason, investigating the p-doped polymers are more promising (Spinks et al., 2006). Nevertheless, the key downside of CPs is based upon their deprived stability of cycling while using as bulk materials and hence, show a restricted cycle life. Swelling, shrinking, cracking or breaking in the doping/de-doping procedure of continuous charge-discharge methods are associated with conducting polymers films and so, regularly worsen their conducting behavior (Frackowiak et al., 2006; Simon et al., 2008). The composites of nanostructured CPs with different materials are advisable to more stabilize the cycling. The deposition of Poly(Tri(4-(Thiophen-2-yl)Phenyl)Amine) (pTTPA) on vastly porous films or templated nanotube structures returned a greatly higher capacitance of about 950 F g^{-1} in 100 mM tetrabutylammonium tetrafluoroborate in acetonitrile (Roberts et al., 2009). A ternary nanocomposite of rGO/PPy/Cu₂O-Cu(OH)₂ was prepared by another group to use in electrode material for supercapacitors. This ternary composite showed a remarkable gravimetric specific capacitance (997 F g^{-1} at a current density of 10 A g^{-1}) in three electrode systems. The graphene EDLC, composed with the pseudocapacitive properties of PPy and Cu₂O-Cu(OH)₂, increased the energy and power densities up to 20 Wh kg^{-1} and 8000 W kg^{-1} , respectively (Asen & Shahrokhian, 2017). Ates *et al* prepared a ternary nanocomposite, rGO/TiO₂/PPy by oxidative polymerization of pyrrole

monomer and added the rGO and TiO₂ nanoparticles during polymerization process. They utilized the prepared ternary nanocomposite as positive electrode material in the supercapacitor assembly and achieved the energy density of 2.03 Wh kg⁻¹ with the corresponding power density of 18.3 kW kg⁻¹. They observed high Coulombic efficiency with retention capacity of about 100 % (Ates et al., 2018). These promising results foreground the use of ternary nanocomposites in energy storage devices. The conducting polymers are known to be mechanically weak, hence the composites can be considered to save from mechanical breaking of the polymer in the extended cycling (Frackowiak et al., 2006).

In this thesis, two of the most popular conducting polymers such as polypyrrole, polyaniline and their composites, were synthesized at laboratory scale and subsequently used as an electrode material in supercapattery assemblies.

2.2.2.1 Polypyrrole

PPy is regarded as one of the most anticipating materials for pseudocapacitors out of the existing CPs, because of their light weight, low in cost and high in electrical conductivity when compared with many of other commercially accessible CPs (Hepowit et al., 2012). It was first introduced in 1960s and is considered a primarily conducting polymer bearing attractive possessions (Bolto et al., 1963). It offers flexibility in electrochemical processing which is much greater than various other conducting polymers. PPy possesses a greater density and so can give a high per unit volume capacitance (400-500 Fcm⁻³). Though, the dense growth give rise to restricted access for dopant ions to the interior sites of the polymer, which will reduce the per gram capacitance, especially for denser layers on electrodes. Also, the oxidation potential is lesser for pyrrole (0.8 V) in the comparison to various heterocyclic monomers. PPy is indeed seen as one of those fewer CPs that can be manufactured in aqueous solutions.

The PANI formation needs acidic aqueous media whereas PTh needs organic solvents for its growth. These factors made PPy an outstanding material out of the other existing CPs (Ansari, 2006).

(a) ***Synthesis of Polypyrrole***

Polymerization of pyrrole monomer (Figure 2.11) is carried out to form polypyrrole (PPy). The work on conductive polymers including polypyrrole was acknowledged in 2000 by presenting them a Nobel Prize (Strom & Rasmussen, 2011). A chemical polymerization of pyrrole monomer with an appropriate oxidizing agent is required to synthesis PPy as shown in equation 2.3, when it is required in bulk. While, thin film electrodes are synthesized through electrochemical polymerization of pyrrole monomer. Thin films formed in this way are usually layered on an electrode surface through anodic oxidation of the monomer along with an electrolyte solution. The utilization of binders can be prevented through this method, and so the PPy can be immediately developed on the self-supporting substrate.

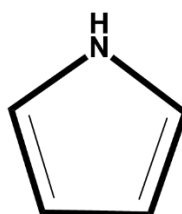
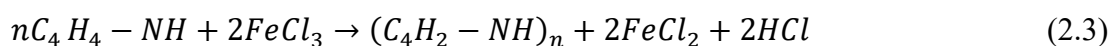
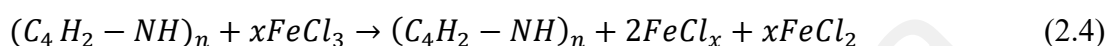


Figure 2.11: Structural formula of pyrrole monomer

In usual practice, PPy is synthesized through oxidation of pyrrole monomer by using as appropriate oxidizing agent, *i.e.*, ferric chloride (FeCl_3). Some surfactant could also be used to control or modify the morphology of the synthesized polypyrrole. The chemical process can be presented in the following simplified chemical equation 2.3.



Polymerization usually comes in action through the existence of the *pi*-radical cation $C_4H_4NH^+$. The C-2 carbon of an unoxidized pyrrole monomer is attacked by electrophile to form a dimeric cation $[(C_4H_4NH)_2]^{++}$. The method replicates itself over and over again to obtain polymer molecule as shown below in a chemical equation 2.4. The oxidation (p-doping) of the polymer give rise to conductive forms of PPy which are presented below in a simplified equation 2.4.



2.2.2.2 Polyaniline

Polyaniline belongs to the family of semi-flexible rod and is a conducting polymer. The discovery of this compound was reported before a century and half, but it attracted the scientists in early 1980s because of its higher electrically conductive nature. Polyaniline proved to be applicable in various striking processing properties amongst the family of conducting polymers and organic semiconductors. Over last 50 years, this compound is proved to be amongst the most studied conducting polymers due to its chemistry and rich characteristics (Li et al., 2008).

Well defined diverse oxidation states are attributed to PANI each having unique name as formerly accredited by Green and Woodhead can be found below in Figure 2.12 (Huang et al., 1986; Wnek, 1986). These oxidation states are found in different ranges from the completely reduced to the entirely oxidized compounds like leucoemeraldine via protoemeraldine, emeraldine and nigraniline to the pernigraniline, respectively. In distinction of other polyaromatics, PANI is not conducting in the total oxidized state and the oxidation states given above are not conductive. To make PANI as a conducting compound, the intermediate oxidized states based upon emeraldine should go through protonation for producing the charge carriers and so the mentioned mechanism is termed

as the “protonic acid doping”. This mechanism makes PANI exclusive since this does not need any addition or removal of electrons from an insulator to develop its conductivity (Ray et al., 1989). Doping with the oxidants like iodine helps in the development of PANI in diverse states, though, the conductivity is far lesser than that is produced through protonic acid doping mechanism. The process of conduction is supposed to contain polaronic carriers like the protonated emeraldine that comprises a delocalized poly (semiquinone radical cation).

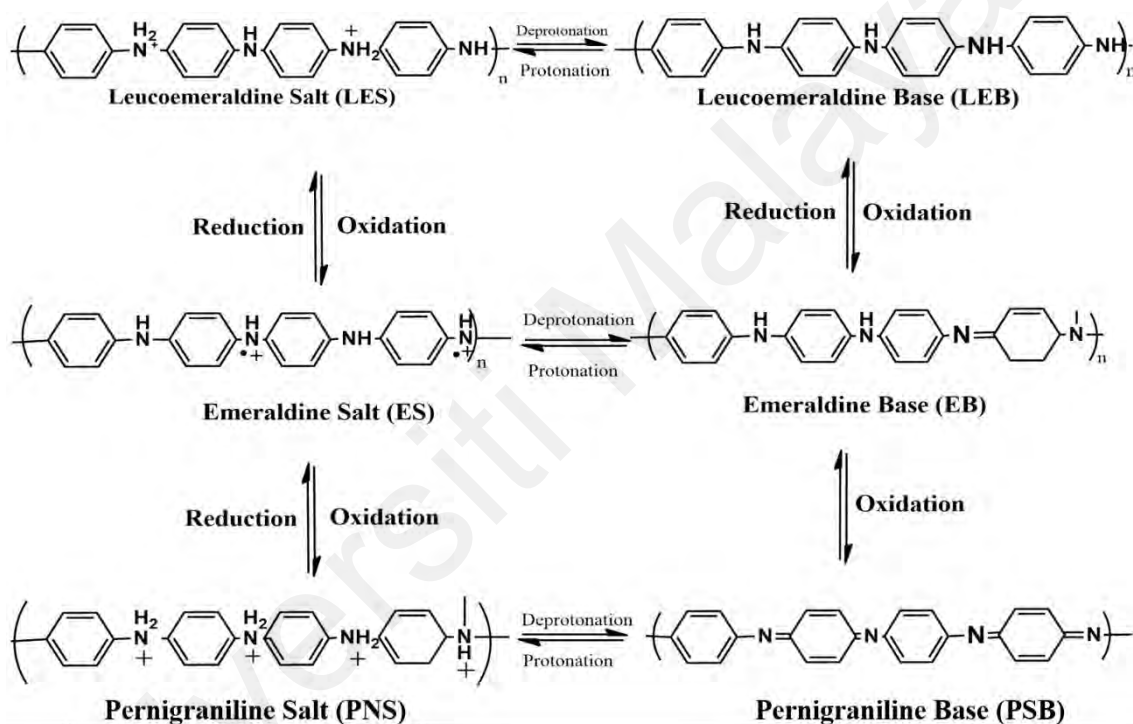


Figure 2.12: Schematic illustration of polyaniline in different oxidation states (Le et al., 2017).

Polyaniline in its emeraldine base because of higher stability at room temperature is viewed as the most beneficial form. Rather, when doped with acid and the resultant conductivity is about 10 orders of magnitude higher (Macdiarmid & Epstein, 1992). Whereas, polyaniline in leucoemeraldine and pernigraniline forms doped with acids show very weak conductivity (D'Aprano et al., 1992). The conductivity of polyaniline in its undoped form is found to be $6.28 \times 10^{-9} \text{ S m}^{-1}$ and a higher value of conductivities of about

$4.60 \times 10^{-5} \text{ S m}^{-1}$ could be attained after doping with 4 % HBr. The oxidation of leucoemeraldine leads to the production of the same material.

(a) ***Synthesis of Polyaniline***

The oxidative polymerization is the most famous synthesis method of PANI. This process involves the polymerization and doping at the same time and so results in an electrochemical or chemical accomplishment.

Polymerizing aniline is used to develop PANI, via a chemical reaction in acidic medium such as HCl, H₂SO₄, and HNO₃ etc. This development is followed by the oxidization of aniline and blending gradually for PANI preparation. The final compound may be passed through further process of chemical doping to better stabilize the polymer and to even out the conductivity (Wessling, 1998).

The acids are utilized to prepare PANI with the suitable oxidizing agents such as (NH₄)₂S₂O₈, K₂S₂O₈ etc. in water. The oxidants are mainly added for withdrawal of a proton with no strong formation of co-ordination bonding whether with the substrate or the main product. Nevertheless, the small amount of oxidant is usually utilized to prevent the oxidative degradation of the prepared compound (polymer).

A report presented by Gospodinova *et al* that the proliferation of aniline polymerization goes ahead through a redox mechanism in between the rising chain (an oxidant) and aniline (a reductant) by adding monomer units into the end of the rising chain (Gospodinova & Terlemezyan, 1998). If a strong oxidant, (NH₄)₂S₂O₈ is added in higher concentrations at the primary step of the polymerization, it could enhance the oxidation of oligomers and PANI and also their occurrence in the oxidized form.

2.2.3 Transition Metal Oxides (TMO)

Transition metal oxides (TMO) are considerably attracting the devotion in the area of energy storage devices because of their excellent structural, mechanical, and electronic characteristics, also a high pseudocapacitance attributed to their multiple valence state changes. Normally, the TMOs serve as supercapacitors, can be subdivided into two main categories: noble transition metal oxides (e.g, RuO₂ and IrO₂) and base transition metal oxides (Co₃O₄, MnO₂, NiO, etc.). The later, category is much cheaper with an environment friendly character than that of the former category. The metal oxides also show outstanding capacitive behavior and so is being utilized by scientific community like hot cakes in all areas of science (Henrich & Cox, 1994; Noguera, 1996; Rodriguez & Fernández-García, 2007). The TMOs and mixed transition metal oxides (MTMOs) are highly appropriate materials for supercapacitors because of their multiple oxidation states the ions hold, make them superior in the specific capacitance. Furthermore, hybridized MTMOs are with graphene nanosheets enhanced electrical conductivity and enlarge the specific surface area for faradaic redox reaction (Low et al., 2018). Since, the electrode material plays a pivotal role in the capacitive function of a supercapacitor. Characteristically, a larger specific capacitance is possessed by a pseudocapacitor and the energy density is also much higher than an EDLC owing to the multiple oxidation states of TMOs that offer fast redox reaction to enhance the capacitance (Lota et al., 2011; Xu et al., 2014). So, the TMOs are utilized greatly as electrodes for pseudocapacitor which is mainly because of their changeable valence which is a cause of a supreme pseudocapacitance that permits the ion-electron intercalation in the lattice of the metal compounds as well as greater inherent stability (Taberna et al., 2006; Xu et al., 2015).

(a) Synthesis of Transition Metal Oxides

The metal oxides play pivotal role in diverse fields of physics, chemistry, and materials science. However, the synthesis procedures for the development of metal oxide nanostructures play key role to tune the morphology, shape, and orientation. These fundamental aspects that determine the physiochemical properties greatly influenced by synthesis procedures using bottom up and top down fabrication technologies. In order to get the high yield, several methods are being employed. Some of the methods have been discussed here in details.

1) Chemical Methods

The chemical synthesis techniques or bottom up methods are most favorite synthesis procedures for industrial scale production of metal oxides. These are possibly the most widely used techniques to control morphology and size of the nanostructures. In such synthesis protocols, chemical reduction of metallic salts or the decomposition of metal-organic compounds are done in well-designed series of chemical steps. To regulate the morphology and size of the nanostructures, metallic salts are reduced by different reducing agents and utilizing various surfactants at optimized conditions. However, to obtain the uniform morphology, growth and to deaggregate the carbon support such as multiwalled carbon nanotubes, reduced graphene oxide and conducting polymers are used. The most widely used chemical methods are described below.

i) Co-precipitation Method

It is one of the easiest and commonly used method for the development of nanostructures. In this synthesis technique, aqueous solution with particular amount of metal oxide precursors such as metal acetates, nitrates, chlorides, phosphates, etc., is prepared followed by the addition of base which helps to form complex with metal ions.

Thus, as a result of complexation, metal hydroxide is produced which could be converted to respective metal oxide either by heating the reaction mixture or by calcination of the prepared metal hydroxide solid. Very often, particle size and uniformity are compromised. However, these issues could be addressed by using surfactants. Being straight forward, easy to follow, low temperature and energy efficient, this method is highly favorable for industrial purpose (Fernández-García & Rodríguez, 2011).

ii) Hydrothermal Method

The most admired technique for the preparation of metal oxides is hydrothermal. British geologist Roderick Murchison used it at very first. He described the water action at risen atmospheric conditions (temperature and pressure) which brought the deviations in the earth's crust by developing the formation of rocks minerals. It has been successfully employed for the synthesis of microporous crystals, superionic conductors, chemical sensing oxides, complex oxide ceramics, fluorides and magnetic materials. In hydrothermal synthesis, reaction mixture is placed in a metal container and subjected to heat at elevated temperature and buildup of pressure due to high temperature help to attain the nano size morphology of the prepared material. In this technique, one can obtain an easy and controllable size, shape distribution and crystallinity of the prepared nanomaterials through the adjustment of various parameters such as temperature, time, pH of the reaction solution, volume of the solution, solvent type and surfactant. Scientists successfully prepared different morphologies such as nano ribbons, nanorods, nano beads, nanoflowers, nanocubes etc., by optimizing such parameters (Shahid et al., 2015).

iii) Microemulsion Method

The microemulsion method is known to be ideal method to prepare nanostructures of inorganics. However, the process of the formation of nanostructures in the microemulsion

still has not been fully discovered. In this method, when reactants are blended, reactants exchange starts occurring in the microemulsion through the collision of water droplets. The exchange of reactants takes place very rapidly and precipitates start forming up in the nanodroplets along with the coagulation of primary particles and the nucleation growth, which results in the formation of the ultimate nanoparticles fenced by water or stabilized by surfactants. The microemulsions sets up at normal temperature and facile to synthesize contrary to liposomes and macroemulsion which need elevated pressure and homogeneity during synthesis. The prepared nanoparticles exhibit high degree of crystallinity, less aggregation and high specific surface area (Malik et al., 2012; Uskoković & Drofenik, 2005).

iv) Sol-gel Method

A wet chemical procedure called “sol-gel” in which a chemical solution, in short form sol, or colloidal particles are utilized to prepare an integrated network called ‘gel’. Usually, metal chlorides and metal alkoxides are the starting materials used in this technique. After going through the hydrolysis and polycondensation reaction, a colloidal is formed in which nanoparticles are fully spreaded in the solvent. The sol undergoes toward the development of an inorganic nanoparticles network comprising a liquid phase (gel). Consequently, the metal centers are connected through oxo (M-O-M) or hydroxo (M-OH-M) bridges, producing metal-oxo or metal hydroxo polymers into the solution. Water is removed through the condensation to produce gel. During condensation, the hydroxyl moieties polymerize and produce porous as well as dense hydroxide network. Finally, the gel is dried and calcined at high temperature to produce porous metal oxide nanostructures. The beauty of this technique is that the synthesized material is relatively higher in purity, synthesis at low temperature and ease in controlling the degree of porosity. The flexibility of the procedure allows to introduce small amount of dopants in

the solution and obtain an even spread in the resultant material (Interrante & Hampden-Smith, 1997; Livage et al., 1988).

v) Template Method

As the eco-friendly synthesis methods are becoming more popular to reduce the environmental pollution, template synthesis method is the choice for those who prefer green chemistry synthesis. In this method, host template material with uniform voids is used to trap the nanoparticles precursor. Metal oxide nanoparticles can grow over the host template and the template is then removed in the final stage by using solvents that can dissolve the template resulting in very fine and with uniform pore size nanostructured metal oxide. The role of the template is double folds. Primarily, it permits the procreation of structure at the best potential duplicability and operates as a skeleton to manage the diverse functions of a device, the active component, and the diverse interfaces. In this method, very fine with uniform pore size and diverse morphologies can be produced in a very controlled fashion (Ciesla & Schüth, 1999; Wang & Xia, 2006).

2) Physical Methods

The physical synthesis of nanomaterials is classified as top down technique. Such techniques involve, physical process to convert bulk materials into nano sized materials. It is mandatory for physical methods to employ mechanical forces such as milling and grinding and vapor phase deposition etc. Few of the usual physical methods are discussed below:

i) Mechanical Attrition

It is one of the simplest ways of producing nanoparticles of solid bulk material in the powder form. In this technique, mechanical milling or attrition is employed to convert bulk material into micro or nano sized materials. Ball milling and rod techniques are the

major types in this category that has been paid much consideration as an influential tool for the fabrication of low dimension materials at room temperature. However, the choice of the milling process depends upon the required particle size of the material. The objectives of milling are to convert large scale material into nanoscale material and to merge smaller particles in new phases. Contrasting to other synthetic procedures defined above, mechanical attrition produces nanostructures in the structural disintegration of cruder grained structures as an alternative of assembly of clusters (Koch, 2003).

The system of ball milling and rod milling has been reached to ample attention as an effective tool to produce numerous advanced materials. The distinctive technique of mechanical attrition is conducted at normal atmosphere. The technique has been operated upon, low energy tumbling mill, high energy mills, and vibratory and centrifugal type milling (Suryanarayana, 2001).

ii) Mechanochemical Synthesis

This technique comprises of mechanical ways like milling, friction and shear of chemical transformation of the substances at nanoscale (Xu et al., 2015). The mechanical methods supply the required energy for the activation of the chemical reaction which makes them a good combination of transforming materials at molecular level and is a facile method of synthesis (Rajput, 2015). There is a standard solid state displacement that occurs in mechanochemical combined process through mechanical forces that supports the transformation into smallest particles upto 5 nm (Lue, 2007) and this process has been implementing since long to prepare a variety of nanoparticles of metal oxides (Rajput, 2015). This combined process seems to control various parameters like the byproduct volume fraction through the mechanical milling process, by controlling the time of milling, the collision energy in milling, ratio of ball to powder, size of the balls, degree of heat, and through the agents that control the overall method.

iii) Chemical Vapor Deposition (CVD)

CVD helps to synthesize high performance nanomaterials. This technique is employed greatly to form thin films. The materials are usually deposit their thin films on the preheated substrates through the gas phase vapors. The activation energy is needed to initiate the CVD for the preparation of nanoparticles which could be taken from the laser, heat or UV radiations etc. which categorizes CVD into few subtypes depending upon the base of the activation energy (Sherman, 1987). When the energy of initiation is supplied through high degree of heat around 900 °C, this is termed as thermal CVD. The initiation energy when is triggered through plasma between 300-700 °C, that process is termed as plasma CVD. The laser assisted CVD comprises pyrolysis process of bulk solids by taking heat from the thermal energy of the laser which leads to the synthesis of the nanomaterials. Photo-assisted CVD depends upon the UV radiation that triggers a chemical reaction to liberate the photon energy which finally breaks down the chemical bond of the reactant compound. The chemical vapor condensation is a technique introduced in 1994. This technique also supports the pyrolysis of the vapors coming from the metal precursors at the reduced atmospheric pressure. The nanoparticles of many metal oxides have been prepared using CVD technique (Chang et al., 1994; Rajput, 2015).

iv) Laser Ablation

High power pulsed lasers are operated upon to synthesize the nanoparticles in laser ablation technique which is quite precise and efficient method of producing uniform sized nanoparticles. This process can easily be seen in two steps. First, the solid materials are vaporized. Second, the expansion of the irradiated material in the atmospheric gas is occurred (Amoruso et al., 2005). The solid vapors produced by pulsed lasers are captured as nanoparticles (Han et al., 2002).

2.2.3.2 Properties of Metal Oxides

(a) *Surface Properties*

The surface decides the chemical and physical properties of any material whether it is at nanoscale or bulk. Surface plays pivotal role in the mobility of anything across the surface whether it is interface energy, also can start or end any chemical process such as catalysts. When the bulks are processed to be in nano-sizes, the volume may remain the same, but the total surface area improves significantly which is considered a highly increased surface to volume ratio than the bulk.

The chemical properties of the materials are generally determined by which chemical groups are existing on their surfaces. At nanoscale, the materials usually have considerable quantity of atoms exist at their interfaces which makes surface related properties highly significant like adsorption of several compounds, melting and boiling points, morphologies, and chemical nature. This is the reason that the melting points of nanoparticles of any materials will be much lower than the bulk metal oxides because of the easy removal of the surface atoms in comparison of the bulk atoms. That means a decrease in required energy defeats the intermolecular forces which hold the atoms together, and hence a decrease in the melting point. So, the surface properties go through a drastic change after a material is converted into nanoscale which could easily be exploited in various fields of research.

(b) *Electrical Properties*

Based upon the importance of electrical properties of the metal oxides, several applications such as sensors, photocatalysis etc. are under consideration. Ionic conductivity is observed in metal oxides which depends upon the size of the nanostructures of the metal oxides which is very much important to control (Mao & Chen,

2007). According to Boltzmann statistics, the fundamental band energy gap is a decisive factor for a certain amount of charge carriers in the metal oxides which are responsible for electronic conduction of n-type for electrons and p-type for holes. The number of these electrons and holes can be impressively increased through non-stoichiometry which could be equilibrated easily through decreased vacancies of mobile cation/oxygen in metal oxides just like hopping-type electrons and holes conduction. According to modified Fick's second law, ionic conduction could also occur because of thermal activation in respective site to site movements inside the crystal lattice (Mao & Chen, 2007).

In polycrystalline oxides, the characteristics of the charge carriers are significantly influenced by their sizes as conductivity and surface properties of these oxides go in parallel. The total surface energy and the strain on the boundaries of the particles play in the electrostatic potential and are impressively modified, at nanoscale in comparison to the bulk material. The supply of charge carriers or defects inside the crystal lattice would undertake substantial variations from bulk materials to nanomaterials. The charge carriers exists over the whole material of nanoparticles as a consequence of the reduction of the shielded electrostatic potential on the surface of nanoparticles (Rodriguez & Fernández-García, 2007). Based upon the derived effects of the nanoparticles, it is noteworthy that nanoscale metal oxides help to improve conductivity as many orders of magnitude greater than that of the similar micro-crystalline or bulk metal oxides and hence is accredited to a significant increase of the electronic influence.

(c) ***Other Properties***

Metal oxides reveal several other distinguishing mechanicals, catalytic, adsorption and chemical properties due to which their huge industrial applications are seen as an active composition in the area of catalysis because of their photocatalytic nature which could be better benefitted to improve recent energy crises. The first photocatalytic splitting of

water through TiO_2 (initial photocatalyst suitable for splitting of water and origin of novel area of heterogenous photocatalysis), was described by Fujishima and Honda in 1972. Due to the large surface to volume ratio and improved surface binding energies, metal oxides can be used as adsorbents in the removal of environmental pollutants. The nano-metal oxides seem to be stable toward thermal and mechanical modifications and radioactive radiations. Hence, metal oxides can be exploited for an irreversible, more selective, and very efficient elimination of the hugely amounted pollutants from water. So, the nano scaled metal oxides show very notable characteristics which are being applied on large scale in the area of nuclear-energy, water treatment dairy, and chemical industries.

2.2.3.3 Cobalt Oxide (Co_3O_4)

In recent years, cobalt oxide (Co_3O_4) has been particularly appealing as an ideal battery grade material, owing to its exceptionally good redox properties, low environmental toxicity, high theoretical capacity (890 mA h g^{-1}) and simple cost effective synthesis protocol, which potentially can substitute the utilization of high-cost and non-environmental friendly RuO_2 and other transition metal oxides (Chou et al., 2008; Liu et al., 2018). Its nanostructures in different morphologies have been successfully synthesized by applying various approaches such as Co_3O_4 nano-cubes (Liu et al., 2013), Co_3O_4 nano-rods (Meng et al., 2015), Co_3O_4 nano-wires (Xia et al., 2011), Co_3O_4 nano-flowers (Balouch et al., 2015). The electrochemical properties of Co_3O_4 are greatly dependent on the structural morphology of the material and the electronic states of the metal (Kang et al., 2004).

Cobalt oxide respired a new name as a capable catalyst in the research of nano-metal oxides (Moro et al., 2013) which is a p-type semiconductor possesses a spinal structure with direct and indirect band gap. Furthermore, Co_3O_4 crystal comprises of exclusive

structure (Xie et al., 2009) with non-magnetic Co^{3+} and magnetic Co^{2+} inhabiting octahedral and tetrahedral sites respectively, inside the crystal. These polar sites of Co_3O_4 crystal can constitute a pivotal part in the catalytic activity, specifically enabling rapid transfer of charge kinetics at the electrode surface. The exceptional crystal structure along with various morphologies and the high aspect ratio make it a supreme entrant for electro-catalytic applications. Owing to these special features, nanostructures of Co_3O_4 (Mu et al., 2013) have been stated for electro-catalytic applications. To improve the effective electrochemical surface area and dropping the charge transfer resistance, the hybridization of Co_3O_4 nanoparticles with carbon-based materials and conductive polymers is considered very effective. The Co_3O_4 nanostructures seated on carbon materials are recently reported a huge potential for energy storage applications (Numan et al., 2016).

2.3 Noble Metals

The precious metals, for example, silver (Ag) and gold (Au) have been widely studied and used for various applications. The metals and their rare occurrence are clearly noticed from their names. Gold and silver were merely known noble metals since prehistoric times. The first metal known to man was gold with silver and copper. Gold was recognized readily by the ancient civilization as a valuable metal. A special interest in gold was expressed by folk tales, numerous legends and even the bible. In the middle ages, several attempts were made to make gold out of different chemical elements. The Latin word 'aurum' meaning 'shining dawn' is the matter/source of word gold.

Silver in its pure form is almost white, soft, lustrous, very ductile, and malleable. The silver has excellent heat and electrical conductivity properties. Its symbol Ag is derived from the Latin word 'argentum'. Silver is one of the scarcest elements in the known metals. Mostly, silver used now a days is gained from the silver ores, together with

argentite. Due to its very high conductivity, it is in high demand, but the huge cost makes it non-viable to use in electrical drives. Silver is applicable highly in the electrical industries, printed circuits, and electrical contacts in the computer keyboards. In oxidation reaction, it is also used as catalyst because of its catalytic nature.

(a) *Uses of Noble Metals*

The noble metals discussed above were firstly used in the jewelries and in the investments. The precious gold and silver have been employed to make coins and currencies since age-old times. Dentistry has used gold for centuries. The noble and catalytic properties make them of greater use in a vast range of industries (Housecroft & Sharpe, 2008). The noble metals are also growing in demand in the nanoscale manufacturing. Nanoparticles made up of precious metals are of great importance in the imaging technique, biology, medicine, and sensing due to their unique physicochemical properties (Jain et al., 2008; Lai-Kwan & Chang, 2012). The size-related properties which are different from bulk material, malleability, color, surface plasmon resonance, high surface to volume ratios, and simplicity of functionalization through simple chemistry make noble metal NPs very demanding in drug delivery, molecular diagnostics, analytical purposes and medical therapeutics.

The NPs made up of precious metals, especially Ag and Au, are amongst the most studied NPs. Many techniques are growing at rapid rate to determine the metal ionic species and organic together with biologically active compounds grounded on the practice of gold NPs (Upadhyayula, 2012; Wu et al., 2011). A combination of polymeric materials with precious metals to prepare composites to be implemented in catalysis, organic batteries, optoelectronic devices, sensors, microelectronics, and medicine due to the exclusive catalytic, magnetic, optical, and electrical properties (Yang et al., 2015). Several compounds developed by using gold are employed greatly in medicines attributed

to their anti-rheumatoid activity. Electronics and metal industries are growing more in demand of gold.

The gold and silver are two highly conductive metals, therefore, they are used in various applications where need to enhance electrical conductivity by using different engineering strategies in the form of nanostructures such as doping by chemical methods or physical mixing in a small amount in various composite materials or in different thin films by physical depositions techniques such as molecular beam epitaxy, radio frequency sputtering, and pulse laser deposition etc. The semiconductor materials have wide band gap; therefore, they are less conductive in nature. As silver and gold have narrow band gap, consequently which makes them highly conductive materials. Therefore, mixing, doping or decoration in the form of nanostructures of these precious metals in an optimized manner could dramatically enhance the conductivity of the composites or thin films developed with metal oxides or some other conducting polymers. However, being precious metals, only a small amount could be doped/decorated to get their maximum benefits to make them commercially and practically affordable. For example, Pandey *et al* electrochemically synthesized polypyrrole- silver nanocomposite and used in urea biosensor application (Pandey et al., 2018). The electrodes made of nanocomposite of PPy-Ag exhibited Nernstian behavior along with maximum slope of 57 mV showing the good detection limit compared to pure PPy. In another work, Tang and his co-workers prepared multilayer super-short carbon nanotubes (SSCNTs) by modifying the raw multiwalled carbon nanotubes through a simple ultrasonic oxidation-cut method which were subsequently used to prepare SSCNTs/PANI/Ag and PANI/Ag composites for supercapacitor application (Tang et al., 2016). It was seen that the composites displayed outstanding capacitive function along with a specific capacitance as large as 615 F g^{-1} at 1 A g^{-1} that is considered much larger than that is offered by PANI/Ag (454 F g^{-1}) and PANI (316 F g^{-1}). The results pointed SSCNTs/PANI/Ag composite, an auspicious type

of electrode material for the applications of efficient energy storage. Shahid *et al* prepared composite of reduced graphene oxide, cobalt oxide, and gold (rGO-Co₃O₄@Au) through hydrothermal synthesis method of one-pot to selectively detect hydrazine. The nanocomposite of rGO-Co₃O₄@Au revealed improved electro-catalytic activity to oxidation of hydrazine in phosphate buffer (pH 7.2). Amperometry technique was implemented to detect the hydrazine. There was linear response of current ranging between 10–620 μ M that is quite higher than the values reported formerly (Shahid et al., 2018).

It is clear from the above discussion that optimized use of small amount of precious metal in the form of nanostructure with different combination in the form of nanocomposite plays vital role to enhance the electrochemical activity of the binary or ternary nanocomposites. The transition metal oxides decorated with noble metal nanoparticles are greatly beneficial for many applications. Therefore, for an improved rate performance of pseudocapacitors, Au and Ag doped metal oxide electrodes have been studied broadly (Kang et al., 2013; Lu et al., 2012).

2.4 Ternary Nanocomposites as Electrode Material

Several redox active metal oxides such as NiO, MnO₂, MoO₂, Fe₂O₃, and Co₃O₄, etc., were utilized as electrode materials for energy storage devices with improved performance (Iwama et al., 2017). With the evolving technology in the 21st century, that needs better electrochemical performances, pristine metal oxides as electrode materials are unable to manage the current energy demand because of the underrated performance. The metal oxide nanostructures as standalone material experience increased particle aggregation which substantially reduce its active sites, cause fast capacity diminishing and structural falsification in charge-discharge reactions (Fang et al., 2013). Therefore, it is required to integrate nanostructures with the extremely conductive base. Carbon

materials such as MWCNTs, graphene, and conducting polymers are the perfect platform which not only enables the mechanism of charge transfer but can also avoid the agglomeration of NPs, heading for increasing electrochemical surface area and the cycling stability (Shahid et al., 2017).

The MWCNTs hold exclusive structure and extraordinary physiochemical properties like the electronic structure of sp^2 hybridized carbon (Popov, 2004). The metal oxide such as in Co_3O_4 , the Co^{2+} and Co^{3+} are reactive toward sp^2 hybridized carbon of the MWCNTs, therefore, Co_3O_4 nanostructures can be grafted onto the MWCNTs through the reaction between sidewalls of MWCNTs and cobalt ions. The MWCNTs are considered having tremendously narrow conductors bear diameters of several atomic distances, show ballistic electron transport, large porosity and are hollow in structure. Due to these special characteristics, they become an ideal platform to back metal oxide NPs which can clearly decrease the aggregations of the particle and enhance fast electron shuttling for metal oxide nanostructures deposited onto the MWCNTs network, specifically, in electrochemical applications. So, intercalation of Co_3O_4 nanostructure onto the MWCNTs network can stop fast capacity fading, structural distortion, and particle aggregations (Ozoemena & Chen, 2016). Additionally, the synergic outcome can be presented by metal oxide nanostructures hybridization with carbon matrices to fully optimize the electrochemical functioning. Though, the larger band gap of metal oxides results in lazy electron transfer. So, noble metals (Ag and Au) could be utilized to augment the conductivity of the ternary composite through channels of extended electron transfer which can constitute to the redox reaction. It is well known that other conducting platforms such as rGO and conducting polymers forming ternary composites with metal oxide and noble metals possess improved performance as an electrode material compared to pristine metal oxide or binary composites.

CHAPTER 3: MATERIALS AND METHODS

In this chapter, the description of chemicals and materials used for the development of ternary nanocomposites and their analysis studies are given. The detailed explanations of functionalization of MWCNTs, synthesis of GO, Co₃O₄ nanograins, PPy, PANI, Ag/Co₃O₄@MWCNTs, Au/Co₃O₄@MWCNTs, Ag/Co₃O₄@rGO, Ag/Co₃O₄@PPy, and Ag/Co₃O₄@PANI nanocomposites have been presented. In the last part, the details of instrumentations, parameters, and the analytical methods used for the morphological, structural and electrochemical studies have been described.

3.1 Materials

Materials and chemicals used for this thesis research work are summarized in Table 3.1.

Table 3.1: Materials and Chemicals.

Material/Chemicals	Formula	Purity (%)	Supplier
Potassium Permanganate	KMnO ₄	99.9	Friendemann Schmidt
Sulphuric Acid	H ₂ SO ₄	95-98	Fisher Scientific
Silver Nitrate	AgNO ₃	99.9	Sigma Aldrich
Cobalt Chloride	CoCl ₂ .6H ₂ O	99.9	Sigma Aldrich
Ammonia Hydroxide	NH ₄ OH	28	Friendemann Schmidt
Hydrochloric Acid	HCl	37	Fisher Scientific
Phosphoric Acid	H ₃ PO ₄	85	Fisher Scientific
Hydrogen Peroxide	H ₂ O ₂	28	Sigma Aldrich
Ethanol	C ₂ H ₅ OH	>99	EAM, Malaysia

Table 3.1, continued.

Material/Chemicals	Formula	Purity(%)	Supplier
Acetone	C ₃ H ₆ O	>99	EAM, Malaysia
poly (vinylidene fluoride)	-(C ₂ H ₂ F ₂) _n -	99	Sigma Aldrich
Potassium Hydroxide	KOH	99.9	R & M Chemicals
1-Methyl-2-pyrrolidinone	C ₅ H ₉ NO	99.5	Sigma Aldrich
Graphite Flake	-----	>99	Sigma Aldrich
Acetylene Black	-----	>95	Sigma Aldrich
Activated Carbon	AC	----	Kurary chemical
Multiwalled Carbon Nanotubes	MWCNTs	>90	Sigma Aldrich
Ferric Chloride	FeCl ₃	99.9	Friendemann Schmidt
p-Toluenesulfonic Acid	CH ₃ C ₆ H ₄ SO ₃ H	>98.5	Sigma Aldrich
Pyrrrole	C ₄ H ₅ N	>98	Sigma Aldrich
Aniline	C ₆ H ₅ NH ₂	>99	R & M Chemicals

3.2 Synthesis of Ternary Nanocomposites

All the ternary nanocomposites were synthesized by one-pot hydrothermal route. The reaction temperature was kept at 150 °C for fixed time of 5 hours. Hydrothermal route was preferred by virtue of its simplicity and choice of tuning various synthesis parameters (pH, temperature, time and concentration of reagents or precursors) (Lencka et al., 2000). The appropriate quantity of powdered reagents together with solvent were put in a teflon lined autoclave and heated from room temperature to high temperature which consequently helped to achieve the required pressure in a certain fixed period of time. The buildup of pressure due to increased temperature helps to obtain the required morphology and particle size of the sample. The electrolyte thermodynamics allowed us to predict optimum reaction conditions (Lencka et al., 2000).

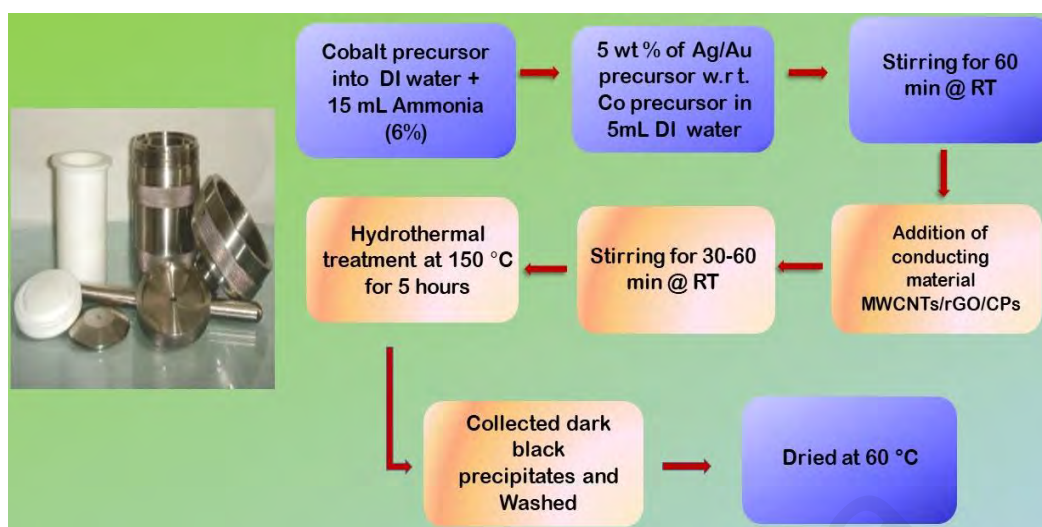


Figure 3.1: Schematic illustration of the synthesis of the ternary nanocomposites by hydrothermal method.

3.2.1 Functionalization of Multiwalled Carbon Nanotubes

The functionalization MWCNTs was performed by acid treatment in order to use them in MWCNTs based composites. Appropriate amount of MWCNTs powder was added in a mixture of 3:1 sulphuric/nitric acid (V:V) and stirred using magnetic stirrer for 1 hour. Then, the mixture was sonicated for 6 hours at room temperature followed by washing with DI water until pH reached to 7. The treated MWCNTs were dried overnight at 50 °C in a vacuum oven. The acid treatment of MWCNTs was done in order to increase their dispersion in water by functionalizing them with electronegative functional groups and removal of amorphous carbon as well as metal residue (Datsyuk et al., 2008).

3.2.2 Synthesis of Graphene Oxide

Graphene oxide (GO) was prepared by following simplified Hummer's method. In this process, 3 g of graphite flakes, 360 mL of sulphuric acid (H₂SO₄), 40 mL of phosphoric acid (H₃PO₄), and 18 g of potassium permanganate (KMnO₄) were mixed carefully in 1 litre glass beaker under constant stirring for 3 days at atmospheric temperature until the graphite was completely oxidized. The mixture was turned to dark brown from dark green color. The oxidation process was stopped with ice containing H₂O₂ and to control the

temperature of the mixture. The centrifugation technique was simply utilized to wash the graphite oxide by decanting the supernatant each time. The graphite oxide was exfoliated during washing with DI water which produced the thick graphite solution and at last obtained GO gel.

3.2.3 Synthesis of Cobalt Oxide Nanograins

The synthesis of Co_3O_4 nanograins was carried out by simple one pot hydrothermal method. In this procedure, 1 mM of $\text{CoCl}_2 \cdot 6\text{H}_2\text{O}$ was added in 35 mL deionized water under constant stirring. When the added cobalt oxide salt was completely dissolved then 15 mL of NH_4OH (6 %) was slowly added at a rate of 1 mL min^{-1} to the solution under constant stirring. After the addition of NH_4OH , the total volume of the solution became 50 mL and the whole solution was subjected to stir for another 30 to 60 minutes. Then the whole reaction mixture (50 mL) was transferred into a hydrothermal cell of 100 mL volume. After following the standard operating procedure, the hydrothermal cell was sealed and transferred into preheated ($150 \text{ }^\circ\text{C}$) oven and kept it for 5 hours at constant temperature of $150 \text{ }^\circ\text{C}$. When the hydrothermal cell was cooled, opened it with complete precautions and collected the dark black precipitates. Washed them 3-4 times with deionized water, finally with ethanol to removes any impurities and dried at $60 \text{ }^\circ\text{C}$.

3.2.4 Synthesis of Polypyrrole

PPy was synthesized by the polymerization of pyrrole in the presence of FeCl_3 as an oxidizing agent. In a typical process, 500 mL of 0.5 M pyrrole was prepared in 0.1 M *p*TSA solution and to which 500 mL of 0.5 M FeCl_3 solution was added. The entire setup was left for vigorous stirring for 6 hours, afterwards it was filtered and washed with excess of water and ethanol. Thus, obtained PPy was dried at $80 \text{ }^\circ\text{C}$ for 6 hours and finally stored in desiccator for experiments.

3.2.5 Synthesis of Polyaniline

PANI was synthesized by the oxidative polymerization of aniline in the presence of potassium persulfate (PPS) as an oxidizing agent. In a typical process, two solutions were prepared, firstly, 0.1 moles of aniline were dispersed in 250 mL of 1 M HCl and other solution containing 0.05 moles of PPS in 1 M HCl. To the dispersion of aniline, the solution of oxidant was added slowly, and the entire system was put under stirring conditions for 24 hours which resulted in greenish-black precipitates. The greenish-black precipitates of PANI were filtered and washed with excess of water and ethanol to remove salts, oligomers, and other impurities. The PANI was de-doped with excess of ammonia, thereafter, washed with excess of water, ethanol and further doped with 1.0 M HCl to render it conductive. Thus, the obtained PANI emeraldine salt was heated in an air oven for 12 hours and thereafter stored in a desiccator for further use.

3.2.6 Synthesis of Multiwalled Carbon Nanotubes Based Ternary Nanocomposites, (Ag/Co₃O₄@MWCNTs) and (Au/Co₃O₄@MWCNTs)

1 mM of CoCl₂.6H₂O was added in 20 mL DI water and 15 mL NH₄OH added dropwise at a rate of 1 mL min⁻¹ followed by one-hour constant stirring at room temperature. A 5 wt. % of AgNO₃ with respect to the cobalt precursor was separately dissolved in 5 mL of DI water and added dropwise in the above solution under constant stirring. 16 wt. % of the MWCNTs (with respect to the cobalt precursor) dispersed in 10 mL of DI water was added dropwise to the above solution. Finally, the total 50 mL solution was then shifted to teflon lined stainless steel autoclave and kept for hydrothermal reaction at 150 °C for 5 hours. The precipitates formed during the hydrothermal reaction were collected, washed several times with the copious amount of DI water and with ethanol by centrifugation and dried at 60 °C in hot air oven. The same procedure was repeated to prepare Co₃O₄@MWCNTs in the absence of AgNO₃.

For the synthesis of ternary nanocomposite Au/Co₃O₄@MWCNTs, the same above-mentioned procedure was adopted by using the gold precursor instead of silver in Ag/Co₃O₄@MWCNTs.

3.2.7 Synthesis of Reduced Graphene Oxide Based Ternary Nanocomposite, (Ag/Co₃O₄@rGO)

In the synthesis of the Ag/Co₃O₄@rGO composite, a freshly prepared 20 mL of GO solution of concentration 1 mg mL⁻¹ was transferred dropwise in 25 mL of ethanol under constant stirring. A 10 mL solution containing 1 mM of CoCl₂.6H₂O was added dropwise into the above solution under constant stirring at 60 °C. Then, 15 mL of NH₄OH (6 %) was slowly added at 1 mL min⁻¹ to the above mixture under constant stirring and let the solution stirred for an hour. A 5 wt. % of AgNO₃ in 5 mL of DI was separately dissolved in appropriation with the cobalt precursor and added dropwise in the above solution while keep stirring constantly. Afterward, followed the same procedure as mentioned above in section (3.2.6). The settled precipitates of Ag/Co₃O₄@rGO nanocomposites were then washed using DI water and ethanol several times which were dried at 60 °C in an oven. The binary nanocomposite (Co₃O₄@rGO) was synthesized by following the same steps in the absence of silver nanoparticles' precursor.

3.2.8 Synthesis of Conducting Polymers Based Ternary Nanocomposites, (Ag/Co₃O₄@PPy) and (Ag/Co₃O₄@PANI)

For the preparation of Ag/Co₃O₄@PPy and Co₃O₄@PPy nanocomposite, PPy (1 gm) was added under continuous stirring in the hydrothermal reaction mixture instead of MWCNTs as discussed above in the section (3.2.6) for the synthesis of multiwalled carbon nanotubes based ternary nanocomposites.

In case of Ag/Co₃O₄@PANI and Co₃O₄@PANI nanocomposites, simply PANI was used instead of PPy to synthesize the PANI based binary and ternary nanocomposites by

following the same hydrothermal synthesis procedure as for Ag/Co₃O₄@PPy under same conditions.

3.3 Characterization Techniques

3.3.1 Electron Microscopy Studies

The surface morphology, particle size and distribution of particles in the composites were studied by using various electron microscopy techniques such as field emission scanning electron microscopy (FESEM), energy dispersive spectroscopy (EDS), and high resolution transmission electron microscopy (HRTEM).

In FESEM, electron beam is raster scanned over the sample's surface starting from one corner to another corner. When the electron beam falls on the surface, secondary electrons are emitted in particular fashion revealing the topology of the sample and presenting the same copy which is shown on the computer monitor as an image. FESEM employs field emission gun, also known as cold cathode field emitter which does not involve the heating up of the filament and emission is achieved by placing the filament in huge electrical potential gradient. Thus, the images produced using FESEM is cleaner and of high resolution instead of the images obtained through simple scanning electron microscopy (SEM). In this work FESEM (JEOL JSM-7600F) was used for images recording of the samples.

Energy dispersive spectroscopy is an analytical technique used for the elemental analysis or chemical characterization of a sample. It follows on an interaction of some source of X-ray excitation and a sample under investigation. This technique is based on the fundamental principle that each element has a unique atomic structure allowing a unique set of peaks on its electromagnetic emission spectrum which is the main principle of spectroscopy (Lyman et al., 2012). EDS is usually fitted with FESEM. Apart from the

compositional analysis, its mapping feature also provide the distribution of different particles in the compound/composite material which could be used as an evidence for proper mixing or uniform distribution of constituent elements. Oxford EDS system was used in this work for analysis fitted with FESEM.

Transmission electron microscopy provides direct images of the atomic structure of the samples; hence, it is possible to have direct information about the crystallographic structure of materials from images. High phase contrast images as small as a crystal cell can be acquired. This technique is widely used in advanced characterization of materials, allowing the acquisition of information about punctual defects, stacking faults, precipitates, and grain boundaries. Transmission electron microscope (TEM) images were obtained by JEOL ARM 7600 in this research work.

3.3.2 X-ray Diffraction Analysis

X-ray diffraction (XRD) is widely used non-destructive technique for the analysis of materials such as liquids and powders. XRD provides the identification of crystalline phases of the material under investigation which are subsequently applied for material identification. The properties and functions of materials primarily depend on the crystal structures.

The crystallinity of the samples in this work were determined using X-ray diffraction Rigaku Ultima IV, X-ray diffractometer (XRD) equipped with Cu-K α source ($\lambda = 1.5418$ Å) at a scan rate of 0.02 s $^{-1}$. The samples were scanned in the 2θ range of 5° to 80° . The generated data was analyzed using PANanalytical X'pert Highscore software.

3.3.3 X-ray Photoelectron Spectroscopy Analysis

The elemental composition, chemical state, and electronic state of the elements that exist in the sample is determined through X-ray photoelectron spectroscopy (XPS) analysis. The sample was prepared by dispersing the sample powder into ethanol solvent

and coated on cleaned silicon wafer. The survey spectra were recorded in the range of 0 - 1100 eV at a pass energy of 200 eV with a resolution of 1 eV, while high resolution spectra were recorded with a pass energy of 50 eV within a resolution of 0.1 eV. X-ray photoelectron spectroscopy (XPS) was performed on a PHI 5000 Versa Probe Scanning Electron Spectroscopy for Chemical Analysis (ESCA) Microprobe (PHI 5000 Versa Probe II, USA) in an ultrahigh vacuum chamber ($\sim 10^{-10}$ mbar) using monochromatic Al-K α ($h\nu=1486.6$ eV) anode. Deconvolution of each spectrum by curve fitting of XPS core-level spectra was done using Multipack software (version 9, ULVAC-PHI, Inc.).

3.4 Electrochemical Analysis

3.4.1 Preparation of Electrodes

The electrode used in electrochemical (EC) measurements was fabricated by blending 7.5 mg (75 wt. %) of the prepared active material, 1.5 mg (15 wt. %) of activated carbon (AC) and 1.0 mg (10 wt. %) of poly (vinylidene fluoride) (PVdF) in N-Methyl-2-pyrrolidinone (NMP) and stirred for several hours until a homogenous slurry was obtained. Then, the nickel foam (1×1 cm² area) was surfaced by drop cast method with above prepared slurry and kept in an oven at a temperature of 90 °C for 12 hours to let it dry. The average mass loading of active material was about $\sim 5.00 \pm 0.5$ mg.

The mass loading of the active material on the Ni foam can be calculated by the following steps;

Mass of bare Ni foam: m_1 mg

Total mass of dried coated Ni foam: m_2 mg

The net mass loading of the active material (mg) = $(m_2 - m_1)$ mg \times 75%.

75% is referring to the weight percentage of active material.

The measured mass loading of Ag/Co₃O₄@MWCNTs, Au/Co₃O₄@MWCNTs, Ag/Co₃O₄@rGO, Ag/Co₃O₄@PPy and Ag/Co₃O₄@PANI on Ni foam (without acetylene black and PVDF) was approximately 5.00±0.5 mg (0.005±0.0005 g) (Zhang & Pan, 2015).

3.4.2 Electrochemical Studies

The suitability of prepared samples in all five projects toward the supercapattery application was evaluated using three electrodes cell in 1 M KOH solution at atmospheric temperature. The active material coated nickel foam (1×1 cm²) served as working, Ag/AgCl as reference, and platinum foil (1x1 cm² area) as counter electrodes. Cyclic voltammetry (CV) in the range of 0-0.5 V versus Ag/AgCl, electrochemical impedance spectroscopy (EIS) in 0.01-100 kHz range at an alternating voltage of 10 mV (R.M.S) and galvanic charge-discharge (GCD) at various potential and current densities measurements were recorded with Gamry Interface 1000 electrochemical workstation to characterize the synthesized nanomaterials. In each research project among the prepared set of samples, the electrochemically best performing sample was utilized for two electrode supercapattery assembly where active material coated electrode served as an anode while carbonaceous material coated electrode was used as a cathode. The assembled devices were studied again using two electrode cell system using CV and GCD in the potential range of 0-1.5 V and EIS in 0.01-100 kHz range at an alternating voltage of 10 mV (R.M.S) in 1 M KOH electrolyte solution to evaluate their performance in terms of energy density, power density as well as cyclic stability.

CHAPTER 4: RESULTS AND DISCUSSION

This chapter includes the detailed discussions of the results obtained for all five systems, *i.e.*, Ag/Co₃O₄@MWCNTs, Au/Co₃O₄@MWCNTs, Ag/Co₃O₄@rGO, Ag/Co₃O₄@PPy and Ag/Co₃O₄@PANI.

4.1 Multiwalled Carbon Nanotubes Based Ternary Nanocomposites

Among the family of transition metal oxides, Co₃O₄ in cubic spinel structure has drawn particular attention due to its higher theoretical capacity, reversibility and relatively rich in abundance (Deng et al., 2009; Wang et al., 2015; Yuan et al., 2012). In cobalt oxide (Co₃O₄), cobalt ions exist in two oxidation states such as Co²⁺ and Co³⁺, which are situated at the interstitial tetrahedral and octahedral sites of the closed packed face centered cubic structure formed by the oxygen ions, respectively. The distribution of Co²⁺ and Co³⁺ over the tetrahedral and octahedral sites, respectively, offer diverse polar sites in Co₃O₄ crystals along with high surface to volume ratio and prominent catalytic activity which can promote not only in determining the charges but also enhance fast charge transfer kinetics on the electrode surface (Numan et al., 2017). However, cobalt oxide nanograins undergo high particle aggregation which considerably reduce its active sites, cause rapid capacity fading and structural distortion during charge-discharge reaction (Fang et al., 2013). Therefore, it is necessary to incorporate Co₃O₄ nanograins with the highly conductive platform. Carbon materials such as multiwalled carbon nanotubes (MWCNTs) and graphene are the ideal platform which not only facilitate the charge transfer mechanism but also prevent the agglomeration of nanoparticles, leading to increase the cycling stability and electrochemical surface area (Shahid et al., 2017).

Among carbonaceous matrices, MWCNTs possess unique structure and remarkable physiochemical properties such as its electronic structure in which each carbon atom is

sp^2 hybridized (Popov, 2004). As the Co^{2+} and Co^{3+} are reactive toward sp^2 hybridized carbon of the MWCNTs, therefore, Co_3O_4 nanograins can be grafted onto the MWCNTs through the reaction between sidewalls of MWCNTs and cobalt ions. The MWCNTs are extremely narrow conductors with diameters in the range of several atomic distances, show ballistic electron transport, high porosity and are hollow in structure. These characteristic features make them ideal platform to support metal oxide nanoparticles which can significantly reduce the particle aggregations and boost rapid electron shuttling for metal oxide nanostructures grown onto the MWCNTs network, especially, in electrochemical applications. Hence, intercalation of Co_3O_4 nanograins onto the MWCNTs network can prevent from rapid capacity fading, structural distortion, and particle aggregations (Ozoemena & Chen, 2016). Furthermore, the synergic effect can be introduced by hybridizing the nanostructures of metal oxide with carbon matrices to completely optimize for electrochemical performance. Since, band gap of metal oxides is higher which results in sluggish electron transfer. Therefore, noble metals M (M=Ag/Au) can enhance the conductivity of the nanocomposite by providing extended electron transfer channels which can contribute to increase the efficiency of redox reaction.

On the basis of above discussion mechanism, the ternary nanocomposites of M/ Co_3O_4 @MWCNTs were synthesized by a facile single step hydrothermal process, characterized and utilized for application studies. The schematic illustration of the formation mechanism of ternary nanocomposites are shown below in Figure 4.1.

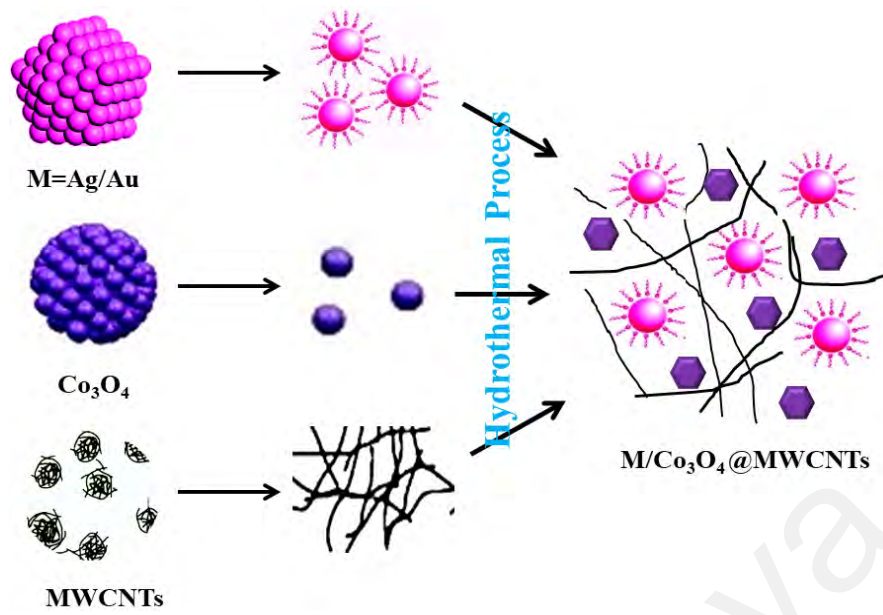


Figure 4.1: Schematic representation of the formation of ternary nanocomposite of cobalt oxide nanoparticles intercalated in MWCNTs matrix and decorated with noble metal M(Ag/Au).

Universiti Malaysia

4.2 System 1: Multiwalled Carbon Nanotubes Incorporated with Silver Nanoparticles and Cobalt Oxide Nanograins (Ag/Co₃O₄@MWCNTs), Ternary Nanocomposite

4.2.1 Surface Morphology Study

To analyze the surface morphology of the Co₃O₄ nanograins and the nanocomposites, FESEM images were taken at different magnifications. Figure 4.2 represents the typical morphological scans of Co₃O₄ nanograins, Co₃O₄@MWCNTs, and Ag/Co₃O₄@Ag nanocomposite, uniformly dispersed on the silicon substrate. It can be noticed from Figure 4.2(a) that the pure Co₃O₄ exhibited granular structure with particle size approximately ~30 nm. The unaided Co₃O₄ nanograins were highly aggregated, leading to poor exposure of their cubic faces. However, the particles aggregation was significantly reduced in Co₃O₄@MWCNTs nanocomposite which can be seen in the FESEM micrograph (Figure 4.2(b)) due to the uniform growth of Co₃O₄ nanograins at oxygen containing functional groups on MWCNTs during the hydrothermal reaction. Figure 4.2(c) and (d) show the low and high magnification images of Ag/Co₃O₄@MWCNTs nanocomposites. The presence of ultra-small nanoparticles on Co₃O₄ nanograins and MWCNTs correspond to the Ag nanoparticles which are decorated uniformly on Co₃O₄@MWCNTs (Figure 4.2(d)). It is evident from FESEM images that Co₃O₄ nanograins and Ag nanoparticles were successfully integrated with MWCNTs matrix. Further, it was analyzed with TEM to get clear view of the ternary nanocomposite and the distribution of Co₃O₄ nanograins and Ag NPs. Figure 4.3 shows the TEM image of the ternary nanocomposite taken at low and high magnifications. The growth and uniform distribution of nanoparticles on MWCNTs network could be observed in Figure 4.3(a) while Figure 4.3(b) identifies the presence of Co₃O₄ nanograins and Ag NPs nanoparticles on the MWCNTs matrix.

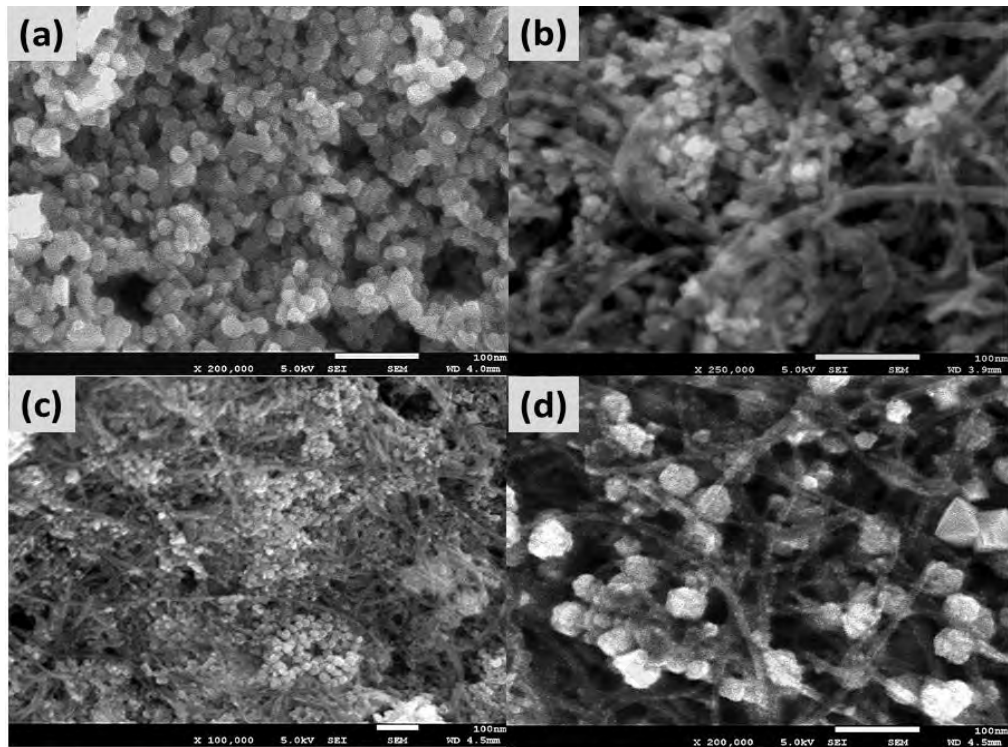


Figure 4.2: FESEM images of (a) Co₃O₄ nanograins, (b) Co₃O₄@MWCNTs binary nanocomposite (c) low magnification image of Ag/Co₃O₄@MWCNTs ternary nanocomposites, and (d) high magnification image of Ag/Co₃O₄@MWCNTs ternary nanocomposites.

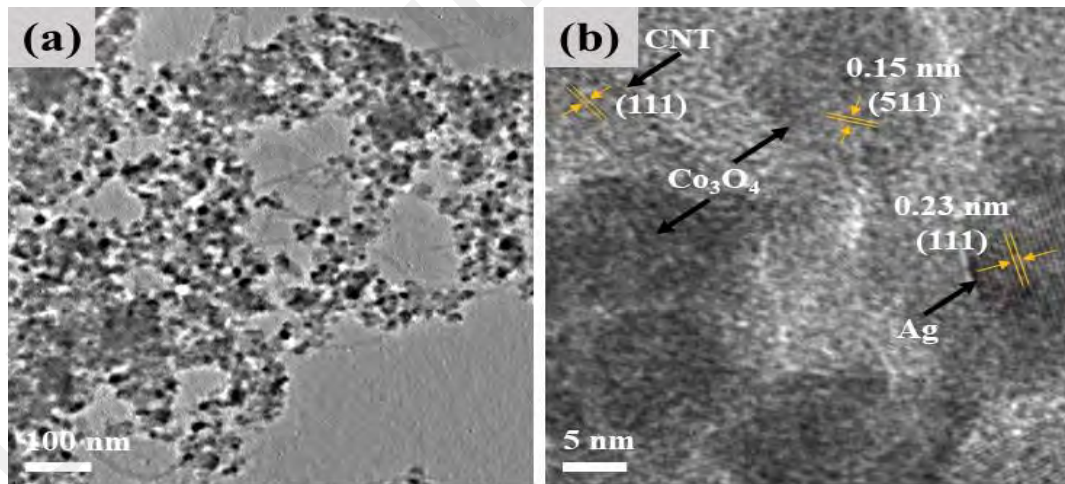


Figure 4.3: HRTEM images of Ag/Co₃O₄@MWCNTs ternary nanocomposite (a) at low and (b) at high magnifications.

Figure 4.4 represents the percentage composition of different elements and their corresponding mapping present in the Ag/Co₃O₄@MWCNTs nanocomposite. Figure 4.4(a) shows the selected rectangular area used for EDS studies. The presence of Pt was due to the coating on the sample to avoid charging and Si peak appears from the substrate

(Figure 4.4(b)). The EDS analysis was conducted on randomly selected areas, reveals the presence of carbon which comes from MWCNT, Co from Co_3O_4 , and Ag nanoparticles, which confirms the formation of $\text{Ag}/\text{Co}_3\text{O}_4@\text{MWCNTs}$ nanocomposite. It can be seen that the prepared nanocomposite is highly pure which is also supported by XRD results. Moreover, the color scheme used in the mapping of EDS analysis provides the insight to assure the uniform distribution of all individual nanoparticles throughout the nanocomposite. Figure 4.4(c), (d) and (e) demonstrate the distribution of the individual elemental mapping of the Ag (blue color), Co (green) and C (maroon color) in the nanocomposite, respectively. Figure 4.4(f) verifies the uniform distribution of Co_3O_4 nanograins and Ag nanoparticles on the MWCNTs networks.

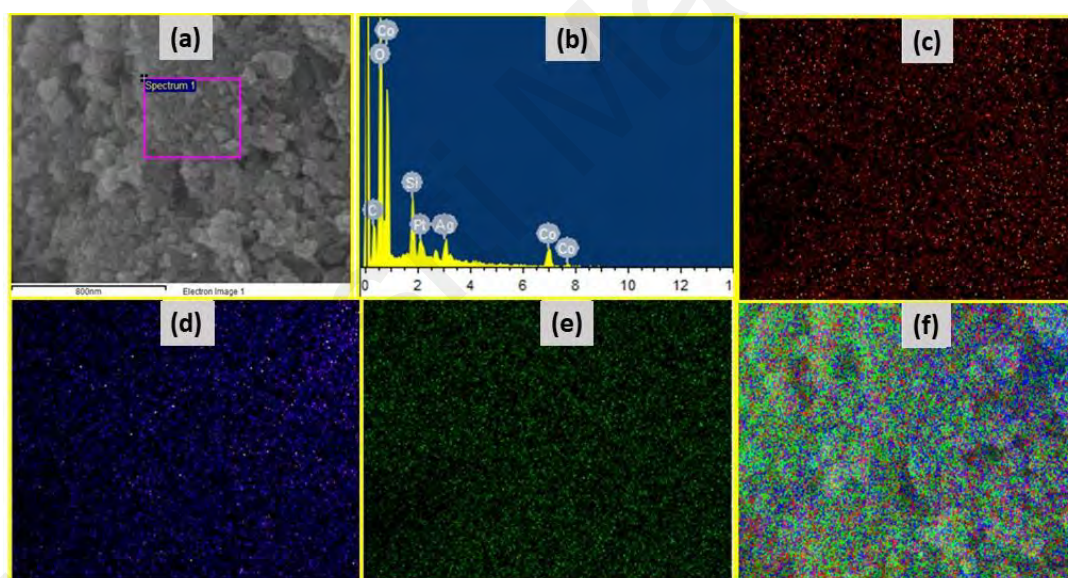


Figure 4.4: (a) FESEM image of the $\text{Ag}/\text{Co}_3\text{O}_4@\text{MWCNTs}$ nanocomposite at low magnification used for EDS, (b) EDS spectrum of $\text{Ag}/\text{Co}_3\text{O}_4@\text{MWCNTs}$ nanocomposite, (c) elemental mapping of Ag, (d) elemental mapping of Co, (e) elemental mapping of C, (f) elemental mapping showing the uniform distribution of C, Ag and Co in the $\text{Ag}/\text{Co}_3\text{O}_4@\text{MWCNTs}$, ternary nanocomposites.

4.2.2 X-ray diffraction Analysis

The structural analysis and crystallinity of the prepared pure Co_3O_4 and its nanocomposites were evaluated by XRD. Figure 4.5 shows the XRD patterns of the pure Co_3O_4 , $\text{Co}_3\text{O}_4@\text{MWCNTs}$, and $\text{Ag}/\text{Co}_3\text{O}_4@\text{MWCNTs}$ nanocomposites. It is evident from the XRD patterns that diffraction pattern of Co_3O_4 nanograins as well as its nanocomposites with MWCNTs and Ag, exhibit very sharp peaks which reveals their polycrystalline nature. The pure Co_3O_4 nanograins displayed characteristic peaks at 2θ values of 18.81° , 30.95° , 36.47° , 44.35° , 58.72° and 64.52° that correspond to (111), (220), (311), (400), (511) and (440) lattice planes, respectively. All the diffraction peaks of Co_3O_4 nanograins are well indexed with the cubic phase with space group $\text{Fd}\bar{3}\text{m}$ (ICDD-PDF 96-900-5893). The peak intensities of Co_3O_4 nanograins in $\text{Co}_3\text{O}_4@\text{MWCNTs}$ and $\text{Ag}/\text{Co}_3\text{O}_4@\text{MWCNTs}$ nanocomposites decreased slightly compared to pure Co_3O_4 nanograins due to the introduction of MWCNTs that covered some of the Co_3O_4 nanograins. This revealed the successful integration of Co_3O_4 nanograins with MWCNTs. The characteristic peaks of Ag are evident in $\text{Ag}/\text{Co}_3\text{O}_4@\text{MWCNTs}$ nanocomposite at 2θ value of 38.23° , 44.42° , 64.62° and 77.44° , which are attributed to (111), (200), (220) and (311) lattice planes respectively, representing the presence of cubic structure Ag with space group $\text{Fm}\bar{3}\text{m}$ in the ternary nanocomposite (ICDD-Pdf No.00-001-1164). The hybridization of the noble metals such as Ag in the nanocomposite produces the synergistic effect by providing the transfer channel which ultimately enhances the electrochemical performance of the ternary nanocomposite.

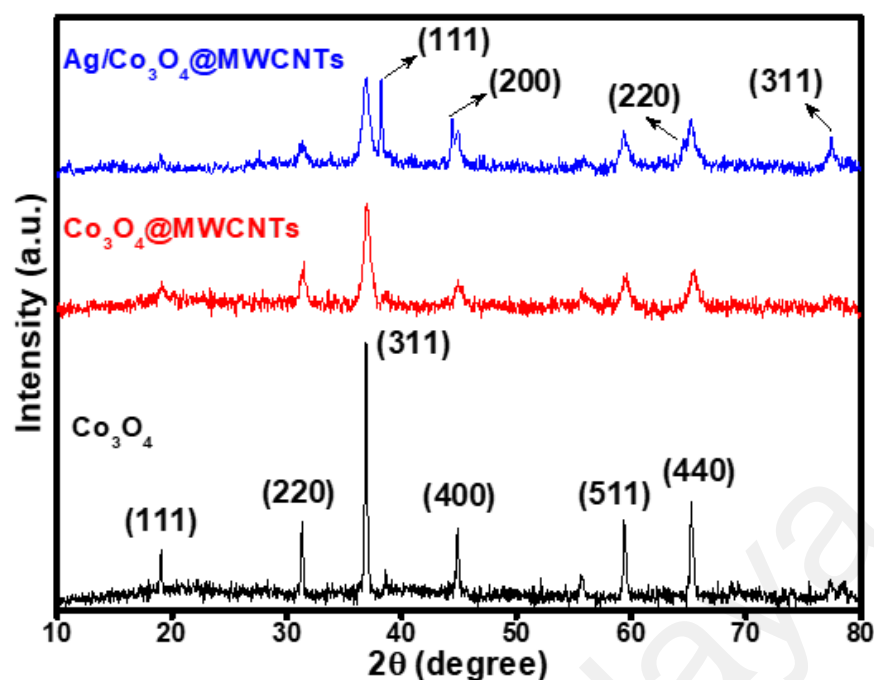


Figure 4.5: XRD patterns of pure Co_3O_4 nanograins, $\text{Co}_3\text{O}_4@MWCNTs$ and $\text{Ag}/\text{Co}_3\text{O}_4@MWCNTs$ nanocomposites.

4.2.3 X-ray Photoelectron Spectroscopy (XPS) Analysis

XPS is considered a powerful tool to discover the identity of the composed surface as well as the metal oxidation states to provide a synergetic support to prepare material. A survey scan of the prepared $\text{Ag}/\text{Co}_3\text{O}_4@MWCNT$ ternary nanocomposite was performed in order to confirm the presence of all elements contribute in the nanocomposite. The scan of the elemental composition is shown in Figure 4.6(a). In Figure 4.6(b) the low intensity carbon peak was assigned to residual carbon from the sample and hydrocarbons from the XPS instrument (Ansari et al., 2014). The C *1s* peaks can be deconvoluted into two large peaks at 284.12 eV, 285.52 eV and a significantly low peak at 288.16 eV corresponding to the C-C, C-O-C and O-C=O of related to the carbon of MWCNTs and some of the other impurities due to its functionalization, respectively. The peaks obtained from Co *2p* are clearly seen in Figure 4.6(c) with strong peaks at 782.21 and 780.69 eV. The absence of specific peaks such as 787 and 804 eV come from CoO, confirms the formation of Co_3O_4 (Natile & Glisenti, 2003). Figure 4.6(d) shows the spread of O *1s* peaks with an intense peak at 530.79 eV attributes to the metal-oxygen bonding and a weaker peak at

532.40 eV testifies the adsorption of oxygen on the surface (Marik et al., 2012). Whereas, the spread of synergetic Ag 3d is shown in Figure 4.6(e). Two prominent and intense Ag 3d_{5/2} and Ag 3d_{3/2} peaks are obvious at 373.31 and 367.13 eV owing to spin-orbital split of around 6.18 eV which is a clear evidence of the Ag presence in its metal form (Marik et al., 2012).

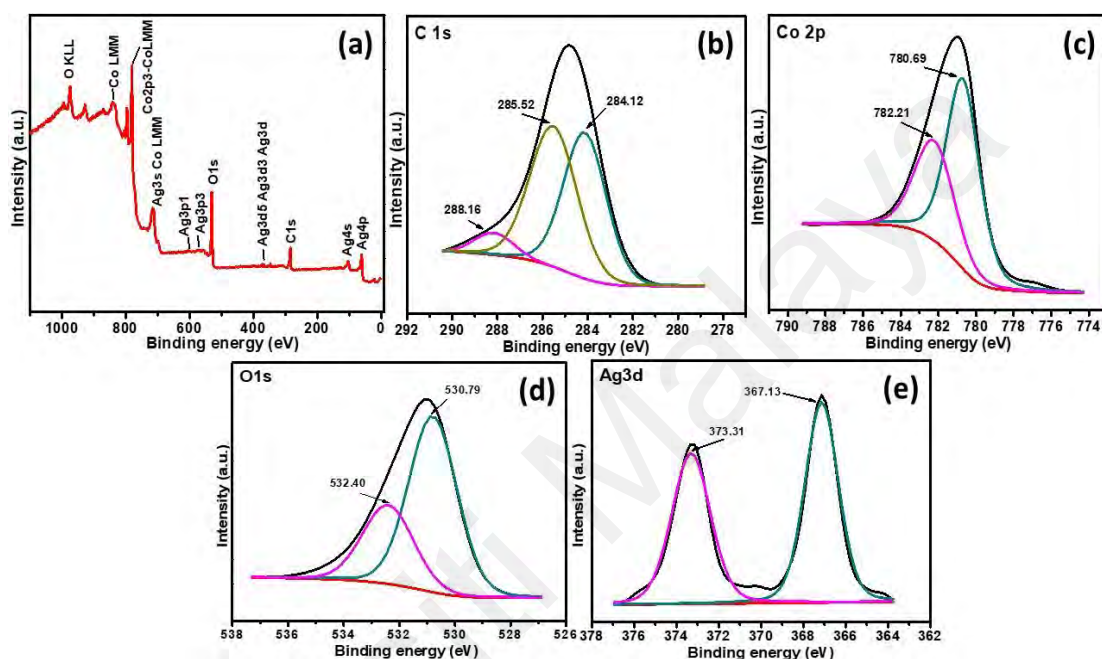


Figure 4.6: (a) XPS survey scanning of the Ag/Co₃O₄@MWCNTs, ternary nanocomposites. The high resolution spectra (b) C 1s region, (c) Co 2p region, (d) O 1s region and (e) Ag 3d region.

4.2.4 Electrochemical Analysis of Co₃O₄, Co₃O₄@MWCNTs and Ag/Co₃O₄@MWCNTs, Ternary Nanocomposite

(a) Cyclic Voltammetry (CV) Analysis

Figure 4.7 shows the cyclic voltammetric (CV) response of Co₃O₄, Co₃O₄@MWCNTs and Ag/Co₃O₄@MWCNTs nanocomposites at different scan rates (3, 5, 10, 20, 30, 40, and 50 mVs⁻¹) in the potential range of 0-0.5 V in standard three electrodes cell system at room temperature. Figure 4.7(a) demonstrates the comparison of bare Ni foam and Co₃O₄ in the three electrodes cell system at scan rate of 3 mV s⁻¹. It is evident that the contribution in the current density from Ni foam is negligible in the overall current density of Co₃O₄

CV scans when measured in 1 M KOH electrolyte solution. The CV curve of Co₃O₄ nanograins (Figure 4.7(a)) consists of two pairs of asymmetric redox shoulder peaks due to the formation of multiple Co₃O₄ phases and also it undergoes to different oxidation states (Tummala et al., 2012). The cathodic and anodic crests occur at the +ve and -ve current density in CV curve, respectively which correspond to the oxidation and reduction processes to the Co₃O₄ moieties. These peaks showed the redox transitions of the Co(II), Co(III) and Co(IV) due to faradaic behavior (Tummala et al., 2012). They are situated at 0.35/0.24 V and 0.42/0.39 V (vs Ag/AgCl) at 3 mV s⁻¹ resulting from reversible transition between Co₃O₄ and CoOOH (II/III) and between CoOOH and CoO₂ (III/IV). Redox peaks attribute to the dispersal of electrolyte in the materials suggesting that Co₃O₄ nanograins are showing battery type behavior (Pan et al., 2010; Tummala et al., 2012). The oxidation reduction process takes place in two sequential steps in an alkaline medium (1 M KOH) as shown in equation (4.1) and (4.2) (Xiang et al., 2013).



Figure 4.7(b), (c) and (d) depict the CV curves of Co₃O₄, Co₃O₄@MWCNTs and Ag/Co₃O₄@MWCNTs nanocomposites at different scan rates, respectively. It is evident from Figure 4.7(c) that redox peak current of the Co₃O₄@MWCNTs nanocomposite was significantly increased compared to Co₃O₄ nanograins due to the presence of MWCNTs. The introduction of MWCNT significantly reduced particle aggregations leading to exposure of more active sites of electrode material for the redox reactions. In addition, the porous structure of MWCNT and its edge sites at the walls as well as at the ends provide rapid charge transfer kinetics, which aid to faradaic reactions (Kurusu et al., 2006). However, in case of Ag/Co₃O₄@MWCNTs, ternary nanocomposite (Figure 4.7(d), the distortion in the CV curves and shift in redox peaks were not significant compared to pristine Co₃O₄ and Co₃O₄@MWCNTs, binary nanocomposite. This reveals

the highly electrochemical reversible behavior of the nanocomposite. The significant increase in the redox peak observed was due to the synergistic effect of Ag nanoparticles by providing extended channels for electron transfer during redox process due to their excellent electronic conductivity, consequently, the electrochemical performance of the Ag/Co₃O₄@MWCNTs, ternary nanocomposites can be remarkably improved by decorating with Ag nanoparticles (Wang et al., 2017). Therefore, it was expected that the decoration of Co₃O₄@MWCNTs, nanocomposite with Ag nanoparticles could further improve its conductivity and capacity performance (Xia et al., 2015). The comparison of CV curves of pristine Co₃O₄ nanograins, Co₃O₄@MWCNTs binary and Ag/Co₃O₄@MWCNTs, ternary nanocomposites at a scan rate of 3 mVs⁻¹ are shown in Figure 4.7(e). The high electrochemical performance was also due to the high electrochemical surface area of Ag/Co₃O₄@MWCNTs, ternary nanocomposites followed by the electrochemical surface area of Co₃O₄@MWCNTs and Co₃O₄ nanograins. Additionally, Ag/Co₃O₄@MWCNTs, ternary nanocomposites executed high and reversible peak current compared to its counterparts. The higher background current for Co₃O₄@MWCNTs, binary nanocomposite compared to Co₃O₄ nanograins is ascribed to the highly conductive platform of the MWCNT in Co₃O₄@MWCNTs, nanocomposites. The specific capacity through CV curve was estimated by the following equation (4.3).

$$Q_s = \frac{1}{vm} \int_{v_i}^{v_f} I \times V dV \quad (4.3)$$

where, Q_s stands for the specific capacity (C g⁻¹), v stands for the scan rate (V s⁻¹), m is the mass loading of the active material (g) and the integral term is equivalent to the anodic peak area under the CV curve. The maximum specific capacity achieved for Ag/Co₃O₄@MWCNTs, ternary nanocomposites were 98.00 C g⁻¹ which is significantly higher in value compared to 62.30 and 41.50 C g⁻¹ for Co₃O₄@MWCNTs, binary nanocomposite and Co₃O₄ nanograins, respectively.

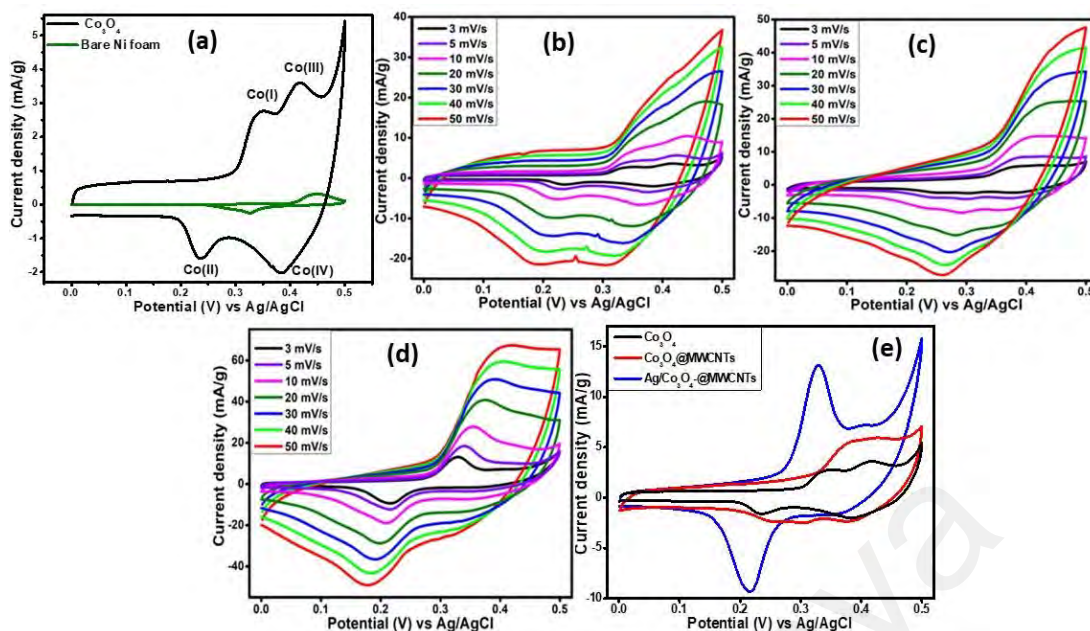


Figure 4.7: (a) Comparison of CV curves of pure Co_3O_4 and bare Ni foam. Cyclic voltammograms at diverse scan rates (b) Co_3O_4 nanograins, (c) Co_3O_4 @MWCNTs, (d) $\text{Ag}/\text{Co}_3\text{O}_4$ @MWCNTs, ternary nanocomposite and (e) comparison of CV curves of pure Co_3O_4 nanograins, Co_3O_4 @MWCNTs and $\text{Ag}/\text{Co}_3\text{O}_4$ @MWCNTs at a scan rate of 3 mV s^{-1} .

(b) *Galvanostatic Charge-discharge (GCD) Analysis*

The plots of galvanostatic discharge were recorded for all samples at different current densities ($0.6\text{-}3.0 \text{ A g}^{-1}$) in a potential range of $0\text{-}0.5 \text{ V}$ and are depicted in Figure 4.8. Non-linearity of the discharge curves of all samples in Figures 4.8(a), (b) & (c) reveals that all nanocomposites exhibit battery type behavior. The ternary nanocomposites, $\text{Ag}/\text{Co}_3\text{O}_4$ @MWCNTs gave longest discharge time compared to Co_3O_4 nanograins, and MWCNT decorated with Co_3O_4 (Figure 4.8(d)). The longest discharge time of the binary and ternary nanocomposites compared to pure Co_3O_4 nanograins demonstrating that the presence of MWCNTs and Ag doping were able to extend the duration of energy dissipation time due to the large interfacial area accessible to the OH^- for faradaic reactions (He et al., 2016). The specific capacity of the nanocomposites (Q_s) was calculated from their discharge plots by the following equation (4.4).

$$Q_s = \frac{I \times \Delta t}{m} \quad (4.4)$$

where, I notate the discharge current (A), Δt stands for the discharge time (s) and m is the mass (g) of the active material. The estimated specific capacities are 39.24, 55.33 and 83.90 C g⁻¹ for Co₃O₄, Co₃O₄@MWCNTs and Ag/Co₃O₄@MWCNTs nanocomposites, respectively at a current density of 0.6 A g⁻¹.

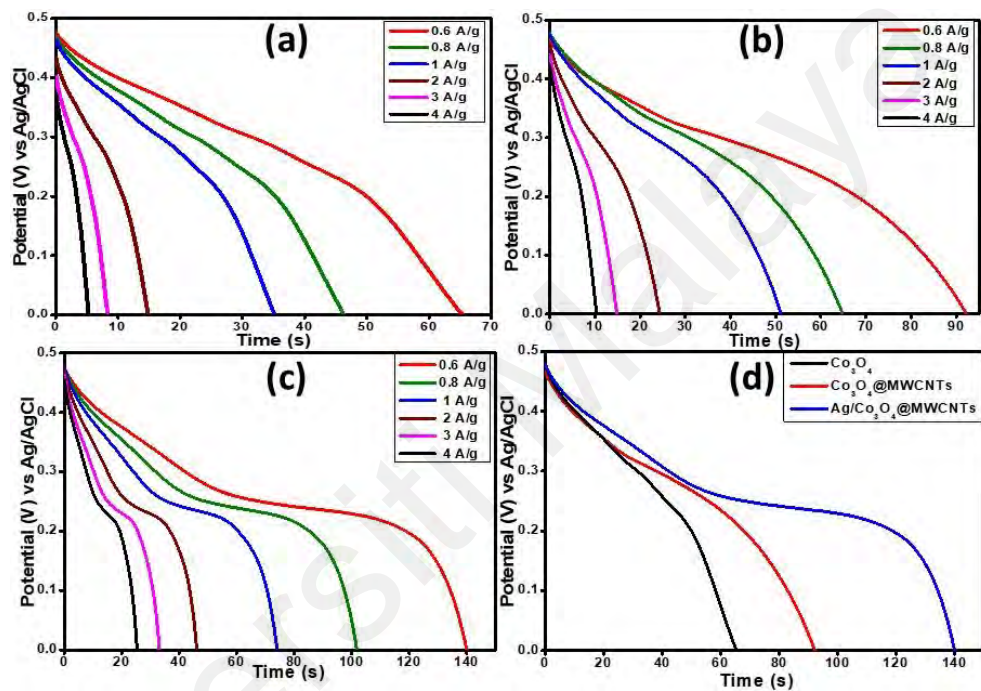


Figure 4.8: Discharge curves of (a) Co₃O₄ nanograins, (b) Co₃O₄@MWCNTs (c) Ag/Co₃O₄@MWCNTs nanocomposites at diverse current densities (d) comparative discharge curves of pure Co₃O₄ nanograins, Co₃O₄@MWCNTs and Ag/Co₃O₄@MWCNTs nanocomposites at a current density of 0.6 A g⁻¹.

Figure 4.9(a) represents the capacity retention of all samples at higher current densities. It is noteworthy here that the Q_s values show a gradual decrease with increase in the current densities which was due to the asynchronous shuttling of charges with respect to the current rates (Figure 4.9(a)). Furthermore, the process of diffusion or migration of electrolyte ions through the electrodes at higher current density values was also sluggish (Fu et al., 2006). The value of Q_s for Ag/Co₃O₄@MWCNTs nanocomposite was decreased to 74.00 C g⁻¹ with a retention value of 88.00 %, whereas, the values of Q_s

for $\text{Co}_3\text{O}_4@\text{MWCNTs}$ and Co_3O_4 nanograins were decreased to 41.30 (74.00 %) and 21.20 C g^{-1} (54.00 %), respectively. It is clear that pure Co_3O_4 nanograins exhibits the lowest performance compared to its counterpart nanocomposites, which is due to the high aggregations and low conductivity of the Co_3O_4 nanograins, resulting in the poor electrochemical performance. However, the introduction of MWCNTs into the Co_3O_4 nanograins increased the rate capability which may be due to high dispersion and the intercalation of Co_3O_4 nanograins onto the MWCNTs networks. A remarkable enhancement in Q_s and rate capability were observed when the $\text{Co}_3\text{O}_4@\text{MWCNTs}$ nanocomposite was decorated with Ag nanoparticles. Therefore, anchoring of Ag with $\text{Co}_3\text{O}_4@\text{MWCNTs}$ nanocomposite further boosted the performance of final nanocomposite.

(c) ***Electrochemical Impedance Spectroscopy (EIS) Analysis***

Electrochemical impedance spectroscopy (EIS) was also implemented in the frequency range of 0.1-100 kHz at an AC voltage of 10 mV (R.M.S.) to know the intrinsic mechanism occurred on the electrodes. The spectra obtained from AC impedance of all nanocomposites are shown in Figure 4.9(b). The high frequency region has been used to evaluate the resistance trend of the electrode. The total equivalent resistance of the system is calculated from the X-intercept of the plot with the real axis in the system. The diameter of the extended semicircle provides the resistance originated from the charge transfer kinetics (R_{ct}) which is colligated with the proliferous geometry and the conductivity of the electrode/electrolyte interface (Zhou et al., 2004). The capacitive behavior of the system is evaluated from the straight line taking off after the frequency knee point. However, in a case to approach ideal situation capacitive behavior should exhibit a straight line nearly parallel to the imaginary axis. Warburg impedance or diffusion

resistance is estimated from the slope of the straight line in the low frequency region (Huang et al., 2003).

The Nyquist plots of EIS spectra for Co_3O_4 , $\text{Co}_3\text{O}_4@\text{MWCNT}$, and $\text{Ag}/\text{Co}_3\text{O}_4@\text{MWCNTs}$ nanocomposites modified electrodes are shown in Figure 4.9(b). A straight line and semicircle can be seen at low frequency and high frequency regions, respectively. The impedance behavior of $\text{Ag}/\text{Co}_3\text{O}_4@\text{MWCNTs}$ nanocomposite modified electrode exhibited very close to ideal EDLC with a low R_{ct} value (1.26Ω) and highly vertical line in low frequency region. Whereas, $\text{Co}_3\text{O}_4@\text{MWCNTs}$ predicts a larger semicircle (with R_{ct} value of 3.1Ω) than $\text{Ag}/\text{Co}_3\text{O}_4@\text{MWCNTs}$ but smaller than Co_3O_4 nanograins (R_{ct} value of 4.9Ω) which indicates that it has higher charge transfer resistance than ternary nanocomposite ($\text{Ag}/\text{Co}_3\text{O}_4@\text{MWCNTs}$) but lesser than the Co_3O_4 nanograins. Warburg impedance concluded by the straight line generated from the diffusion of OH^- within the electrode material. The $\text{Ag}/\text{Co}_3\text{O}_4@\text{MWCNTs}$ nanocomposite demonstrated the most vertical line parallel to the imaginary axis which represents its enhanced charge storage behavior. Better conductivity can be attributed to the conductive nature of the MWCNTs and synergic effect of the Ag nanoparticles. Equivalence series resistance (ESR) is accounted for the consolidation of participation from (i) resistance introduces discontinuity in the process of charge transfer between the liquid electrolyte (ionic conductivity) and the solid oxide (electronic conductivity) (ii) contact resistance between current collector, Ni foam and (iii) intrinsic resistance of the electrode material (Meher & Rao, 2011). The ESR value for $\text{Ag}/\text{Co}_3\text{O}_4@\text{MWCNTs}$, $\text{Co}_3\text{O}_4@\text{MWCNTs}$ and Co_3O_4 nanograins were found to be 0.9 , 1.9 , and 1.6Ω , respectively. The Co_3O_4 nanograins have higher diffusion resistance due to agglomeration than $\text{Ag}/\text{Co}_3\text{O}_4@\text{MWCNTs}$ nanocomposites. Furthermore, highly aggregated nature of Co_3O_4 nanograins reduced the effective electrochemical surface area of the material which leads to low specific capacity. Whereas in $\text{Ag}/\text{Co}_3\text{O}_4@\text{MWCNTs}$ nanocomposite,

Co_3O_4 nanograins form nodes onto MWCNT matrix providing a large accessible surface area for the deposition of nanostructured Ag particles and ultimately increasing the redox active surface area for the more effective EC activity. Moreover, the nano sized MWCNT, Co_3O_4 , and Ag reduced the pathway traced for the electronic shuttling to the Ni foam leading to the highest retention likened to pristine Co_3O_4 and Co_3O_4 @MWCNTs nanocomposite.

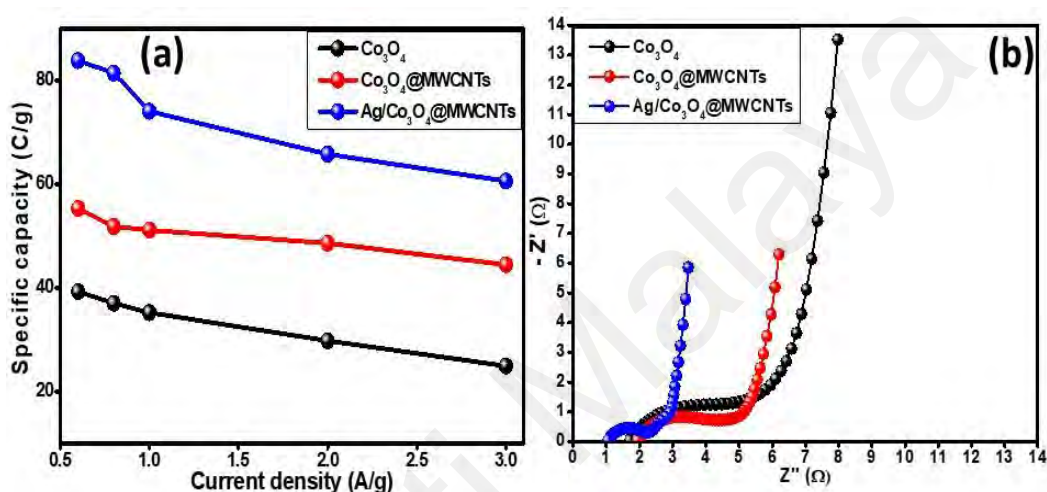


Figure 4.9: (a) Specific capacity of Co_3O_4 nanograins, Co_3O_4 @MWCNTs, and Ag/ Co_3O_4 @MWCNTs nanocomposites at different current densities, (b) Nyquist plots of pure Co_3O_4 nanograins, Co_3O_4 @MWCNT, and Ag/ Co_3O_4 @MWCNTs nanocomposites.

4.2.5 Electrochemical Performance of Assembled, Ag/ Co_3O_4 @MWCNTs//AC Supercapattery

(a) Cyclic Voltammetry (CV) Analysis

Supercapattery being hybrid device combines the features of capacitor and battery in a single device. Its wider operation voltage window is one of the prime features which are responsible for enhancement of the energy density. Therefore, supercapattery was fabricated by combining ternary nanocomposite, Ag/ Co_3O_4 @MWCNTs and AC as active materials for +ve and -ve electrodes (Ag/ Co_3O_4 @MWCNTs//AC), respectively as shown in Figure 4.10(a). Before assembling the device, individually CV curves for both, AC and Ag/ Co_3O_4 @MWCNTs nanocomposite were obtained in a cell system of three electrodes

to approximate the maximum stable working potential. Figure 4.10(b) reveals that the maximum possible potential window for Ag/Co₃O₄@MWCNTs//AC supercapattery could be the combination of potential window of Ag/Co₃O₄@MWCNTs nanocomposite (0-0.5 V) and AC (-1.0-0 V). Therefore, the window of the stable potential for fabricated supercapattery can be extended to the maximum voltage of 1.5 V. Figure 4.10(c) depicts the CV curves of Ag/Co₃O₄@MWCNTs//AC supercapattery at various potential windows at a scan rate of 10 mV s⁻¹. It is obvious from Figure 4.10(c) that EDLC effect was dominant until 0.5 V (as CV curve was almost rectangular with no prominent peak). This means that most of the energy storage was contributed by the physical adsorption and intercalation of electrolyte ions at electrode electrolyte interface. However, beyond 0.5 V, redox peaks appeared in the CV curve manifesting that the faradaic reactions start contributing for energy storage. But after 1.4 V, CV curve start to distort by climbing parallel to the y-axis, which affirmed that the maximum stable potential window can be extendable maximum to 1.5 V. Figure 4.10(d) represents the CV curves of the device at different scan rates (from 3 to 200 mVs⁻¹). The presence of the initial rectangular area of CV curve followed by wide redox peaks is contributed by the faradaic and capacitive behavior arising from Ag/Co₃O₄@MWCNTs nanocomposite and AC, respectively. It is clear from Figure 4.10(d) that the intensity of the redox peaks was amplified with the scan rate whereas the shape of the CV curves was well conserved, proposing an excellent stability and rate capability of the device even at 200 mV s⁻¹ (Wang et al., 2015).

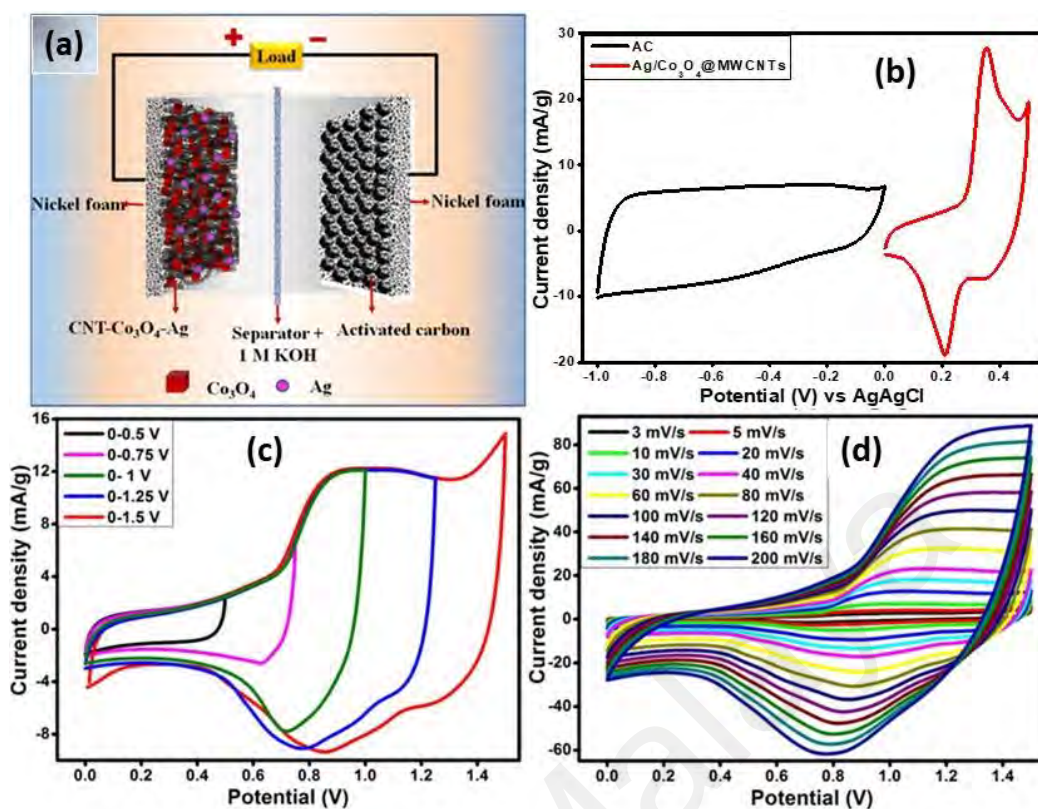


Figure 4.10: (a) Schematic of the assembled Ag/Co₃O₄@MWCNTs//AC supercapattery, (b) comparative CV curves of Ag/Co₃O₄@MWCNTs as +ve and AC as -ve electrode carried out at the scan rate of 10 mV s⁻¹ in a system of three electrodes cell in 1 M KOH electrolyte, (c) CV curve of Ag/Co₃O₄@MWCNTs//AC supercapattery measured at a diverse potential window at a scan rate of 10 mV s⁻¹ and (d) CV curves of Ag/Co₃O₄@MWCNTs//AC supercapattery assessed at various scan rates.

(b) *Galvanostatic Charge-discharge (GCD) Analysis*

The GCD plots of the Ag/Co₃O₄@MWCNTs//AC supercapattery at different potential windows and current densities are shown in Figures 4.11(a) and (b), respectively. The charge-discharge behavior of Ag/Co₃O₄@MWCNTs//AC device at different potential windows is illustrated in Figure 4.11(a) which shows that redox process is well dominated up to the potential of 1.5 V at a constant current density of 1 A g⁻¹. The GCD studies were conducted in a potential window of 0-1.5 V at various current densities, 0.4, 0.6, 0.8, 1.0, 2.0, 3.0 and 4.0 A g⁻¹ (illustrated in Figure 4.11(b)). The fabricated hybrid device produced symmetric curves at different potential windows, suggesting good capacitive demeanor with highly reversible electrochemical redox reaction.

The power density, (P) and energy density, (E) are the prime parameters to evaluate the functioning of energy storage devices. For the evaluation of both parameters, following equations (4.5) and (4.6) have been exploited.

$$E(\text{Wh} / \text{kg}) = \frac{\Delta V \times Q_s}{2 \times 3.6} \quad (4.5)$$

$$P(\text{W} / \text{kg}) = \frac{E \times 3600}{\Delta t} \quad (4.6)$$

where, ΔV is the potential window, Q_s is the specific (C g^{-1}) capacity and Δt (s) is discharge time. The fabricated supercapattery stored a maximum energy density, $E = 16.50 \text{ Wh kg}^{-1}$ at a power density of 297.50 W kg^{-1} for current density of 0.4 A g^{-1} . However, the value of E was slightly decreased to 11.00 Wh kg^{-1} with the significant increase in the value of P to 2.70 kW kg^{-1} , when a current density was enhanced to 4.0 Ag^{-1} . These values are comparable to the recently reported results in the literature, for example, Ni-Co oxide//AC (7.4 Wh kg^{-1} at 1902.9 W kg^{-1}) (Tang et al., 2012), NiCo_2O_4 -rGO//AC (23.3 Wh kg^{-1} at 324.9 W kg^{-1}) (Tang et al., 2012), C/CoNi₃O₄//AC (29.0 Wh kg^{-1} at 130.0 W kg^{-1}) (Zhu et al., 2014), Ni₃(PO₄)₂//AC (76.0 Wh kg^{-1} at 500.0 W kg^{-1}) (Omar et al., 2016), PANI@MoO₃ (71.9 Wh kg^{-1} at 254.0 W kg^{-1}) (Peng et al., 2014) and Ni//AC (30.0 Wh kg^{-1} at 330.0 W kg^{-1}) (Ganesh et al., 2006).

The cycling stability evaluation of supercapattery is an important parameter for its practical application. The cycling stability of Ag/Co₃O₄@MWCNTs//AC supercapattery was performed at a current density of 4.0 A g^{-1} (Figure 4.12). At the beginning, the specific capacity value was increased up to 250 cycles due to gradual activation of the nanocomposite and increase in the penetration of electrolytic ions into the active material (Mai, 2015; Nadiah et al., 2017). After 250 cycles, there is a gradual decay in specific capacity percentage and becomes almost stable at about 1000 cycles. From 1000 to 3000

cycles, specific capacity decay is only 6.90 %. This affirms the excellent stability of assembled supercapattery and makes it suitable for practical use (Omar et al., 2016).

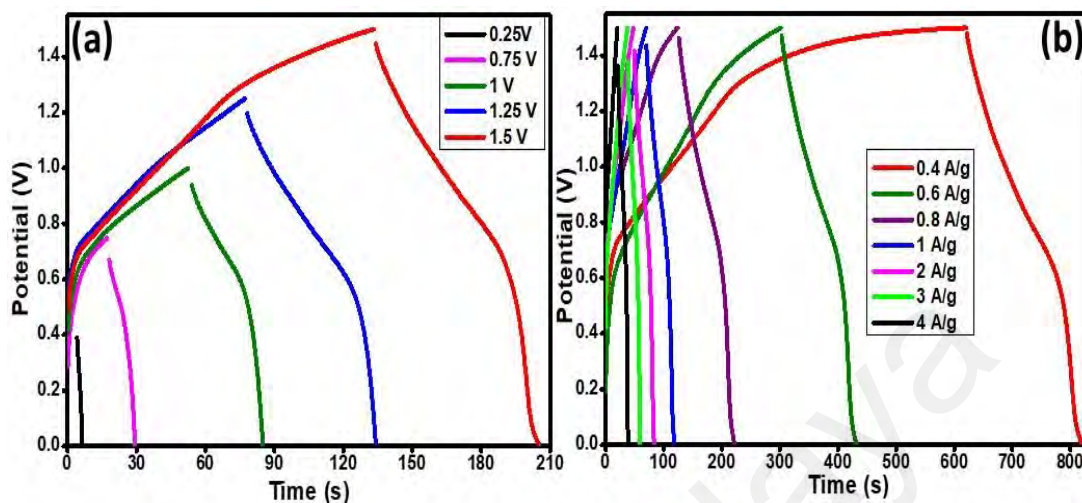


Figure 4.11: GCD curves of Ag/Co₃O₄@MWCNTs//AC supercapattery at (a) different potential windows and (b) different current densities.

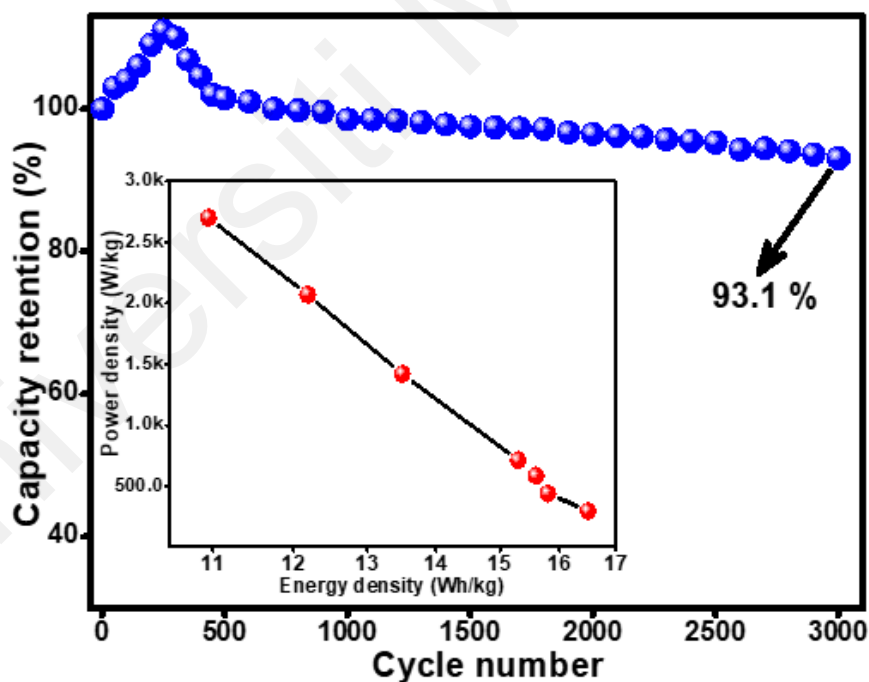


Figure 4.12: Cycling stability of Ag/Co₃O₄@MWCNTs//AC supercapattery and inset figure showing the energy density versus power density results.

4.3 System 2: Gold Nanoparticles, Cobalt oxide Nanograins and Multiwalled Carbon Nanotubes Based Ternary Nanocomposite, (Au/Co₃O₄@MWCNTs)

4.3.1 Surface Morphology Study

FESEM is a valuable technique to characterize the morphology and microstructure of the prepared materials. The morphology of Co₃O₄@MWCNTs binary and Au/Co₃O₄@MWCNTs ternary nanocomposites are first studied by FESEM at different magnifications, as shown in Figure 4.13. Nevertheless, the aggregation is significantly reduced after introduction of MWCNTs in the Co₃O₄@MWCNTs binary nanocomposite shown in Figure 4.13(a). The Co₃O₄ NPs were uniformly grown by a hydrothermal technique at oxygen containing functional groups on the MWCNTs matrix. Figures 4.13(b) and (c) represent the FESEM micrographs of Au/Co₃O₄@MWCNTs ternary nanocomposite at a different resolution to illustrate the disaggregation of nanoparticles over the MWCNTs matrix. The ultra-small Au NPs on Co₃O₄ and MWCNTs are uniformly decorated on MWCNTs and Co₃O₄. The images also indicate the successful integration of Co₃O₄ and Au NPs onto the MWCNTs matrix.

TEM images of ternary nanocomposite are shown in Figure 4.14. A clear distribution of the cobalt oxide and gold nanoparticles could be observed onto the MWCNTs matrix in Figure 4.14(a) at low magnification. Figure 4.14(b) shows the high magnification image of the nanocomposite where a clear distinct shape and size of both component nanoparticles could be observed. Inset Figure 4.14(b) shows that gold nanoparticles are relatively small spherical in shape (~ 10-20 nm) while cobalt oxide particles are bigger (~20-30 nm) and semispherical. This clearly reveals the de-aggregated morphology, size, and shape of the ternary nanocomposite.

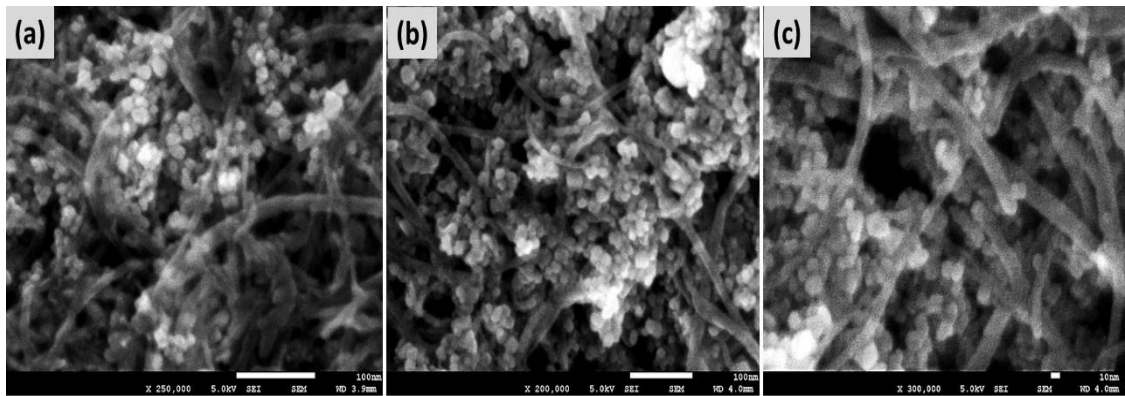


Figure 4.13: FESEM images of (a) Co₃O₄@MWCNTs binary nanocomposite; (b) low and (c) high magnification images of Au/Co₃O₄@MWCNTs sample showing Co₃O₄ and Au NPs decorated on MWCNTs network.

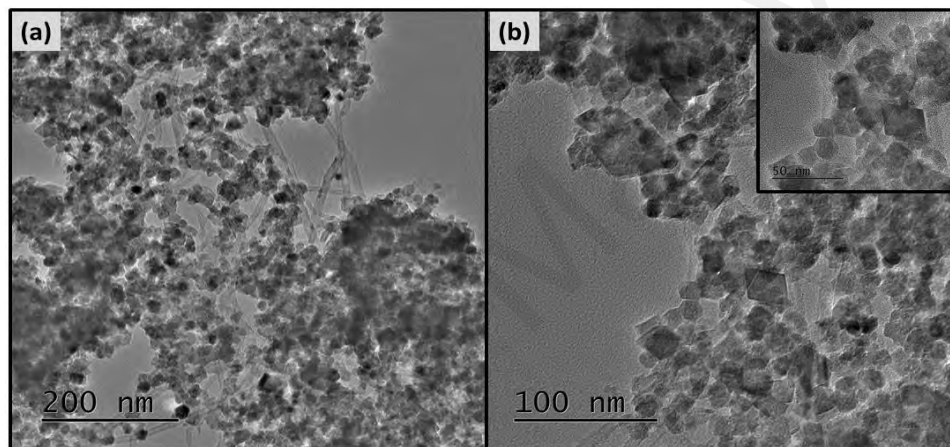


Figure 4.14: TEM images of Au/Co₃O₄@MWCNTs ternary nanocomposite, (a) at low and (b) at high magnifications. The inset Figure 4.14(b) showing the Co₃O₄ and Au nanoparticles.

Figure 4.15 depicts the constituent elemental spectra and their corresponding EDS mapping in the Au/Co₃O₄@MWCNTs ternary nanocomposite. The nanocomposite was characterized by selecting random areas using EDS analysis. The carbon is attributed to the MWCNTs, Co indicates the Co₃O₄ and Au peak indicates the presence of Au NPs. This confirms the successful emergence of Au/Co₃O₄@MWCNTs ternary nanocomposites. Moreover, the image mapping with distinguished colors indicates the even distribution of all the individual constituents of the ternary nanocomposite across the matrix presented in Figure 4.15(a) to (e). Particularly, Figure 4.15(f) verifies the even distribution of both the Co₃O₄ and Au on the MWCNTs network.

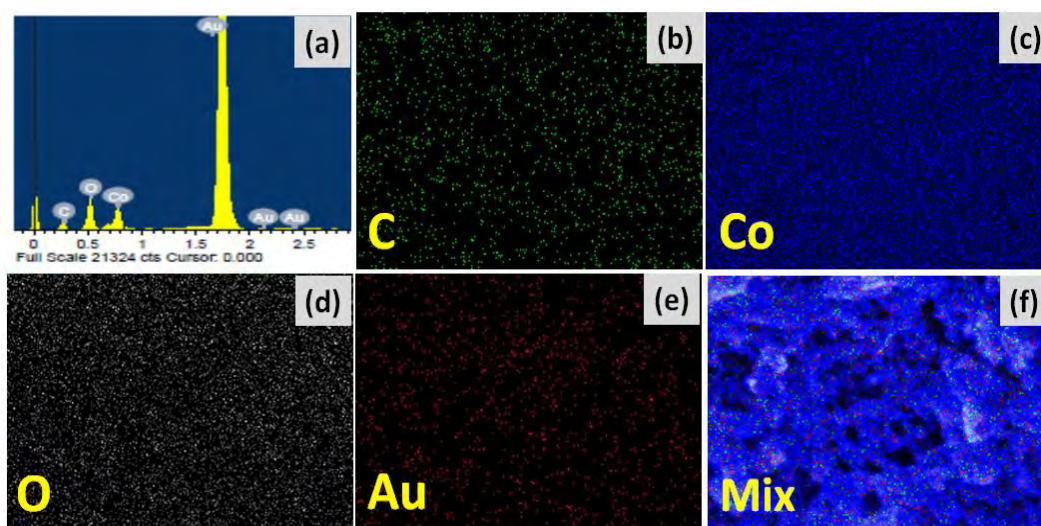


Figure 4.15: (a) EDS spectrum shows the elemental composition and, EDS-elemental mapping of (b) C, (c) Co, (d) O, (e) Au content of the Au/Co₃O₄@MWCNTs ternary nanocomposite. (f) Mix-verifies the even distribution of both the Co₃O₄ and Au NPs on the MWCNTs network.

4.3.2 X-ray diffraction Analysis

XRD patterns were recorded for the Co₃O₄ as well as its Co₃O₄@MWCNTs and Au/Co₃O₄@MWCNTs nanocomposites, as shown in Figure 4.16. The peak intensities

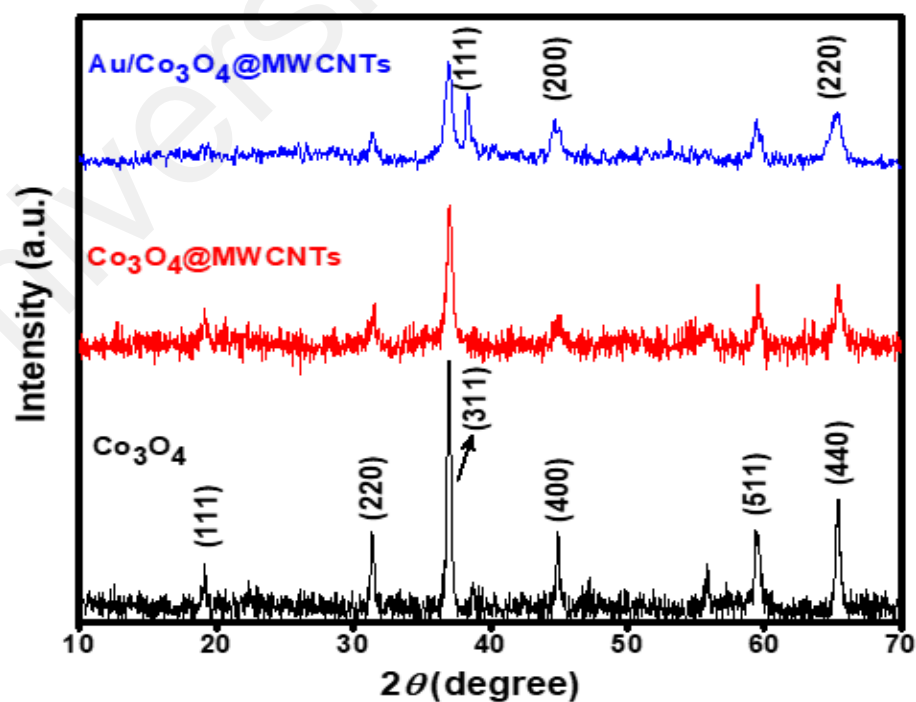


Figure 4.16: XRD pattern of the Co₃O₄, Co₃O₄@MWCNTs binary and Au/Co₃O₄@MWCNTs ternary nanocomposites scanned in the 2θ range of 10° - 70° .

considerably reduced in $\text{Co}_3\text{O}_4@\text{MWCNTs}$ and $\text{Au}/\text{Co}_3\text{O}_4@\text{MWCNTs}$ nanocomposites due to the fact that MWCNTs probably have partially covered the Co_3O_4 NPs. This indicates the successful integration of MWCNTs and Co_3O_4 in the binary matrix. The characteristic peaks of Au ascribed to (111), (200) and (220) at 38.10° , 44.37° and 65° respectively, in the $\text{Au}/\text{Co}_3\text{O}_4@\text{MWCNTs}$ are corresponding to the cubic structure of Au and well indexed with the ICDD-PDF-00-002-1095 card number. The successful integration of MWCNTs and Au NPs to form a ternary nanocomposite has been confirmed by SEM-scanning and EDS mapping too. It is expected that inclusion of Au NPs may increase the conductivity by facilitating with the transfer channel which could eventually improve the EC functioning of the as synthesized ternary nanocomposite.

4.3.3 X-ray Photoelectron Spectroscopy (XPS) Analysis

The surface composition and elemental chemical states of the $\text{Au}/\text{Co}_3\text{O}_4@\text{MWCNTs}$ ternary nanocomposite material were analyzed by XPS as shown in Figure 4.17. The survey scan spectrum of $\text{Au}/\text{Co}_3\text{O}_4@\text{MWCNTs}$ ternary nanocomposite shown in Figure 4.17(a) displays sharp and well defined peaks at various binding energies such as 84.35, 284.75, 531.47 and 779.97 eV corresponding to Au $4f$, C $1s$, O $1s$, and Co $2p$, respectively. The two peaks appeared at about 84.35 and 88.06 eV are attributed to the $4f_{7/2}$ and $4f_{5/2}$, respectively, of the typical metallic Au (Figure 4.17(b)) (Bayazit et al., 2016; Shan et al., 2008; Smith, 2009). The O $1s$ spectrum (Figure 4.17(c)) exhibits a strong peak at ~ 529.98 eV and a relatively low intensity peak at ~ 531.47 eV that indicates the presence of at least two kinds of O chemical states; the crystal lattice oxygen (O_L) and hydroxyl oxygen (O_H) (Ai et al., 2015; Cui et al., 2014). A third, relatively low intensity peak at 533.43 eV is ascribed to the C-O bond and indicates the direct bonding of oxygen and carbon atoms (Rafique et al., 2017). The curve fitted C $1s$ spectrum is shown in Figure 4.17(d). The main peak at 284.75 eV is attributed to the sp^2 C-C and the other two peaks are ascribed to the sp^3 C-C and the carbonyl C (C=O) at ~ 285.83 eV and

288.88 eV, respectively. (Han et al., 2011; Mattevi et al., 2009; Noh et al., 2014; Rafique et al., 2018; Seredych et al., 2010) Curve fitting for Co core-level spectrum (Figure 4.17(e)) shows the characteristic peaks of Co $2p_{3/2}$ at and Co $2p_{1/2}$ at 779.97 eV and 795.95 eV, with two shake-up satellite peaks, which represents the typical peak formation for Co_3O_4 phase (Feng et al., 2015; Huang et al., 2013; Qorbani et al., 2015).

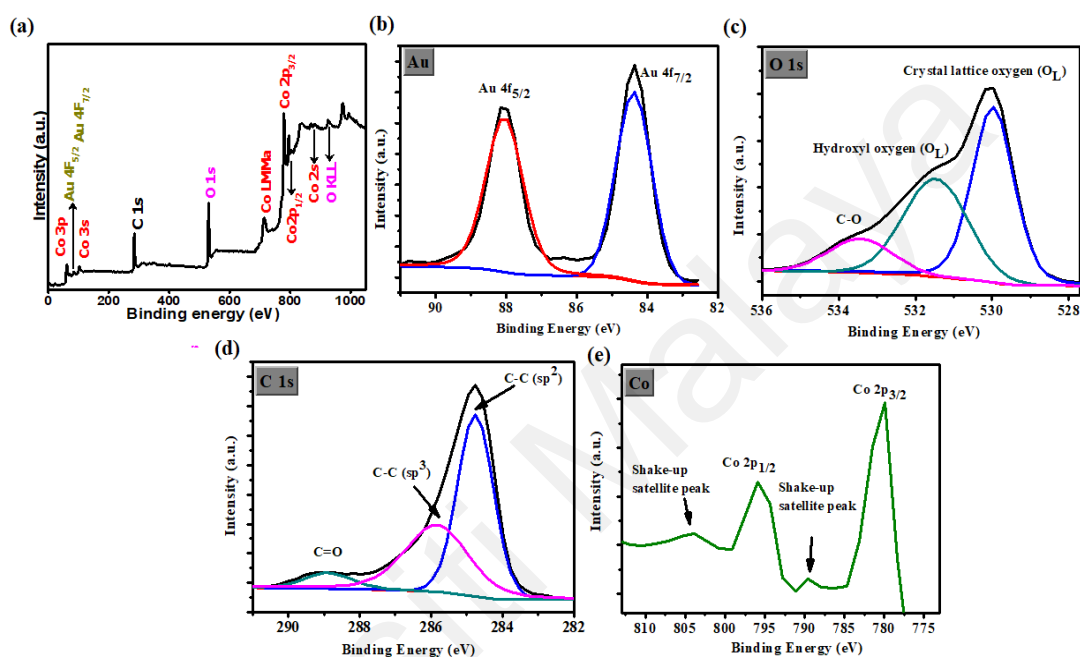


Figure 4.17: (a) A survey spectrum of Au/ Co_3O_4 @MWCNTs, ternary nanocomposites, core-level XPS spectra of (b) Au $4f$, (c) O $1s$, (d) C $1s$ and (e) Co $2p$.

4.3.4 Electrochemical Analysis of Gold, Cobalt Oxide, and Multiwalled Carbon Nanotubes, ($\text{Au}/\text{Co}_3\text{O}_4$ @MWCNTs) Based Ternary Nanocomposite

(a) Cyclic Voltammetry (CV) Analysis

The electrochemical studies of the modified electrode were conducted in a standard three electrode cell system at diverse scanning rates up to 50 mV s^{-1} in 1 M KOH aqueous electrolyte in a potential window of 0.0– 0.5 V (vs. Ag/AgCl). The performance was evaluated on the basis of the capacity difference of the Co_3O_4 , its Co_3O_4 @MWCNTs

binary and Au/Co₃O₄@MWCNTs ternary nanocomposite variants as shown in Figure 4.18(a-c), respectively. It is observed that the increase in the voltammetric currents is in direct proportion to the scan rates. The typical CV curves of the unaided Co₃O₄ consist of the strong redox peaks that shifted toward higher (anodic peaks) and lower (cathodic peaks) potentials at the higher scan rates (Figure 4.18(a)). The shift in peak potential is due to the poor conductivity of the electrode due to the high particle aggregations. Additionally, polarization and potential kinetic irreversibility of electrolyte ions access to the electrode interface is responsible for the observed peak potential shift. There is a linear increase in the peak potential with the varied scan rates indicating the good reversibility (Cui et al., 2014). The well-defined pair of Co₃O₄ redox peaks exhibit the properties of typical faradaic behavior of a battery-type electrode. However, the battery-type materials based on metal oxides should not be confused with the pseudo-capacitivity of the materials, because the electrochemical signature of battery type and pseudocapacitive material is different (Dubal et al., 2015). In case of Co₃O₄@MWCNTs, high redox peak current was observed compared to unaided Co₃O₄, which is due to high accessible of sites for electrolyte for redox reactions (as MWCNTs significantly reduced particle aggregations) (Figure 4.18 (b)). However, redox peak for Co₃O₄@MWCNTs appears to be at higher potential compared to unaided Co₃O₄ which is due to the growth of fewer independent Co₃O₄ nanoparticles in solution phase during hydrothermal reaction instead of nucleation on MWCNTs (Jokar & Shahrokhian, 2014). It is noteworthy that the redox peaks come from the reversibility of cobalt ions transitions with the hydroxyl ion (OH⁻) of the alkaline media. Moreover, Figure 4.18(c) illustrates that the composition of Au/Co₃O₄@MWCNTs ternary nanocomposite did not significantly distort the CV curves, ultimately, no pronounced shift was observed in the redox peaks compared to the individual Co₃O₄ or Co₃O₄@MWCNTs binary nanocomposite. This phenomenon is associated with the good reversibility behavior of the ternary nanocomposite. In addition,

a significant increase in the intensity of the Au/Co₃O₄@MWCNTs redox peaks is attributed to the increased conductivity of Au NPs enriched with the extended electron transfer channels during the oxidation and reduction process. This fact implies that synergy of Au NPs in the ternary nanocomposite and its decoration on the MWCNTs matrix can definitely improve the electrochemical functioning of the resultant device owing to the enhanced conductivity and capacity fading of the ternary nanocomposite (Xia et al., 2015). Figure 4.18(d) compares the performance of individual Co₃O₄, its Co₃O₄@MWCNTs binary, and Au/Co₃O₄@MWCNTs ternary nanocomposites at a scan rate of 3 mV s⁻¹. Moreover, the Au/Co₃O₄@MWCNTs ternary nanocomposite, due to the high conductivity of MWCNTs matrix and Au NPs, exhibits relatively high background current compared to pristine Co₃O₄ NPs.

The reactions mechanism in 1 M KOH is based on the equations (4.1) and (4.2). It is noteworthy that the CV curves did not display the distinguished pseudocapacitive behavior (rectangular CV curve), that is “steady change of capacitance over the entire potential window”, which is coherent with the formerly published findings that describe the electrochemical performance in terms of specific capacity contrary to the specific capacitance (Ai et al., 2015). The specific capacity values of all the materials can be computed according to equation (4.3).

The Au/Co₃O₄@MWCNTs ternary nanocomposites showed the highest specific capacity of 108.80 C g⁻¹ compared to Co₃O₄@MWCNTs binary nanocomposites (57.00 C g⁻¹) and Co₃O₄ (40.90 C g⁻¹) single material.

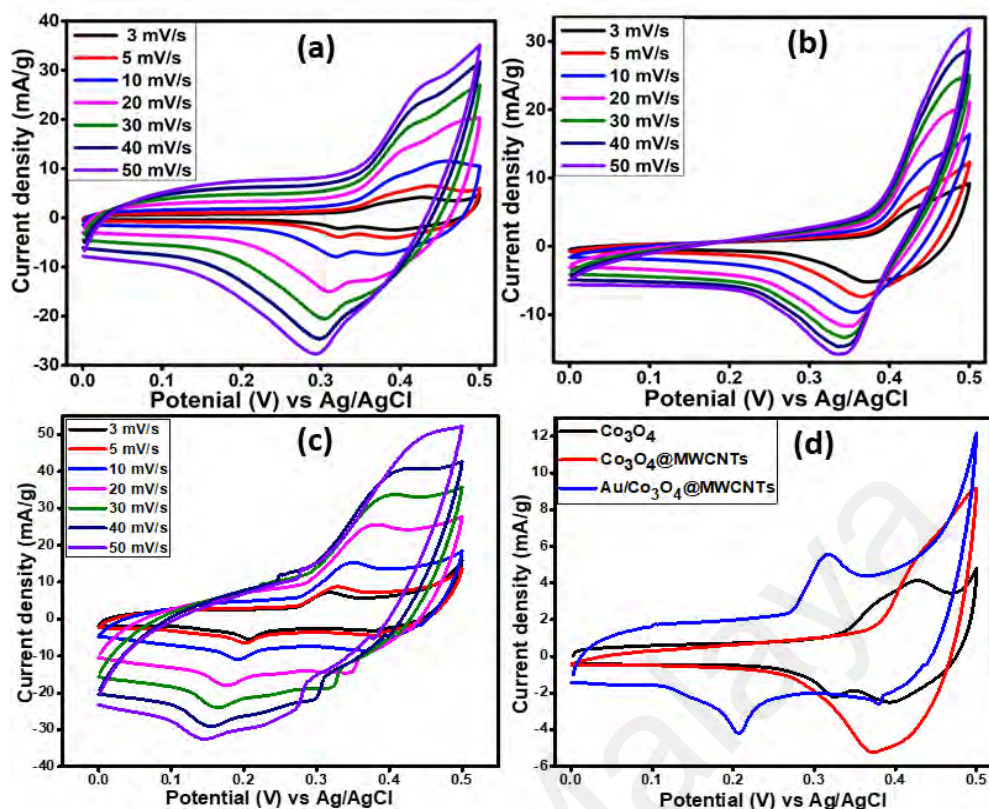


Figure 4.18: CV curves of (a) pristine Co₃O₄NPs (b) Co₃O₄@MWCNTs binary and (c) Au/Co₃O₄@MWCNTs ternary nanocomposite measured at varied scan rates. (d) CV curves to compare the electrochemical performance of Co₃O₄ NPs, Co₃O₄@MWCNTs binary and Au/Co₃O₄@MWCNTs ternary nanocomposites recorded at 3 mV s⁻¹.

(b) Electrochemical Impedance Spectroscopy (EIS) Analysis

Figure 4.19(a) exhibits the specific capacity of all three variants of electrode materials at different scan rates. The Q_s values experienced a gradual decay at increased scan rates due to the unsynchronized movement of charges at the corresponding current densities. Moreover, the diffusion or migration of electrolyte ions demonstrates slow diffusion or migration through the electrodes at higher scan rates (Fu et al., 2006). The Q_s values were decreased to 12.38, 23.71 and 33.42 C g⁻¹ for Co₃O₄, Co₃O₄@MWCNTs binary, and Au/Co₃O₄@MWCNTs, ternary nanocomposites electrodes, respectively at high scan rates. These values clearly indicate the performance limitation of Co₃O₄ as standalone

electrode materials compared to their binary and ternary nanocomposites. Significantly improved performance of the binary and ternary nanocomposites is attributed to the ability of MWCNTs to disaggregate Co_3O_4 NPs and enhanced conductivity due to the inclusion of highly conductive Au NPs. However, MWCNTs have increased the rate capability, probably due to disaggregation and random growth of Co_3O_4 NPs on the MWCNTs matrix. It is thus clear from the results illustrated in Figure 4.19(a) that hybridization of MWCNTs and Au along with the Co_3O_4 base-material has remarkably improved the electrochemical performance of the ternary nanocomposite.

The EIS studies are highly regarded as the principal method to evaluate the fundamental behavior of the electrochemical storage devices, particularly, intrinsic mechanism of the electrodes (Fan et al., 2011; Sugimoto et al., 2005). The Nyquist spectra for Co_3O_4 as well as its binary and ternary variant electrodes are shown in Figure 4.19(b). The spectra exhibit a straight line in the low frequency and a semicircle in the high frequency region. The semicircle at high frequency region determines the charge transfer resistance (R_{ct}) at electrode electrolyte interface. The value of R_{ct} depends upon the conductivity of the electrode, its porosity and dimension of electrode material (Wang et al., 2018; Zheng et al., 2018). The nearly vertical line in the low frequency region corresponding to the $\text{Au}/\text{Co}_3\text{O}_4@\text{MWCNTs}$ ternary nanocomposite suggests the nearly ideal capacitive behavior of a supercapacitor with low R_{ct} values. A line parallel to the y-axis ascribes the increased charge storage capability of the $\text{Au}/\text{Co}_3\text{O}_4@\text{MWCNTs}$ ternary nanocomposite which is obviously expected. The hybridization of MWCNTs and Au along with Co_3O_4 NPs has ultimately enhanced the conductivity of the resultant nanocomposite. In addition, the Co_3O_4 exhibited the largest semicircle than its binary and ternary variants that indicates its relatively higher charge transfer resistance. It is noteworthy that the agglomeration of Co_3O_4 induces the higher diffusion resistance compared to its variants. Furthermore, the aggregation of Co_3O_4 induces the low specific

capacity owing to agglomeration induced less EC active sites. Contrary to this, the Co_3O_4 NPs form nodes onto the MWCNTs matrix that ultimately provides the large accessible electroactive sites for the Au NPs. Thus, the redox active sites can be increased to carry out electrochemical activity more efficiently. Moreover, the MWCNTs, Co_3O_4 , and Au which are in very low dimensions forming the ternary nanocomposite and able to squeeze the path traced for the electronic insertion/disinsertion to the Ni foam, resulting in the highest retention when equated to unaided Co_3O_4 and Co_3O_4 @MWCNTs nanocomposite.

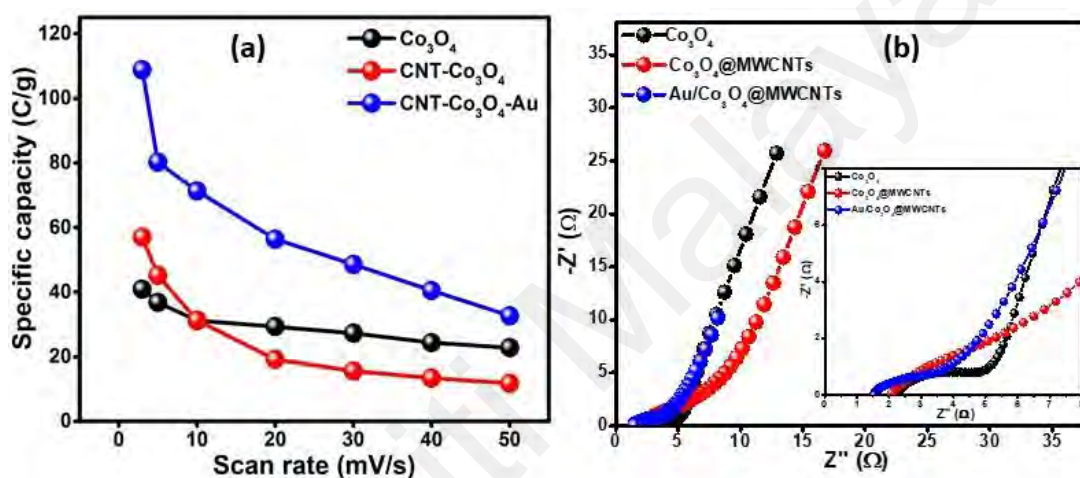


Figure 4.19: (a) Specific capacities of Co_3O_4 NPs, Co_3O_4 @MWCNTs binary and $\text{Au/Co}_3\text{O}_4$ @MWCNTs ternary nanocomposites at various scanning rates, (b) Nyquist plots of the Co_3O_4 NPs, Co_3O_4 @MWCNTs binary and $\text{Au/Co}_3\text{O}_4$ @MWCNTs ternary nanocomposites. Inset Figure 4.19(b) shows the EIS spectrum in high frequency region.

(c) **Galvanostatic Charge-discharge (GCD) Analysis**

The GCD curves were recorded to evaluate the capacity performance of the Co_3O_4 and its nanocomposite in a potential range of 0-0.5 V at varied current densities ($0.1\text{-}1.0\text{ A g}^{-1}$), as presented in Figure 4.20 (a-d). The non-linearity of the curves is associated with the faradic behavior which is showing the battery type characteristics of the electrodes. Taking into account, the charge-discharge curves of all three materials, ternary nanocomposite ($\text{Au/Co}_3\text{O}_4$ @MWCNTs) possesses the longest discharge time and hence depicts the best performing electrode material compared to its counterpart electrodes.

The specific capacity (Q_s) values of the modified electrodes can be determined from the discharge trends by exploiting the equation (4.4). The computed specific capacities are 109.77, 57.17 and 41.30 C g⁻¹ for Au/Co₃O₄@MWCNTs, Co₃O₄@MWCNTs, and Co₃O₄, respectively at a current density of 0.6 A g⁻¹.

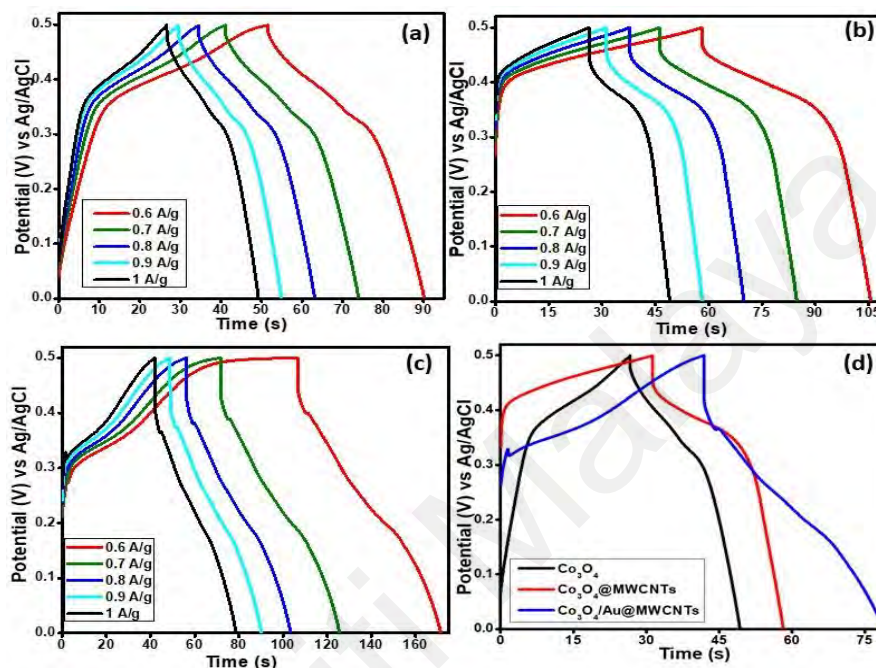


Figure 4.20: GCD curves at various current densities, (a) Co₃O₄, (b) Co₃O₄@MWCNTs, (c) Au/Co₃O₄@MWCNTs and (d) comparison curves for all three variants at a current density of 0.9 A g⁻¹.

4.3.5 Electrochemical Performance of Assembled Au/Co₃O₄@MWCNTs//AC Supercapattery

The EC evaluation of the electrode materials is generally performed in two and three electrodes configurations. The two electrodes configuration is believed to possess relatively closer approach to the real application of electrochemical storage device (Li et al., 2016; Zhang et al., 2017). Therefore, the supercapattery was assembled in the two electrodes configuration using the best performing electrode material *e.g.* Au/Co₃O₄@MWCNTs ternary nanocomposite, in order to further evaluate its performance. Before assembling the two electrodes configuration, individual CV curves

for positive (Au/Co₃O₄@MWCNTs) and negative (AC) electrodes were obtained in the three cells configuration to estimate the maximum stable working potential window as shown in Figure 4.21(a). It is evident from the results that the potential range can be extended up to 1.5 V, by combining the 0 to 0.5 V for Au/Co₃O₄@MWCNTs and -1 to 0 V for AC. Figure 4.21(b) depicts CV curves of an optimized Au/Co₃O₄@MWCNTs, ternary nanocomposite in two electrodes configuration at varied scan rates from 3 to 100 mV s⁻¹. Nearly rectangular curves with no prominent peak until 0.5 V clearly indicate the EDLC effect which specifies that energy storage occurred due to the intercalation of OH⁻ ions at the electrode interface. Moreover, energy storage was induced by faradaic reactions after 0.5 V as the oxidation-reductions peaks also emerged in the mechanism. It can be seen that the curve started to distort beyond 1.5 V and climbed upwards along the vertical axis, which indicates the maximum limit of the potential range. Initially, almost rectangular CV curve indicates the ideal capacitive behavior that is attributed to the AC followed by the wide redox peaks arise from Au/Co₃O₄@MWCNTs nanocomposite. Moreover, the amplified intensity of the redox peaks at a higher scan rate and the conserved CV curves clearly indicate the efficacy of the material in terms of stability and rate capability of the resultant device even at higher scan rates, *i.e.*, 100 mV s⁻¹ (Wang et al., 2015).

The GCD curves of the best performing electrode material (Au/Co₃O₄@MWCNTs, ternary nanocomposite) based on the two electrodes configuration, were obtained at high and low current densities as shown in Figure 4.21(c) and (d), respectively at 0.4, 0.5, 0.6, 0.7, 0.8, 0.9 1.0, 1.5, 2.0, 2.5 3.0, 3.5 and 4.0 A g⁻¹. The charge-discharge behavior indicates that the redox process dominates up to the maximum potential window. The typical symmetric GCD curves at varied current densities demonstrated that the devices possess excellent capacitive behavior with prominent reversible redox mechanism.

The power density, (P) and energy density, (E) values are derived using the equations (4.5) and (4.6). The ternary nanocomposite-based device possesses an energy density, $E=18.80 \text{ Wh kg}^{-1}$ and power density of 302.00 W kg^{-1} at 0.4 A g^{-1} current density. However, the significant increase in the power density up to $2577.60 \text{ W kg}^{-1}$ lowered the E value to 9.94 Wh kg^{-1} when current density was increased to 4.0 A g^{-1} .

Figure 4.22(a) shows the Nyquist plot of the assembled supercapattery incorporating Au/Co₃O₄@MWCNTs, ternary nanocomposite as a positive electrode material. As expected, a small semicircle is observed in the high frequency region showing the low charge transfer resistance and the almost vertical line parallel to the imaginary axis demonstrates the high charge storage capability of the device. A good cycle life is a fundamental requirement for a supercapattery device. The cycle life test was carried out for the Au/Co₃O₄@MWCNTs//AC supercapattery over 3500 cycles by charging and discharging at a current density of 4.0 A g^{-1} between 0 and 1.5 V. The device showed outstanding electrochemical stability and experienced only 8.10 % deterioration in the initial capacity after 3500 cycles. Therefore, the retention of 91.90 % after 3500 cycles (Figure 4.22(b)) for the Au/Co₃O₄@MWCNTs//AC supercapattery is promising for its further realization in practical applications.

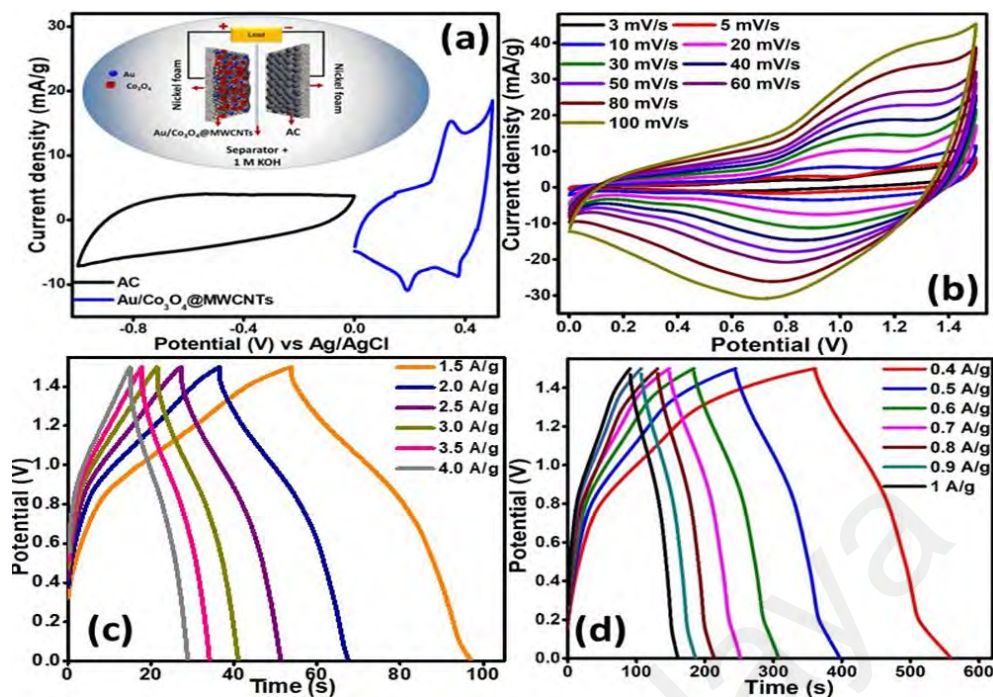


Figure 4.21: (a) The graphical presentation of assembled supercapattery and comparative CV curves of Au/Co₃O₄@MWCNTs, ternary nanocomposites and AC electrodes performed in a two electrodes cell in KOH aqueous solution at a scan rate of 10 mV s⁻¹. (b) CV curves of optimized Au/Co₃O₄@MWCNTs, ternary nanocomposites based supercapattery measured at different potential windows. Galvanostatic charge-discharge curves of Au/Co₃O₄@MWCNTs, ternary nanocomposite based supercapattery device at (c) high and (d) low current densities.

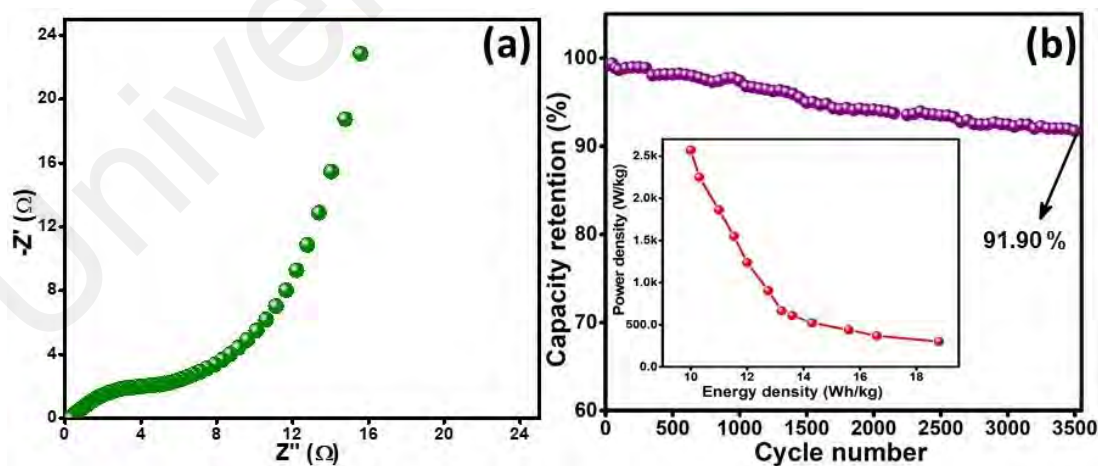


Figure 4.22: (a) Nyquist plot of Au/Co₃O₄@MWCNTs//AC assembled device, (b) cyclic performance of the Au/Co₃O₄@MWCNTs, ternary nanocomposites electrode as a function of the number of cycles at a current density of 4.0 A g⁻¹ in 1 M KOH. The inset shows the power density decay vs energy density of the assembled devices.

4.4 Reduced Graphene Oxide Based Ternary Nanocomposite

The researchers have utilized various approaches to synthesize Co_3O_4 nanocomposites with graphene. Recently, Liang and co-workers prepared Co_3O_4 nanostructures on graphene platform by a hydrothermal process and evidenced escalated electro-catalytic performance (Liang et al., 2011). Similarly, Nguyen *et al* also exploited hydrothermal technique for the preparation of $\text{Co}_3\text{O}_4/\text{rGO}$ composite for sensor and electrochemical capacitor applications (Nguyen et al., 2016). Hydrothermal synthesis is preferred over other synthesis approaches because the required amount of deionized water and precursors are encased in a teflon lined autoclave and simply heated to required temperatures. The buildup of high pressure due to the increase in temperature helps to achieve the desired nano sized particles over an optimized time scale. It is a facile synthesis technique and all parameters such as reagent percentage, pH, time and temperature are easily controllable (Shahid et al., 2015).

In this work, facile single step hydrothermal technique was employed to synthesize the $\text{Ag}/\text{Co}_3\text{O}_4/\text{rGO}$ nanocomposites for the superior performance supercapattery applications. The higher band gap of transition metal oxides could help the noble metal to increase the rapid electron transfer mechanism by facilitating the extended transfer channels to the electrons. The decoration of nanocomposite with a noble metal such as Ag can further help to promote its electrochemical activity by the synergistic effect. Thus, ternary nanocomposites enhanced cycling stability, specific capacity and rate capability which ultimately increase the electrochemical performance of the system.

4.5 System 3: Silver Nanoparticles and Cobalt Oxide Nanograins Grown on Reduced Graphene Oxide, (Ag/Co₃O₄@rGO)

4.5.1 Surface Morphology Study

The FESEM study of the newly prepared ternary nanocomposite (Ag/Co₃O₄@rGO) is depicted in Figure 4.23. The wrapped rGO sheets around the Co₃O₄ nanograins could be examined in the relatively low-resolution image of the Co₃O₄@rGO nanocomposite in Figure 4.23(a). The rGO can be the best choice to decrease the degree of aggregation of Co₃O₄ nanograins. The even growth of Co₃O₄ nanograins on rGO nanosheets provides the evidence that single step facile hydrolysis method is the effective strategy for the synthesis of Co₃O₄@GO nanocomposite and permit better dispersion compared to other complex chemical or physical routes. The size and geometry of the nanograins were well retained after the synthesis of a binary nanocomposite. Figures 4.23(b) and (c) are representing the ternary nanocomposite Ag/Co₃O₄@rGO at low and high magnifications, respectively. The as produced ternary nanocomposite Ag/Co₃O₄@rGO ensued from the decoration of binary nanocomposite with the silver metal nanoparticles. Figure 4.23(c) clearly shows the arrows in yellow color, pointing towards tiny dots came from the decoration of Ag nanoparticles which are smaller in size than the Co₃O₄ nanograins. It is a soft transition metal and is selected for decoration because of its higher electrical and thermal conductivities (Shahid et al., 2018). So, in the compounded ternary nanocomposite, the less aggregation of nanograins was due to the growth on rGO matrix and decoration of silver nanoparticles could help to boost its EC performance by increasing the electroactive sites.

Transmission electron microscopy (TEM) images of Ag/Co₃O₄@rGO ternary nanocomposite is shown in Figure 4.24. The components (Co₃O₄ and Ag) of the ternary nanocomposite are well distributed over the reduced graphene oxide matrix and could be observed in Figure 4.24(a) which is taken at relatively low magnification. Figure 4.24(b)

represents the high magnification image of the ternary nanocomposite which shows the size and shape of the Co_3O_4 and Ag nanoparticles. In set Figure 4.24(b) clearly distinguish the shape and size of both Co_3O_4 and Ag nanoparticles. The approximate sizes are 50 nm and 25 nm for Co_3O_4 and Ag nanoparticles, respectively. The Co_3O_4 nanoparticles are irregular spherical and bigger in size while Ag nanoparticles are semispherical and relatively smaller in size. The TEM images reveal the successful distribution of both nanoparticles over the reduced graphene oxide sheets.

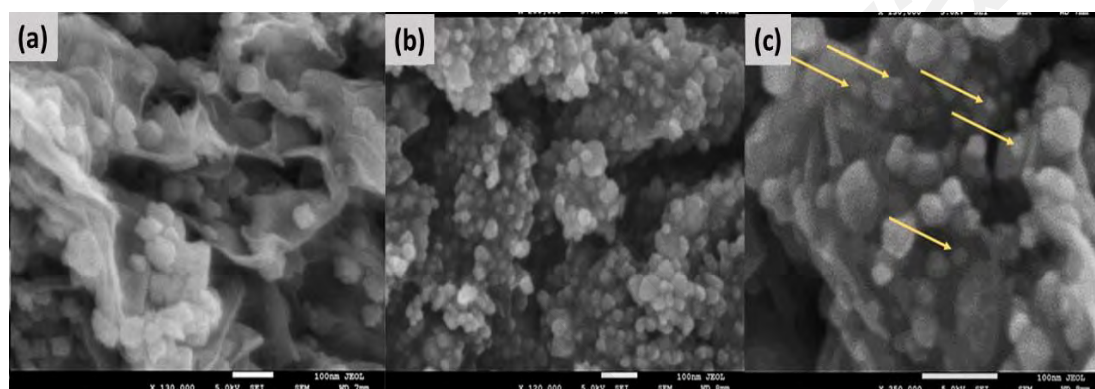


Figure 4.23: FESEM micrographs of (a) Co_3O_4 @rGO binary nanocomposites (b) low and (c) high magnification images of the $\text{Ag}/\text{Co}_3\text{O}_4$ @rGO, ternary nanocomposite.

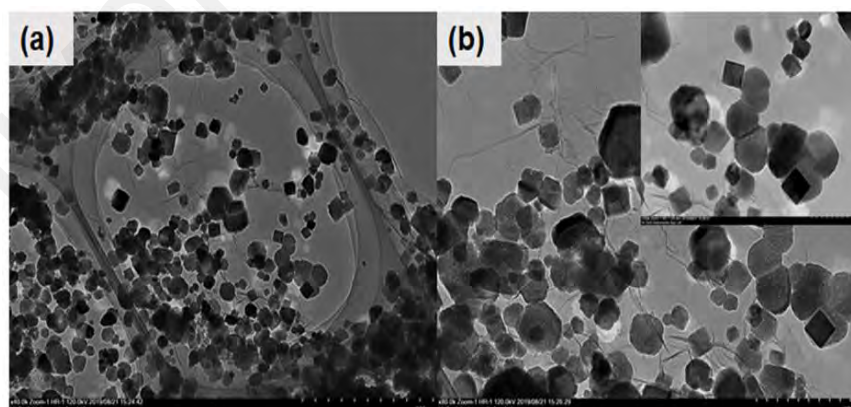


Figure 4.24: TEM images of the $\text{Ag}/\text{Co}_3\text{O}_4$ @rGO ternary nanocomposite (a) at low and (b and inset) at high magnifications.

The elemental mapping was conducted through the EDS technique to further confirm the presence of all elements in the synthesized $\text{Ag}/\text{Co}_3\text{O}_4$ @rGO ternary nanocomposites. The spectrum in Figure 4.25(a) distinctly shows the peaks of all elements, (C, O, Co, and

Ag), contributed in the synthesis of the $\text{Ag}/\text{Co}_3\text{O}_4@\text{rGO}$ and a Si peak is from the $1 \times 1 \text{ cm}^2$ silicon substrate. The peaks spectrum is a test of the purity of the as prepared ternary nanocomposite, whereas the high purity of the nanocomposite was proved through the absence of any of the impurity peaks. A relatively low-resolution compounded image of the as produced $\text{Ag}/\text{Co}_3\text{O}_4@\text{rGO}$ nanocomposite is clearly shown in Figure 4.25(b). Whereas, Figure 4.25(c-f) presents the elemental mapping of the individual components (C, O, Co and Ag respectively) of the $\text{Ag}/\text{Co}_3\text{O}_4@\text{rGO}$ nanocomposite. The densities of C and O are higher which is clear from the highly dense distribution of blue and yellow dots in Figure 4.25(c-d). While, Figure 4.25(e-f) shows a low density of Co and Ag. The uniform decoration of Co and Ag nanoparticles are clearly evident from Figure 4.25(b).

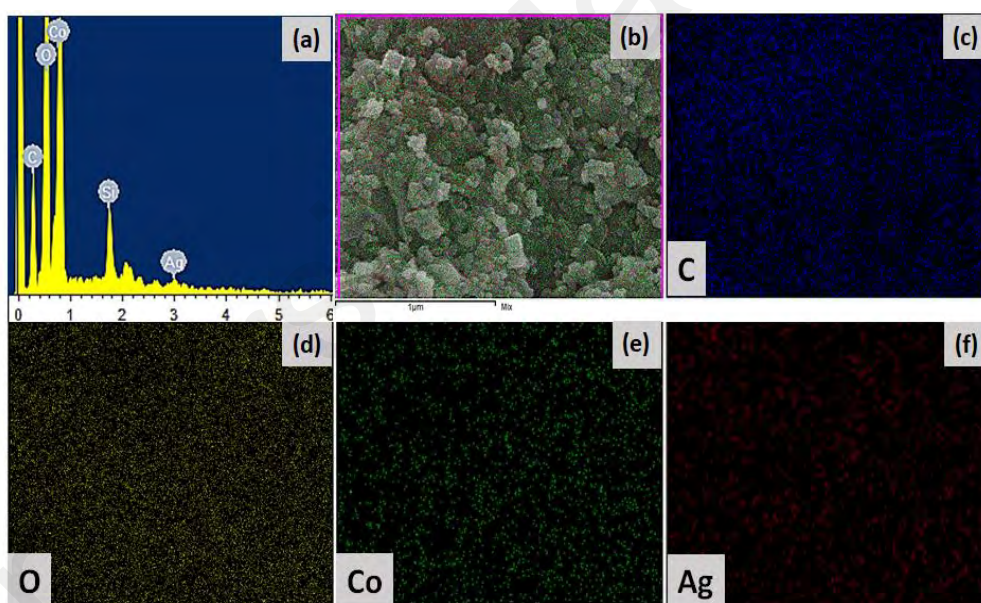


Figure 4.25: (a) EDS spectrum of the $\text{Ag}/\text{Co}_3\text{O}_4@\text{rGO}$, ternary nanocomposites, (b) compounded image demonstrating the even distribution of cobalt, silver, and carbon in the $\text{Ag}/\text{Co}_3\text{O}_4@\text{rGO}$, ternary nanocomposites, (c) the representation of elemental scan of carbon, (d) Oxygen, (e) Cobalt, and (f) Silver.

4.5.2 X-ray diffraction Analysis

In order to confirm how the Ag/Co₃O₄@rGO nanocomposite is compounded together, XRD patterns were recorded. The XRD peaks are shown in Figure 4.26. The bottom peak pattern (black) is a clear spectrum of nanograins of Co₃O₄ containing prominent peaks from only unaided Co₃O₄ nanograins. The exact pattern is seen in the middle peak pattern (red), where the Co₃O₄ is grown on a sheet of rGO, since no peak from rGO has been observed in this pattern which is clear evidence of low graphitization because of the growth of Co₃O₄ nanograins on the rGO sheet (Liu et al., 2013). This confirms once again a growth of Co₃O₄ nanograins on the rGO sheet as shown in FESEM image in Figure 4.24(a). This shows that the rGO sheet has not been broken down and neither has gone through graphitization and just provided the conductive platform to Co₃O₄ nanograins. The top diffraction spectrum (blue) in the graph has indicated some sharp peaks arising from Ag nanoparticles in Ag/Co₃O₄@rGO ternary nanocomposite at diffraction angle of 38.04°, 44.32°, 64.65° and 77.46°, corresponding to (111), (200), (220) and (311) planes respectively, showing the existence of a space group Fm3m(225) of cubic structure of Ag nanoparticles (PDF No. 001-1164) (Shameli et al., 2012; Singh et al., 2010), which demonstrates the presence of Ag nanoparticles clearly in the Ag/Co₃O₄@rGO ternary nanocomposite. The formation of Ag nanoparticles was also supported by FESEM image in Figure 4.24(c) (pointed out through yellow arrows). The XRD peaks of Ag metal nanoparticles is another confirmation of a quasi-uniform Ag decoration of Co₃O₄@rGO nanocomposite. The quasi-uniform decoration has also been observed and is evidenced from the red and green dot images of EDS results of the as prepared ternary nanocomposite.

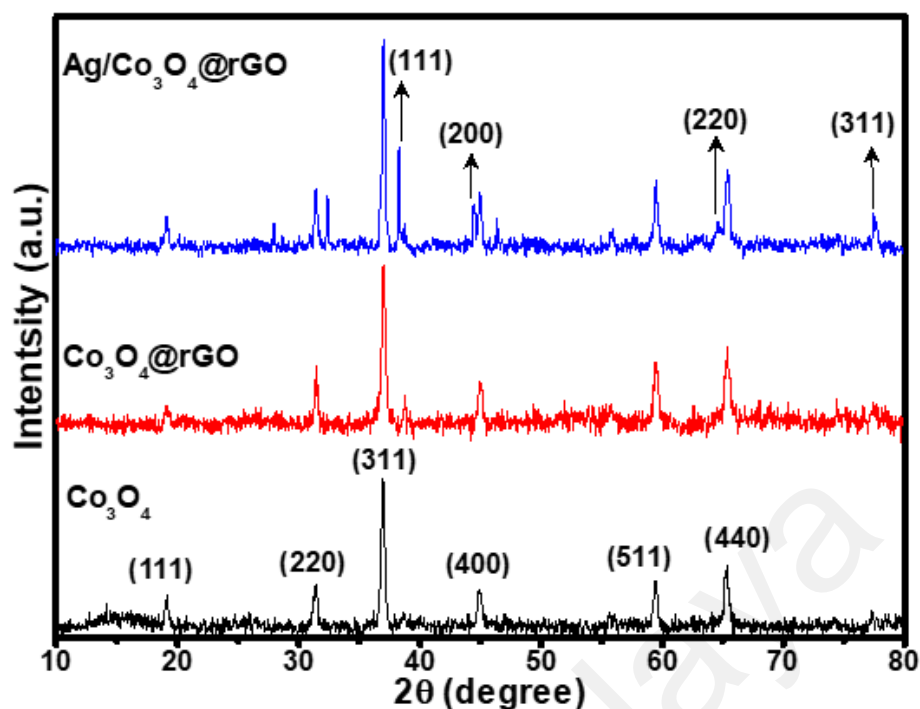


Figure 4.26: XRD patterns of pure Co₃O₄ nanograins (black), Co₃O₄@rGO (red) and Ag/Co₃O₄@rGO nanocomposite (blue).

4.5.3 X-ray Photoelectron Spectroscopy (XPS) Analysis

The surface of as synthesized ternary nanocomposite was analyzed using XPS, a surface analysis technique, to get the meaningful data of the chemical states of the prepared material. The XPS spectrum usually resulted from the excitation of the under test material using mono energies of aluminum $K\alpha$ X-rays which can cause the emission of photoelectrons from the surface of under test material. The emission lines are very helpful to predict the chemical states based upon the binding energy position and the intensity of each line of the studied material. Figure 4.27(a) shows the obtained main spectrum consisting of all lines clearly originating from the components/elements of the studied ternary nanocomposite (Ag/Co₃O₄@rGO). The main spectrum in the extreme ultraviolet region (200-800 eV) was further deconvoluted into a few sub-regions of the binding energy axis. The single peak of C $1s$ was observed at 284.13 eV and was deconvoluted into its components. The four peaks of C $1s$ are shown in Figure 4.27(b) with their binding energies at 284.13 (HOPG), 285.30 (sp^3), 286.83 and 288.95 eV. The

first two peaks 284.13 and 285.30 eV are attributed to the non-oxygenated sp^2 and sp^3 carbon hybridization having C=C and C≡C while the functional groups C-O to 286.83 and C=O to 288.95 eV (Abouali et al., 2015; Lesiak et al., 2014; Numan et al., 2017; Tan et al., 2016; Xiong et al., 2012).

Figure 4.27(c) shows the resolved components of O $1s$ in three peaks at 529.61, 530.77, 533.30 eV. The first peak shown at 529.61 eV is associated with the Co_3O_4 lattice oxygen (Numan et al., 2017), rest of the three peaks are affiliated with the oxygen present in the water adsorbed on the Co_3O_4 surface, cobalt monoxide, oxygenated bonds as C-O and C=O, and hydroxide ions (Li et al., 2006; Xiong et al., 2012). The Ag peak was also resolved into three components at 368.10 for $3d_{5/2}$ and 374.34 eV for $3d_{3/2}$ with strong peaks and a weak peak at 371.00 eV for $3d_{5/2}$ (which shows loss feature) as shown in Figure 4.27(d). The two strong peaks demonstrate the presence of Ag in the metal form and splitting of Ag covers 368-374 eV (Ferraria et al., 2009; Ma et al., 2014; Tan et al., 2015; Tian et al., 2017; Zhou et al., 2013).

Figure 4.27(e) demonstrates the splitting of Co $2p$ peak which is fitted with two Gaussian peaks. The two major peaks are seen around 780.10 eV for Co $2p_{3/2}$ and at around 796.80 eV for Co $2p_{1/2}$ with a gap of 16.70 eV between them, which is a demonstration of the standard spectrum Co_3O_4 (Tan et al., 2015). A weak peak at 788.80 eV is attributed to shake-up satellite at higher BE (Huang et al., 2012).

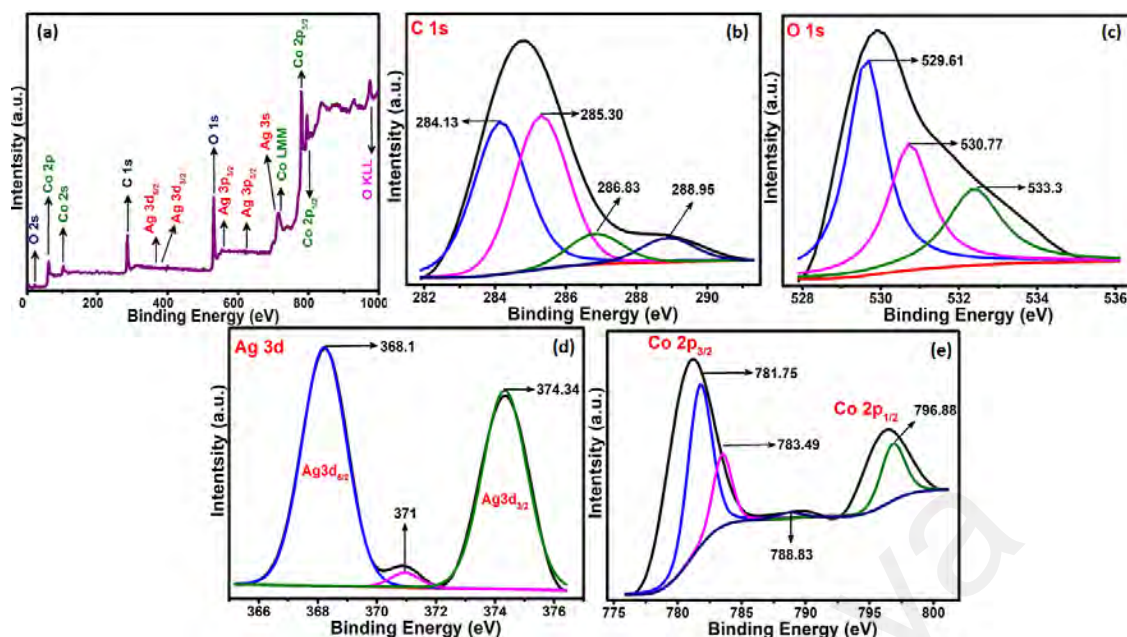


Figure 4.27: (a) Survey scanning of the Ag/Co₃O₄@rGO, ternary nanocomposites. High resolution spectra (b) C 1s region, (c) O 1s region, (d) Ag 3d region and (e) Co 2p_{2/3} region.

4.5.4 Electrochemical Analysis of Silver Nanoparticles and Cobalt Oxide Nanograins Grown on Reduced Graphene Oxide, (Ag/Co₃O₄@rGO)

(a) Cyclic Voltammetry (CV) Analysis

The cyclic voltammetry investigations were performed in a three electrodes cell system and the recorded voltammograms for Co₃O₄ nanograins, Co₃O₄@rGO binary nanocomposites, and Ag/Co₃O₄@rGO ternary nanocomposites in a range of 0-0.5 V at various scan rates are presented in Figure 4.28. It can be observed that voltammograms for Co₃O₄ (Fig 4.28(a)) showed well defined two pairs of oxidation and reductions peaks at a slow scan rate due to different oxidation states and multiple phases of Co₃O₄ nanograins (Tummala et al., 2012). However, asymmetric redox peaks and the slight shift in peak potential were observed at higher scanning rates which shows the poor mobility of the electrolyte ions during the electrochemical reaction at the interface of electrolyte and electrode (Duraismy et al., 2015). The rate capability counts mainly on the penetration of electrolyte ions, the adsorption of ions as well as the charge transfer mechanism on the electrode surface. Any of these phenomena if relatively slow at higher

scan rate could lead to reduce the specific capacity (Li et al., 2011). The reversible peaks of redox reaction show the battery type properties of the material. The redox processes that take place in 1 M KOH are shown in equations (4.1) and (4.2).

Figure 4.28(b) and (c) represent the voltammetric behavior of $\text{Co}_3\text{O}_4@\text{rGO}$ and $\text{Ag}/\text{Co}_3\text{O}_4@\text{rGO}$ nanocomposites, respectively. The voltammograms of $\text{Ag}/\text{Co}_3\text{O}_4@\text{rGO}$ nanocomposite clearly show Ag redox peaks which indicate that Ag nanoparticles are also contributing to the electrochemical reaction which further proves Ag as a component in the ternary nanocomposite. The redox process that Ag undergoes in 1 M KOH is presented as follows in equation (4.7).



Due to the contribution of a higher surface area of rGO and electronic conductivity of Ag into the ternary nanocomposite which provides the extended channel for charge transportation, the highest current density was observed for $\text{Ag}/\text{Co}_3\text{O}_4@\text{rGO}$. There is no significant distortion in the voltammograms of $\text{Ag}/\text{Co}_3\text{O}_4@\text{rGO}$ at a higher scan rate which indicates the outstanding rate capability of the ternary nanocomposite.

The unsupported Co_3O_4 nanograins were highly aggregated which lead to the reduction of electrochemical surface-active sites. Only a few faces of redox active sites of Co_3O_4 nanograins were exposed to an electrolyte. On the other hand, graphene being a highly conductive material is used as a platform to the less conductive materials to enhance their conductivity by providing the free electrons available in the graphene matrix. When these nanograins were grown on the reduced graphene sheets, the particle aggregations were significantly reduced by exposing more sites of nanograins which in turn increase the redox activeness, consequently, enhance the EC performance of the material used as an electrode. The improvement in electrochemical performance can be

seen by the higher peak current density of $\text{Co}_3\text{O}_4@\text{rGO}$ nanograins (Figure 4.28(d)). The precious metals (Pt, Au, Ag) play a pivotal role to increase the electronic conductivity of the material by offering the extended channel for electronic shuttling or by producing the synergistic effect by contributing in the redox reaction. Therefore, the efficiency of the nanocomposite was further enhanced by decoration the $\text{Co}_3\text{O}_4@\text{rGO}$ with Ag nanoparticles. Ag nanoparticles not only provide the channels for charge transportation, but it also contributes to redox reactions. The comparison voltammograms of Co_3O_4 nanograins, $\text{Co}_3\text{O}_4@\text{rGO}$, and $\text{Ag}/\text{Co}_3\text{O}_4@\text{rGO}$ nanocomposites could be observed in Figure 4.28(d).

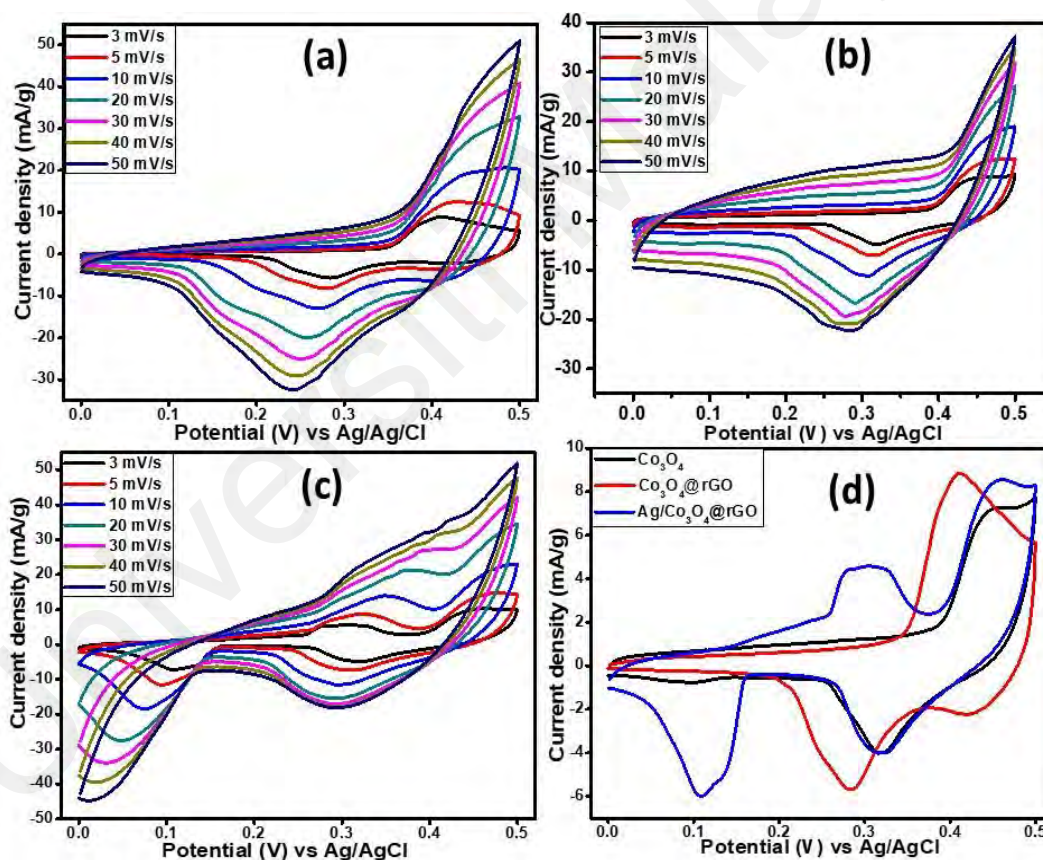


Figure 4.28: Cyclic voltammograms of (a) Co_3O_4 nanograins, (b) $\text{Co}_3\text{O}_4@\text{rGO}$, (c) $\text{Ag}/\text{Co}_3\text{O}_4@\text{rGO}$ ternary nanocomposite at diverse scanning rates and (d) comparison CV curves of pure Co_3O_4 nanograins, $\text{Co}_3\text{O}_4@\text{rGO}$ binary nanocomposite and $\text{Ag}/\text{Co}_3\text{O}_4@\text{rGO}$ ternary nanocomposite at 5 mV s^{-1} scan rate.

The specific capacity of all working electrodes can be estimated using the equation (4.3). The calculated specific capacities at a scan rate of 3 mV s^{-1} are 51.20, 64.00 and 98.30 C g^{-1} for Co_3O_4 , $\text{Co}_3\text{O}_4@\text{rGO}$, and $\text{Ag}/\text{Co}_3\text{O}_4@\text{rGO}$, respectively.

(b) **Galvanostatic Charge-discharge (GCD) Analysis**

Galvanostatic charge-discharge investigations were conducted to estimate the stability of the electrodes prepared with Co_3O_4 nanograins, Co_3O_4 nanograins grown on rGO matrix and $\text{Co}_3\text{O}_4@\text{rGO}$ nanocomposite decorated with Ag nanoparticles. Figure 4.29 (a-c) represents the galvanostatic charge-discharge plots for all prepared electrodes at diverse current densities in the range of $0.2\text{-}3.0 \text{ A g}^{-1}$ at a potential of $0\text{-}0.5 \text{ V}$. Due to redox behavior at electrode/electrolyte interface, quasi-symmetric discharge curves vouch for the pseudocapacitive property of the electrodes which is also agreed with the CV curves. It has been observed that discharge time was decreased inversely with the current density in all cases. Figure 4.29(d) clearly demonstrates that the $\text{Ag}/\text{Co}_3\text{O}_4@\text{rGO}$ nanocomposite has the longest discharge time compared to its counterpart electrodes. As the electrochemical active sites play a pivotal role in order to improve the efficiency of an electrode. In case of pure metal oxides, agglomeration of nanoparticles considerably reduces this factor which affects its performance. While in case of the $\text{Co}_3\text{O}_4@\text{rGO}$ nanocomposite, cobalt oxide nanograins were grown on graphene matrix which is uniformly distributed, reducing the agglomeration and increasing the exposed electroactive sites of the nanograins. As the graphene is in a conducting plate form helping the nanocomposite further to boost its electrochemical efficiency. The superior efficiency of the $\text{Ag}/\text{Co}_3\text{O}_4@\text{rGO}$ nanocomposite is associated with the further decoration of Ag nanoparticles which enhance its efficiency by contributing to the electrochemical redox reaction.

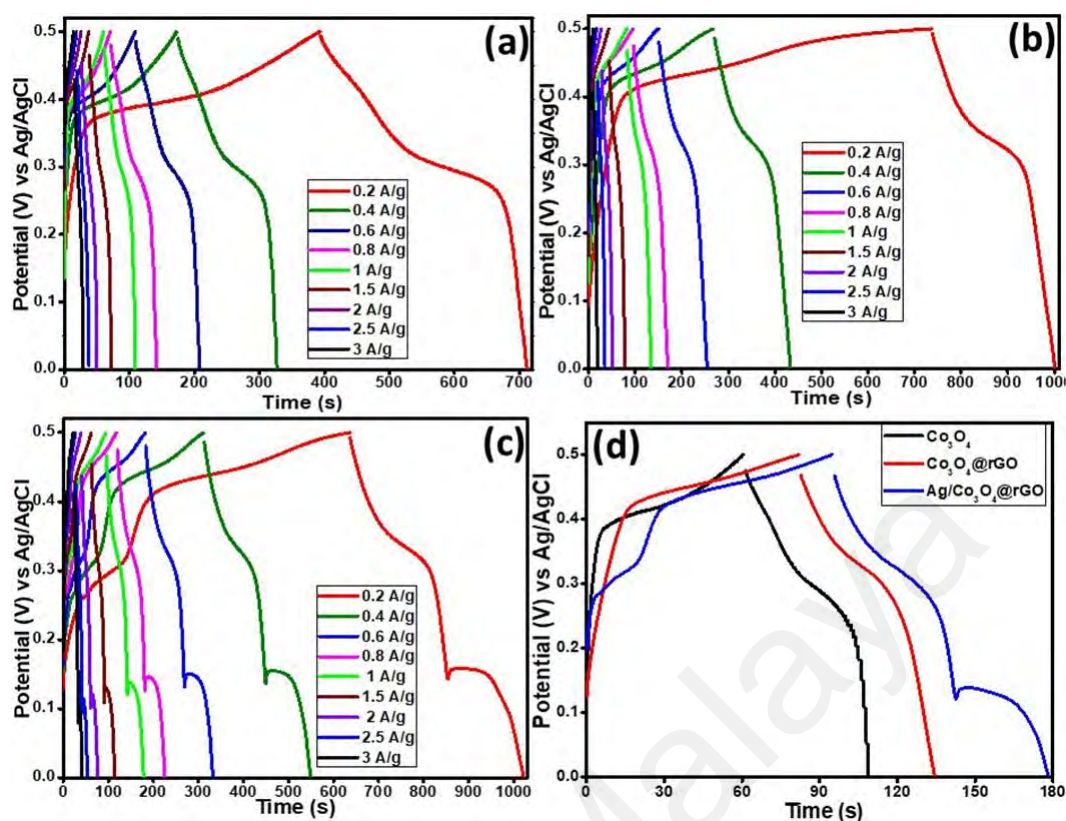


Figure 4.29: Charge-discharge plots at various current densities of (a) Co₃O₄ nanograins, (b) Co₃O₄@rGO, (c) Ag/Co₃O₄@rGO and (d) Comparative charge-discharge plots of unaided Co₃O₄, Co₃O₄@rGO and Ag/Co₃O₄@rGO ternary nanocomposite at a constant current density (1.0 A g⁻¹).

The specific capacity, (Q_s) of the electrodes has been evaluated using the equation (4.4). The Q_s values were estimated for Ag/Co₃O₄@rGO, Co₃O₄@rGO and Co₃O₄ are 94.20, 63.98 and 58.92 C g⁻¹, respectively at a current density of 0.2 A g⁻¹. It is obvious from the above calculated values that the specific capacity performance of Co₃O₄@rGO with Ag nanoparticles is much higher compared to pure Co₃O₄ nanograins and Co₃O₄@rGO binary nanocomposite. Figure 4.30 shows that the specific capacity values are higher at low current densities, whereas a gradual decline has been observed when the current densities are stepped up from 0.2 A g⁻¹ to 3.0 A g⁻¹. In fact, sluggish movements of the electric charges could not synchronize with high current densities leading to decrease the specific capacity. Herein, Figure 4.30 clearly demonstrate this effect where the Q_s value in case of Ag/Co₃O₄@rGO reduces from 94.20 C g⁻¹ to 57.19 C g⁻¹ with a retention capacity of 60.71 %. Similarly, Co₃O₄@rGO and Co₃O₄ retain 56.13 %

(decreased from 63.98 to 35.91 C g⁻¹) and 40.00 % (decreased from 58.92 to 23.57 C g⁻¹), respectively. This data shows that pristine Co₃O₄ nanograins are showing the lowest capacity retention whereas, the ternary nanocomposite, Ag/Co₃O₄@rGO takes the precedence as a highly efficient capacitive material among the other two because rGO provides a conducting plate form which reduces aggregation of nanograins, increasing active sites and the decoration of Ag nanoparticles further enhance its electrochemical efficiency by increasing electrochemical active sites and also contributing in the redox reaction. Therefore, the electrochemical efficiency of the ternary nanocomposite electrode is superior compared to its counterpart electrodes which provide the evidence that the Ag nanoparticles are also playing an effective role in order to boost its efficiency in a redox reaction.

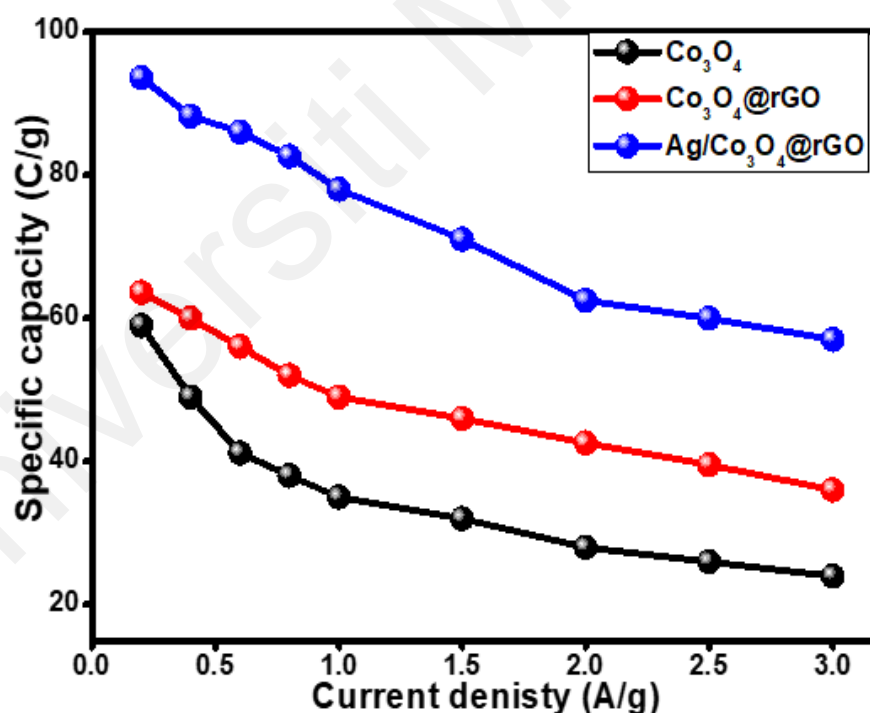


Figure 4.30: Specific capacity of Co₃O₄ nanograins (black), Co₃O₄@rGO (red), and Ag/Co₃O₄@rGO (blue) nanocomposites at different current densities.

(c) *Electrochemical Impedance Spectroscopy (EIS) Analysis*

The EIS studies were carried out to examine and compare the associated mechanism occurred on the electrodes surface modified with Co_3O_4 , $\text{Co}_3\text{O}_4@\text{rGO}$, and $\text{Ag}/\text{Co}_3\text{O}_4@\text{rGO}$ nanocomposite in 0.01-100 kHz range at an alternating voltage of 10 mV (R.M.S). Figure 4.31 shows the EIS spectra of the modified electrodes. The region of high frequency in the spectra gives the resistance parametric information of the working electrodes. The semicircle diameter in the graph estimates the resistance arises from charge transfer kinetics which is affiliated with electrode/electrolyte interface and geometry of the electrode (Zhou et al., 2004). A straight line, when taken off from the frequency knee point manifest the capacitive behavior of the electrode. In the case of ideality, the straight line supposed to be parallel to the imaginary axis. The slope of the line in a region of low frequency provides the diffusion resistance (Warburg impedance, W) (Huang et al., 2003).

The graphical demonstration of the EIS spectra in the form of Nyquist plot has been illustrated in Figure 4.31 for modified electrodes with Co_3O_4 , $\text{Co}_3\text{O}_4@\text{rGO}$ and $\text{Ag}/\text{Co}_3\text{O}_4@\text{rGO}$ nanocomposites. As expected, a semicircle in the region of high frequency and a straight line in the region of low frequency could be noticed in the plots for all modified electrodes with different parametric values. In the graph, $\text{Ag}/\text{Co}_3\text{O}_4@\text{rGO}$ modified electrode shows the impedance behavior by showing a vertical line in the low frequency portion which is close to an ideal EDLC along with a low charge transfer resistance (R_{ct}). Inset Figure 4.31 clearly illustrates the comparison of impedance behavior of the three modified electrodes in the high frequency region. The $\text{Co}_3\text{O}_4@\text{rGO}$ nanocomposite traces a bigger semicircle than the $\text{Ag}/\text{Co}_3\text{O}_4@\text{rGO}$ but smaller than the Co_3O_4 in the high frequency region which vouches that $\text{Ag}/\text{Co}_3\text{O}_4@\text{rGO}$ has the least charge transfer resistance among the others. Also, the ternary nanocomposite

shows the highest line parallel to the imaginary axis which proves that it has an escalated charge storage capacity due to the better conductivity of the reduced graphene oxide and synergistic effect of the Ag nanoparticles. There are three factors which play a prime role in the equivalent series resistance. Firstly, due to resistance, the discontinuity in ionic conductivity and electronic conductivity occurs during the charge transfer mechanism. Secondly, the resistance between Ni foam and the connecting leads. The last one is intrinsic resistance of the electrode substrate (Huang et al., 2003). The highest diffusion resistance has been observed in the case of Co_3O_4 nanograins due to high particle aggregations which effectively reduce the electroactive sites of the material leading to a low specific capacity. However, when Co_3O_4 nanograins were grown on reduced graphene nano sheets, then these nanograins were uniformly distributed over rGO, consequently, reducing the aggregation of nanograins and increasing the active sites which help to improve the specific capacity. In case of the ternary nanocomposite, Ag nanoparticles were decorated on the uniformly dispersed Co_3O_4 nanograins grown on the rGO matrix which further improved the electroactive sites and facilitated the electronic shuttling due to its higher conductive nature. The ternary nanocomposite which is composed of nanomaterials, *i.e.*, Co_3O_4 , rGO and Ag is highly conductive and reduced the pathways follow for the electronic movement to the nickel foam resulting to high specific capacity even at high current density which make it more appropriate material for the applications of supercapattery compared to the other materials under investigations.

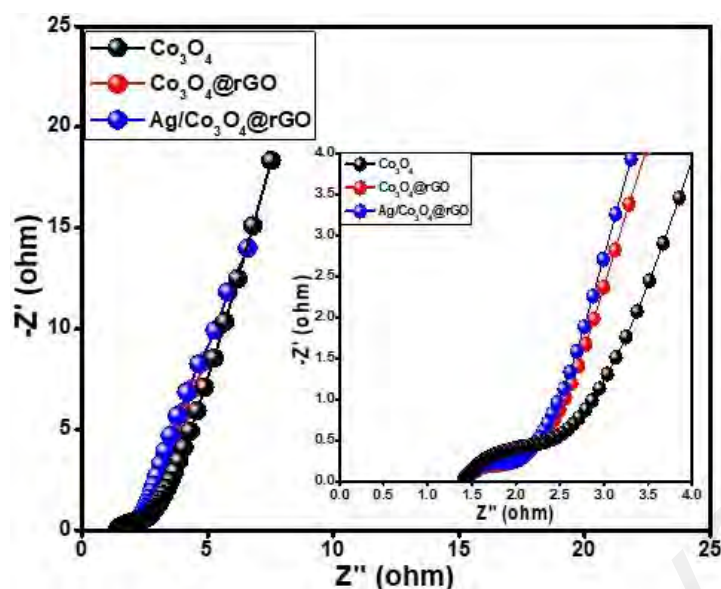


Figure 4.31: Nyquist plots of pure Co_3O_4 nanograins, $\text{Co}_3\text{O}_4@\text{rGO}$, and $\text{Ag}/\text{Co}_3\text{O}_4@\text{rGO}$ nanocomposites and the inset Figure is showing high frequency region.

4.5.5 Electrochemical Performance of Assembled $\text{Ag}/\text{Co}_3\text{O}_4@\text{rGO}/\text{AC}$ Supercapattery

Supercapattery is a hybrid device which has the characteristic features of both capacitor and battery. In supercapattery, the energy density is the characteristic parameter which is improved by expanding the operating voltage window. Herein, the supercapattery has been assembled using ternary nanocomposite, $\text{Ag}/\text{Co}_3\text{O}_4@\text{rGO}$ as a positive electrode and AC as a negative electrode ($\text{Ag}/\text{Co}_3\text{O}_4@\text{rGO}/\text{AC}$) as illustrated in Figure 4.32(a). In the electrochemical studies, first of all, the individual cyclic voltammograms were run for both ternary nanocomposite $\text{Ag}/\text{Co}_3\text{O}_4@\text{rGO}$ and AC in a conventional three electrodes cell at ambient room conditions. It allows us to estimate the maximum possible operating potentials *i.e.*, (0-0.5 V) and (-1.0-0 V) for $\text{Ag}/\text{Co}_3\text{O}_4@\text{rGO}$ and AC respectively, presented in Figure 4.32(b). It is evident from Figure 4.32(b) that the potential window for fabricated $\text{Ag}/\text{Co}_3\text{O}_4@\text{rGO}/\text{AC}$ supercapattery can be extended from 0 to 1.5 V (combining the potential range of AC and $\text{Ag}/\text{Co}_3\text{O}_4@\text{rGO}$ nanocomposite). Therefore, the maximum stable working potential for assembled device was kept 0-1.5 V. Figure 4.32(c) represents the voltammograms of $\text{Ag}/\text{Co}_3\text{O}_4@\text{rGO}/\text{AC}$

at various scanning rates (3-100 mV s⁻¹) in a potential window of 0-1.5 V. It could be noticed that no peaks were observed in the range of 0-0.3 V in the voltammograms scanned for supercapattery indicates the capacitive contribution of AC, which reveals that energy storage mechanism at electrode and electrolyte interface in this potential range follows the adsorption and intercalation of electrolyte ions. Thus, beyond 0.3 V, peaks start appearing in the voltammograms which show that the redox reactions start occurring to contribute in the energy storage mechanism of the device. The voltammograms around 1.5 V started deforming and continue rising upwards along y-axis which established the evidence of operating potential limit of the device under investigation. As stated, the supercapattery possesses the characteristic features of both capacitor and battery for the charge storage process. From the above discussion, it could be explained that the assembled device performance is based on both mechanisms *i.e.*, in potential window 0-0.3 V energy storage is contributed by capacitive or non-faradic behavior while beyond 0.3 to 1.5 V redox reactions are dominant in the energy storage mechanism. The shape, constancy and amplification of voltammogram scans at diverse scanning rates (3 to 100 mV s⁻¹) demonstrated better rate capability and stability of the assembled supercapattery. Figure 4.32(d) represents the charge-discharge plots of the assembled Ag/Co₃O₄@rGO//AC device at various densities of the applied current from 0.6 to 3.0 A g⁻¹ in a window of 0-1.5 V potential.

The symmetrical charge-discharge plots represent the capacitive nature combined with highly reversible redox reactions. The non-linearity of the curves is due to the contribution of faradic reactions of the Ag/Co₃O₄@rGO. The charge-discharge curves have been used to estimate the specific capacity (Q_s) of the assembled device using the equation (4.4). The Q_s value of Ag/Co₃O₄@rGO //AC is 115.80 C g⁻¹ at a current density of 0.6 A g⁻¹ and dropped down to 63.00 C g⁻¹ when current density was stepped up to 3.0 A g⁻¹.

In order to estimate the efficiency of the assembled device, power density (P) and energy density (E) are the key parametric quantities which have been estimated by exploiting the equations (4.5) and (4.6). The assembled device Ag/Co₃O₄@rGO//AC bank in at a current density of 0.6 A g⁻¹, the energy density and power density, $E = 23.63$ Wh kg⁻¹ and 440.00 W kg⁻¹ respectively. Whereas, a slight decrease was observed in the value of E (12.88 Wh kg⁻¹) and a substantial increase in the value of P to 2 kW kg⁻¹, when a current density was stepped up to 3.0 A g⁻¹. The results of the assembled device is higher than the recently published work in various articles such as Ni₃(PO₄)₂//AC (Omar et al., 2016), PANI-CuCo₂O₄//AC (Omar et al., 2017) and PANI//MoO₃ (Peng et al., 2014).

Figure 4.33(a) shows the Nyquist plot of the assembled device. In the high-frequency region, it shows semicircle and straight line in the low frequency region, which was expected for the assembled supercapattery. The semicircle diameter measurement indicates the low cell resistance, suggesting a short path that electrons travel. In the low frequency region, the high slope of the line in the Nyquist plot indicates low interfacial diffusion resistance proposing the fast ion diffusion and mass transport at the electrode/electrolyte interface.

In order to evaluate the viability of the assembled supercapattery using modified nickel foam with Ag/Co₃O₄@rGO nanocomposite, it is important to examine its long-term cyclic stability studies which was done over 3000 charge-discharge cycles at a current density of 3.0 A g⁻¹. Figure 4.33(b) represents that the assembled supercapattery electrode retains 85.50 % specific capacity after 3000 cycles. The gradual activating process of the electrode in an electrolyte tends to increase the capacity retention up to 400 cycles and then it becomes stable over the full-scale studies of 3000 cycles. The excellent characteristic stability of assembled supercapattery using a modified electrode with ternary nanocomposite assures its viability for practical usage.

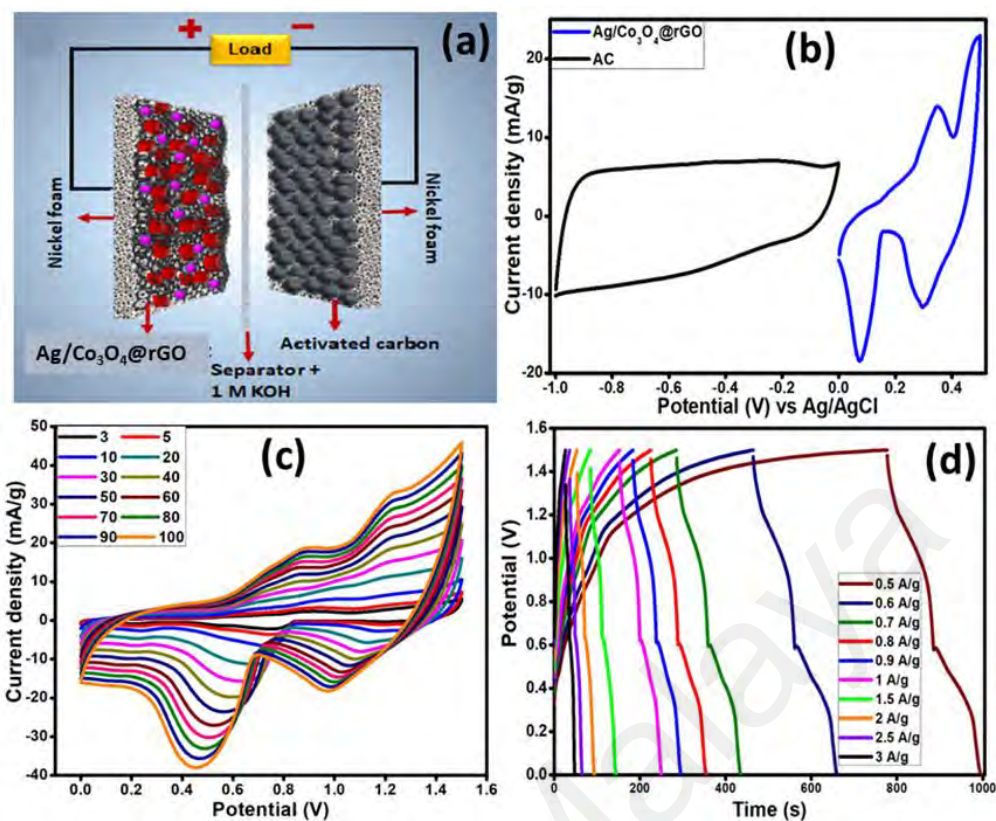


Figure 4.32: (a) Graphical presentation of the assembled Ag/Co₃O₄@rGO//AC supercapattery, (b) voltammograms of Ag/Co₃O₄@rGO and AC electrode performed at a scanning rate of 10 mV s⁻¹ in a three electrodes cell in 1 M KOH solution, (c) CVs of Ag/Co₃O₄@rGO//AC device assessed at diverse scanning rates and (d) GCD curves of Ag/Co₃O₄@rGO//AC supercapattery at different current densities.

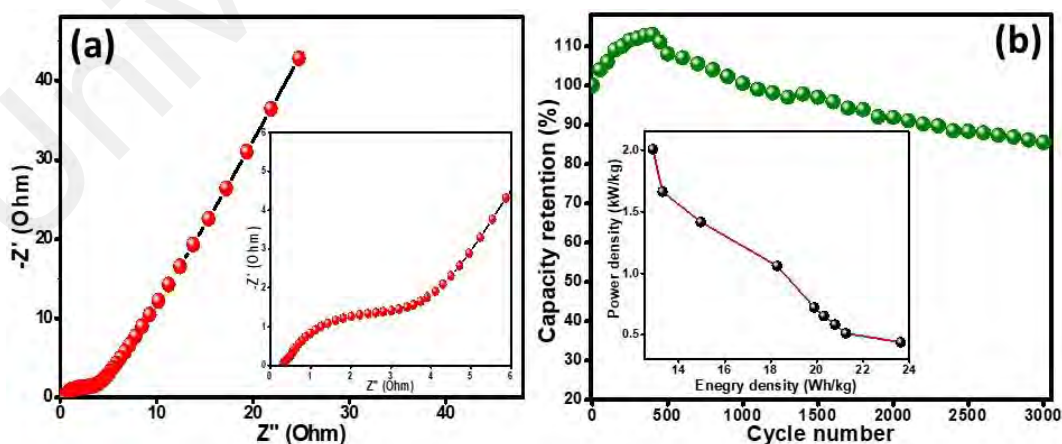


Figure 4.33: (a) Nyquist plots for Ag/Co₃O₄@rGO//AC supercapattery. Figure 4.33(b) showing the cycling stability of Ag/Co₃O₄@rGO//AC supercapattery and the inset plot is for energy density decay versus power density.

4.6 Conducting Polymers Based Ternary Nanocomposites

Among the CPs, polypyrrole and polyaniline has gained much attention due to its tunable electrical conductivity, high specific capacitance, low cost, and environmental stability which make it suitable for various applications such as light emitting diodes, sensors, actuators, batteries, and electrochemical supercapacitors (Mike & Lutkenhaus, 2013). In order to attain good electrochemical response of the CPs electrodes, a suitable amount of the polymer need to be loaded for various applications which results in the depletion of specific capacitance and increase in the impedance. Moreover, the poor capacity retention also limits its scope in supercapattery applications (Fu et al., 2013). Therefore, engineering strategies were exploited by blending the CPs in the form of composite with some suitable dopant such as metal oxides which could lessen the impedance and escalate the cycling stability (Salunkhe et al., 2015). In fact, PPy and PANI are the CPs that can be synthesized in aqueous solutions. The combination of both classes of pseudocapacitive materials (CPs and metal oxides) certainly has their advantages.

In the recent years, cobalt oxide (Co_3O_4) has gained much attention due to its favorable properties, especially, for supercapattery applications and many research articles have been published covering numerous electrochemical studies (Kandalkar et al., 2008; Salunkhe et al., 2015; Xu et al., 2010). The metal oxides in the nano-size dimensions have high surface area to volume ratio which tends to aggregate when they are in pure form. The aggregation reduces the electroactive sites of the material which ultimately results in the capacity fading of the device. However, when metal oxide nanoparticles are blended or grown on some conducting platforms such as conducting polymers, multiwalled carbon nanotubes or graphene oxide then the issue of aggregation could be appropriately addressed (Numan et al., 2016; Omar et al., 2017). Conducting polymers

are the most promising pseudocapacitive materials due to their above mentioned peculiar properties such as flexibility in preparation processes, light weightlessness, low cost and high electrical conductivity (Snook et al., 2011).

As, PPy and PANI are redox active materials possessing ability to store energy through faradaic reaction, but poor mechanical stability of the polymeric materials has been observed due to shrinkage and swelling in the repeated redox reactions which limits their usage for EC energy storage devices. Furthermore, slower diffusion of electrolyte ions occurs through the polymer matrix due to the disordered placement of molecules in the polymeric chain. However, with the elegant synergy between both materials (CPs and metal oxides), remarkable electrochemical performances can be realized as the composite of CPs (PPy and PANI) and Co_3O_4 could take the advantage of high electrical conductivity of PPy/PANI and the high energy storage capacity of Co_3O_4 . These days, noble metal such as silver has been widely used to enhance the conductivity of transition metals. These noble materials as additives can improve the specific capacitance, conductivity, and chemical and thermal stabilities of the electrode materials. Wu *et al.* showed that Ag assists in electron transfer ability of MoS_2 leading to outstanding electrochemical storage ability (Wu et al., 2017). Thus, it can be expected that addition of Ag to the PPy/PANI and Co_3O_4 composite can deliver high capacitance along with the combination of high stability owing to the synergistic effect of the components. The synthesis of ternary nanocomposites of PPy/PANI embedded with cobalt oxide and silver nanoparticles are reported by a feasible combination of chemical route and hydrothermal method for high performance electrode material for supercapattery applications. Hydrothermally prepared Co_3O_4 nanograin were doped with certain weight percentage of PPy/PANI matrix and finally decorated with silver nanoparticles to obtain the ternary nanocomposites, $\text{Ag}/\text{Co}_3\text{O}_4@\text{CPs}$. To get the structural, morphological and

compositional insights, various analytical techniques were exploited and finally used as an electrode material in supercapattery assemblies.

4.7 System 4: Polypyrrole (PPy) Incorporated with Silver Nanoparticles and Cobalt Oxide Nanograins (Ag/Co₃O₄@PPy) Based Ternary Nanocomposite

4.7.1 Surface Morphology Study

Figure 4.34 and 4.35 shows the morphological analysis of PPy, Co₃O₄@PPy and Ag/Co₃O₄@PPy by FESEM and TEM at different magnifications. In Figure 4.34(a) pure PPy shows highly agglomerated globular morphology of varying sizes ~200-400 nm and the globules are linked with each other to form lumps of different sizes. In the case of Co₃O₄@PPy (Figure 4.34(b)), the Co₃O₄ nanograins decorated on the surface of PPy and in the vicinity can be clearly seen. It can be interpreted that some Co₃O₄ nanograins are deeply embedded inside the PPy globules, which are not distinctly seen. Apart from this, less agglomeration of PPy is seen in Ag/Co₃O₄@PPy (Figure 4.34(c)) which might be due to the growth of Co₃O₄ or Ag nanoparticles between different polymer chains, thereby resulting in breakage/separation of polymeric globules. The long chain interconnected globules of PPy containing embedded or surface decorated with Ag or Co₃O₄ and their porous nature is expected to provide fast transport and short path for ion diffusion (Alshahrie & Ansari, 2019).

The TEM images of Ag/Co₃O₄@PPy in Figure 4.35 (a & b) show round, tubular and globular appearance of PPy as well as large number of Co₃O₄ and Ag nanoparticles. The PPy is seen to be surrounded by well linked Co₃O₄ and Ag nanoparticles with few of nanoparticles embedded inside the polymeric structures. At higher magnification, Co₃O₄ (~15-30 nm) and Ag (~14-25 nm) of varying sizes and dimensions from cubes to irregular cubes and hexagonal structure can be seen in the polymeric background. The inset in FESEM Figure 4.34(c) shows well linked Ag and Co₃O₄ on the surface of PPy, which also suggests strong intercalation between PPy and nanomaterials. The EDS analysis

(Figure 4.36) shows the presence of C, O, Co, Ag, and N, while the elemental mapping results show their uniform distribution, thereby suggesting the successful formation of Ag/Co₃O₄@PPy.

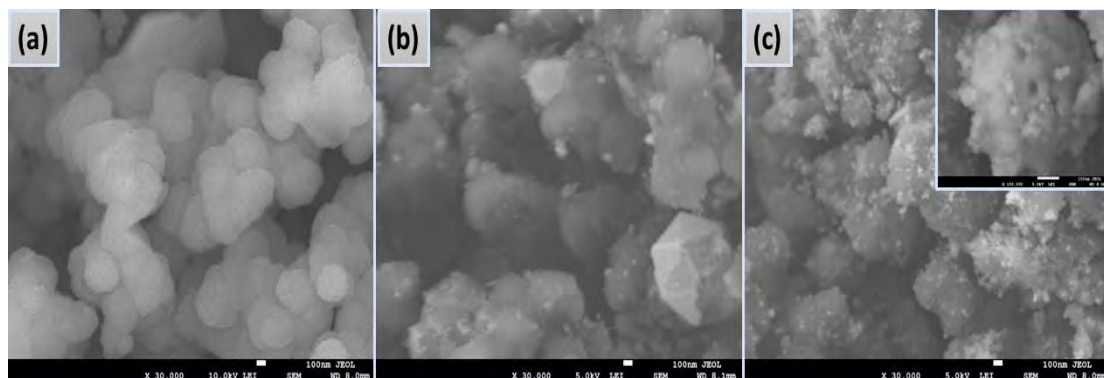


Figure 4.34: FESEM images of (a) pure PPy, (b) Co₃O₄@PPy, binary nanocomposite, (c) Ag/Co₃O₄@PPy, ternary nanocomposite and inset Figure 4.30(c) showing Co₃O₄ and Ag NPs well linked on the PPy.

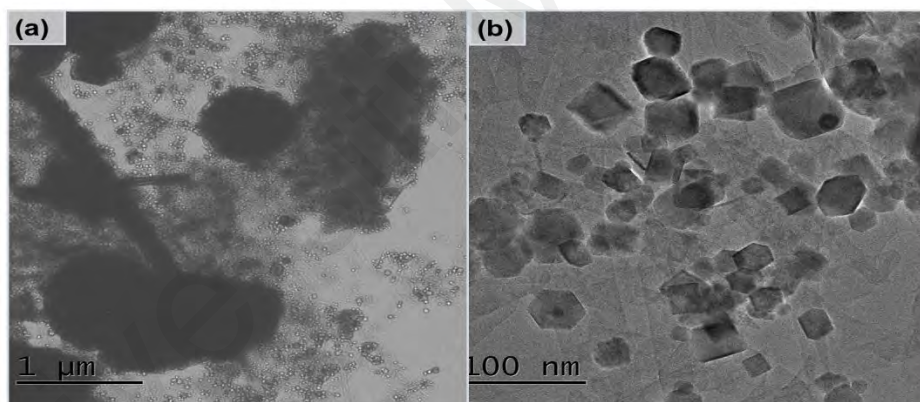


Figure 4.35: TEM images of ternary nanocomposite, Ag/Co₃O₄@PPy (a) low magnification and (b) high magnification.

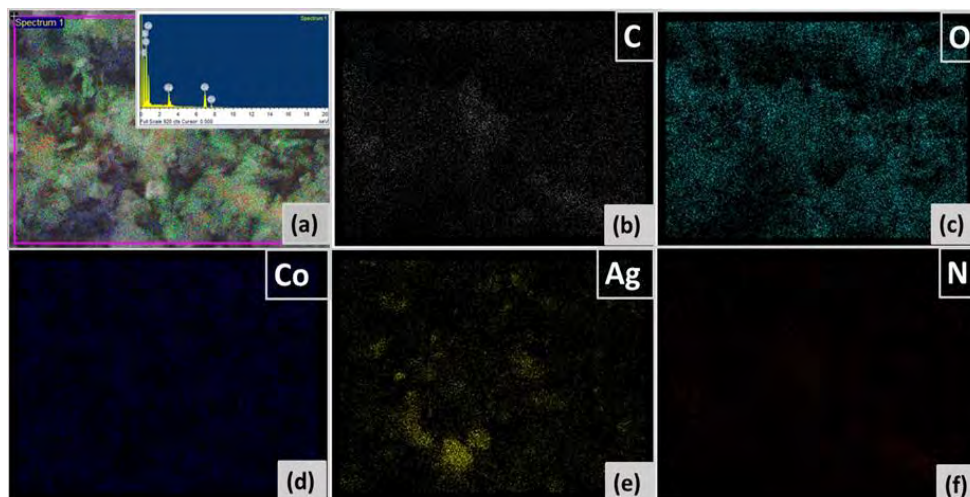


Figure 4.36: (a) EDS spectrum shows the elemental composition and verify the even distribution of both, Co_3O_4 and Ag NPs on the PPy matrix. EDS-elemental mapping is presented by (b) C, (c) O, (d) Co and (e) Ag contents of the $\text{Ag}/\text{Co}_3\text{O}_4@\text{PPy}$ ternary nanocomposites.

4.7.2 X-ray diffraction Analysis

XRD was done to evaluate the structural characteristics and crystallinity of the PPy, Co_3O_4 , $\text{Co}_3\text{O}_4@\text{PPy}$, and $\text{Ag}/\text{Co}_3\text{O}_4@\text{PPy}$ nanocomposites (Figure 4.37).

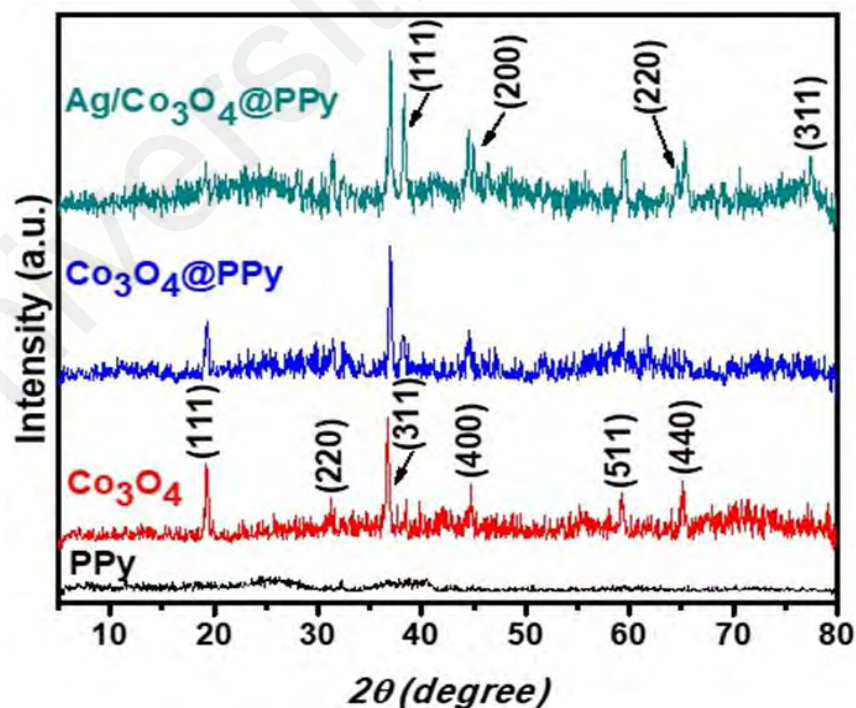


Figure 4.37: XRD pattern of PPy, Co_3O_4 , $\text{Co}_3\text{O}_4@\text{PPy}$ binary and $\text{Ag}/\text{Co}_3\text{O}_4@\text{PPy}$, ternary nanocomposites scanned in the 2θ range of 5° - 80° .

Figure 4.37 shows that PPy is highly amorphous with a characteristic broad peak at 2θ value of $\sim 25^\circ$ due to the scattering from PPy chains at the interplanar spacing (Chougule et al., 2011). For the $\text{Co}_3\text{O}_4@\text{PPy}$ nanocomposites, it has a similar XRD pattern to the Co_3O_4 , confirming the presence of Co_3O_4 in the nanocomposites. However, the peaks of Co_3O_4 are slightly diffused and are of much reduced intensity in $\text{Co}_3\text{O}_4@\text{PPy}$ which might be due to the incorporation of Co_3O_4 inside the PPy (Zhang et al., 2014). The XRD pattern of $\text{Ag}/\text{Co}_3\text{O}_4@\text{PPy}$ is similar to that of $\text{Co}_3\text{O}_4@\text{PPy}$ and the peak of Ag is highly diffused and not distinctive, which might be due to its small amount as well as due to the influence of the amorphous PPy as mentioned above. The existence of the PPy has also been previously reported to influence the degree of crystallization of metal oxide materials (Zhang et al., 2014).

4.7.3 X-ray Photoelectron Spectroscopy (XPS) Analysis

XPS was used to examine the chemical states and surface composition of $\text{Ag}/\text{Co}_3\text{O}_4@\text{PPy}$ nanocomposites. The XPS survey spectra of $\text{Ag}/\text{Co}_3\text{O}_4@\text{PPy}$ composites (Figure 4.38(a)) revealed five major sets of peaks corresponding to the C $1s$, O $1s$, N $1s$, Co $2p_{3/2}$ and Ag $3d_{5/2}$ and no trace of any impurity was observed. The carbon peak in Figure 4.38(b) is assigned to the residual carbon from the sample and hydrocarbons from the XPS instrument. The high resolution XPS spectra of C $1s$ revealed that the spectra is dominated by the aliphatic carbon C-C/C-H peak (284.84 eV), whereas C-O-C (285.52 eV) and O-C=O (288.29 eV) contributions present at higher BE appear in much lower concentrations (Greczynski & Hultman, 2017). It might be interpreted that the contaminants C-O-C and O-C=O imparts additional functionality to the PPy chain, which may act as the sites for interaction with the Co_3O_4 and Ag. The deconvolution of O $1s$ peak (Figure 4.38(c)) into two peaks at 530.91 and 532.40 eV corresponds to the oxygen in Co_3O_4 and organic C-O respectively (Cordoba et al., 2017; Thu et al., 2019). The N $1s$ can be split into three peaks (Figure 4.38(d)). The peak at 398.87 is due to the

(-NH-) in the PPy ring. The other peaks at higher binding energies may be attributed to the oxidized/protonated nitrogen. The peak at 400.86 eV is indicative of $\text{-NH}^{+\cdot}$ in the polaron charge carrier species while the other peak at 403.04 eV is due to the $\text{=NH}^{+\cdot}$, a bipolaron charge carrier species (Malitesta et al., 1995). The shifting of these peaks to higher binding energies in comparison to pure PPy (binding energies 397.8, 399.7, and 400.5 eV) may also suggest interaction between the components i.e. PPy, Co_3O_4 and Ag (Su et al., 2012). The Co $2p_{3/2}$ XPS spectrum of Co_3O_4 nanocrystals in Figure 4.38(e) is deconvoluted into three components at 780.29, 782.06, and 789.83 eV. The peaks at 779.5 and 780.8 eV correspond to Co^{3+} and Co^{2+} species, respectively and the last component peak at 789.83 eV is due to satellite shake-up peaks from Co^{3+} ions. This data provides the direct evidence for the presence of Co_3O_4 phase in the composite (Xia et al., 2013). The Ag $3d$ photoelectron peak in Figure 4.38(f) showed two individual peaks at 367.94 eV for Ag $3d_{5/2}$ and 374.11 eV for Ag $3d_{3/2}$. The 6.0 eV difference between the binding energy of these photoelectron peaks is also characteristic of metallic Ag, which is further evidence of the reduction of Ag salt under hydrothermal conditions (Ansari et al., 2014).

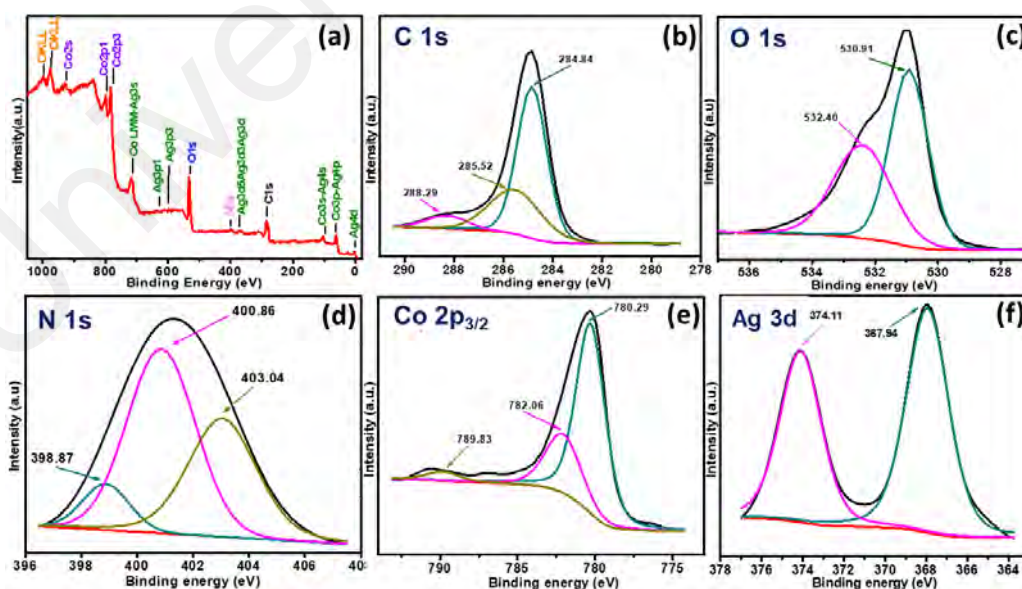


Figure 4.38: (a) Survey scan spectra of ternary nanocomposite $\text{Ag}/\text{Co}_3\text{O}_4@\text{PPy}$ and the presentation of high resolution spectra of C $1s$ (b), O $1s$ (c), N $1s$ (d), Co $2p_{3/2}$ (e) and (f) Ag $3d$.

4.7.4 Electrochemical Analysis of Polypyrrole (PPy), $\text{Co}_3\text{O}_4@\text{PPy}$, and $\text{Ag}/\text{Co}_3\text{O}_4@\text{PPy}$ Ternary Nanocomposite

(a) Cyclic Voltammetry (CV) Analysis

The electrochemical studies of the pure PPy and its composites ($\text{Co}_3\text{O}_4@\text{PPy}$ and $\text{Ag}/\text{Co}_3\text{O}_4@\text{PPy}$) were performed in 1 M KOH solution in the potential range of 0 to 0.5 V using cyclic voltammetry (CV) technique. Their CV at scan rates of 3, 5, 10, 20, 30, 40 and 50 mV s^{-1} are shown in Figure 4.39. The resultant CV curves in all cases display well defined pair of oxidation and reduction peaks and demonstrated a linear increase in the current density with the increasing scan rates which shows the good electrochemical capacitance and reversibility behavior of the PPy polymers (Figure 4.39(a)) and its composite materials (Yan et al., 2010). A slight shift in the peak potential could be seen in voltammograms when the scan rate is increased which may be associated to the rate of diffusion of OH^- ions to the electrode material. The inner and outer surface of the polymer is utilized at slow scan rate while at the higher scans, only outer pores of the surface is utilized which tend to shift the peak potential due to slow movement of OH^- ions. It is clear from Figure 4.39(b) that the current density is much higher for binary composite compared to pure PPy due to the additional effect of the Co_3O_4 nanoparticles. According to the literature, the surface adsorption of high concentration of alkali ions can decrease the electrolyte starvation near the electrode surface and reduce the internal resistance of the electrode, that factor helps to improve the pseudocapacitance resulting from the cobalt oxide particles surface reaction. These results show the overall capacitance of the electrode increases due to the presence of the Co_3O_4 nanoparticles. As the noble metal such as silver, being very conductive also produced the synergistic effect when added in a small quantity to the nanocomposite. Therefore, in case of ternary nanocomposite *i.e.* $\text{Ag}/\text{Co}_3\text{O}_4@\text{PPy}$, the highest current density was observed, showing the additional effect of silver nanoparticles (Figure 4.39(c)). Figure 4.39(d) shows the comparison of the three

electrode materials and demonstrates the clear enhancement of current density by applying the binary and ternary blend approach of PPy with cobalt oxide and silver nanoparticles. The specific capacity (Q_s) of the three electrode material (PPy, $\text{Co}_3\text{O}_4@\text{PPy}$ and $\text{Ag}/\text{Co}_3\text{O}_4@\text{PPy}$) can be calculated using equation (4.3). The Q_s values calculated at 3 mV s^{-1} for PPy, $\text{Co}_3\text{O}_4@\text{PPy}$ and $\text{Ag}/\text{Co}_3\text{O}_4@\text{PPy}$ are 182.26, 274.28, and 370.94 C g^{-1} , respectively.

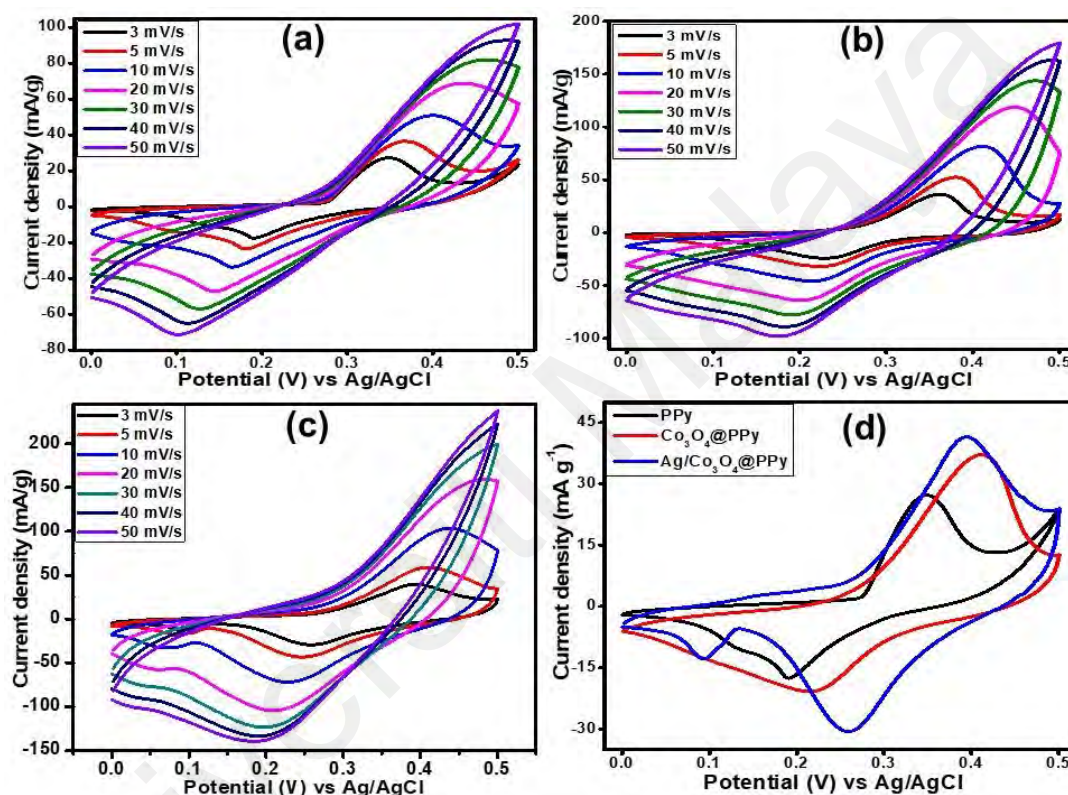


Figure 4.39: CV curves of (a) PPy, (b) $\text{Co}_3\text{O}_4@\text{PPy}$ binary and (c) $\text{Ag}/\text{Co}_3\text{O}_4@\text{PPy}$ ternary nanocomposites measured at varied scan rates. (d) CV curves to compare electrochemical performance of PPy, $\text{Co}_3\text{O}_4@\text{PPy}$ binary and $\text{Ag}/\text{Co}_3\text{O}_4@\text{PPy}$, ternary nanocomposites recorded at 3 mV s^{-1} .

(b) *Galvanostatic Charge- discharge (GCD) Analysis*

PPy has been attractive electrode material for supercapattery due to its high accessible surface area and prominent electrical conductivity. The specific capacity of the pristine PPy is 143.28 C g^{-1} . To improve its electrochemical performance, the PPy was blended

to form binary and ternary composites with Co_3O_4 and silver nanoparticles for supercapattery applications. It is clear from the SEM micrographs that PPy plays a role of a perfect backbone for deaggregation of Co_3O_4 and both together provide the additional effect in order to increase the EC performance of the PPy composites. Figure 4.40(a-d) displays mirror like GCD curves for PPy, Co_3O_4 @PPy and $\text{Ag}/\text{Co}_3\text{O}_4$ @PPy in 1 M KOH solution at a galvanostatic current density of 1.4, 1.8, 2.2, 2.6, 3.0, 3.4, 3.8, 4.2 A g^{-1} at a constant potential of 0.5 V which advocate that the charge-discharge process of the pure and composites is reversible and also agrees with the CV curves. It could be noticed from the comparison of GCD curves (Fig. 4.40(d)) that the EC performance of the ternary nanocomposite is the best among the three samples which is due to the synergistic effect of the metal oxide and addition of the silver nanoparticles.

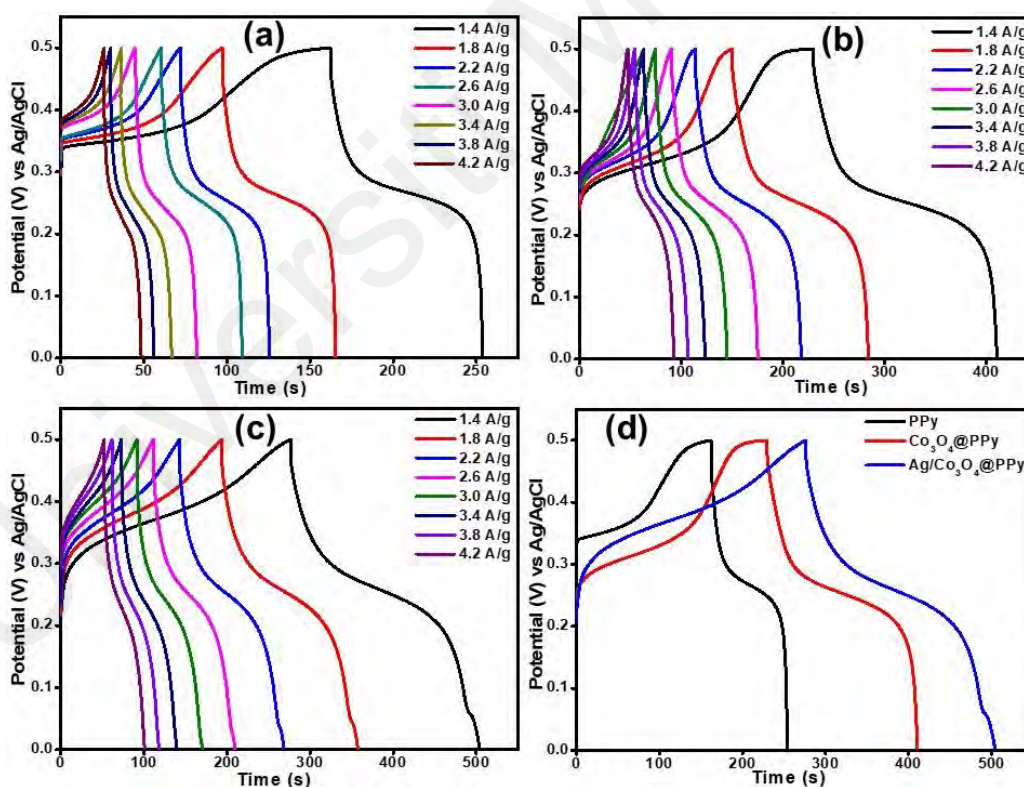


Figure 4.40: GCD curves at various current densities, (a) PPy, (b) Co_3O_4 @PPy, (c) $\text{Ag}/\text{Co}_3\text{O}_4$ @PPy and (d) comparison curves for all three variants at current density of 1.4 Ag^{-1} .

The specific capacity (Q_s) analysis of the PPy and its composites have been performed from the discharged curves using the equation (4.4). The calculated Q_s values for PPy, $\text{Co}_3\text{O}_4@\text{PPy}$ and $\text{Ag}/\text{Co}_3\text{O}_4@\text{PPy}$ are 143.28, 280.68, 355.64 C g^{-1} , respectively at a current density of 1.4 A g^{-1} . The Q_s values for three materials clearly demonstrate that the EC performance of ternary nanocomposite is the best which makes it a suitable material for energy storage device fabrications.

Figure 4.41 represents the specific capacities versus current density curves. It shows that Q_s values decrease as the current density increases due to the limited shuttling of the OH^- ions through the electrode materials. The binary and ternary composites demonstrate higher specific capacity than the pure one due to the decoration of Co_3O_4 onto the PPy polymer matrix which effectively reduce the agglomeration of metal oxide, consequently exposed more electroactive sites, thereby alleviating the ion transport in the electrode material and further boost is provided by the addition of silver nanoparticles in ternary nanocomposite material. The ternary nanocomposite, $\text{Ag}/\text{Co}_3\text{O}_4@\text{PPy}$ shows the highest specific capacity among the three samples due to a synergistic effect of metal and metal oxide in polymeric matrix. Therefore, the outstanding EC performance of the synthesized ternary nanocomposite materials can be associated to the additional effect of three components and their unique morphologies.

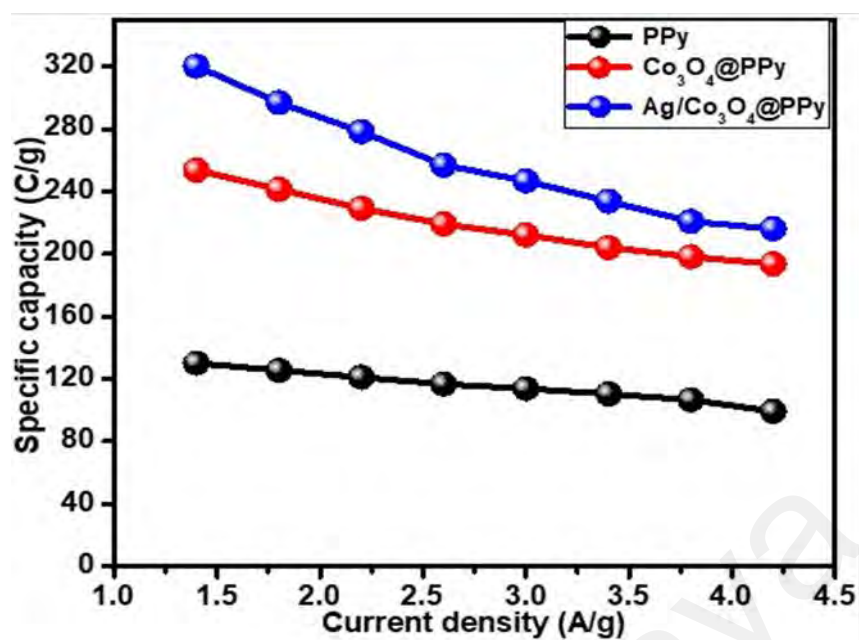


Figure 4.41: Showing specific capacity versus current density decay of PPy, Co₃O₄@PPy binary and Ag/Co₃O₄@PPy ternary nanocomposites.

(c) *Electrochemical Impedance Spectroscopy (EIS) Analysis*

The EIS studies were carried out to examine and compare the associated mechanism occurred on the electrodes surface modified with PPy, Co₃O₄@PPy and Ag/Co₃O₄@PPy nanocomposite in 0.01-100 kHz range at an alternating voltage of 10 mV (R.M.S). Figure 4.42 represents the typical Nyquist plot of pure PPy and its composite materials. The plot demonstrates a straight line in the low frequency region and a semicircle in the high frequency region. For the evaluation of internal resistance of the electrode in an open circuit, a straight line from the point of intersection with the real axis in the high frequency region mainly composed of three parameters *i.e.*, electrolytic ionic resistance, intrinsic properties of the active material, and lastly the contact resistance between the active material and the current collector. The semicircle related to faradic reactions is associated to the charge transfer resistance at the electrode/electrolyte interface. The low ESR value and comparatively straight line in the low frequency region may be due to the

incorporation of Co_3O_4 into the composite, which enhanced the electrochemical properties of $\text{Co}_3\text{O}_4@\text{PPy}$. From the EIS studies, it could be noticed that the ternary composite is best performing material compared to pure and binary composite due to the successful incorporation of Co_3O_4 and Ag nanoparticles into the polymer as it traces the shortest semicircle in the low frequency region and a vertical line parallel to imaginary axis when compared to pure PPy and its binary composite. Therefore, the ternary composite of PPy possess high charge storage capacity and less charge transfer resistance due to the intercalation of nanoparticles to PPy allowing the penetration of electrolyte ions because of porosity, which is helping faster charge transfer kinetics, consequently, making it a suitable electrode material for device fabrication.

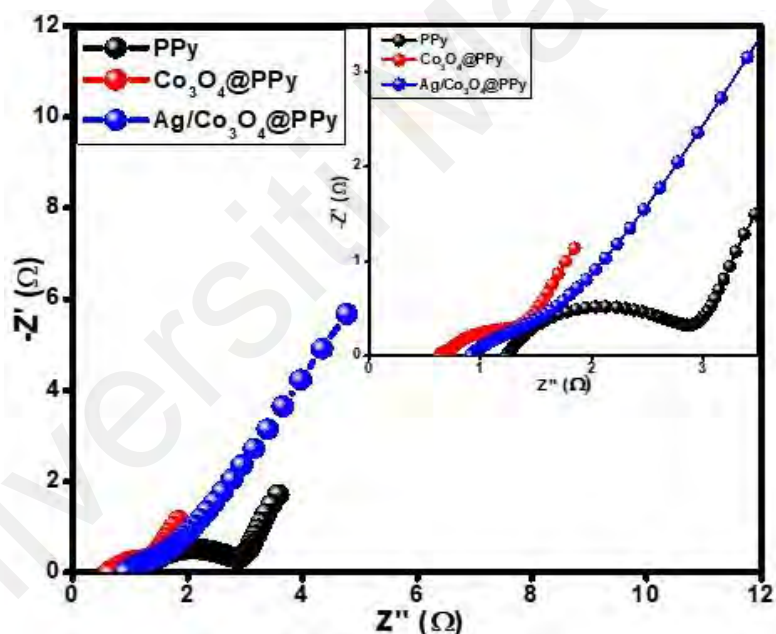


Figure 4.42: Nyquist plots of pure PPy, $\text{Co}_3\text{O}_4@\text{PPy}$, and $\text{Ag}/\text{Co}_3\text{O}_4@\text{PPy}$ nanocomposites. Inset Figure shows the high frequency region of the plot.

4.7.5 Electrochemical Performance of Assembled $\text{Ag}/\text{Co}_3\text{O}_4@\text{PPy}/\text{AC}$ Supercapattery

Supercapattery consists of two electrode assembly in which capacitive material is applied as a negative electrode and battery grade as a positive electrode to combine the

effect of capacitor and battery in one to gain the benefit of both systems. Here in the device construction, the Ag/Co₃O₄@PPy was used as a positive electrode and AC as a negative electrode to fabricate the resultant device Ag/Co₃O₄@PPy//AC. Figure 4.43(a) demonstrates the graphical presentation of supercapattery. Before assembling the device, individual CVs were run in a standard three electrode cell system in order to evaluate the maximum working potential for both materials (Ag/Co₃O₄@PPy, AC) as well as to ensure the proper electrochemical response of both electrodes in their individual domains. It is clear from Figure 4.43(b) that the potential window for capacitive material is 0-0.5 V and for pseudocapacitive material -1.0-0 V. So, by combining the individual potentials of both materials, the maximum stable working potential for supercapattery is estimated to be 0 to 1.5 V. The EC analysis of the fabricated devices were then performed in 1 M KOH electrolyte solution at an ambient condition (Figure 4.42 (c)). Figure 4.43(d) displays the voltammograms at various scanning rates ranging from 3 to 100 mV s⁻¹. It is obvious from the voltammograms that a pair of pronounced redox peaks were observed and current density increases with the increasing scanning rates. In addition to that, shape of the voltammograms is well conserved even at high scan rate which evidenced the good rate capability of the device.

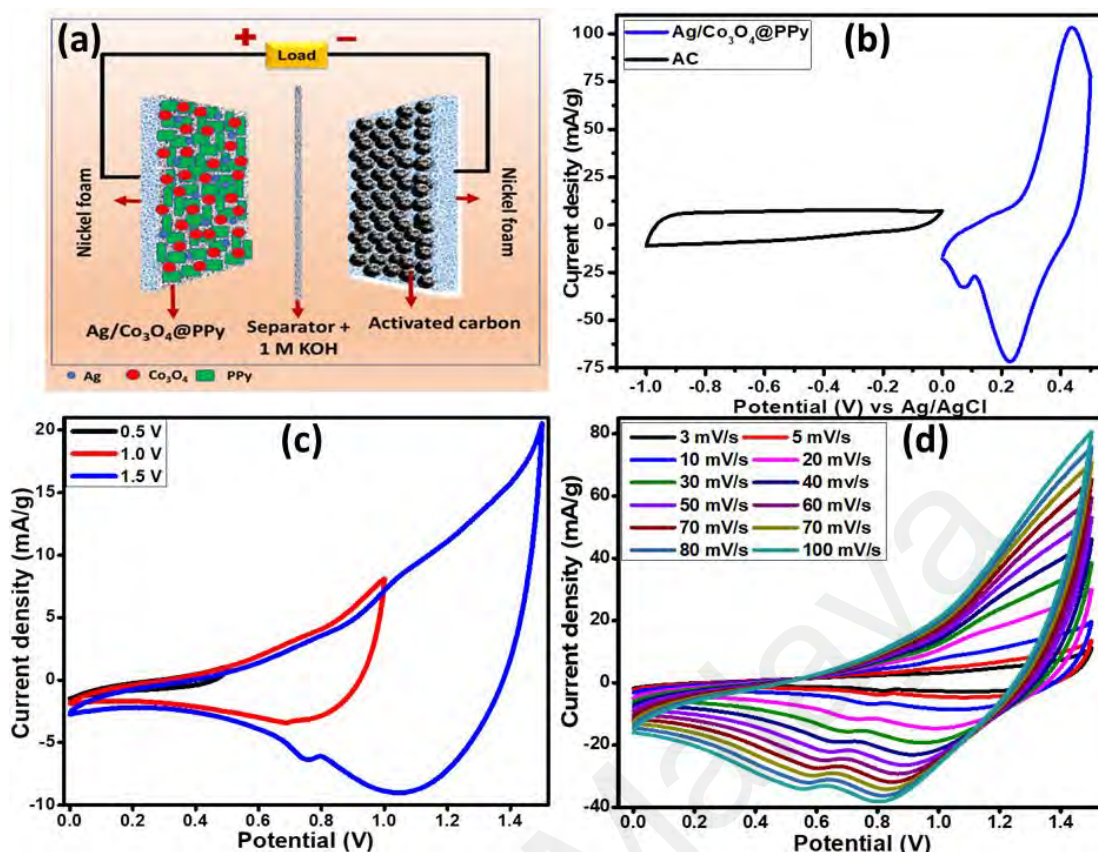


Figure 4.43: (a) Graphical presentation of the assembled supercapattery incorporating ternary nanocomposites, Ag/Co₃O₄@PPy as a positive material, (b) voltammograms of Ag/Co₃O₄@PPy and AC electrodes performed at a scanning rate of 10 mV s⁻¹ in a standard three electrodes cell system in 1 M KOH solution, (c) CV of assembled Ag/Co₃O₄@PPy//AC device assessed at diverse potential in 1 M KOH electrolyte and (d) CV curves of Ag/Co₃O₄@PPy//AC supercapattery at different scanning rates from 3 to 100 mV s⁻¹.

The GCD profiles of the devices under investigation are presented in Figure 4.44(a) at various current densities such as 0.7, 0.8, 0.9, 1.0, 1.5, 2.0, 2.5 and 3.0 A g⁻¹ at a constant potential of 1.5 V. The nonlinear GCD curves provide the evidence of the occurrence of redox reaction during the course of charge-discharge mechanism.

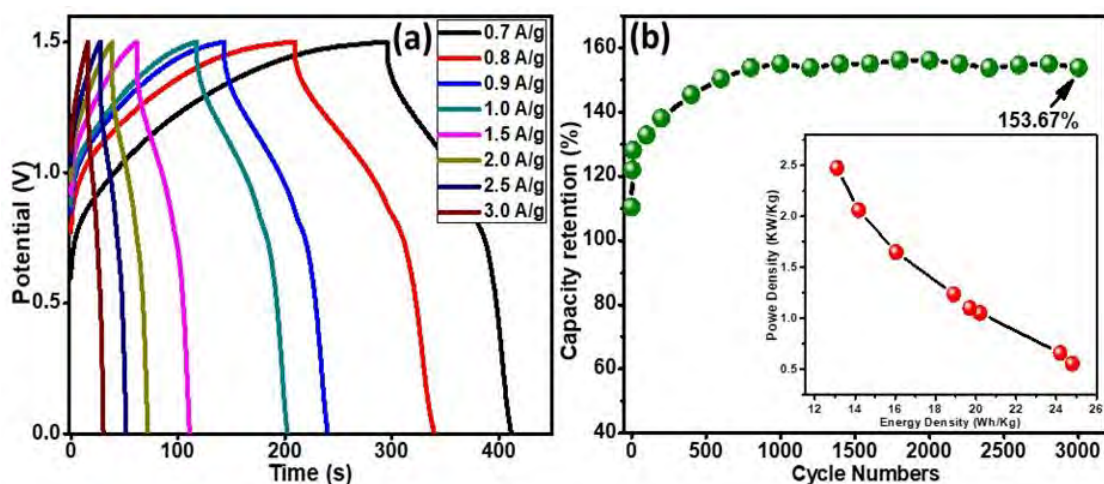


Figure 4.44 : (a) Galvanostatic charge-discharge curves of supercapattery devices using $\text{Ag}/\text{Co}_3\text{O}_4@\text{PPy}$, ternary nanocomposites as a positive electrode material at various current densities ranging from 0.7 to 3.0 A g^{-1} (b) Cyclic performance of the $\text{Ag}/\text{Co}_3\text{O}_4@\text{PPy}$ ternary nanocomposites electrode in an assembled device as a function of the number of cycles at a current density of 3.0 A g^{-1} in 1 M KOH . The inset Figure 4.44(b) shows the power density decay vs energy density of the assembled devices.

The fabricated supercapattery displayed a highly reversible EC behavior (Li et al., 2013). The specific capacity of the device was estimated using the equation (4.4).

The estimated specific capacity (Q_s) is 123.97 C g^{-1} at 0.7 A g^{-1} . However, it depleted down to 64.62 C g^{-1} when the current density was escalated to 3.0 A g^{-1} maintaining the capacity retention of 52.12% , thereby exhibiting the good rate performance.

The relation between energy density (E) and power density (P) is demonstrated by a Ragone plot and presented in inset Figure 4.44(b). The (E) and (P) were computed by exploiting the equations (4.5) and (4.6).

The assembled supercapattery achieved the maximum energy storage density of 24.79 Wh kg^{-1} with the corresponding power density of 554.40 W kg^{-1} at a current density of 0.7 A g^{-1} . The energy density decay was observed from 24.79 to 13.46 Wh kg^{-1} when the power density increased from 554.40 to $2475.00 \text{ W kg}^{-1}$, respectively with an increment in the current density from 0.7 to 3.0 A g^{-1} . These observed values are higher than the

recently reported systems in the literature (Niu et al., 2015; Peng et al., 2014; Shahabuddin et al., 2019).

Figure 4.44(b) shows the stability studies carried out in 1 M KOH over 3000 cycles. In the beginning, the specific capacity of the assembled device increases gradually up to 1000 charge-discharge cycles which may be ascribed to the gradual activation of the ternary nanocomposite resulting to the enhancement in the perforation of OH^- within the micropores of the active material (Omar et al., 2017). A complete activation of polymeric ternary nanocomposite takes about 1000 cycles, after that there is stability in the trend which might be due to the strong intercalation of the dopants in the polymer matrix that helped to maintain the capacity retention. Therefore, there is no noticeable decay in the capacity retention over the full-scale study stability of 3000 cycles and after 3000 cycles, 153.67 % capacity retention was observed. These results show the high stability of the PPy based ternary nanocomposites which makes them suitable to exploit in the fabrication of high performance energy storage device

4.8 System 5: Polyaniline (PANI) Incorporated with Silver Nanoparticles and Cobalt Oxide (Ag/Co₃O₄@PANI) Based Ternary Nanocomposite

4.8.1 Surface Morphology Study

Figure 4.45 shows the FESEM images of PANI, Co₃O₄@PANI and Ag/Co₃O₄@PANI nanocomposites. PANI (Figure 4.45(a)) shows fibrous morphology which might be due to its rapid mixing polymerization as explained by Ansari *et al* (Ansari et al., 2014). The binary Co₃O₄@PANI shows sticking of Co₃O₄ particles on PANI fibers as well as large number of Co₃O₄ particles can be seen in the vicinity or buried/trapped inside the interconnected PANI fibers. Similarly, in the ternary Ag/Co₃O₄@PANI, the Ag and Co₃O₄ nanoparticles can be seen sticking to the PANI fibers or buried/trapped inside the interconnected PANI fibers. It must also be mentioned that Ag due to its very small size is not distinctly visible and most of them are expected to be buried inside the matrix of PANI or Co₃O₄@PANI apart from the surficial visible Ag. The TEM image in Figure 4.46 also shows that PANI fibers are several micrometers in length with diameter < 100 nm and Co₃O₄ and Ag nanoparticles are well dispersed as well as aggregated at different regions.

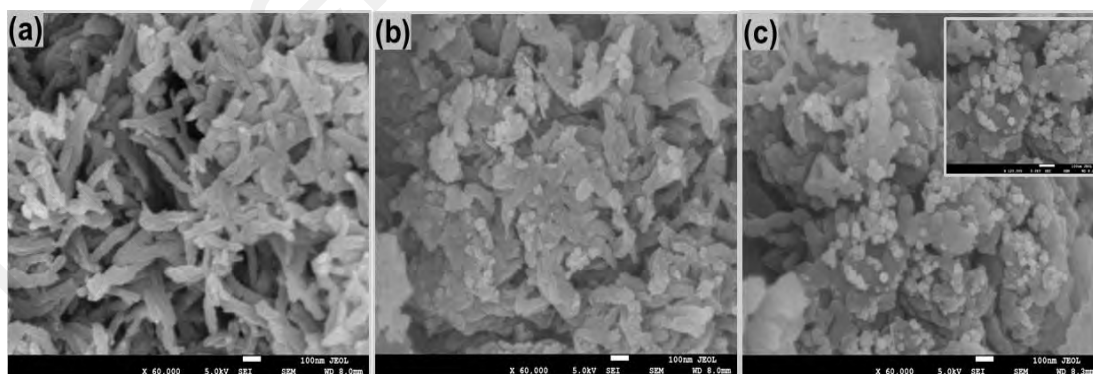


Figure 4.45: FESEM images of (a) PANI, (b) Co₃O₄@PANI binary nanocomposite, (c) Ag/Co₃O₄@PANI ternary nanocomposite and inset Figure 4.45(c) showing the high magnification image of Co₃O₄ and Ag NPs decorated on PANI matrix.

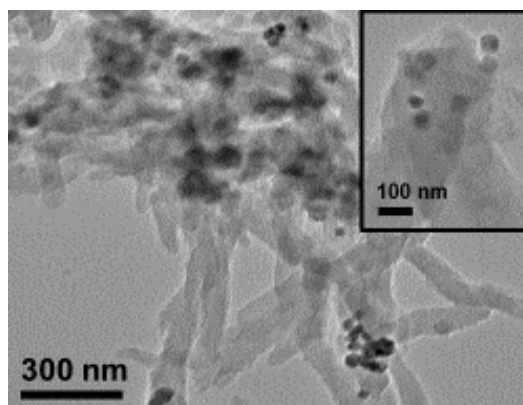


Figure 4.46: TEM images of ternary nanocomposite, Ag/Co₃O₄@PANI and inset image focused on the Co₃O₄ and Ag nanoparticles embedded in the PANI matrix.

The EDS of Ag/Co₃O₄@PANI shows the presence of C, N, O, Co and Ag while the elemental mapping (Figure 4.47) shows the uniform distribution of the respective elements, thereby suggesting the efficacy of the synthesis methodology.

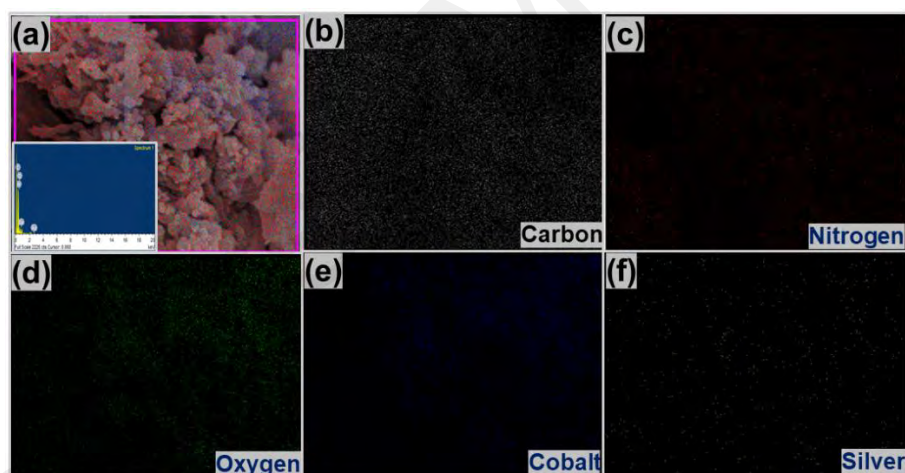


Figure 4.47: (a) EDS spectrum shows the elemental composition and verify the even distribution of both the Co₃O₄ and Ag NPs on the PANI matrix. EDS-elemental mapping is presented by (b) C, (c) N, (d) O, (e) C and (f) Ag contents of the Ag/Co₃O₄@PANI ternary nanocomposite.

4.8.2 X-ray diffraction Analysis

The structural characteristics and crystallinity of PANI, Co₃O₄, Co₃O₄@PANI and Ag/Co₃O₄@PANI nanocomposite were studied by XRD as depicted in Figure 4.48. The broad peaks in PANI show that it is highly amorphous in nature with the observance of

one distinct peak at 2θ angle of 19.50° ascribed to a periodicity parallel to the polymer chain and corresponding to the (010) plane (Mostafaei & Zolriasatein, 2012). In the case of $\text{Co}_3\text{O}_4@\text{PANI}$, the peaks of Co_3O_4 are also present, while the peaks of PANI is not very distinct which can be attributed to its low crystallinity as well as to its similar positioning near to (111) peak of Co_3O_4 . Similarly, in $\text{Ag}/\text{Co}_3\text{O}_4@\text{PANI}$, apart from PANI and Co_3O_4 , additional peaks of Ag at 38.26° , 44.60° , 64.36° and 77.33° 2θ corresponding to the (111), (200), (220) and (311) planes respectively are present (Manigandan et al., 2013). However, it should be mentioned that the peaks of Co_3O_4 and Ag after their incorporation in PANI are of much reduced intensity and original peaks of lower intensity are not distinctly visible in the nanocomposite, which might be due to the amorphous PANI which influences the degree of crystallization as mentioned in other reports (Ansari & Mohammad, 2011).

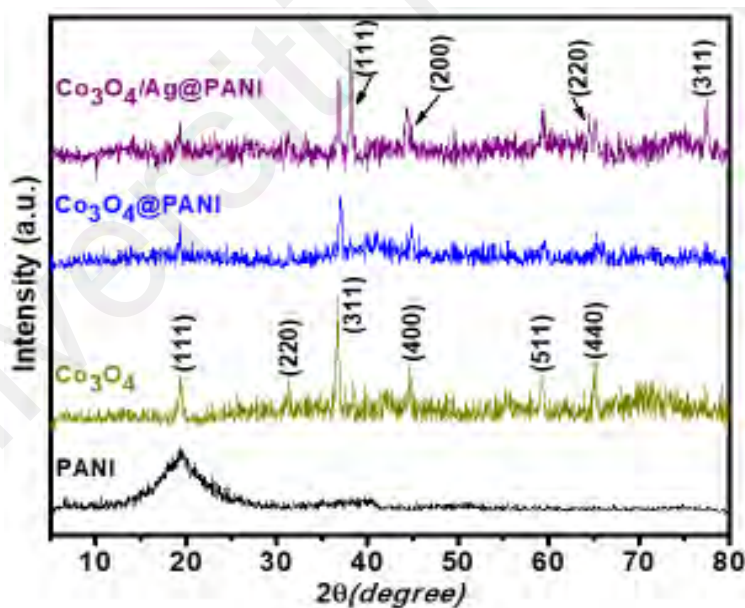


Figure 4.48: XRD pattern of PANI, Co_3O_4 , $\text{Co}_3\text{O}_4@\text{PANI}$ binary and $\text{Ag}/\text{Co}_3\text{O}_4@\text{PANI}$ ternary nanocomposite scanned in the 2θ range of 5° - 80° .

4.8.3 X-ray Photoelectron Spectroscopy (XPS) Analysis

The surface composition and chemical states of Ag/Co₃O₄@PANI nanocomposite was studied by XPS. The survey scan revealed the presence of C 1s, O 1s, N 1s, Co 2p_{3/2} and Ag 3d_{5/2} without any other impurities (Figure 4.49(a)). The carbon peak is due to the residual carbon from the sample and the instrument. The C 1s spectra (Figure 4.49(b)) can be deconvoluted into five peaks at 282.70, 283.62, 284.50, 285.74 and 288.17 eV corresponding to the C-H, C=C, C-C, C-O/C-NH and O-C=O respectively and can be attributed to the ring carbon, hydrogen and other functional groups of PANI. It might be interpreted that the functionalities such as π electrons, C-O/C-NH and O-C=O in PANI are the sites for interaction with Ag or Co₃O₄. The O 1s spectra (Figure 4.49(c)) can be split into three peaks at 529.69, 531.35 and 532.78 eV which is due to the Co-O, hydroxide group and structural water, respectively (Babar et al., 2018). The broad N 1s spectra (Figure 4.49(d)) from 394.00 to 402.00 eV correspond to the quinonoid, benzenoid, protonated benzenoid, and protonated quinonoid of PANI, thereby suggesting that PANI is conductive (Kowalski et al., 2014). The Co 2p spectrum (Figure 4.49(e)) consists of peaks at 780.00 and 796.39 eV corresponding to the Co²⁺ and octahedral Co³⁺. The weak satellite peak at 786.00 eV *i.e.* between 2p_{3/2} and 2p_{1/2} transitions indicates that Co(II) and Co(III) co-exist in the sample which also confirms the presence of Co₃O₄ in the sample (Younis et al., 2013). The Ag 3d (Figure 4.49(f)) shows two deconvoluted peaks at 368.34 and 374.34 eV corresponding to the Ag 3d_{5/2} and Ag 3d_{3/2} respectively. The difference of 6.00 eV between the binding energies is the characteristics of Ag which also confirms the successful reduction of its salt under hydrothermal conditions (Ansari et al., 2014).

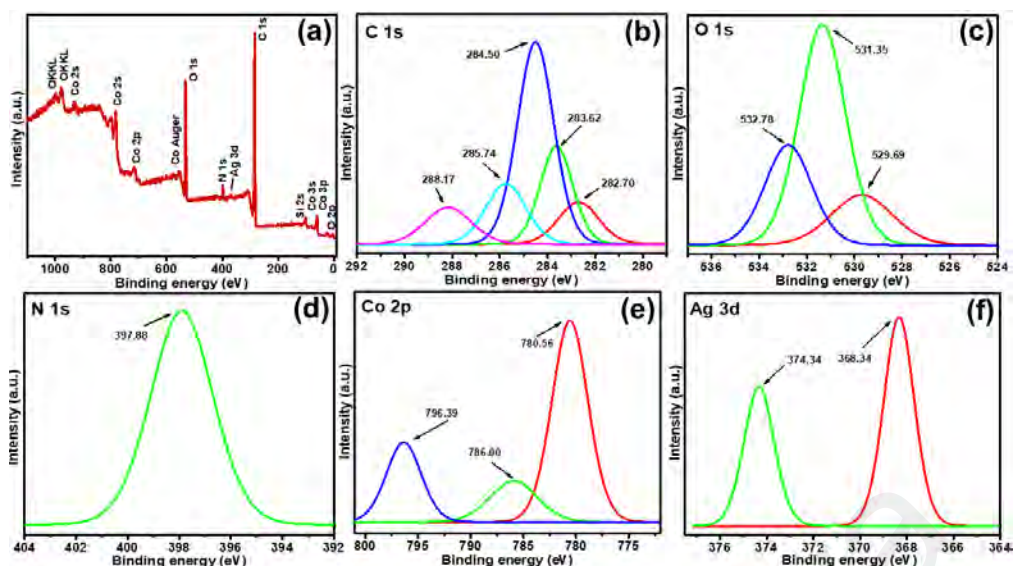


Figure 4.49: (a) XPS survey scan spectra of ternary nanocomposite, Ag/Co₃O₄@PANI. The representation of high resolution spectra of C 1s (b), O 1s (c), N 1s (d), Co 2p_{3/2} (e) and (f) Ag 3d.

4.8.4 Electrochemical Analysis of Polyaniline Incorporated with Silver Nanoparticles and Cobalt Oxide Nanograins Based Ternary Nanocomposite

(a) Cyclic Voltammetry (CV) Analysis

The cyclic voltammetry (CV) was carried out to analyze the voltammetric character of the prepared Ag/Co₃O₄@PANI ternary nanocomposite and their counter parts (PANI, Co₃O₄@PANI) through a typical three electrode cell system at normal temperatures and applied voltages ranging from 0 to 0.5 V vs Ag/AgCl reference electrode in 1 M KOH electrolyte. The electrode materials were scanned at 3, 5, 10, 20, 30, 40 and 50 mV s⁻¹. The first CV scans were performed on PANI, the obtained voltammograms are shown in Figure 4.50(a) with well demarcated set of oxidation and reduction peaks with a direct relation of current density with the scan rate. The direct relationship of current density and the scan rate is a clear explanation of a standard electrochemical characteristic property of the PANI (Genies et al., 1988; Obaid et al., 2014; Zhu et al., 2013). A slow diffusion of OH⁻ ions to PANI could be evidenced by a little shift of cathodic and anodic

extremes at each increased value of sweep rate. The OH^- ions can enter the internal structure of the PANI at a slower sweep but as the sweep rate is faster, the OH^- ions seem to interact only with the outer pores attributed to the peak shifts. The maximum current density reached a value of 60 mA g^{-1} at maximum sweep rate of 50 mV s^{-1} . Whereas, Figure 4.50(b) shows the result of second sample scan with prominent increase in the current density from 80 to 120 mA g^{-1} at 50 mV s^{-1} for the obtained voltammograms for $\text{Co}_3\text{O}_4@\text{PANI}$ binary nanocomposite with clearly separated oxidation and reduction peaks confirming its pseudocapacitive character with an evidence of a reversible faradaic reaction which is distinct from the electric double layer capacitance (Cheng et al., 2017; Lee et al., 2017; Ren et al., 2018). Also, the increased current density is observed which is obliged to the Co_3O_4 component of the prepared binary composite (Padwal et al., 2016). The increase in the current density is attributed to the enhanced integral area of $\text{Co}_3\text{O}_4@\text{PANI}$ than the pure PANI which supports the increased capacitance because of the combined influence of Co_3O_4 with PANI. The Co_3O_4 nanograins along with the porous structure of PANI form a smooth path along which the electron transportation is enhanced through each grain of Co_3O_4 . Moreover, polymerized nature of the PANI further helps in the electric conductivity enhancement of Co_3O_4 and hence an improved faradaic behavior is observed (Wang et al., 2015). The increased currents densities are observed with increased scan rate but the CV character remains unchanged which is a clear evidence of pseudocapacitive behavior suitable to serve as an electrode material for energy storage systems (Lu et al., 2012). The third CV scans were performed on the most envisaged $\text{Ag}/\text{Co}_3\text{O}_4@\text{PANI}$, ternary nanocomposite with a remarkably high current density (177 mA g^{-1} at scan rate of 50 mV s^{-1}) as shown in Figure 4.50(c), compare to pure PANI and $\text{Co}_3\text{O}_4@\text{PANI}$ binary nanocomposite upholding the same CV character without any distortion in its cathodic and anodic pattern which is again a clear demonstration of the pseudocapacitive character with faradaic reversibility. A noble

metal (Ag) and cobalt oxide both possess the highest thermal and electrical conductivity belong to the group of transition metals. When the both are added in PANI, the effect was clearly enhanced for Ag/Co₃O₄@PANI ternary nanocomposite. The high value of achieved current density was credited to the decorated Ag NPs in the prepared ternary nanocomposite due to the additional effect which provides transfer channels for electrons. Figure 4.50(d) demonstrates comparison CVs at scan rate of 3 mV s⁻¹ to distinctly show the increasing trend of current density in all three electrode materials *i.e.* PANI, Co₃O₄/PANI and Ag/Co₃O₄@PANI.

The specific capacity, Q_s of electrode materials were evaluated through the equation (4.3). The Q_s values at scan rate of 3 mV s⁻¹ were obtained which are 77.97 C g⁻¹ for PANI, 207.00 C g⁻¹ for Co₃O₄@PANI and 262.62 C g⁻¹ for Ag/Co₃O₄@PANI.

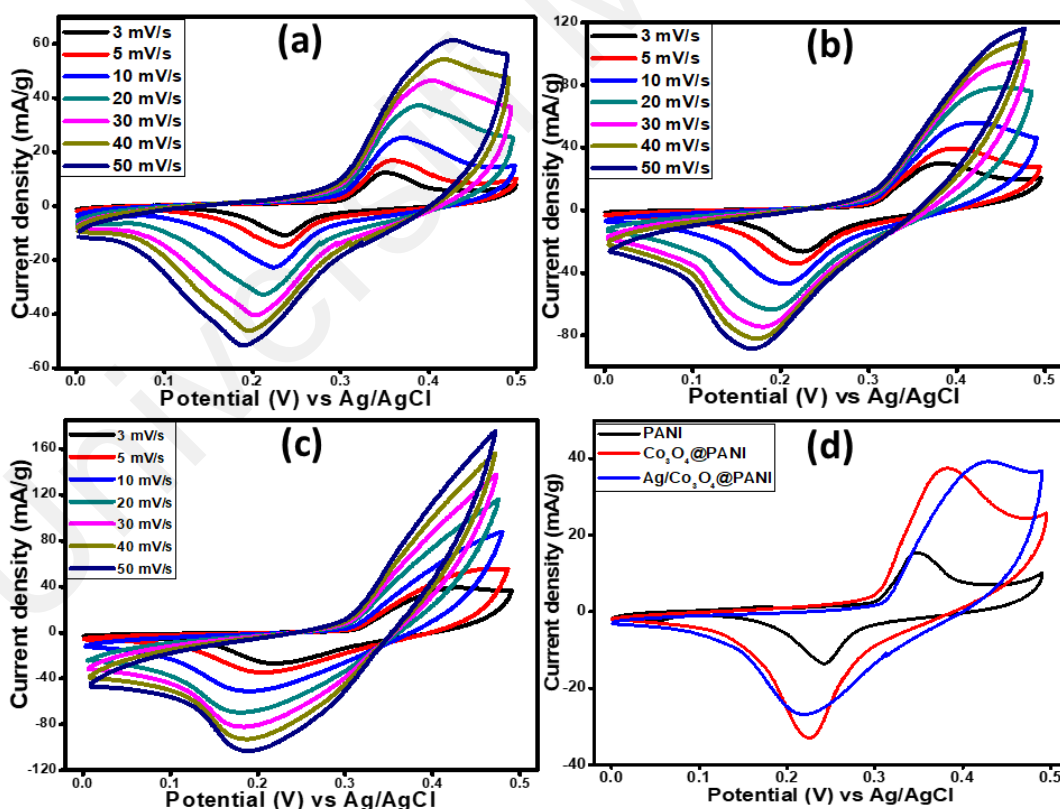


Figure 4.50: CV curves of (a) PANI, (b) Co₃O₄@PANI binary and (c) Ag/Co₃O₄@PANI ternary nanocomposite measured at varied scan rates and (d) CV curves to compare electrochemical performance of PANI, Co₃O₄@PANI binary and Ag/Co₃O₄@PANI ternary nanocomposite recorded at a scan rate of 3 mV s⁻¹.

(b) **Galvanostatic Charge-discharge (GCD) Analysis**

To testify the charge-discharge performance, the GCD behavior was studied at various current densities for all three electrode materials (PANI, $\text{Co}_3\text{O}_4/\text{PANI}$ and $\text{Ag}/\text{Co}_3\text{O}_4@\text{PANI}$) individually as is shown in Figure 4.51(a-c) and also their comparison is presented at current density of 1.5 A g^{-1} in Figure 4.51(d). The ternary nanocomposite $\text{Ag}/\text{Co}_3\text{O}_4@\text{PANI}$ was observed to be the best in terms of longer discharge time among the other two which is clearly demonstrated in Figure 4.51(d) owing to the synergistic effect of Ag NPs along with the deaggregated Co_3O_4 nanograins successfully intercalated in the polymer matrix. The values of specific capacity, Q_s were obtained through the GCD curves for all three samples under investigation using equation (4.4). The calculated Q_s values at a current density of 1.5 A g^{-1} are 95.76, 187.40 and 289.34 C g^{-1} and at a current density of 4.5 A g^{-1} are 54.50, 87.12 and 179.15 C g^{-1} for PANI, $\text{Co}_3\text{O}_4@\text{PANI}$ and $\text{Ag}/\text{Co}_3\text{O}_4@\text{PANI}$, respectively. From the study of all Q_s values obtained at the lowest and the highest current densities for all prepared samples, it is easy to reach a conclusion that the ternary nanocomposites are the best performance electrode material that drives a strong evidence to use it in EC energy storage systems.

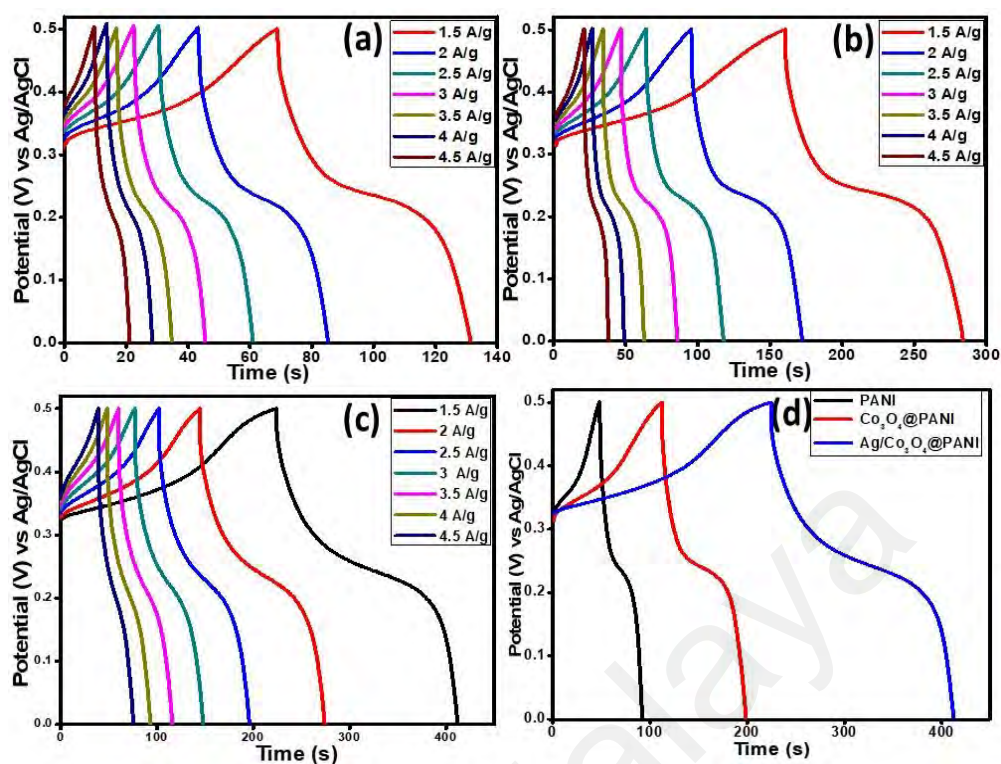


Figure 4.51: GCD curves at various current densities, (a) PANI, (b) $\text{Co}_3\text{O}_4/\text{PANI}$, (c) $\text{Ag}/\text{Co}_3\text{O}_4/\text{PANI}$ and (d) comparison of GCD curves for all three variants at current density of 1.5 A g^{-1} .

The obtained specific capacities were plotted against the current densities and the graph obtained is shown in Figure 4.52 for all three materials. The trends in each of three cases is clearly seen to be similar but the ternary nanocomposite shows higher specific capacity at lower current density which decreases gradually with the increase in current density. This behavior points to the fact that the OH^- ions transit partially at the electrodes at higher current density. Since, the enhanced value of specific capacity is observed in the case of binary and ternary nanocomposites compared to pure PANI attributing the more conducting effects of Co_3O_4 when intercalated with PANI that helps in reducing the agglomeration effects of Co_3O_4 thereby resulting the increased electroactive sites which facilitates the charge transportation through the polymer matrix. The decoration with Ag NPs further added synergistic effect in the form of prepared $\text{Ag}/\text{Co}_3\text{O}_4/\text{PANI}$ nanocomposite making it the best among the three materials with an outstanding execution of EC feature.

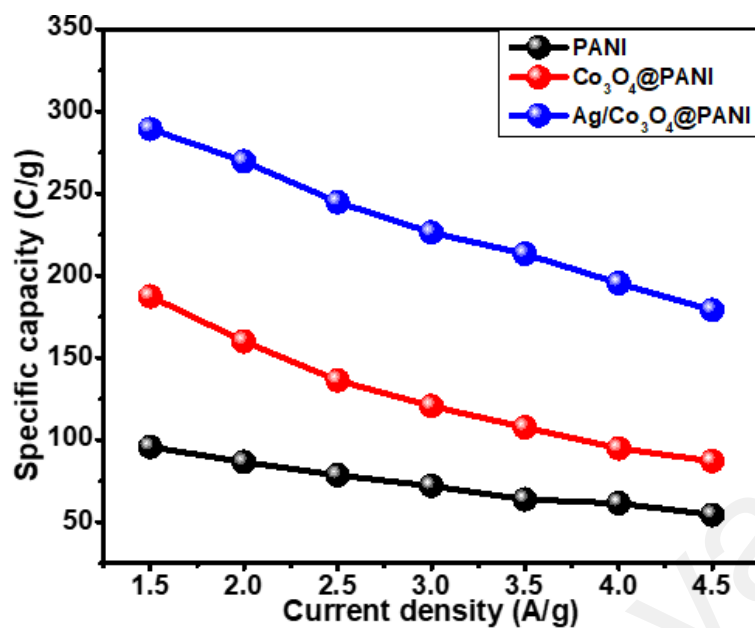


Figure 4.52: Specific capacity versus current density plot of PANI, Co₃O₄@PANI and Ag/Co₃O₄@PANI nanocomposites.

(c) *Electrochemical Impedance Spectroscopy (EIS) Analysis*

Figure 4.53 shows the Nyquist plot for the performed EIS study to testify the phenomena occurred on the electrode surface in each of the three materials at an AC voltage of 10 mV (R.M.S) at the frequency range of 0.01 to 100 KHz. The plots of each of the three active materials show the straight lines at low frequencies and the semicircles at high frequencies. The Faradaic behavior is determined from the obtained semicircles which depends upon the resistance in the transformation of the charges at the interface of electrode and the electrolyte. The obtained straight line at low frequencies and the low ESR value can be attributed to incorporate Co₃O₄ in PANI that might have provided an enhancement of electrochemical character of the binary nanocomposite. The performed EIS study provides an insight about the prepared ternary nanocomposite, Ag/Co₃O₄@PANI, to be the best when compared to other active electrode materials because of the combined effect of Ag and Co₃O₄ with PANI in the form of ternary

nanocomposite. The inset shown in Figure 4.53, represents the high frequency region of the Nyquist plot to demonstrate the visibility of the semicircles traced by the samples under EIS studies, showing that the ternary nanocomposite displays the shortest semicircle compared to other electrode materials and at low frequencies with a most vertical line parallel to the imaginary axis. This confirms the performance of Ag/Co₃O₄@PANI with the highest capacity of charge storage and least resistance against the charge transfer because of the possible intercalation of Ag NPs and Co₃O₄ nanograins in PANI with more penetrated permeability of electrolyte ions and hence improved kinetics of charge transfer making it an excellent candidate for electrochemical energy storage system.

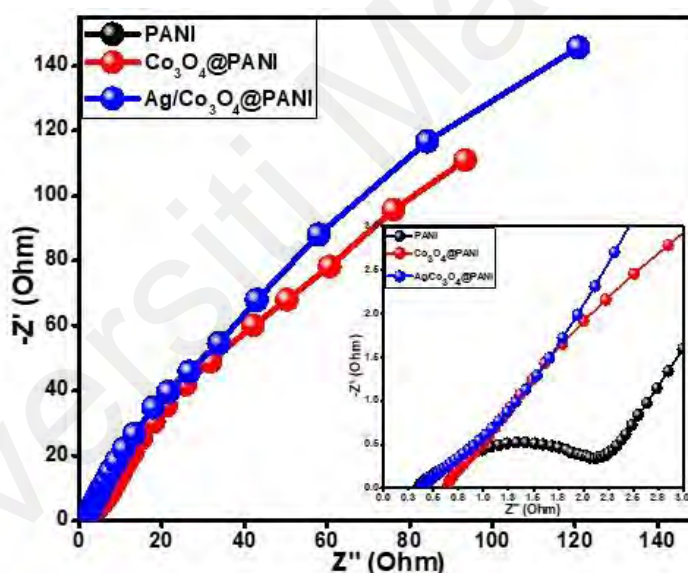


Figure 4.53: Nyquist plot of pure PANI, Co₃O₄@PANI, and Ag/Co₃O₄@PANI nanocomposites. Inset Figure shows the enlarged high frequency region.

4.8.5 Electrochemical Performance of Assembled Ag/Co₃O₄@PANI//AC Supercapattery

Two electrodes are usually assembled (negative and positive electrodes composed of capacitive and battery grade material respectively) to construct supercapattery (a compounded influence of a supercapacitor and a battery in single device), to be benefitted

from two different systems in a single device. A supercapattery was devised by taking Ag/Co₃O₄@PANI as positive and AC as negative electrode as shown by a graphical scheme in Figure 4.54(a). The higher potential window limits of the active materials (Ag/Co₃O₄@PANI) and activated carbon (AC) were determined independently by a three electrodes system. The CVs for each of the active and AC materials were run to assure the EC signature individually which is presented in Figure 4.54(b). The potential windows (-1.0-0 and 0-0.5 V) for AC and the battery grade material are also shown in Figure 4.54(b). The possible stable potential window obtained was 1.5 V through the collective combination of AC and battery grade material (Ag/Co₃O₄@PANI). The fabricated supercapattery (Ag/Co₃O₄@PANI//AC) in which Ag/Co₃O₄@PANI serves as a positive electrode material and AC as a negative electrode material was then tested for EC character in 1 M KOH electrolyte in a two electrodes setup at room temperature. The CV scans were performed in various potential windows from 0 to 0.5 V to a maximum of 0 to 1.5 V in five sets of experiments to confirm the stable working potential of the assembled device, shown in Figure 4.54(c). The performed CV studies are shown in Figure 4.54(d) at a range of sweep scan rates between 3 and 200 mV s⁻¹ in a potential window of 0-1.5 V. The obtained voltammograms show no distortion in the typical anodic and cathodic peak patterns, rather showed the enhanced current density as the sweep rates were increased which proved that it follows the EC characteristics.

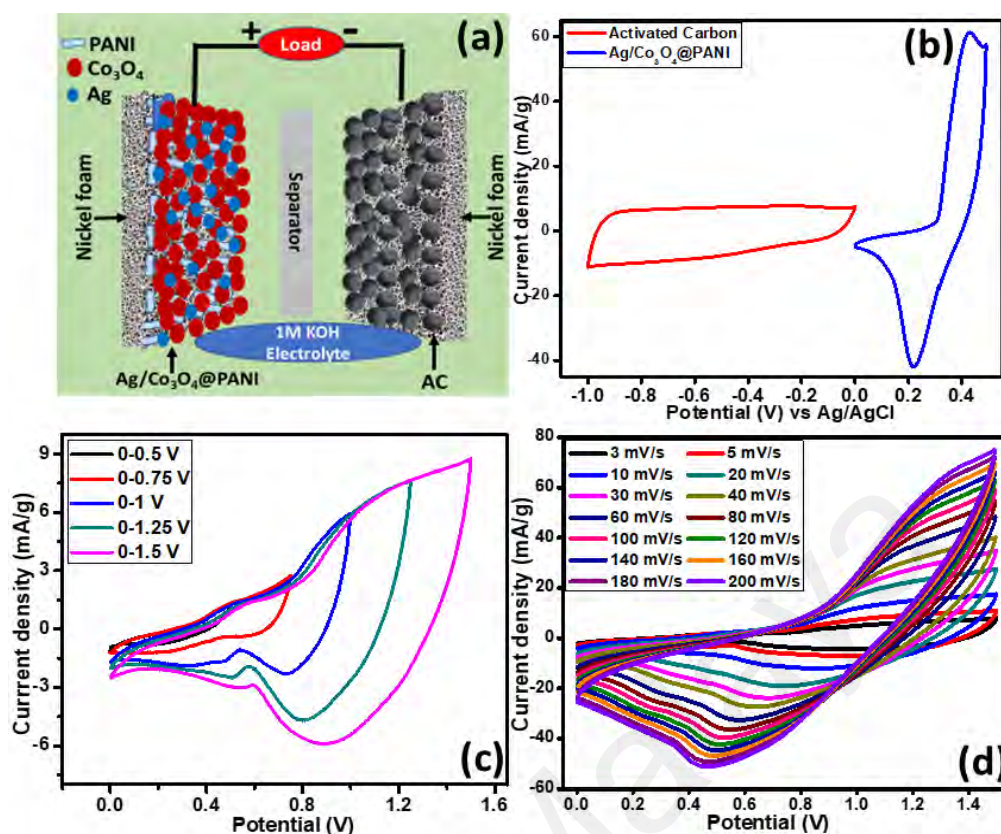


Figure 4.54: (a) Graphical presentation of the assembled supercapattery incorporating ternary nanocomposites, Ag/Co₃O₄@PANI as a positive electrode material and AC as a negative electrode material, (b) CVs of Ag/Co₃O₄@PANI and AC at a scanning rate of 3 mV s⁻¹ in a standard three electrodes cell system in 1 M KOH, (c) CV scans of two electrodes assembled device at different potential windows and (d) CV curves of Ag/Co₃O₄@PANI//AC supercapattery at different scanning rates from 3 to 200 mV s⁻¹ in 1 M KOH electrolyte in two electrodes cell system.

The GCD studies were performed at various potentials from 0.5 to 1.5 V for the fabricated supercapattery device at current density 0.2 A g⁻¹ as shown in Figure 5.55(a). Also, the charge-discharge studies were carried out at a set of different current densities comprise the values between 0.2 to 2.0 A g⁻¹, shown in Figure 4.55 (b). The obtained curves were nonlinear in behavior which clearly point out the existence of faradaic character of the device while following the charging and discharging mechanism.

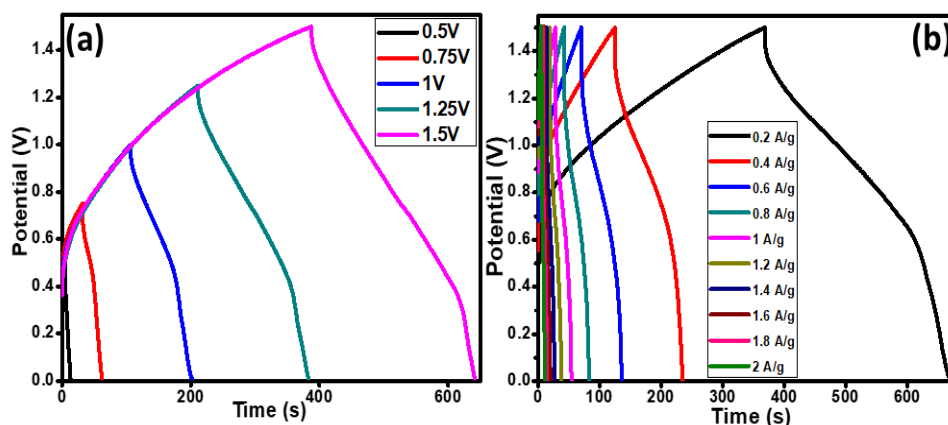


Figure 4.55: (a) Charge-discharge plots of the assembled device, Ag/Co₃O₄@PANI//AC supercapattery at different potentials at current density 0.2 A g⁻¹ and (b) charge-discharge plots at various current densities ranging from 0.2 to 2.0 A g⁻¹ at potential 1.5 V.

Ragone plot is presented to demonstrate the trend of power density (P) and energy density (E) as indicated in Figure 4.56 (a). The E and P evaluated using the equations (4.5) and (4.6), respectively.

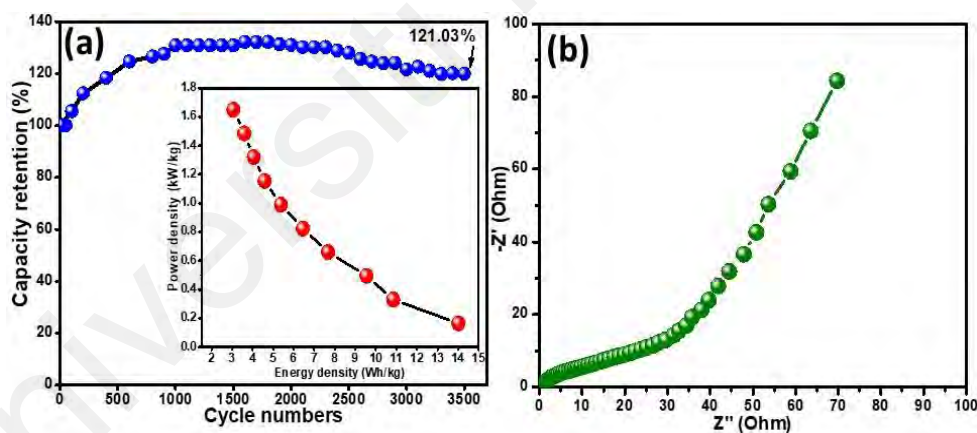


Figure 4.56 : (a) cycling stability studies of Ag/Co₃O₄@PANI//AC supercapattery. Inset Figure 4.56(a) shows the energy density versus power density studies relations and (b) Nyquist plot of the assembled device.

The maximum energy storage density and power density at a current density of 0.2 Ag⁻¹ was 14.01 Wh kg⁻¹ and 165.00 W kg⁻¹, respectively. The energy density trend was found to be in inversely proportion to the power density and a decrease in current density was observed from 14.01 to 3.06 Wh kg⁻¹ with the corresponding power density increase from 165.00 to 1650.00 W kg⁻¹ as shown in the inset Figure 4.56(a). These parametric

values assured the superior performance of the supercapattery assembled with the ternary nanocomposite, Ag/Co₃O₄@PANI as an efficient electrode material.

In order to prove the viability of the electrode materials, especially in case of conducting polymers, famous for the biggest drawback of their stability issue which kept them away for their utilization in EC energy storage applications because their shrinkage and swelling character during charge and discharge mechanism depleted their conductivity by effecting the backbone of the polymer chain. Therefore, the stability performance was monitored of the assembled device by running over 3500 charge

discharge cycles in 1 M KOH electrolyte as shown in Figure 4.56(a). It can be seen that there is a gradual increase in the cyclic performance until ~ 1000 cycles due to gradual activation of the ternary nanocomposites and remain almost stable until 2500 cycles and then start decreasing thereby showing the cyclic stability of 121.03 % to its initial value after 3500 cycles.

The Nyquist plot of the fabricated supercapattery was also obtained with a straight line at lower frequencies and a semicircle with a shortest radius in the higher frequency region which is attributed to least resistance to the charge transfer in the electrode/electrolyte interface as shown in Figure 4.56(b), which is also a strong evidence of the superior performance of the utilized active electrode material in device fabrication.

The assembled device performance where ternary nanocomposite (Ag/Co₃O₄@PANI) has been utilized as a positive electrode material in terms of energy density, power density and cyclic stability demonstrated good results which foregrounds it as a promising electrode material for energy storage systems (supercapattery).

4.9 Comparison of the Developed Systems

The carbonaceous based systems Ag/Co₃O₄@MWCNTs, Au/Co₃O₄@MWCNTs and Ag/Co₃O₄@rGO produced excellent results toward the application of supercapattery. The results obtained for all systems under investigation are presented in the Table 4.1. It can be noticed that in the comparison table, the MWCNTs based ternary nanocomposites, i.e., Ag/Co₃O₄@MWCNTs and Au/Co₃O₄@MWCNTs where silver and gold were utilized in the nanocomposites showed minor variations in the evaluation parameters such as specific capacity, power density, energy density, and capacity retention for supercapattery. On comparing MWCNTs and rGO based ternary nanocomposites, the rGO containing ternary nanocomposite (Ag/Co₃O₄@rGO) showed better performance in terms of specific capacity, energy density as well as power density. Thus, it can be concluded that rGO based ternary nanocomposite can provide stored energy over a longer period of time to the load than MWCNTs based ternary nanocomposites with a minor compromise on the cyclic life (~ 6 %).

Both graphene and MWCNTs have exceptional mechanical and electronic properties, and thus are widely utilized for host of similar applications. Despite these similarities, there are still differences between them as graphene is considered 2D while MWCNTs is regarded 1D. Also, defect less graphene, when ideally structured with perfect honeycomb lattice is a zero-band-gap semiconductor, whereas MWCNTs show either metallic or semiconducting properties and their different diameters, lengths, and functional group content can greatly affect the electrical properties. The $2s$, $2p_x$ and $2p_y$ orbitals from each carbon atom in the graphene lattice hybridize into three sp^2 orbitals, each developing a σ bond with an adjacent carbon atom. The remaining un-hybridized p_z orbitals which are perpendicular to the graphene lattice, form a conjugated π bond network in which the delocalized electrons are responsible for the electronic properties of graphene. The

transport velocity of graphene is only three hundred times lower than the speed of light and thus it possesses extraordinary high charge carrier mobility (Katsnelson, 2007; Wang et al., 2013). Breaking the honeycomb lattice, for example by creating edges, alters the conductivity of graphene and, depending on the crystallographic orientation of the lattice, zig-zag and armchair edges are observed, each characterized by specific chemical reactivity and electronic properties. The chemical reactivity of the carbon atoms localized on a graphene edge differs from the relative inertness of the basal plane (Liu et al., 2016). Broken σ bonds at the edges develop radical groups with accessible and highly active electrons. The conjugation system is different on a zig-zag edge compared to an armchair edge, yielding significant discrepancies in reactivity (Kim et al., 2015). Local defects in the graphene lattice such as dislocations or imperfections can also be considered as edges as they define a termination of the conjugated honeycomb network (Zhang & Huang, 2017). The presence of edges and defects in graphene promote new possibilities to tailor its chemistry with additional implications on the physical and electrical properties. Due to these facts, rGO based ternary nanocomposites produced better results than the MWCNTs based ternary nanocomposites.

The CPs based systems, $\text{Ag}/\text{Co}_3\text{O}_4@\text{PPy}$ and $\text{Ag}/\text{Co}_3\text{O}_4@\text{PANI}$ performed well as ternary nanocomposites when utilized as an electrode material for supercapattery development. However, PPy based ternary nanocomposite produced better results compared to PANI based ternary nanocomposite. It is clear from the comparison table (Table 4.1) that the energy density, power density and cyclic stability of PPy, based ternary nanocomposite are higher than PANI based ternary nanocomposite. The strong intercalation of nanoparticles with PPy which is evidenced by the high capacity retention and its favorable morphology may helped to produce better performance. Similar trend has also been reported in other research articles (Liu et al., 2012; Mahore et al., 2015).

Overall, among the five systems, PPy based ternary nanocomposite takes the privilege of superior performance when utilized in the development of supercapattery as an electrode material.

The conducting polymers are known for their excellent electrical conductivity. They possess alternating single σ and double π bonds, and these π -conjugated systems lend the CPs their inherent optical, electrochemical, and electrical/electronic properties. The most effect on the physical properties of CPs are their conjugation length, degree of crystallinity and intra- and inter-chain interactions. On coating CPs with metal oxides produce improved electrochemical performance and maintain good cycling stability (Jabeen et al., 2016). The performance of the nanocomposites for energy storage system depends on number of factors, such as deagglomeration of nanoparticles, morphology, surface area, charge transfer resistance and selection of the electrolyte used. All these factors greatly influence the performance of the energy storage systems. The PPy based ternary nanocomposite show better results than other systems which may be due the better incorporation and better distribution of the metal and metal oxide nanoparticles on the PPy surface, resulting in uniform morphology with high degree of exposed active sites of nanoparticles and porosity which help the fast insertion and de-insertion of the electrolyte ions into material. Consequently, low charge transfer resistance ensures more facile ion transport which ultimately enhances the Faradic reaction and hence improves the capacitance performance of the system. It is evident from the following Table 4.1 that the specific capacity value of PPy based ternary nanocomposite is the highest (123.97 C g^{-1}) among all other systems, providing the evidence of its better capacitive behavior.

Table 4.1: Comparison of specific capacity, power density, energy density and capacity retention of all five ternary nanocomposites based systems.

Systems	Q_s (C g ⁻¹)	P (W kg ⁻¹)	E (Wh kg ⁻¹)	Capacity Retention (%)
1- Ag/Co ₃ O ₄ @MWCNTs	85.00	297.50	16.50	93.10
2- Au/Co ₃ O ₄ @MWCNTs	81.00	302.00	18.80	91.90
3- Ag/Co ₃ O ₄ @rGO	115.80	440.00	23.63	85.50
4- Ag/Co ₃ O ₄ @PPy	123.97	554.40	24.79	153.67
5- Ag/Co ₃ O ₄ @PANI	67.27	165.00	14.01	121.03

CHAPTER 5: CONCLUSION

5.1 Conclusion

The practicality and performance of supercapattery electrodes hinges on the engineering of high performance novel materials which should be cost effective without sacrificing the electrochemical performance and secondly to develop them by a feasible fabrication method to be able to synthesize homogeneous electrode materials while keeping the effective interactions at nano level. The recent evolution in the area of nanotechnology offered the methodologies which are helpful to enhance the performance by many folds of the energy storage devices by exploiting the nanoscale electrode materials prepared by altering various synthesis parameters and composition of constituent elements to develop novel nanomaterials. The aim of this thesis research is to develop the range of ternary nanocomposite electrode materials by a facile, hydrothermal method which could ultimately enhance the performance of the supercapattery.

The outcomes of all five systems presented in this thesis demonstrate the effect of different conducting platforms used in order to deaggregate the metal oxide nanoparticles because the efficiency of electrode materials largely depends on the available active sites of the material. The synergistic effect in the electrochemical signature could be introduced by decorating the nanocomposites with noble metals which are highly conductive due to their narrow band gap. Five systems of cobalt oxide and noble metals were developed using different conductive matrices such as MWCNTs, rGO, PPy and PANI, and characterized their morphologies and structures using FESEM, TEM, EDS, XRD and XPS. Electrochemical characterization was performed using CV, GCD and EIS and performance parameters of the assembled devices were studied in terms of specific capacity, energy density and power density.

In system 1, ternary nanocomposite, Ag/Co₃O₄@MWCNTs was prepared by a single step hydrothermal process which was characterized by several analytical techniques to confirm the successful formation and uniform distribution of Co₃O₄ nanograins and Ag nanoparticles onto the MWCNTs matrix. Electrochemical studies revealed that the performance of ternary nanocomposite is superior compared to the pristine Co₃O₄ nanograins and Co₃O₄@MWCNTs nanocomposite in terms of the specific capacity. This improvement is particularly due to the conducting platform provided by MWCNTs and synergic effect of noble metal nanoparticles (Ag) in the ternary nanocomposite. Furthermore, the assembled supercapattery, Ag/Co₃O₄@MWCNTs//AC achieved high energy density, 16.50 Wh kg⁻¹ at a power density of 297.50 W kg⁻¹ which was ascribed due to the combination of Ag/Co₃O₄@MWCNTs with AC. The cycling stability evaluation of the device showed the superior long term stability with capacity retention of 93.10 % of the initial value even after 3000 cycles.

In system 2, a supercapattery based on novel Au/Co₃O₄@MWCNTs ternary nanocomposite as a positive electrode and AC as a negative electrode, has been assembled in 1 M KOH electrolyte. The as prepared nanocomposite of Co₃O₄ and Au NPs decorated on MWCNTs to form ternary nanocomposite potentially possessed enhanced electroactive sites and conductivity due to the disaggregation of Co₃O₄ NPs and highly conductive Au NPs. The ternary nanocomposite was cycled reversibly in a stable potential region of 0-1.5 V that demonstrated the enhanced energy density of 18.80 Wh kg⁻¹ and corresponding power density of 302.00 W kg⁻¹ at a current density of 0.4 A g⁻¹. More importantly, the ternary nanocomposite prevents the degradation of the resultant electrode during cyclic lifetime, resulting in a promising cyclic life with a retention value of 91.90 % even after 3500 reversible cycles. Therefore, the newly synthesized Au/Co₃O₄@MWCNTs ternary nanocomposite in the present study can be regarded as a

promising candidate for its exploitation in high performing energy storage devices possessing high energy density, longer cyclic life, and excellent rate capability.

In system 3, a simple one-step hydrothermal process was followed for the synthesis of Ag/Co₃O₄@rGO, Co₃O₄@rGO and Co₃O₄ for electrochemical storage application. The nanograins (Co₃O₄) were grown on the rGO framework decorated with silver nanoparticles showed the superior electrochemical performance when tested by CV, GCD, and EIS techniques compared to the other samples (Co₃O₄@rGO and Co₃O₄). The superior performance is due to the reduced aggregations of nanograins and decoration of silver nanoparticles which ultimately increase the active sites of the ternary nanocomposite. The assembled supercapattery (Ag/Co₃O₄@rGO//AC) demonstrated a high energy density, 23.63 Wh kg⁻¹ at a power density of 440.00 W kg⁻¹ which was described due to the combination of Ag/Co₃O₄@rGO with AC. Moreover, it showed the high specific capacity (115.80 Cg⁻¹) at 0.6 Ag⁻¹, fantabulous reversibility with a cycling efficiency of ~ 85.50 % after 3000 cycles in an alkaline media (1 M KOH) foreground the efficacy of the utilized synthesis protocol. The as synthesized ternary nanocomposite may act as a replacement electrode material for applications in supercapattery and could open the door for the development of superior performance electrochemical storage devices.

In system 4, the ternary nanocomposite, Ag/Co₃O₄@PPy and binary nanocomposite, Co₃O₄@PPy were prepared with low cost hydrothermal method while PPy was synthesized by oxidative polymerization of pyrrole monomer in the presence of FeCl₃ as an oxidizing agent. The prepared electrode materials were characterized with various analytical techniques. The prepared materials were tested electrochemically through cyclic voltammetry, galvanostatic charge-discharge and electrochemical impedance spectroscopy and produced well defined redox behavior. The ternary nanocomposite in

three electrodes cell demonstrated the highest specific capacity (355.64 C g^{-1}) compared to binary nanocomposite (280.68 C g^{-1}) and pure PPy (143.28 C g^{-1}) which is due to the successful incorporation of Co_3O_4 nanograins into the PPy and the additional effect of silver nanoparticles that promoted the effective charge transport mechanism through the polymer matrix. The assembled device ($\text{Ag}/\text{Co}_3\text{O}_4@\text{PPy}/\text{AC}$) consisting of ternary nanocomposite as a positive and activated carbon as negative electrode delivered high energy density of 24.79 Wh kg^{-1} at a high power density of 554.40 W kg^{-1} . Furthermore, the stability study revealed that the fabricated device showed enhanced cyclic stability with a capacity retention of 153.67 % of the initial value even after 3000 cycles.

In system 5, the synthesis of PANI was carried out by oxidative polymerization of aniline monomer and then used in the development of $\text{Co}_3\text{O}_4@\text{PANI}$ and $\text{Ag}/\text{Co}_3\text{O}_4@\text{PANI}$ by hydrothermal method. Their characterizations were performed by various techniques such as FESEM, TEM, EDS, XPS, and XRD. Finally, the ternary nanocomposite sample which was producing good EC results was used in supercapattery assemblies. The fabricated device comprises of ternary nanocomposite as an anode material delivered power density of 165.00 W kg^{-1} with the corresponding energy density of 14.01 Wh kg^{-1} at a current density of 0.20 A g^{-1} . The cyclic stability value was 121.03 % after 3500 cycles, showing an excellent result.

It is evident from the outcome of different systems that material architect plays an important role in supercapattery technology. Conductivity, deagglomeration, selection of the constituent elements of nanocomposites and synthesis protocol play key role for improving energy density, power density and cyclic life of the energy storage devices. The in-depth knowledge of nano architecture of electrode materials as well as engineering strategies are vital for improving the energy storage performance of the

systems. The conducting polymers, especially polypyrrole based ternary nanocomposites are good candidates for electrochemical energy storage applications.

5.2 Future Work

The demand for high energy storage systems is growing at a rapid pace due to the trend of miniature and smart technology. The ternary nanocomposites based on noble metals have the ability to enhance the electrochemical signature of the electrode materials and demonstrate a higher specific capacity by providing transfer channels or by contributing in a redox reaction. Furthermore, the combination in the ternary nanocomposites of conducting polymers, metal oxides, and noble metals substantially enhance the electrochemical performance through the conductivity and charge-discharge ability. It is crucial to utilize the noble metals economically in order to enhance the performance of supercapattery because they are quite costly. In the future, to achieve the target of assembling the superior performance supercapattery, two kind of noble metals based nanocomposites could be utilized by overcoming some of the problems which hindered their use at a commercial scale. Even though, excellent performance has been demonstrated by single noble metals based ternary nanocomposites, but their applications are limited to the laboratory scale. Thus, an extensive research needs to be done in order to find a general, cost effective and facile procedure for developing two kind of noble metals based nanocomposites material which could be utilized at an industrial scale. In order to meet these challenges, the trend of using two kind of noble metal-based materials in high performance supercapattery demand efficient technologies that can help to develop two kind of noble metals based composites at nanoscale range so as to increase the overall surface to volume ratio and hence to reduce the noble metals loading. If we can address these issues well, the two kind of noble metal-based nanocomposites will have a very broad application prospect in supercapattery.

REFERENCES

- Abouali, S., Akbari Garakani, M., Zhang, B., Xu, Z.-L., Kamali Heidari, E., Huang, J.-q., . . . Kim, J.-K. (2015). Electrospun carbon nanofibers with in situ encapsulated Co_3O_4 nanoparticles as electrodes for high-performance supercapacitors. *ACS Applied Materials & Interfaces*, 7(24), 13503-13511.
- Ai, G., Mo, R., Li, H., & Zhong, J. (2015). Cobalt phosphate modified TiO_2 nanowire arrays as co-catalysts for solar water splitting. *Nanoscale*, 7(15), 6722-6728.
- Alshahrie, A., & Ansari, M. O. (2019). High Performance Supercapacitor Applications and DC Electrical Conductivity Retention on Surfactant Immobilized Macroporous Ternary Polypyrrole/Graphitic- C_3N_4 @Graphene Nanocomposite. *Electronic Materials Letters*, 15(2), 238-246.
- Amoruso, S., Ausanio, G., Bruzzese, R., Vitiello, M., & Wang, X. (2005). Femtosecond laser pulse irradiation of solid targets as a general route to nanoparticle formation in a vacuum. *Physical Review B*, 71(3), 033406-033410.
- Ansari, Khan, M. M., Ansari, M. O., Lee, J., & Cho, M. H. (2014). Visible light-driven photocatalytic and photoelectrochemical studies of Ag-SnO₂ nanocomposites synthesized using an electrochemically active biofilm. *RSC Advances*, 4(49), 26013-26021.
- Ansari, M. O., Khan, M. M., Ansari, S. A., Lee, J., & Cho, M. H. (2014). Enhanced thermoelectric behaviour and visible light activity of Ag@TiO₂/polyaniline nanocomposite synthesized by biogenic-chemical route. *RSC Advances*, 4(45), 23713-23719.
- Ansari, M. O., & Mohammad, F. (2011). Thermal stability, electrical conductivity and ammonia sensing studies on p-toluenesulfonic acid doped polyaniline: titanium dioxide (pTSA/Pani:TiO₂) nanocomposites. *Sensors and Actuators B: Chemical*, 157(1), 122-129.
- Ansari, R. (2006). Polypyrrole conducting electroactive polymers: synthesis and stability studies. *Journal of Chemistry*, 3(4), 186-201.
- Asen, P., & Shahrokhian, S. (2017). A high performance supercapacitor based on graphene/polypyrrole/ Cu_2O - $\text{Cu}(\text{OH})_2$ ternary nanocomposite coated on nickel foam. *The Journal of Physical Chemistry C*, 121(12), 6508-6519.
- Ates, M., Caliskan, S., & Gazi, M. (2018). A ternary nanocomposites of graphene/TiO₂/polypyrrole for energy storage applications. *Fullerenes, Nanotubes and Carbon Nanostructures*, 26(10), 631-642.
- Azar, C., Lindgren, K., & Andersson, B. A. (2003). Global energy scenarios meeting stringent CO₂ constraints—cost-effective fuel choices in the transportation sector. *Energy Policy*, 31(10), 961-976.

- Babar, P., Lokhande, A., Pawar, B., Gang, M., Jo, E., Go, C., . . . Kim, J. H. (2018). Electrocatalytic performance evaluation of cobalt hydroxide and cobalt oxide thin films for oxygen evolution reaction. *Applied Surface Science*, 427, 253-259.
- Baird, T., Fryer, J., & Grant, B. (1971). Structure of fibrous carbon. *Nature*, 233(5318), 329-330.
- Baker, R., & Waite, R. (1975). Formation of carbonaceous deposits from the platinum-iron catalyzed decomposition of acetylene. *Journal of Catalysis*, 37(1), 101-105.
- Balouch, Q., Ibupoto, Z. H., Khaskheli, G. Q., Soomro, R. A., Samoon, M. K., & Deewani, V. K. (2015). Cobalt oxide nanoflowers for electrochemical determination of glucose. *Journal of Electronic Materials*, 44(10), 3724-3732.
- Banerjee, S., Hemraj-Benny, T., & Wong, S. S. (2005). Covalent surface chemistry of single-walled carbon nanotubes. *Advanced Materials*, 17(1), 17-29.
- Bayazit, M. K., Hodge, S. A., Clancy, A. J., Menzel, R., Chen, S., & Shaffer, M. S. (2016). Carbon nanotube anions for the preparation of gold nanoparticle–nanocarbon hybrids. *Chemical Communications*, 52(9), 1934-1937.
- Béguin, F., Presser, V., Balducci, A., & Frackowiak, E. (2014). Carbons and electrolytes for advanced supercapacitors. *Advanced Materials*, 26(14), 2219-2251.
- Bolto, B. A., McNeill, R., & Weiss, D. (1963). Electronic conduction in polymers. III. Electronic properties of polypyrrole. *Australian Journal of Chemistry*, 16(6), 1090-1103.
- Brousse, T., Bélanger, D., & Long, J. W. (2015). To be or not to be pseudocapacitive? *Journal of The Electrochemical Society*, 162(5), A5185-A5189.
- Brusso, B., & Chaparala, S. (2014). The Evolution of Capacitors [History]. *IEEE Industry Applications Magazine*, 20(6), 8-12.
- Chabot, V., Higgins, D., Yu, A., Xiao, X., Chen, Z., & Zhang, J. (2014). A review of graphene and graphene oxide sponge: material synthesis and applications to energy and the environment. *Energy & Environmental Science*, 7(5), 1564-1596.
- Chang, W., Skandan, G., Hahn, H., Danforth, S., & Kear, B. (1994). Chemical vapor condensation of nanostructured ceramic powders. *Nanostructured Materials*, 4(3), 345-351.
- Cheng, G., Kou, T., Zhang, J., Si, C., Gao, H., & Zhang, Z. (2017). O₂²⁻/O⁻ functionalized oxygen-deficient Co₃O₄ nanorods as high performance supercapacitor electrodes and electrocatalysts towards water splitting. *Nano Energy*, 38, 155-166.
- Choi, W., Lahiri, I., Seelaboyina, R., & Kang, Y. S. (2010). Synthesis of graphene and its applications: a review. *Critical Reviews in Solid State and Materials Sciences*, 35(1), 52-71.
- Chong, M. Y., Numan, A., Liew, C. W., Ramesh, K., & Ramesh, S. (2017). Comparison of the performance of copper oxide and yttrium oxide nanoparticle based hydroxyethyl cellulose electrolytes for supercapacitors. *Journal of Applied Polymer Science*, 134(13), 44636-44645.

- Chou, S.-L., Wang, J.-Z., Liu, H.-K., & Dou, S.-X. (2008). Electrochemical deposition of porous Co_3O_4 nanostructured thin film for lithium-ion battery. *Journal of Power Sources*, 182(1), 359-364.
- Chougule, M. A., Pawar, S. G., Godse, P. R., Mulik, R. N., Sen, S., & Patil, V. B. (2011). Synthesis and characterization of polypyrrole (PPy) thin films. *Soft Nanoscience Letters*, 1(01), 6-10.
- Ciesla, U., & Schüth, F. (1999). Ordered mesoporous materials. *Microporous and Mesoporous Materials*, 27(2), 131-149.
- Conway, B. (1999). *The Electrolyte Factor in Supercapacitor Design and Performance: Conductivity, Ion Pairing and Solvation*. Springer, United States.
- Cordoba, M., Miranda, C., Lederhos, C., Coloma-Pascual, F., Ardila, A., Fuentes, G., . . . Ramírez, A. (2017). Catalytic performance of Co_3O_4 on different activated carbon supports in the benzyl alcohol oxidation. *Catalysts*, 7(12), 384-395.
- Cui, F., Xu, L., Cui, T., Yao, T., Yu, J., Zhang, X., & Sun, K. (2014). Facile synthesis of ultrasmall TiO_2 nanocrystals/porous carbon composites in large quantity and their photocatalytic performance under visible light. *RSC Advances*, 4(63), 33408-33415.
- D'Aprano, G., Leclerc, M., & Zotti, G. (1992). Stabilization and characterization of pernigraniline salt: the "acid-doped" form of fully oxidized polyanilines. *Macromolecules*, 25(8), 2145-2150.
- Datsyuk, V., Kalyva, M., Papangelis, K., Parthenios, J., Tasis, D., Siokou, A., . . . Galiotis, C. (2008). Chemical oxidation of multiwalled carbon nanotubes. *Carbon*, 46(6), 833-840.
- Deng, M.-J., Huang, F.-L., Sun, I.-W., Tsai, W.-T., & Chang, J.-K. (2009). An entirely electrochemical preparation of a nano-structured cobalt oxide electrode with superior redox activity. *Nanotechnology*, 20(17), 175602-175606.
- Dillon, E. C., Wilton, J. H., Barlow, J. C., & Watson, W. A. (1989). Large surface area activated charcoal and the inhibition of aspirin absorption. *Annals of Emergency Medicine*, 18(5), 547-552.
- Douglas, H., & Pillay, P. (2005). *Sizing ultracapacitors for hybrid electric vehicles*. Paper presented at the 31st Annual Conference of IEEE Industrial Electronics Society, 2005. IECON 2005.
- Dubal, D. P., Ayyad, O., Ruiz, V., & Gomez-Romero, P. (2015). Hybrid energy storage: the merging of battery and supercapacitor chemistries. *Chemical Society Reviews*, 44(7), 1777-1790.
- Duraisamy, N., Numan, A., Ramesh, K., Choi, K.-H., & Ramesh, S. (2015). Investigation on structural and electrochemical properties of binder free nanostructured nickel oxide thin film. *Materials Letters*, 161, 694-697.

- Evans, A., Strezov, V., & Evans, T. J. (2009). Assessment of sustainability indicators for renewable energy technologies. *Renewable and Sustainable Energy Reviews*, 13(5), 1082-1088.
- Fan, Z., Yan, J., Wei, T., Zhi, L., Ning, G., Li, T., & Wei, F. (2011). Asymmetric supercapacitors based on graphene/MnO₂ and activated carbon nanofiber electrodes with high power and energy density. *Advanced Functional Materials*, 21(12), 2366-2375.
- Fang, Z., Xu, W., Huang, T., Li, M., Wang, W., Liu, Y., . . . Cheng, M. (2013). Facile scalable synthesis of Co₃O₄/carbon nanotube hybrids as superior anode materials for lithium-ion batteries. *Materials Research Bulletin*, 48(10), 4419-4423.
- Feng, C., Zhang, J., He, Y., Zhong, C., Hu, W., Liu, L., & Deng, Y. (2015). Sub-3 nm Co₃O₄ nanofilms with enhanced supercapacitor properties. *ACS Nano*, 9(2), 1730-1739.
- Fernández-García, M., & Rodriguez, J. A. (2011). *Encyclopedia of Inorganic and Bioinorganic Chemistry*. John Wiley & Sons, United States.
- Ferraria, A. M., Boufi, S., Battaglini, N., Botelho do Rego, A. M., & ReiVilar, M. (2009). Hybrid systems of silver nanoparticles generated on cellulose surfaces. *Langmuir*, 26(3), 1996-2001.
- Frackowiak, E., Khomenko, V., Jurewicz, K., Lota, K., & Béguin, F. (2006). Supercapacitors based on conducting polymers/nanotubes composites. *Journal of Power Sources*, 153(2), 413-418.
- Friend, R., Gymer, R., Holmes, A., Burroughes, J., Marks, R., Taliani, C., . . . Lögdlund, M. (1999). Electroluminescence in conjugated polymers. *Nature*, 397(6715), 121-128.
- Fu, H., Du, Z.-j., Zou, W., Li, H.-q., & Zhang, C. (2013). Carbon nanotube reinforced polypyrrole nanowire network as a high-performance supercapacitor electrode. *Journal of Materials Chemistry A*, 1(47), 14943-14950.
- Fu, Q., Tietz, F., & Stöver, D. (2006). La_{0.4}Sr_{0.6}Ti_{1-x}Mn_xO_{3-δ} Perovskites as Anode Materials for Solid Oxide Fuel Cells. *Journal of The Electrochemical Society*, 153(4), 74-83.
- Ganesh, V., Pitchumani, S., & Lakshminarayanan, V. (2006). New symmetric and asymmetric supercapacitors based on high surface area porous nickel and activated carbon. *Journal of Power Sources*, 158(2), 1523-1532.
- Genies, E., Lapkowski, M., & Penneau, J. (1988). Cyclic voltammetry of polyaniline: interpretation of the middle peak. *Journal of Electroanalytical Chemistry and Interfacial Electrochemistry*, 249(1-2), 97-107.
- González, A., Goikolea, E., Barrena, J. A., & Mysyk, R. (2016). Review on supercapacitors: technologies and materials. *Renewable and Sustainable Energy Reviews*, 58, 1189-1206.

- Gospodinova, N., & Terlemezyan, L. (1998). Conducting polymers prepared by oxidative polymerization: polyaniline. *Progress in Polymer Science*, 23(8), 1443-1484.
- Grahame, D. C. (1947). The electrical double layer and the theory of electrocapillarity. *Chemical Reviews*, 41(3), 441-501.
- Greczynski, G., & Hultman, L. (2017). C 1s peak of adventitious carbon aligns to the vacuum level: dire consequences for material's bonding assignment by photoelectron spectroscopy. *Chemical Physical Chemistry Journal*, 18(12), 1507-1512.
- Han, M., Gong, Y., Zhou, J., Yin, C., Song, F., Muto, N., . . . Iwata, Y. (2002). Plume dynamics during film and nanoparticles deposition by pulsed laser ablation. *Physics Letters A*, 302(4), 182-189.
- Han, P., Yue, Y., Liu, Z., Xu, W., Zhang, L., Xu, H., . . . Cui, G. (2011). Graphene oxide nanosheets/multi-walled carbon nanotubes hybrid as an excellent electrocatalytic material towards $\text{VO}^{2+}/\text{VO}_2^+$ redox couples for vanadium redox flow batteries. *Energy & Environmental Science*, 4(11), 4710-4717.
- He, C., Sun, S., Peng, H., Tsui, C. P., Shi, D., Xie, X., & Yang, Y. (2016). Poly (ionic liquid)-assisted reduction of graphene oxide to achieve high-performance composite electrodes. *Composites Part B: Engineering*, 106, 81-87.
- Henrich, V., & Cox, P. (1994). The surface chemistry of metal oxides. Cambridge University Press, UK.
- Hepowit, L. R., Kim, K. M., Kim, S. H., Ryu, K. S., Lee, Y. M., & Ko, J. M. (2012). Supercapacitive properties of electrodeposited polypyrrole on acrylonitrile-butadiene rubber as a flexible current collector. *Polymer Bulletin*, 69(7), 873-880.
- Housecroft, C., & Sharpe, A. (2008). Inorganic Chemistry (Vol. 3). Prentice Hall, United States.
- Huang, H., Zhu, W., Tao, X., Xia, Y., Yu, Z., Fang, J., . . . Zhang, W. (2012). Nanocrystal-constructed mesoporous single-crystalline Co_3O_4 nanobelts with superior rate capability for advanced lithium-ion batteries. *ACS Applied Materials & Interfaces*, 4(11), 5974-5980.
- Huang, J.-E., Li, X.-H., Xu, J.-C., & Li, H.-L. (2003). Well-dispersed single-walled carbon nanotube/polyaniline composite films. *Carbon*, 41(14), 2731-2736.
- Huang, S., Jin, Y., & Jia, M. (2013). Preparation of graphene/ Co_3O_4 composites by hydrothermal method and their electrochemical properties. *Electrochimica Acta*, 95, 139-145.
- Huang, W.-S., Humphrey, B. D., & MacDiarmid, A. G. (1986). Polyaniline, a novel conducting polymer. Morphology and chemistry of its oxidation and reduction in aqueous electrolytes. *Journal of the Chemical Society, Faraday Transactions 1: Physical Chemistry in Condensed Phases*, 82(8), 2385-2400.
- Hummers, W. S., & Offeman, R. E. (1958). Preparation of graphitic oxide. *Journal of the American Chemical Society*, 80(6), 1339-1339.

- Iijima, S. (1991). Helical microtubules of graphitic carbon. *Nature*, 354(6348), 56-58.
- Inami, N., Mohamed, M. A., Shikoh, E., & Fujiwara, A. (2007). Synthesis-condition dependence of carbon nanotube growth by alcohol catalytic chemical vapor deposition method. *Science and Technology of Advanced Materials*, 8(4), 292-295.
- Interrante, L. V., & Hampden-Smith, M. J. (1997). *Chemistry of Advanced Materials: An Overview*. John Wiley & Sons, Germany.
- Iwama, E., Kisu, K., Naoi, W., Simon, P., & Naoi, K. (2017). *Enhanced Hybrid Supercapacitors Utilizing Nanostructured Metal Oxides*. Elsevier, Netherland.
- Jabeen, N., Xia, Q., Yang, M., & Xia, H. (2016). Unique core-shell nanorod arrays with polyaniline deposited into mesoporous NiCo₂O₄ support for high-performance supercapacitor electrodes. *ACS Applied Materials & Interfaces*, 8(9), 6093-6100.
- Jacobsson, S., & Johnson, A. (2000). The diffusion of renewable energy technology: an analytical framework and key issues for research. *Energy Policy*, 28(9), 625-640.
- Jafarian, M., Mahjani, M., Heli, H., Gobal, F., Khajehsharifi, H., & Hamed, M. (2003). A study of the electro-catalytic oxidation of methanol on a cobalt hydroxide modified glassy carbon electrode. *Electrochimica Acta*, 48(23), 3423-3429.
- Jain, P. K., Huang, X., El-Sayed, I. H., & El-Sayed, M. A. (2008). Noble metals on the nanoscale: optical and photothermal properties and some applications in imaging, sensing, biology, and medicine. *Accounts of Chemical Research*, 41(12), 1578-1586.
- Jokar, E., & Shahrokhian, S. (2014). Growth control of cobalt oxide nanoparticles on reduced graphene oxide for enhancement of electrochemical capacitance. *International Journal of Hydrogen Energy*, 39(36), 21068-21075.
- Kandalkar, S. G., Gunjekar, J., & Lokhande, C. (2008). Preparation of cobalt oxide thin films and its use in supercapacitor application. *Applied Surface Science*, 254(17), 5540-5544.
- Kang, J., Hirata, A., Kang, L., Zhang, X., Hou, Y., Chen, L., . . . Chen, M. (2013). Enhanced Supercapacitor Performance of MnO₂ by Atomic Doping. *Angewandte Chemie International Edition*, 52(6), 1664-1667.
- Kang, Y.-M., Kim, K.-T., Kim, J.-H., Kim, H.-S., Lee, P. S., Lee, J.-Y., . . . Dou, S. (2004). Electrochemical properties of Co₃O₄, Ni-Co₃O₄ mixture and Ni-Co₃O₄ composite as anode materials for Li ion secondary batteries. *Journal of Power Sources*, 133(2), 252-259.
- Katsnelson, M. I. (2007). Graphene: carbon in two dimensions. *Materials Today*, 10(1-2), 20-27.
- Khare, V., Nema, S., & Baredar, P. (2016). Solar-wind hybrid renewable energy system: A review. *Renewable and Sustainable Energy Reviews*, 58, 23-33.
- Kim, B. K., Sy, S., Yu, A., & Zhang, J. (2015). *Handbook of Clean Energy Systems*. Wiley, UK.

- Koch, C. (2003). Top-Down Synthesis Of Nanostructured Materials: Mechanical And Thermal Processing Methods. *Reviews on Advanced Materials Science*, 5(2), 91-99.
- Kötz, R., & Carlen, M. (2000). Principles and applications of electrochemical capacitors. *Electrochimica Acta*, 45(15-16), 2483-2498.
- Kouhnavard, M., Ludin, N. A., Ghaffari, B. V., Sopian, K., & Ikeda, S. (2015). Carbonaceous Materials and Their Advances as a Counter Electrode in Dye-Sensitized Solar Cells: Challenges and Prospects. *Chemistry and Sustainability Energy and Materials*, 8(9), 1510-1533.
- Kowalski, G., Pielichowski, J., & Grzesik, M. (2014). Characteristics of polyaniline cobalt supported catalysts for epoxidation reactions. *The Scientific World Journal*, 2014(1), 1-9.
- Koyama, T., Endo, M., & Onuma, Y. (1972). Carbon fibers obtained by thermal decomposition of vaporized hydrocarbon. *Japanese Journal of Applied Physics*, 11(4), 445-452.
- Krause, A., Kossyrev, P., Oljaca, M., Passerini, S., Winter, M., & Balducci, A. (2011). Electrochemical double layer capacitor and lithium-ion capacitor based on carbon black. *Journal of Power Sources*, 196(20), 8836-8842.
- Kuperman, A., & Aharon, I. (2011). Battery-ultracapacitor hybrids for pulsed current loads: A review. *Renewable and Sustainable Energy Reviews*, 15(2), 981-992.
- Kurusu, F., Tsunoda, H., Saito, A., Tomita, A., Kadota, A., Kayahara, N., . . . Gotoh, M. (2006). The advantage of using carbon nanotubes compared with edge plane pyrolytic graphite as an electrode material for oxidase-based biosensors. *Analyst*, 131(12), 1292-1298.
- Kurzweil, P., & Garcke, J. (2017). Overview of batteries for future automobiles. Elsevier.
- Lai-Kwan, C., & Chang, H.-T. (2012). From bioimaging to biosensors: noble metal nanoparticles in biodetection. Pan Stanford, United States.
- Le, T.-H., Kim, Y., & Yoon, H. (2017). Electrical and electrochemical properties of conducting polymers. *Polymers*, 9(4), 150-159.
- Lee, Y.-W., Kim, B.-S., Hong, J., Choi, H., Jang, H.-S., Hou, B., . . . Morris, S. M. (2017). Hierarchically assembled tubular shell-core-shell heterostructure of hybrid transition metal chalcogenides for high-performance supercapacitors with ultrahigh cyclability. *Nano Energy*, 37, 15-23.
- Lencka, M. M., Oledzka, M., & Riman, R. E. (2000). Hydrothermal synthesis of sodium and potassium bismuth titanates. *Chemistry of Materials*, 12(5), 1323-1330.
- Lesiak, B., Stobinski, L., Malolepszy, A., Mazurkiewicz, M., Kövér, L., & Tóth, J. (2014). Preparation of graphene oxide and characterisation using electron spectroscopy. *Journal of Electron Spectroscopy and Related Phenomena*, 193, 92-99.

- Li, B., Xie, Y., Wu, C., Li, Z., & Zhang, J. (2006). Selective synthesis of cobalt hydroxide carbonate 3D architectures and their thermal conversion to cobalt spinel 3D superstructures. *Materials Chemistry and Physics*, 99(2-3), 479-486.
- Li, D., Huang, J., & Kaner, R. B. (2008). Polyaniline nanofibers: a unique polymer nanostructure for versatile applications. *Accounts of Chemical Research*, 42(1), 135-145.
- Li, J., Zeng, X., Ren, T., & van der Heide, E. (2014). The Preparation of Graphene Oxide and Its Derivatives and Their Application in Bio-Tribological Systems. *Lubricants*, 2(3), 137-161.
- Li, J., Zhao, W., Huang, F., Manivannan, A., & Wu, N. (2011). Single-crystalline Ni(OH)₂ and NiO nanoplatelet arrays as supercapacitor electrodes. *Nanoscale*, 3(12), 5103-5109.
- Li, Y., Louarn, G., Aubert, P.-H., Alain-Rizzo, V., Galmiche, L., Audebert, P., & Miomandre, F. (2016). Polypyrrole-modified graphene sheet nanocomposites as new efficient materials for supercapacitors. *Carbon*, 105, 510-520.
- Li, Z., Zhou, Z., Yun, G., Shi, K., Lv, X., & Yang, B. (2013). High-performance solid-state supercapacitors based on graphene-ZnO hybrid nanocomposites. *Nanoscale Research Letters*, 8(1), 473-482.
- Liang, Y., Li, Y., Wang, H., Zhou, J., Wang, J., Regier, T., & Dai, H. (2011). Co₃O₄ nanocrystals on graphene as a synergistic catalyst for oxygen reduction reaction. *Nature Materials*, 10(10), 780-786.
- Liu, F., & Xue, D. (2015). Electrochemical energy storage applications of “pristine” graphene produced by non-oxidative routes. *Science China Technological Sciences*, 58(11), 1841-1850.
- Liu, J., An, J., Ma, Y., Li, M., Ma, R., Yu, M., & Li, S. (2012). Electrochemical properties comparison of the polypyrrole nanotube and polyaniline nanofiber applied in supercapacitor. *The European Physical Journal-Applied Physics*, 57(3), 30702-30708.
- Liu, J., Jiang, J., Qian, D., Tan, G., Peng, S., Yuan, H., . . . Liu, Y. (2013). Facile assembly of a 3D rGO/MWCNTs/Fe₂O₃ ternary composite as the anode material for high-performance lithium ion batteries. *RSC Advances*, 3(35), 15457-15466.
- Liu, W.-W., Lau, W.-M., & Zhang, Y. (2018). The electrochemical properties of Co₃O₄ as a lithium-ion battery electrode: a first-principles study. *Physical Chemistry Chemical Physics*, 20(38), 25016-25022.
- Liu, W., Lu, C., Li, H., Tay, R. Y., Sun, L., Wang, X., . . . Chen, Z. (2016). based all-solid-state flexible micro-supercapacitors with ultra-high rate and rapid frequency response capabilities. *Journal of Materials Chemistry A*, 4(10), 3754-3764.
- Liu, X., Long, Q., Jiang, C., Zhan, B., Li, C., Liu, S., . . . Dong, X. (2013). Facile and green synthesis of mesoporous Co₃O₄ nanocubes and their applications for supercapacitors. *Nanoscale*, 5(14), 6525-6529.

- Livage, J., Henry, M., & Sanchez, C. (1988). Sol-gel chemistry of transition metal oxides. *Progress in Solid State Chemistry*, 18(4), 259-341.
- Loryuenyong, V., Totepvimarn, K., Eimburanaprat, P., Boonchompoo, W., & Buasri, A. (2013). Preparation and characterization of reduced graphene oxide sheets via water-based exfoliation and reduction methods. *Advances in Materials Science and Engineering*, 2013(1), 1-5.
- Lota, G., Fic, K., & Frackowiak, E. (2011). Carbon nanotubes and their composites in electrochemical applications. *Energy & Environmental Science*, 4(5), 1592-1605.
- Low, W. H., Khiew, P. S., Lim, S. S., Siong, C. W., & Ezeigwe, E. R. (2018). Recent development of mixed transition metal oxide and graphene/mixed transition metal oxide based hybrid nanostructures for advanced supercapacitors. *Journal of Alloys and Compounds*, 75, 1324-1356.
- Lu, X., Zhai, T., Zhang, X., Shen, Y., Yuan, L., Hu, B., . . . Wang, Z. L. (2012). WO₃-x@Au@MnO₂ Core-Shell Nanowires on Carbon Fabric for High-Performance Flexible Supercapacitors. *Advanced Materials*, 24(7), 938-944.
- Lu, Z., Yang, Q., Zhu, W., Chang, Z., Liu, J., Sun, X., . . . Duan, X. (2012). Hierarchical Co₃O₄@Ni-Co-O supercapacitor electrodes with ultrahigh specific capacitance per area. *Nano Research*, 5(5), 369-378.
- Lue, J. T. (2007). Physical properties of nanomaterials. *Encyclopedia of Nanoscience and Nanotechnology*, 10(1), 1-46.
- Lyman, C. E., Newbury, D. E., Goldstein, J., Williams, D. B., Romig Jr, A. D., Armstrong, J., . . . Lifshin, E. (2012). Scanning electron microscopy, X-ray microanalysis, and analytical electron microscopy: a laboratory workbook. Plenum Press, United States.
- Ma, L., Shen, X., Ji, Z., Zhu, G., & Zhou, H. (2014). Ag nanoparticles decorated MnO₂/reduced graphene oxide as advanced electrode materials for supercapacitors. *Chemical Engineering Journal*, 252, 95-103.
- Macdiarmid, A. G., & Epstein, A. J. (1992). Polyaniline: interrelationships between molecular weight, morphology, Donnan potential and conductivity. *MRS Online Proceedings Library Archive*, 247(1) 565-576.
- Mahore, R., Kondawar, S., Burghate, D., & Meshram, B. (2015). Electrochemical performance of polyaniline/CNT/MnO₂ and polypyrrole/CNT/MnO₂ ternary nanocomposites as electrode materials for supercapacitor. *Journal of the Chinese Advanced Materials Society*, 3(1), 45-56.
- Mai, L. (2015). Semiconductor nanowire battery electrodes, Materials, Synthesis, Characterization and Applications. Woodhead Publishing, UK.
- Malik, M. A., Wani, M. Y., & Hashim, M. A. (2012). Microemulsion method: A novel route to synthesize organic and inorganic nanomaterials: 1st Nano Update. *Arabian Journal of Chemistry*, 5(4), 397-417.

- Malitesta, C., Losito, I., Sabbatini, L., & Zambonin, P. (1995). New findings on polypyrrole chemical structure by XPS coupled to chemical derivatization labelling. *Journal of Electron Spectroscopy and Related Phenomena*, 76, 629-634.
- Manigandan, R., Giribabu, K., Suresh, R., Vijayalakshmi, L., Stephen, A., & Narayanan, V. (2013). Cobalt oxide nanoparticles: characterization and its electrocatalytic activity towards nitrobenzene. *Chemical Science Transactions*, 2(1), 47-50.
- Mao, S. S., & Chen, X. (2007). Selected nanotechnologies for renewable energy applications. *International Journal of Energy Research*, 31(6-7), 619-636.
- Marik, S., Moran, E., Labrugère, C., Toulemonde, O., & Alario-Franco, M. A. (2012). $\text{Mo}_x\text{Cu}_{1-x}\text{Sr}_2\text{YCu}_2\text{O}_y$ ($0.3 \leq x \leq 1$) revisited: Superconductivity, magnetism and the molybdenum oxidation state. *Journal of Solid State Chemistry*, 191, 40-45.
- Mattevi, C., Eda, G., Agnoli, S., Miller, S., Mkhoyan, K. A., Celik, O., . . . Chhowalla, M. (2009). Evolution of electrical, chemical, and structural properties of transparent and conducting chemically derived graphene thin films. *Advanced Functional Materials*, 19(16), 2577-2583.
- Meher, S. K., & Rao, G. R. (2011). Ultralayered Co_3O_4 for high-performance supercapacitor applications. *The Journal of Physical Chemistry C*, 115(31), 15646-15654.
- Meng, T., Xu, Q.-Q., Wang, Z.-H., Li, Y.-T., Gao, Z.-M., Xing, X.-Y., & Ren, T.-Z. (2015). Co_3O_4 nanorods with self-assembled nanoparticles in queue for supercapacitor. *Electrochimica Acta*, 180, 104-111.
- Meregalli, V., & Parrinello, M. (2001). Review of theoretical calculations of hydrogen storage in carbon-based materials. *Applied Physics A*, 72(2), 143-146.
- Mike, J. F., & Lutkenhaus, J. L. (2013). Recent advances in conjugated polymer energy storage. *Journal of Polymer Science Part B: Polymer Physics*, 51(7), 468-480.
- Miller, J. R., & Simon, P. (2008). Electrochemical capacitors for energy management. *Science*, 321(5889), 651-652.
- Moro, F., Tang, S. V. Y., Tuna, F., & Lester, E. (2013). Magnetic properties of cobalt oxide nanoparticles synthesised by a continuous hydrothermal method. *Journal of Magnetism and Magnetic Materials*, 348, 1-7.
- Mostafaei, A., & Zolriasatein, A. (2012). Synthesis and characterization of conducting polyaniline nanocomposites containing ZnO nanorods. *Progress in Natural Science: Materials International*, 22(4), 273-280.
- Mu, J., Zhang, L., Zhao, M., & Wang, Y. (2013). Co_3O_4 nanoparticles as an efficient catalase mimic: Properties, mechanism and its electrocatalytic sensing application for hydrogen peroxide. *Journal of Molecular Catalysis A: Chemical*, 378, 30-37.
- Nadiah, N., Omar, F. S., Numan, A., Mahipal, Y., Ramesh, S., & Ramesh, K. (2017). Influence of acrylic acid on ethylene carbonate/dimethyl carbonate based liquid

electrolyte and its supercapacitor application. *International Journal of Hydrogen Energy*, 42(52), 30683-30690.

- Natile, M. M., & Glisenti, A. (2003). New NiO/Co₃O₄ and Fe₂O₃/Co₃O₄ nanocomposite catalysts: synthesis and characterization. *Chemistry of Materials*, 15(13), 2502-2510.
- Nguyen, T. T., Deivasigamani, R. K., Kharismadewi, D., Iwai, Y., & Shim, J.-J. (2016). Facile synthesis of cobalt oxide/reduced graphene oxide composites for electrochemical capacitor and sensor applications. *Solid State Sciences*, 53, 71-77.
- Niu, H., Yang, X., Jiang, H., Zhou, D., Li, X., Zhang, T., . . . Qu, F. (2015). Hierarchical core-shell heterostructure of porous carbon nanofiber@ZnCo₂O₄ nanoneedle arrays: advanced binder-free electrodes for all-solid-state supercapacitors. *Journal of Materials Chemistry A*, 3(47), 24082-24094.
- Noguera, C. (1996). *Physics and chemistry at oxide surfaces*. Cambridge University Press, United Kingdom.
- Noh, Y.-J., Park, S.-C., Hwang, I.-T., Choi, J.-H., Kim, S.-S., Jung, C.-H., & Na, S.-I. (2014). High-performance polymer solar cells with radiation-induced and reduction-controllable reduced graphene oxide as an advanced hole transporting material. *Carbon*, 79, 321-329.
- Numan, A., Duraisamy, N., Omar, F. S., Mahipal, Y., Ramesh, K., & Ramesh, S. (2016). Enhanced electrochemical performance of cobalt oxide nanocube intercalated reduced graphene oxide for supercapacitor application. *RSC Advances*, 6(41), 34894-34902.
- Numan, A., Shahid, M. M., Omar, F. S., Rafique, S., Bashir, S., Ramesh, K., & Ramesh, S. (2017). Binary nanocomposite based on Co₃O₄ nanocubes and multiwalled carbon nanotubes as an ultrasensitive platform for amperometric determination of dopamine. *Microchimica Acta*, 184(8), 2739-2748.
- Numan, A., Shahid, M. M., Omar, F. S., Ramesh, K., & Ramesh, S. (2017). Facile fabrication of cobalt oxide nanograin-decorated reduced graphene oxide composite as ultrasensitive platform for dopamine detection. *Sensors and Actuators B: Chemical*, 238, 1043-1051.
- O'connell, M. J. (2006). *Carbon nanotubes: properties and applications*. CRC Press, United States.
- Obaid, A., El-Mossalamy, E., Al-Thabaiti, S., El-Hallag, I., Hermas, A., & Asiri, A. (2014). Electrodeposition and characterization of polyaniline on stainless steel surface via cyclic, convolutive voltammetry and SEM in aqueous acidic solutions. *International Journal of Electrochemical Science*, 9(2), 1003-1015.
- Omar, F. S., Numan, A., Duraisamy, N., Bashir, S., Ramesh, K., & Ramesh, S. (2016). Ultrahigh capacitance of amorphous nickel phosphate for asymmetric supercapacitor applications. *RSC Advances*, 6(80), 76298-76306.

- Omar, F. S., Numan, A., Duraisamy, N., Ramly, M. M., Ramesh, K., & Ramesh, S. (2017). Binary composite of polyaniline/copper cobaltite for high performance asymmetric supercapacitor application. *Electrochimica Acta*, 227, 41-48.
- Omar, S. F., Numan, A., Duraisamy, N., Bashir, S., Ramesh, K., & Ramesh, S. (2017). A promising binary nanocomposite of zinc cobaltite intercalated with polyaniline for supercapacitor and hydrazine sensor. *Journal of Alloys and Compounds*, 716, 96-105.
- Ozoemena, K. I., & Chen, S. (2016). *Nanomaterials in Advanced Batteries and Supercapacitors*. Springer, Switzerland.
- Padwal, P., Kadam, S., Mane, S., & Kulkarni, S. (2016). Synthesis and characterization of supercapacitive behavior of electrodeposited PANI/Co₃O₄ layered composite electrode. *Journal of the Chinese Advanced Materials Society*, 4(1), 13-23.
- Pan, H., Li, J., & Feng, Y. (2010). Carbon nanotubes for supercapacitor. *Nanoscale Research Letters*, 5(3), 654-668.
- Pandey, A. K., Pandey, P. C., Agrawal, N. R., & Das, I. (2018). Synthesis and characterization of dendritic polypyrrole silver nanocomposite and its application as a new urea biosensor. *Journal of Applied Polymer Science*, 135(3), 45705-45715.
- Paul, P. (2009). *Value Added Products from Gasification Activated Carbon*. Department of Aerospace Engineering Indian Institute of Science, India.
- Peng, H., Ma, G., Mu, J., Sun, K., & Lei, Z. (2014). Low-cost and high energy density asymmetric supercapacitors based on polyaniline nanotubes and MoO₃ nanobelts. *Journal of Materials Chemistry A*, 2(27), 10384-10388.
- Popov, V. N. (2004). Carbon nanotubes: properties and application. *Materials Science and Engineering: R: Reports*, 43(3), 61-102.
- Qorbani, M., Naseri, N., & Moshfegh, A. Z. (2015). Hierarchical Co₃O₄/Co(OH)₂ nanoflakes as a supercapacitor electrode: experimental and semi-empirical model. *ACS Applied Materials & Interfaces*, 7(21), 11172-11179.
- Rafique, S., Abdullah, S. M., Iqbal, J., Jilani, A., Vattamkandathil, S., & Iwamoto, M. (2018). Moderately reduced graphene oxide via UV-ozone treatment as hole transport layer for high efficiency organic solar cells. *Organic Electronics*, 59, 140-148.
- Rafique, S., Abdullah, S. M., Sulaiman, K., & Iwamoto, M. (2017). Layer by layer characterisation of the degradation process in PCDTBT:PC71BM based normal architecture polymer solar cells. *Organic Electronics*, 40, 65-74.
- Rajput, N. (2015). Methods of preparation of nanoparticles-A review. *International Journal of Advances In Engineering & Technology*, 7(6), 1806-1811.
- Ramadoss, A., & Kim, S. J. (2013). Vertically aligned TiO₂ nanorod arrays for electrochemical supercapacitor. *Journal of Alloys and Compounds*, 561, 262-267.

- Ray, A., Asturias, G., Kershner, D., Richter, A., MacDiarmid, A., & Epstein, A. (1989). Polyaniline: Doping, structure and derivatives. *Synthetic Metals*, 29(1), 141-150.
- Raymundo-Pinero, E., Kierzek, K., Machnikowski, J., & Béguin, F. (2006). Relationship between the nanoporous texture of activated carbons and their capacitance properties in different electrolytes. *Carbon*, 44(12), 2498-2507.
- Ren, X., Fan, H., Ma, J., Wang, C., Zhang, M., & Zhao, N. (2018). Hierarchical Co₃O₄/PANI hollow nanocages: synthesis and application for electrode materials of supercapacitors. *Applied Surface Science*, 441, 194-203.
- Roberts, M. E., Wheeler, D. R., McKenzie, B. B., & Bunker, B. C. (2009). High specific capacitance conducting polymer supercapacitor electrodes based on poly (tris (thiophenylphenyl) amine). *Journal of Materials Chemistry*, 19(38), 6977-6979.
- Rodriguez, J. A., & Fernández-García, M. (2007). Synthesis, properties, and applications of oxide nanomaterials. John Wiley & Sons, United States.
- Roy-Mayhew, J. D., & Aksay, I. A. (2014). Graphene materials and their use in dye-sensitized solar cells. *Chemical Reviews*, 114(12), 6323-6348.
- Sadegh, H., & Shahryari-ghoshekandi, R. (2015). Functionalization of carbon nanotubes and its application in nanomedicine: A review. *Nanomedicine Journal*, 2(4), 231-248.
- Salunkhe, R. R., Jang, K., Yu, H., Yu, S., Ganesh, T., Han, S.-H., & Ahn, H. (2011). Chemical synthesis and electrochemical analysis of nickel cobaltite nanostructures for supercapacitor applications. *Journal of Alloys and Compounds*, 509(23), 6677-6682.
- Salunkhe, R. R., Tang, J., Kamachi, Y., Nakato, T., Kim, J. H., & Yamauchi, Y. (2015). Asymmetric supercapacitors using 3D nanoporous carbon and cobalt oxide electrodes synthesized from a single metal-organic framework. *ACS Nano*, 9(6), 6288-6296.
- Sathish, M., Miyazawa, K., & Sasaki, T. (2007). Nanoporous fullerene nanowhiskers. *Chemistry of Materials*, 19(10), 2398-2400.
- Savvatimskiy, A. (2005). Measurements of the melting point of graphite and the properties of liquid carbon (a review for 1963–2003). *Carbon*, 43(6), 1115-1142.
- Schütter, C., Ramirez-Castro, C., Oljaca, M., Passerini, S., Winter, M., & Balducci, A. (2015). Activated carbon, carbon blacks and graphene based nanoplatelets as active materials for electrochemical double layer capacitors: a comparative study. *Journal of The Electrochemical Society*, 162(1), 44-51.
- Seredych, M., Tamashausky, A. V., & Bandosz, T. J. (2010). Graphite oxides obtained from porous graphite: the role of surface chemistry and texture in ammonia retention at ambient conditions. *Advanced Functional Materials*, 20(10), 1670-1679.
- Shahabuddin, S., Arshid, N., Shahid, M. M., Khanam, R., Saidur, R., Pandey, A., & Ramesh, S. (2019). Polyaniline-SrTiO₃ nanocube based binary nanocomposite as

highly stable electrode material for supercapacitors. *Ceramics International*, 450(9), 11428-11437.

- Shahid, M. M., Ismail, A. H., AL-Mokaram, A. M. A. A., Vikneswaran, R., Ahmad, S., Hamza, A., & Numan, A. (2017). A single-step synthesis of nitrogen-doped graphene sheets decorated with cobalt hydroxide nanoflakes for the determination of dopamine. *Progress in Natural Science: Materials International*, 27(5), 582-587.
- Shahid, M. M., Rameshkumar, P., Basirunc, W. J., Wijayantha, U., Chiu, W. S., Khiew, P. S., & Huang, N. M. (2018). An electrochemical sensing platform of cobalt oxide@gold nanocubes interleaved reduced graphene oxide for the selective determination of hydrazine. *Electrochimica Acta*, 259, 606-616.
- Shahid, M. M., Rameshkumar, P., & Huang, N. M. (2015). Morphology dependent electrocatalytic properties of hydrothermally synthesized cobalt oxide nanostructures. *Ceramics International*, 41(10), 13210-13217.
- Shahid, M. M., Rameshkumar, P., Pandikumar, A., Lim, H. N., Ng, Y. H., & Huang, N. M. (2015). An electrochemical sensing platform based on a reduced graphene oxide-cobalt oxide nanocube@platinum nanocomposite for nitric oxide detection. *Journal of Materials Chemistry A*, 3(27), 14458-14468.
- Shameli, K., Ahmad, M. B., Zamanian, A., Sangpour, P., Shabanzadeh, P., Abdollahi, Y., & Zargar, M. (2012). Green biosynthesis of silver nanoparticles using *Curcuma longa* tuber powder. *International Journal of Nanomedicine*, 7, 5603-5610.
- Shan, C., Li, F., Yuan, F., Yang, G., Niu, L., & Zhang, Q. (2008). Size-controlled synthesis of monodispersed gold nanoparticles stabilized by polyelectrolyte-functionalized ionic liquid. *Nanotechnology*, 19(28), 285601-285606.
- Shan, H., Zhao, Y., Li, X., Xiong, D., Dong, L., Yan, B., . . . Sun, X. (2016). Carbon nanotubes cross-linked Zn₂SnO₄ nanoparticles/graphene networks as high capacities, long life anode materials for lithium ion batteries. *Journal of Applied Electrochemistry*, 46(8), 851-860.
- Sharma, P., & Bhatti, T. (2010). A review on electrochemical double-layer capacitors. *Energy Conversion and Management*, 51(12), 2901-2912.
- Sherman, A. (1987). Chemical vapor deposition for microelectronics: principles, technology, and applications (Vol. 1). International Atomic Energy Agency, Austria.
- Shirakawa, H., Louis, E. J., MacDiarmid, A. G., Chiang, C. K., & Heeger, A. J. (1977). Synthesis of electrically conducting organic polymers: halogen derivatives of polyacetylene,(CH)_x. *Journal of the Chemical Society, Chemical Communications*, (16), 578-580.
- Shrestha, L. K., Ji, Q., Mori, T., Miyazawa, K. i., Yamauchi, Y., Hill, J. P., & Ariga, K. (2013). Fullerene nanoarchitectonics: from zero to higher dimensions. *Chemistry–An Asian Journal*, 8(8), 1662-1679.

- Shrestha, L. K., Yamauchi, Y., Hill, J. P., Miyazawa, K. i., & Ariga, K. (2012). Fullerene crystals with bimodal pore architectures consisting of macropores and mesopores. *Journal of the American Chemical Society*, 135(2), 586-589.
- Shukla, A., Sampath, S., & Vijayamohanan, K. (2000). Electrochemical supercapacitors: Energy storage beyond batteries. *Current Science*, 79(12), 1656-1661.
- Simon, P., & Gogotsi, Y. (2010). Materials for electrochemical capacitors. World Scientific, Singapore.
- Simon, P., Gogotsi, Y., & Dunn, B. (2014). Where do batteries end and supercapacitors begin? *Science*, 343(6176), 1210-1211.
- Simon, P., Gogotsi, Y., Schneuwly, A., & Gallay, R. (2008). Materials for electrochemical capacitors nature materials. *Properties and applications of supercapacitors, From The State-of-The-Art to Future Trends*, 7(1), 45-55.
- Singh, A., Jain, D., Upadhyay, M., Khandelwal, N., & Verma, H. (2010). Green synthesis of silver nanoparticles using Argemone mexicana leaf extract and evaluation of their antimicrobial activities. *Digest Journal of Nanomaterials and Biostructures*, 5(2), 483-489.
- Smith, R. A. (2009). Surface Characterisation of Heterogeneous Catalysts by XPS: Part II. *Platinum Metals Review*, 53(2), 109-110.
- Smith, T. (1983). A review of carbon black pigments. *Pigment & Resin Technology*, 12(4), 14-16.
- Snook, G. A., Kao, P., & Best, A. S. (2011). Conducting-polymer-based supercapacitor devices and electrodes. *Journal of Power Sources*, 196(1), 1-12.
- Spinks, G. M., Mottaghitalab, V., Bahrami-Samani, M., Whitten, P. G., & Wallace, G. G. (2006). Carbon-nanotube-reinforced polyaniline fibers for high-strength artificial muscles. *Advanced Materials*, 18(5), 637-640.
- Strom, E. T., & Rasmussen, S. C. (2011). 100+ years of plastics. Leo Baekeland and Beyond. ACS Publications, United States.
- Su, N., Li, H., Yuan, S., Yi, S., & Yin, E. (2012). Synthesis and characterization of polypyrrole doped with anionic spherical polyelectrolyte brushes. *Express Polymer Letters*, 6(9), 697-705.
- Sugimoto, W., Iwata, H., Yokoshima, K., Murakami, Y., & Takasu, Y. (2005). Proton and electron conductivity in hydrous ruthenium oxides evaluated by electrochemical impedance spectroscopy: the origin of large capacitance. *The Journal of Physical Chemistry B*, 109(15), 7330-7338.
- Suryanarayana, C. (2001). Mechanical alloying and milling. *Progress in Materials Science*, 46(1), 1-184.
- Taberna, P.-L., Mitra, S., Poizot, P., Simon, P., & Tarascon, J.-M. (2006). High rate capabilities Fe₃O₄-based Cu nano-architected electrodes for lithium-ion battery applications. *Nature Materials*, 5(7), 567-573.

- Tan, Y., Gao, Q., Li, Z., Tian, W., Qian, W., Yang, C., & Zhang, H. (2016). Unique 1D Co_3O_4 crystallized nanofibers with (220) oriented facets as high-performance lithium ion battery anode material. *Scientific Reports*, 6, 26460-26467.
- Tan, Y., Gao, Q., Yang, C., Yang, K., Tian, W., & Zhu, L. (2015). One-dimensional porous nanofibers of Co_3O_4 on the carbon matrix from human hair with superior lithium ion storage performance. *Scientific Reports*, 5, 12382-12392.
- Tang, C., Tang, Z., & Gong, H. (2012). Hierarchically porous Ni-Co oxide for high reversibility asymmetric full-cell supercapacitors. *Journal of The Electrochemical Society*, 159(5), A651-A656.
- Tang, L., Duan, F., & Chen, M. (2016). Silver nanoparticle decorated polyaniline/multiwalled super-short carbon nanotube nanocomposites for supercapacitor applications. *RSC Advances*, 6(69), 65012-65019.
- Thu, T. V., Van Nguyen, T., Le Duong, X., Le Son, T., Van Thuy, V., Huy, T. Q., & Truong, Q.-D. (2019). Graphene- MnFe_2O_4 -polypyrrole ternary hybrids with synergistic effect for supercapacitor electrode. *Electrochimica Acta*, 314, 151-160.
- Tian, H., Wan, C., Xue, X., Hu, X., & Wang, X. (2017). Effective electron transfer pathway of the ternary $\text{TiO}_2/\text{RGO}/\text{Ag}$ nanocomposite with enhanced photocatalytic activity under visible light. *Catalysts*, 7(5), 156-170.
- Trasatti, S., & Kurzweil, P. (1994). Electrochemical supercapacitors as versatile energy stores. *Platinum Metals Review*, 38(2), 46-56.
- Tummala, R., Guduru, R. K., & Mohanty, P. S. (2012). Nanostructured Co_3O_4 electrodes for supercapacitor applications from plasma spray technique. *Journal of Power Sources*, 209, 44-51.
- Upadhyayula, V. K. (2012). Functionalized gold nanoparticle supported sensory mechanisms applied in detection of chemical and biological threat agents: a review. *Analytica Chimica Acta*, 715, 1-18.
- Uskoković, V., & Drogenik, M. (2005). Synthesis of materials within reverse micelles. *Surface Review and Letters*, 12(02), 239-277.
- Walker Jr, P., Rakszawski, J., & Imperial, G. (1959). Carbon formation from carbon monoxide-hydrogen mixtures over iron catalysts. I. Properties of carbon formed. *The Journal of Physical Chemistry*, 63(2), 133-140.
- Wan, P., Wen, X., Sun, C., Chandran, B. K., Zhang, H., Sun, X., & Chen, X. (2015). Flexible Transparent Films Based on Nanocomposite Networks of Polyaniline and Carbon Nanotubes for High-Performance Gas Sensing. *Small*, 11(40), 5409-5415.
- Wang, Han, X., Sommers, A., Park, Y., T'Joen, C., & Jacobi, A. (2012). A review on application of carbonaceous materials and carbon matrix composites for heat exchangers and heat sinks. *International Journal of Refrigeration*, 35(1), 7-26.

- Wang, G., Zhang, L., & Zhang, J. (2012). A review of electrode materials for electrochemical supercapacitors. *Chemical Society Reviews*, 41(2), 797-828.
- Wang, J., Dou, W., Zhang, X., Han, W., Mu, X., Zhang, Y., . . . Su, Q. (2017). Embedded Ag quantum dots into interconnected Co₃O₄ nanosheets grown on 3D graphene networks for high stable and flexible supercapacitors. *Electrochimica Acta*, 224, 260-268.
- Wang, L., Feng, X., Ren, L., Piao, Q., Zhong, J., Wang, Y., . . . Wang, B. (2015). Flexible solid-state supercapacitor based on a metal–organic framework interwoven by electrochemically-deposited PANI. *Journal of the American Chemical Society*, 137(15), 4920-4923.
- Wang, L., Meric, I., Huang, P., Gao, Q., Gao, Y., Tran, H., . . . Muller, D. (2013). One-dimensional electrical contact to a two-dimensional material. *Science*, 342(6158), 614-617.
- Wang, Q., Chen, D., & Zhang, D. (2015). Electrospun porous CuCo₂O₄ nanowire network electrode for asymmetric supercapacitors. *RSC Advances*, 5(117), 96448-96454.
- Wang, Q., Zhang, Y., Jiang, H., Hu, T., & Meng, C. (2018). In situ generated Ni₃Si₂O₅(OH)₄ on mesoporous heteroatom-enriched carbon derived from natural bamboo leaves for high-performance supercapacitors. *ACS Applied Energy Materials*, 1(7), 3396-3409.
- Wang, X., Li, M., Chang, Z., Yang, Y., Wu, Y., & Liu, X. (2015). Co₃O₄@MWCNT nanocable as cathode with superior electrochemical performance for supercapacitors. *ACS Applied Materials & Interfaces*, 7(4), 2280-2285.
- Wang, Y.-g., & Xia, Y.-y. (2006). Electrochemical capacitance characterization of NiO with ordered mesoporous structure synthesized by template SBA-15. *Electrochimica Acta*, 51(16), 3223-3227.
- Weber, A. Z., Mench, M. M., Meyers, J. P., Ross, P. N., Gostick, J. T., & Liu, Q. (2011). Redox flow batteries: a review. *Journal of Applied Electrochemistry*, 41(10), 1137-1164.
- Wessling, B. (1998). Dispersion as the link between basic research and commercial applications of conductive polymers (polyaniline). *Synthetic Metals*, 93(2), 143-154.
- Wissler, M. (2006). Graphite and carbon powders for electrochemical applications. *Journal of Power Sources*, 156(2), 142-150.
- Wnek, G. E. (1986). A proposal for the mechanism of conduction in polyaniline. *Synthetic Metals*, 15(2-3), 213-218.
- Wu, C.-S., Liu, F.-K., & Ko, F.-H. (2011). Potential role of gold nanoparticles for improved analytical methods: an introduction to characterizations and applications. *Analytical and Bioanalytical Chemistry*, 399(1), 103-118.

- Wu, Z., Xie, L., Xiao, Y., & Wang, D. (2017). Silver wrapped MoS₂ hybrid electrode materials for high-performance supercapacitor. *Journal of Alloys and Compounds*, 708, 763-768.
- Xia, H., Hong, C., Shi, X., Li, B., Yuan, G., Yao, Q., & Xie, J. (2015). Hierarchical heterostructures of Ag nanoparticles decorated MnO₂ nanowires as promising electrodes for supercapacitors. *Journal of Materials Chemistry A*, 3(3), 1216-1221.
- Xia, H., Zhu, D., Luo, Z., Yu, Y., Shi, X., Yuan, G., & Xie, J. (2013). Hierarchically structured Co₃O₄@Pt@MnO₂ nanowire arrays for high-performance supercapacitors. *Scientific Reports*, 3, 2978-2985.
- Xia, X.-h., Tu, J.-p., Mai, Y.-j., Wang, X.-l., Gu, C.-d., & Zhao, X.-b. (2011). Self-supported hydrothermal synthesized hollow Co₃O₄ nanowire arrays with high supercapacitor capacitance. *Journal of Materials Chemistry*, 21(25), 9319-9325.
- Xiang, C., Li, M., Zhi, M., Manivannan, A., & Wu, N. (2013). A reduced graphene oxide/Co₃O₄ composite for supercapacitor electrode. *Journal of Power Sources*, 226, 65-70.
- Xie, X., Li, Y., Liu, Z.-Q., Haruta, M., & Shen, W. (2009). Low-temperature oxidation of CO catalysed by Co₃O₄ nanorods. *Nature*, 458(7239), 746-749.
- Xiong, S., Chen, J. S., Lou, X. W., & Zeng, H. C. (2012). Mesoporous Co₃O₄ and CoO@C Topotactically Transformed from Chrysanthemum-like Co (CO₃)_{0.5}(OH)·0.11H₂O and Their Lithium-Storage Properties. *Advanced Functional Materials*, 22(4), 861-871.
- Xu, De, S., Balu, A. M., Ojeda, M., & Luque, R. (2015). Mechanochemical synthesis of advanced nanomaterials for catalytic applications. *Chemical Communications*, 51(31), 6698-6713.
- Xu, J., Gao, L., Cao, J., Wang, W., & Chen, Z. (2010). Preparation and electrochemical capacitance of cobalt oxide (Co₃O₄) nanotubes as supercapacitor material. *Electrochimica Acta*, 56(2), 732-736.
- Xu, X., Shen, J., Li, N., & Ye, M. (2014). Facile synthesis of reduced graphene oxide/CoWO₄ nanocomposites with enhanced electrochemical performances for supercapacitors. *Electrochimica Acta*, 150, 23-34.
- Xu, Y., Wei, J., Tan, L., Yu, J., & Chen, Y. (2015). A Facile approach to NiCoO₂ intimately standing on nitrogen doped graphene sheets by one-step hydrothermal synthesis for supercapacitors. *Journal of Materials Chemistry A*, 3(13), 7121-7131.
- Yan, J., Fan, Z., Wei, T., Qian, W., Zhang, M., & Wei, F. (2010). Fast and reversible surface redox reaction of graphene-MnO₂ composites as supercapacitor electrodes. *Carbon*, 48(13), 3825-3833.
- Yang, L., Zhang, Z., Nie, G., Wang, C., & Lu, X. (2015). Fabrication of conducting polymer/noble metal composite nanorings and their enhanced catalytic properties. *Journal of Materials Chemistry A*, 3(1), 83-86.

- Younis, A., Chu, D., Lin, X., Lee, J., & Li, S. (2013). Bipolar resistive switching in p-type Co_3O_4 nanosheets prepared by electrochemical deposition. *Nanoscale Research Letters*, 8(1), 36-40.
- Yuan, C., Yang, L., Hou, L., Shen, L., Zhang, X., & Lou, X. W. D. (2012). Growth of ultrathin mesoporous Co_3O_4 nanosheet arrays on Ni foam for high-performance electrochemical capacitors. *Energy & Environmental Science*, 5(7), 7883-7887.
- Zhang, L., Liang, J., Huang, Y., Ma, Y., Wang, Y., & Chen, Y. (2009). Size-controlled synthesis of graphene oxide sheets on a large scale using chemical exfoliation. *Carbon*, 47(14), 3365-3368.
- Zhang, L. L., & Zhao, X. (2009). Carbon-based materials as supercapacitor electrodes. *Chemical Society Reviews*, 38(9), 2520-2531.
- Zhang, S., & Pan, N. (2015). Supercapacitors performance evaluation. *Advanced Energy Materials*, 5(6), 1401401-1401409.
- Zhang, W.-J., & Huang, K.-J. (2017). A review of recent progress in molybdenum disulfide-based supercapacitors and batteries. *Inorganic Chemistry Frontiers*, 4(10), 1602-1620.
- Zhang, X., Wang, J., Liu, J., Wu, J., Chen, H., & Bi, H. (2017). Design and preparation of a ternary composite of graphene oxide/carbon dots/polypyrrole for supercapacitor application: importance and unique role of carbon dots. *Carbon*, 115, 134-146.
- Zhang, X., Zeng, X., Yang, M., & Qi, Y. (2014). Investigation of a branchlike MoO_3 /polypyrrole hybrid with enhanced electrochemical performance used as an electrode in supercapacitors. *ACS Applied Materials & Interfaces*, 6(2), 1125-1130.
- Zheng, J., Zhang, Y., Wang, Q., Jiang, H., Liu, Y., Lv, T., & Meng, C. (2018). Hydrothermal encapsulation of $\text{VO}_2(\text{A})$ nanorods in amorphous carbon by carbonization of glucose for energy storage devices. *Dalton Transactions*, 47(2), 452-464.
- Zhi, M., Xiang, C., Li, J., Li, M., & Wu, N. (2013). Nanostructured carbon-metal oxide composite electrodes for supercapacitors: a review. *Nanoscale*, 5(1), 72-88.
- Zhou, Y.-k., He, B.-l., Zhou, W.-j., Huang, J., Li, X.-h., Wu, B., & Li, H.-l. (2004). Electrochemical capacitance of well-coated single-walled carbon nanotube with polyaniline composites. *Electrochimica Acta*, 49(2), 257-262.
- Zhou, Y., Yang, J., He, T., Shi, H., Cheng, X., & Lu, Y. (2013). Highly stable and dispersive silver nanoparticle-graphene composites by a simple and low-energy-consuming approach and their antimicrobial activity. *Small*, 9(20), 3445-3454.
- Zhu, H., Peng, S., & Jiang, W. (2013). Electrochemical properties of PANI as single electrode of electrochemical capacitors in acid electrolytes. *The Scientific World Journal*, 2013, 1-8.

Zhu, J., Jiang, J., Sun, Z., Luo, J., Fan, Z., Huang, X., . . . Yu, T. (2014). 3D Carbon/Cobalt-Nickel Mixed-Oxide Hybrid Nanostructured Arrays for Asymmetric Supercapacitors. *Small*, 10(14), 2937-2945.

Universiti Malaya